SOME ASPECTS OF HIGH E_T JETS IN p-p COLLISIONS AT LHC

A THESIS

submitted to the

FACULTY OF SCIENCE

PANJAB UNIVERSITY CHANDIGARH

for the degree of

DOCTOR OF PHILOSOPHY

2007

Harinder Singh Bawa

CENTRE OF ADVANCED STUDY IN PHYSICS

PANJAB UNIVERSITY CHANDIGARH

Dedicated to my family.............

Acknowledgement

As I stand at the threshold of earning my doctorate, I am overwhelmed when I recall some of the people who have helped me get this far.

First and the foremost, I would like to thank my Ph.D. advisors Prof. Manjit Kaur and Prof. J.M.Kohli for their constant support, guidance, inspiration & giving me the opportunity to interact with National & International High Energy Physics community. Their careful editing contributed enormously to the production of this thesis

I owe deepest thanks to Prof. Manjit Kaur for taking her precious time and patience with me and for giving me motivation for continued efforts. Her positive outlook and confidence in my research inspired me and gave me confidence. Prof. J.M.Kohli is a truly remarkable advisor who grants students a lot of freedom to explore new ideas. I have greatly benefited both from his excellent technical advice and from his role-model as a successful group leader and researcher.

I am very grateful to Alexandra Nikitenko, the coordinator of the Higgs group, who constantly helped us in physics simulation studies. I also wish my heartiest thanks to Sridhar Dasu & Dan Bradly of Wisconsin University for providing the facility at Wisconsin University Computer server and providing support for full detector simulation and reconstruction of our generated samples.

I deeply thank Chairman, Department of Physics, Panjab University for providing adequate facilities to work in the department. I thanks High Energy Physics group for providing scientific environment for the research work

This research has been supported and funded by various organizations including Council of Scientific Instrument and Research and Department of Science and Technology. I thank them all for their confidence in me.

The Chain of my gratitude would be definitely incomplete if I would forget to thank the first and the major cause of this chain, The Almighty "Waheguru". My deepest and sincere gratitude for inspiring and guiding this humble being.

January 29, 2007 (Harinder Singh Bawa)

Abstract

The Higgs boson is a hypothetical massive scalar elementary particle predicted to exist by the Standard Model of particle physics. It is the only Standard Model particle not yet observed. It plays a key role in explaining the origin of the mass of other elementary particles, in particular the difference between the massless photon and the very heavy W and Z bosons. Low mass Standard Model Higgs decay predominantly into $b\bar{b}$ mode. The relatively high number of signal events at low Higgs masses is nonetheless much smaller compared to the number of background events especially QCD, which makes a search delicate in this channel. One way to reduce an enormous background is to study Weak Boson Fusion produced Higgs boson which is characterized by two high E_T back to back jets in opposite rapidity region. The two high E_T jets at opposite rapidity can be used to tag the events where Higgs is produced.

Since at LHC, the real data will emerge only after year 2007, the simulated data is the need for the physics analysis. In physics simulated data, each event is randomly generated to mimic the real data events. We simulated thousands of events for signal and backgrounds and studied the events in which Higgs (H) of 120 GeV mass is produced and decays through H $\rightarrow b\bar{b}$. The simulated data is generated with proton-proton collisions at center-of-mass energy of 14 TeV by Matrix Element event generator called ALPGEN interfaced with hadronisation algorithm of PYTHIA using specific interface for CMS experiment called CMKIN. The LHC is designed such that the collisions will occur at four points, all of which will be surrounded by detectors to measure their specific results of collision. One of these detectors, the CMS detector, will be used to study the Higgs physics. The generated events are passed through the detector simulation package simulating the CMS detector. The digitisation, reconstruction and analysis of the events was performed using softwares specific for CMS experiment. The final state in this channel is a set of quark-jets in the forward and backward rapidity region and b-jets in the central region. This channel is not a potential discovery channel where Higgs boson can be searched due to large QCD background. This channels can be used for the determination of yukawa coupling of Higgs with bottom quark. The method and the selection cuts are optimized to reduce the QCD background to lower level. Of course, these methods can be applied at all the experiments of LHC in general.

The Panjab University, Chandigarh is a member of the international collaboration which designed and built the CMS detector. The Indian institutions, Panjab University, Chandigarh and TIFR, Mumbai, have taken the complete responsibility in the design and construction of the HCAL sub-system called Outer Hadron Calorimeter. All detector modules which are scintillator trays were fabricated, tested at these centres and shipped to CERN for installation in CMS detector. The author participated in fabrication, assembly and testing of Outer Hadron Calorimeter modules. The present work aims at developing methods and description of the hardware established for fabrication and testing of HO in the CMS detector. The installation of HO in CMS detector is at the verge of completion. The author has also participated in installation of HO in CMS detector at CERN.

The performance of the real assembled calorimeters needs to be evaluated. The best possible method to evaluate the performance of the detector is by exposing them to the beam of particles at various energies, collecting and analysing the data for efficiency. The author has participated in CMS HCAL beam test during the year 2003 at CERN, Geneva for data taking shifts and handling of Data Acquisition System. In CMS HCAL testbeams, the calibration of CMS HO towers or individual tiles during was done in the year using muon beam. These calibration constants have been used in studying the response of HO towers to shower particles, especially pions. Also these constants could be used to monitor the behavior of HCAL towers. The study of the CMS HCAL detector resolution using data collected with pion-beams at different energies is also incorporated.

List of Publications

Publications in International Journal and Collaboration

1) Design, performance and calibration of the CMS forward calorimeter wedges.
G. Bayatian, H.Bawa, et al. CERN-CMS-NOTE-2006-044, Feb 2006. 42pp. (Paper in International Collaboration)
Published in Eur.Phys.J.C53:139-166,2008. (International Journal)

2) Design, performance and calibration of the CMS Hadron-Barrel Calorimeter wedges.
G. Bayatian , H.Bawa, et al. CERN-CMS-NOTE-2006-138, 28 May 2007. 23pp. (Paper in International Collaboration)
Published in Eur.Phys.J.C55:159-171,2008

3) The CMS outer hadron calorimeter.
B.S. Acharya , H.Bawa, et al. CERN-CMS-NOTE-2006-127, Jun 2006. 20pp. (Paper in International Collaboration)
Submitted to Eur.Phys.J.C(Number awaited, 2008)

4) Energy Response and Longitudinal Shower Profiles Measured in CMS HCAL and Comparison With Geant4.
G. Bayatian , H.Bawa, et al. CERN-CMS-NOTE-2006-143, 27 May 2007. 21pp. (Paper in International Collaboration)
Submitted to Eur.Phys.J.C

5) Study of Standard Model H$\rightarrow b\bar{b}$ production via Weak Boson Fusion at CMS
H.S.Bawa, M.Kaur, J.M.Kohli. CERN-CMS-IN-2007-009 (Paper in International Collaboration)

6) Design, Performance, and Calibration of CMS Hadron Endcap Calorimeters.
G.Baiatian, H.Bawa et.al, CMS-NOTE-2008-010, 20 March 2008, 36pp. (Paper in International Collaboration)
Submitted to Eur.Phys.J.C

7) Synchronization and timing in CMS HCAL.
By CMS Collaboration (G. Bayatian, H.Bawa, et al.). CERN-CMS-NOTE-2006-139, May 2007. 9pp. (Paper in International Collaboration)

Papers presented in the Conferences

1) Harinder Singh, M.Kaur, J.M.Kohli, paper presented at XVII DAE HEP symposium,

December - 2006 at IIT, Kharagpur, ***"Study of Standard Model*** $H \rightarrow b\bar{b}$ ***producted via Weak Boson Fusion at CMS"***

2) Harinder Singh, M.Kaur, J.M.Kohli *et al.*, (India CMS Collaboration), paper presented at XVI DAE HEP symposium, November - 2004 at SINP, Kolkata, ***"Muon Trigger Studies using CMS Outer Hadron Calorimeter"***

3) Harinder Singh & Ashok Kumar *et al.*,(India CMS Collaboration), paper presented at XV DAE HEP symposium, November - 2002 at University of Jammu, Jammu ***"Fabrication of outer hadron calorimeter scintillator module for CMS detector"***.

4) Harinder Singh and Ashok Kumar *et al.* (India CMS Collaboration), paper presented at XV DAE HEP symposium, November 11-15, 2002 at University of Jammu, Jammu " **Quality Control Check and Testing of Outer hadron calorimeter Scintillator Module for CMS detector**".

Conference/Seminar/Workshops Attended

1) **V SERC school on Experimental High Energy Physics** held at Panjab University, Chandigarh, March 7-27, 2005.

2) **XVI DAE-BRNS Symposium on High Energy Physics** held at Saha Institute of Nuclear Physics, Kolkata, November 29 - December 03, 2004.

3) **91st Session of Indian Science Congress** held at Panjab University, Chandigarh, January 3-7, 2004.

4) **IV SERC school on Experimental High Energy Physics** held at SINP-VECC, Kolkata, 16 February - 1st March, 2003.

5) **XV DAE-BRNS Symposium on High Energy Physics** held at University of Jammu, Jammu, November 11-15, 2002.

6) Seminar on **Computational Techniques in Physics** held at Panjab University, Chandigarh, March 7-8, 2002.

Contents

List of Figures

List of Tables

Chapter 1

Introduction

High Energy Physics research is focussed on the creation and study of subatomic particles and the interaction between them. These particles constitute the ultimate matter of the universe. In early fifties, there were a few particles like protons, neutrons, electrons and photons which were sufficient to sum up the existence of entire matter around us. Now the number of such particles runs in hundreds and discovery of many more are in the pipeline due to the existence of very high energy accelerators. The highest energy accelerator today is Tevatron at Fermilab, USA with a center of mass energy of 2 TeV. Large Hadron Collider at CERN will provide 14 TeV energy in p-p collision by the end of 2007. Such high energy accelerators are required to basically probe deeper inside the target particle to look for some fine structure in the matter and to create higher and higher mass particles which are yet to be discovered. There are two type of high energy physics accelerators namely the fixed target and collider. In the first case, high energy particles are made to collide with some fixed target and in the second category, the collisions take place due to head-on collision of high energy accelerated particles among themselves. Both Tevatron and LHC are collider accelerators.

Presently it is concluded that in place of having a large number of elementary particles, it is possible that there exist a two basic sets of particles, quarks and leptons and a set of exchange particles called gauge boson like photons in electromagnetic forces.

1.1 Standard Model of the Particle Physics

The behavior of all the known subatomic particles can be described by a single theoretical framework called the Standard Model. It describes the strong, weak and electromagnetic fundamental forces using mediating gauge bosons [1]. The gauge bosons are the gluons for the strong, $W^{\pm}$ and Z bosons for weak and the photons for electromagnetic force. The model also contains fundamental particles which are the constituents of matter. Finally, it predicts the existence of a type of boson known as the Higgs boson, which is yet to be discovered. One guiding principle that led to current ideas about the nature of elementary particles was the concept of Symmetry [2]. The Quark scheme was suggested by the symmetries in the way the mesons and baryons arranged in families. Gel-Mann and Zweig independently proposed in 1964 that the three quarks and anti-quarks combined in many different ways according to the rules of symmetry could explain the existence of many particles. They called these three types of constituents as up-quark, down-quark and strange-quark. In 1974, a new particle was discovered at Stanford Linear Accelerator Center. It was given the dual name J/Psi [3] because of its simultaneous discovery by the two experimental groups which was the bound state of a completely new quark-antiquark pair. The new fourth quark was named charm.

Cabbibo, Kobayashi and Maskawa (CKM) extended the four quarks to six quarks by the addition of new pair i.e bottom and top. All the mesons and baryons till now are made up of various combinations of these quarks. In 1977, a new heavy meson called the Upsilon was discovered at Fermilab [4] and later shown to be the bound state of the bottom and anti-bottom quark pair.

In 1995, the six quark prediction was fulfilled with the discovery of top quark at Tevatron which is a proton-antiproton collider in Fermilab. The top quark is the third-generation up-type quark with a charge of +(2/3) e. It is by far the most massive of the quarks. Its mass is currently measured at 171.4 ± 2.1 GeV [5], nearly as heavy as a gold nucleus. The top quark interacts primarily by the strong interaction but can only decay via the weak force. It almost exclusively decays to a W boson and a bottom quark. The Standard Model predicts its lifetime to be roughly 1×10^{-25} seconds. This is about 20 times faster than the timescale for strong interactions and therefore it does not hadronize giving physicists a unique opportunity to study a bare quark.

Leptons being less massive behaves differently from the mesons and baryons. The name leptons means light particles. The electron and muon being charged particles interact with matter through electromagnetic force, the neutrino being neutral very rarely interacts. In 1962, a first experiment using high energy neutrino beam showed that the electron has its own electron-neutrino and the muon its own muon-neutrino. This was the first evidence for the generations of pairs of fundamental particles. The three pairs of families are electron and electron-neutrino, the muon and muon-neutrino, and the tau and tau-neutrino.

Quarks and leptons have an intrinsic angular momentum called spin, equal to a half-integer (1/2) of basic unit and are labeled as fermions. Particles that have zero or integer spin are called bosons. The table 1.1 gives the properties of quarks and leptons.

Quarks	(u)up-quark	(c)charm-quark	(t)top-quark	Charges=+2/3
Mass	0.0015-0.004 GeV	1.3 GeV	171.4 GeV	
Quarks	(d)down-quark	(s)strange-quark	(b)bottom-quark	Charges=-1/3
Mass	0.004-0.008 GeV	0.08-0.13 GeV	4 GeV	
Leptons	(ν_e)elec-neutrino	(ν_μ)muon-neutrino	(ν_τ)tau-neutrino	Charges=0
Mass	0	0	0	
Leptons	(e)electron	(μ)muon	(τ) tau	Charges= -1
Mass	0.00054 GeV	0.105 GeV	1.9 GeV	

Table 1.1: Three generations of quarks and leptons

1.1.1 Fundamental Forces and Interactions

There are four fundamental forces that exist in nature. These are Gravity, the Weak Force, Electromagnetic and the Strong Force (Table 1.2). Our everyday world is controlled by gravity and electromagnetism. The strong force binds quarks together and holds nucleons in nuclei. The weak force is responsible for the radioactive decay of unstable nuclei and for interactions of neutrinos and other leptons with matter. These forces arises from the exchange of specific particles called gauge bosons, the quanta of the force field.

Force	Relative Strength	Gauge Boson	Mass (relative to proton)	Charge	Spin
Strong	1	Gluon (g)	0	0	1
Electromagnetic	1/137	Photon (γ)	0	0	1
Weak	10^{-9}	$W^{\pm}$, Z	86,97	± 1, 0	1
Gravity	10^{-38}	Graviton (G)	0	0	2

Table 1.2: The four forces and their quanta, the gauge bosons

1.1.2 Unification of the forces

One of the greatest achievements of the twentieth century has been the realization that these four forces may be viewed as manifested from a single force. The unification came almost a century after Maxwell has shown that electric and magnetic phenomenon could themselves be unified in a single force carried by the electromagnetic field. The Electro-Weak theory, which in 1979 won the Nobel Prize for Glashow, Salam and Weinberg, succeeds in unifying the weak and electromagnetic interactions into what is called the electroweak force. The intrinsic strengths of the four different interactions could depend on the temperature or energy level of the interaction. Although these strengths are quite different at present temperatures, the weak interaction depends strongly on the energy and in collisions at near 1000 GeV, it gets just as strong as the electromagnetic interaction. The Electro-Weak theory of standard model explains all this. However, as the temperature drops, the symmetry is broken and the quanta split up into four different gauge bosons of different masses, the $W^{\pm}$(80 GeV), the Z^0 (91 GeV) and the photon γ with zero mass. At room temperature, the massive W and Z do not play an important part. But at very high energies of 300 GeV or more, the difference between the zero mass photon and the heavier W and Z boson is erased and they all act equally strongly. In 1983, the W boson and in 1984, the Z boson were observed at the CERN laboratory in Geneva, in high energy collisions of protons with antiprotons. There is as one piece of evidence of particle named Higgs which is yet to be found. We already discussed that when the temperature drops, basic symmetry of the Electro-Weak theory is broken and the forces separate in strength as the bosons gain mass. This is actually done by the new field called Higgs field. There are many theories proposed to unify the electroweak force with the strong force. These theories are called Grand Unified Theories (GUT).

The theory of Supersymmetry [6] requires a heavy partner for each quark, lepton and gauge boson of the old set, together all of them making up one great family of particles. Supersymmetry (often abbreviated SUSY) is a symmetry that interchanges bosons and fermions. In supersymmetric theories, every fundamental fermion has a bosonic superpartner and vice versa. The three forces strong, electromagnetic and weak all have exactly equal strengths in this theory at a very high energy. If the superparticles are found, it is analogous to discovering antimatter and depending on the details of what is found, it could provide evidence for grand unification and might even provide hints as to how string theory describes nature [7]. In the Minimal Supersymmetric Standard Model, the Higgs has a fermionic superpartner, called the Higgsino, that would have the same mass as itself if supersymmetry was an exact symmetry. Because fermion masses are relatively stable, the Higgs mass inherits this stability.

1.2 Modern Experiments in Particle Physics

Modern version particle physics experiments occupy many square kilometers of land with massive and costly apparatus in underground tunnels. These have been done to get higher and higher collision energies. To create a pair of massive new particle x, one has to generate excess energy above the equivalent of mass of pair $E_{collision} > 2m_x c^2$. High energy is also needed to probe deeper and deeper to smaller length scales in studying the unknown. This is equivalent of using X-rays of shorter wave-lengths to probe smaller crystal structures. On the other hand, to look for rare phenomenon, it is necessary to increase the intensity of particle beams and collision rates. So accelerators are doing their jobs simultaneously, creating higher energies and ever higher intensities.

To observe and interpret the results of collisions, particle detectors have to be developed that can track and analyze the particles coming out resulting from the collision. The detector consists of many different types of complex apparatus and electronics. Collider experiments use huge detectors completely surrounding the interaction point where high energy particles and antiparticles collide head-on. The typical colliders are e^+e^-, $p\bar{p}$ and pp collider at LEP, Tevatron and LHC experiments respectively. To build such a huge detectors keeping the parameters such as efficiency, resolution, material etc making of particle accelerators and detectors has depended heavily on technology. The technology of solid state devices, superconducting magnets, electronics, computers and materials, all have played important role in developments in experimental particle physics. All these very complex detectors are built and operated by large numbers of physicists in collaborations across many countries. One such general purpose detector named Compact Muon Solenoid is being built on Large Hadron Collider (LHC).

1.3 Present Work

One of the primary goals for the proton-proton collider at CERN (LHC) is to find the Higgs boson, the one missing element of the Standard Model. The Standard Model Higgs boson can be produced at the LHC predominantly via gluon-gluon fusion. For light Higgs boson, the dominant decay mode is $H \rightarrow b\bar{b}$. In this scenario, the direct production via gluon-gluon fusion is masked by the large QCD background, and its detection is impracticable. One possibility to reduce the background is to study the central production of Higgs in events with large rapidity gap on either side. The fact that the rapidity gaps appear naturally in Weak Boson Fusion (WBF), one can thus exploit this property to suppress the QCD background. The main features of the signal is to select the events with high E_T quark-jets in the forward and backward directions separated from the centrally produced b-jets by rapidity gaps. Jet candidates were retained as tag-jets if their transverse energy (E_T) collected in a cone size exceeds high value of threshold (High E_T jets). Since at LHC, the real data will emerge only after year 2007, the simulated data is the need for the physics analysis. The aim of the present work is to simulate the 120 GeV Higgs boson produced via Weak Boson Fusion in the CMS detector. The present work aims at generation of thousands of events for both signal and background that mimic the real data events in event generator, passing them through detector simulation software simulating CMS detector, reconstruction and analysis of the events. The aim of the present analysis is to optimize the method and selection cuts that could be used to reduce the QCD background to relatively low level.

The Panjab University, Chandigarh is the member of the international collaboration to design and build the CMS detector. This solenoidal detector has a diameter of about 14 meters, a length of 20 meters and weighs 12,000 tons. The magnet inside the detector will have a 4-Tesla field inside a solenoidal volume of 6-meter diameter and about 12 meters long. The detector has 4 major subsystems. 1) The tracking sub-system that includes a silicon vertex detector. 2) The electromagnetic calorimeter (ECAL) made of lead tungstate crystals. 3) The hadron calorimeter (HCAL) made of brass and scintillator and 4) The muon sub-system. In addition the detector will have the data acquisition system, a trigger system, and on-line and off-line computing.

The Indian institutions Panjab University, Chandigarh and TIFR, Mumbai have taken complete responsibility in the design and construction of the HCAL sub-system called Outer Hadron Calorimeter (HO). All detector modules or scintillator trays were fabricated, tested at these centres. We participated in fabrication, testing and installation of Outer Hadron Calorimeter. The present work also describes the methods and description of the hardware established for fabrication and testing of HO in the CMS detector.

The real assembled detector is also tested using the beam of particles at various energies in CMS HCAL testbeams at CERN. The present work describes the calibration of CMS HCAL modules (HB and HO towers) during CMS HCAL beam tests using muon beams. These calibration constants has been used in studying the response of HCAL towers to shower particles especially pions. Also these calibration constants could be used to monitor the behavior of HCAL towers. The present work also aims in describing the importance of Outer Hadron calorimeter in increasing the energy resolution of CMS Hadron Calorimeter. It also aims at calculating the energy resolution parameters for CMS HCAL using testbeam data. These constants and parameters could be used to determine the energy of any particle passing through the CMS calorimeter.

1.4 Outline of the Thesis

The current Chapter 1 describes the brief history and description of particle physics. It also describes briefly the aim of the research work. The Chapter 2 describes the complete overview and design of LHC and the CMS detector. The physics at LHC and the CMS detector is also discussed. The Chapter 3 describes the need and the importance of

Outer Hadron Calorimeter in CMS detector. The methods and techniques in designing, fabricating and testing of Outer Hadron Calorimeter is fully described. The Chapter 4 describes the complete overview of the CMS HCAL beam test and analysis of the beam test data. This chapter also describes complete Data Acquisition system (DAQ) of CMS Detector. The Chapter 5 describes the brief introduction to physics simulation tools. It also describes the Higgs production and decay modes at hadron collider. The study of the Higgs channel $H \rightarrow b\bar{b}$ produced via Weak Boson Fusion has been presented. In this chapter, the methods and techniques used to reduce the enormous QCD backgrounds is discussed. The invariant mass of Higgs at 120 GeV is reconstructed and the estimate of Higgs events in LHC at $60 fb^{-1}$ integrated luminosity has been presented. Chapter 6 gives the conclusion of all the research work.

Bibliography

[1] G. Kane, Modern Elementary Particle Physics, Addison Wesley Publishing Co., Reading, Massachusetts (1993).

[2] http://assets.cambridge.org/052182/1371/sample/0521821371ws.pdf

[3] http://cerncourier.com/main/article/42/6/14

[4] Inquiring minds (Fermi National Lab), http://www.fnal.gov/pub/inquiring/index.html

[5] Combination of CDF and D0 Results on the Mass of the Top Quark, **arXiv:hep-ex/0608032 v1 10 Aug 2006**, **CDF Note 8393**

[6] http://cerncourier.com/main/article/40/10/19

[7] http://superstringtheory.com/basics/index.html

Further Reading

1) Particle Physics, B.R. Martin and G. Shaw

2) Introduction to Particle Physics, D.H. Perkins

3) Quarks and Leptons, Halzen and B.R.Martin

4) Introduction to Particle Physics, D. Griffith

Chapter 2

The Large Hadron Collider & The CMS Detector

2.1 Introduction

The Large Hadron Collider (LHC) is a particle accelerator and collider located at CERN, near Geneva, Switzerland. Currently under construction, the LHC is scheduled to begin operation in 2007. The LHC is expected to become the world's largest and highest energy particle accelerator which is being funded and built in collaboration with over two thousand physicists from more than 30 universities and laboratories.

The collider is housed in a 27 km circular tunnel located underground at a depth ranging from 50 to 150 meters [1]. The tunnel was formerly used to house the LEP, an electron-positron collider. The 3 meter diameter, concrete-lined tunnel actually crosses the border between Switzerland and France at four points, although the majority of its length is inside France. The collider tunnel contains two pipes enclosed within superconducting magnets cooled by liquid helium, each pipe containing a proton beam. The two beams travel in opposite directions around the ring. Additional magnets are used to direct the beams to four intersection points where interactions between them will take place. The protons will each have an energy of 7 TeV, giving a total collision energy of 14 TeV. It will take around 89 microseconds for an individual proton to travel once around the ring. Rather than continuous beams, the protons will be "bunched" together into approximately 2,800 bunches, so that interactions between the two beams will take place at discrete intervals.

When the collider is first commissioned, it will be operated with fewer bunches, to give a bunch crossing interval of 75 nanoseconds. The number of bunches will later be increased to give the final bunch crossing interval of 25 nanoseconds. In the first three years of operation, the LHC will run at a reduced luminosity of $2 \times 10^{33} cm^{-2} s^{-1}$ and afterwards it will reach to the luminosity of $10^{34} cm^{-2} s^{-1}$. The two luminosity regimes are commonly called low luminosity and high luminosity respectively.

The accelerator complex at CERN is a succession of machines with increasingly higher energies. Each machine injects the beam into the next one, which takes over to bring the beam to an even higher energy, and so on. In the LHC, each particle beam is accelerated up to the record energy of 7 TeV. In addition, each of the LHC's injectors has its own experimental hall, where the beams are used for experiments at lower energies as shown in figure 2.1

The brief description of a proton accelerated through the accelerator complex of CERN is as follows:

- We get protons by stripping orbiting electrons of hydrogen atoms.
- Protons are injected into the PS Booster (PSB) at an energy of 50 MeV from Linac2.
- The booster accelerates them to 1.4 GeV. The beam is then fed to the Proton Synchrotron (PS) where it is accelerated to 25 GeV . Protons are then sent to the Super Proton Synchrotron (SPS) where they are accelerated to 450 GeV.

The protons are finally transferred to the LHC (both in a clockwise and anti-clockwise direction) where they are accelerated to their nominal 7 TeV. The beams will counter-rotate for several hours before colliding at the different points where detectors, CMS, ALICE, ATLAS, LHC-b are positioned.

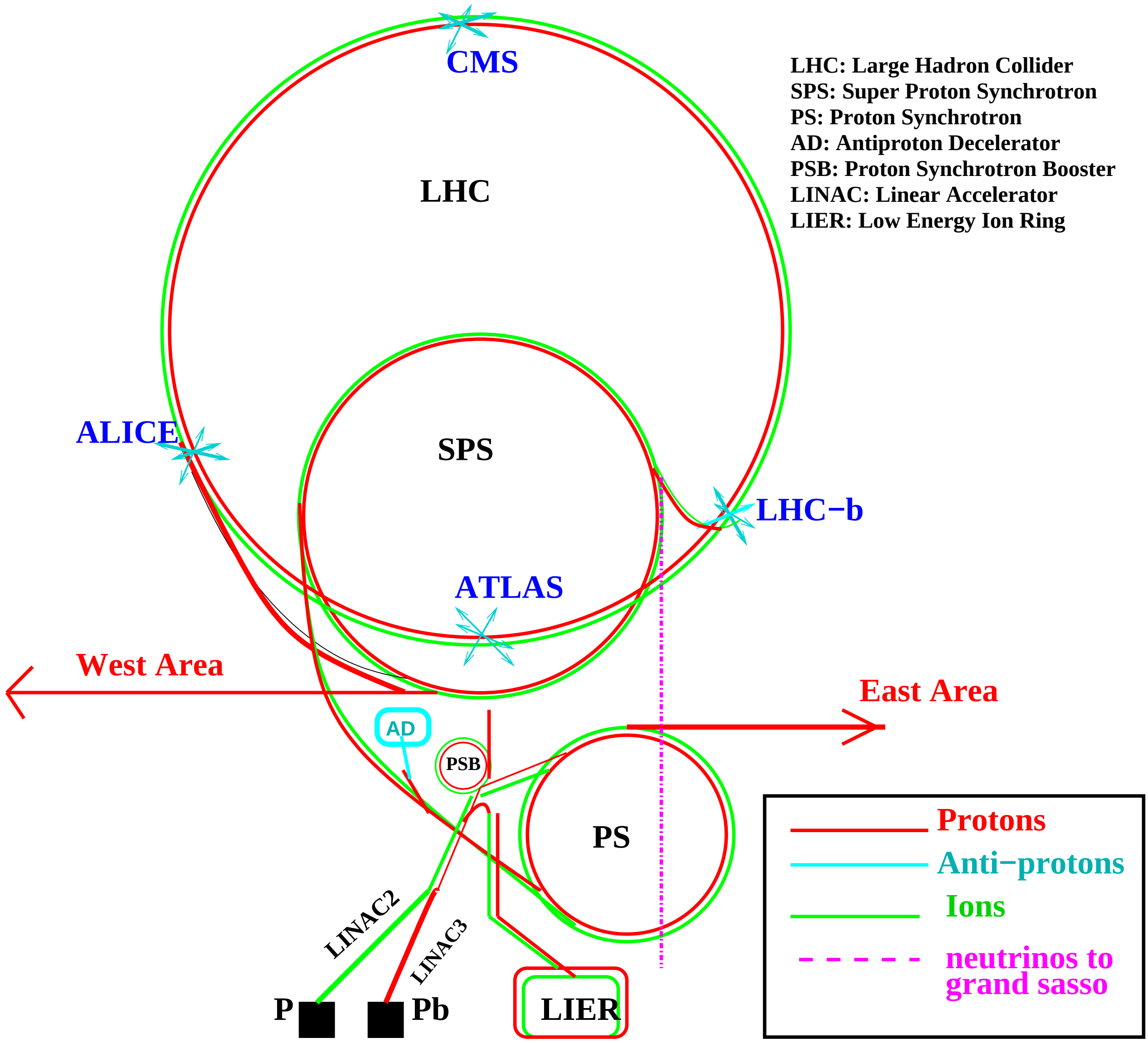

Figure 2.1: The Large Hadron Collider experiments and the pre-accelerators

Lead ions are produced from a highly purified lead sample heated to a temperature of about 550^o C. The lead vapour is ionized by an electron current. Many different charge states are produced with a maximum around Pb^{27+}. These ions are selected and accelerated to 4.2 MeV/un (energy per nucleon) before passing through a carbon foil, which strips most of them into Pb^{54+}. The Pb^{54+} beam is accumulated, then accelerated to 72 MeV/un in the Low Energy Ion Ring (LEIR), which transfers them to the PS. The PS accelerates the beam to 5.9 GeV/un and sends it to the SPS after first passing it through a second foil where it is fully stripped to Pb^{82+}. The SPS accelerates it to 177 GeV/un then sends it to the LHC, which accelerates it to 2.76 TeV/un. Nominal parameters of the LHC machine are given in Table 2.1.

Parameter Units	p - p	$Pb-Pb$
Center-of-mass energy (TeV)	14	1148
Number of particles per bunch	1.1×10^{11}	8×10^7
Number of bunches	2808	608
Designed Luminosity ($cm^{-2}s^{-1}$)	10^{34}	2×10^{27}
Luminosity lifetime (h)	10	4.3
Bunch length (mm)	53	75
Beam radius at interaction point (μm)	15	15
Time between collisions (ns)	24.95	124.75×10^3
Bunch crossing rate (MHz)	40.08	0.008
Circumference (km)	26.659	26.659
Dipole field (T)	8.3	8.3

Table 2.1: Parameters of Large Hadron Collider (LHC) for p-p and Pb-Pb collisions

The final performance of the collider will depend upon many factors. Among the most important are:

- Beam-beam interactions due to the electromagnetic repulsion among particles in the bunch. This effect is more important for denser bunches.
- A fraction of the particles diffuse towards the beam pipe wall and get lost. In this event the particle energy is converted into heat in the surrounding material. The particle beams need to be collimated with high precision.
- Energy losses due to synchrotron radiation will be about 3.8 kW which will be absorbed by the beam pipe at cryogenic temperature. Some photoelectrons, coming from the interaction of photons with the beam pipe, will be included into the accelerated beam.

2.2 Experiments at Large Hadron Collider

LHC consists of eight straight sections available for experimental insertions or utilities as shown in figure 2.2 [2]. The two insertions are located at point 2 (ALICE) and point 8 (LHC-b) for specific physics Pb ions & B-Physics. The two more high luminosity insertions for general purpose physics are located at diametrically opposite straight sections, point 1 (ATLAS) and point 5 (CMS). Their design differs significantly, since two very different solutions were chosen for the configuration of magnetic field. CMS uses a solenoidal field generated by a big superconducting solenoid while ATLAS uses a toroidal field produced by three sets of air-core toroids complemented by small inner solenoid.

A detector based on a toroidal magnet has the advantage that the track p_T resolution is constant as a function of pseudorapidity. A very large air-core toroid allows a good momentum resolution even without the aid of inner tracker; however, it requires very precise detectors with excellent alignment. An iron-core solenoid, on the other hand, can generate a very intense field. The resulting system is very compact and allows calorime-

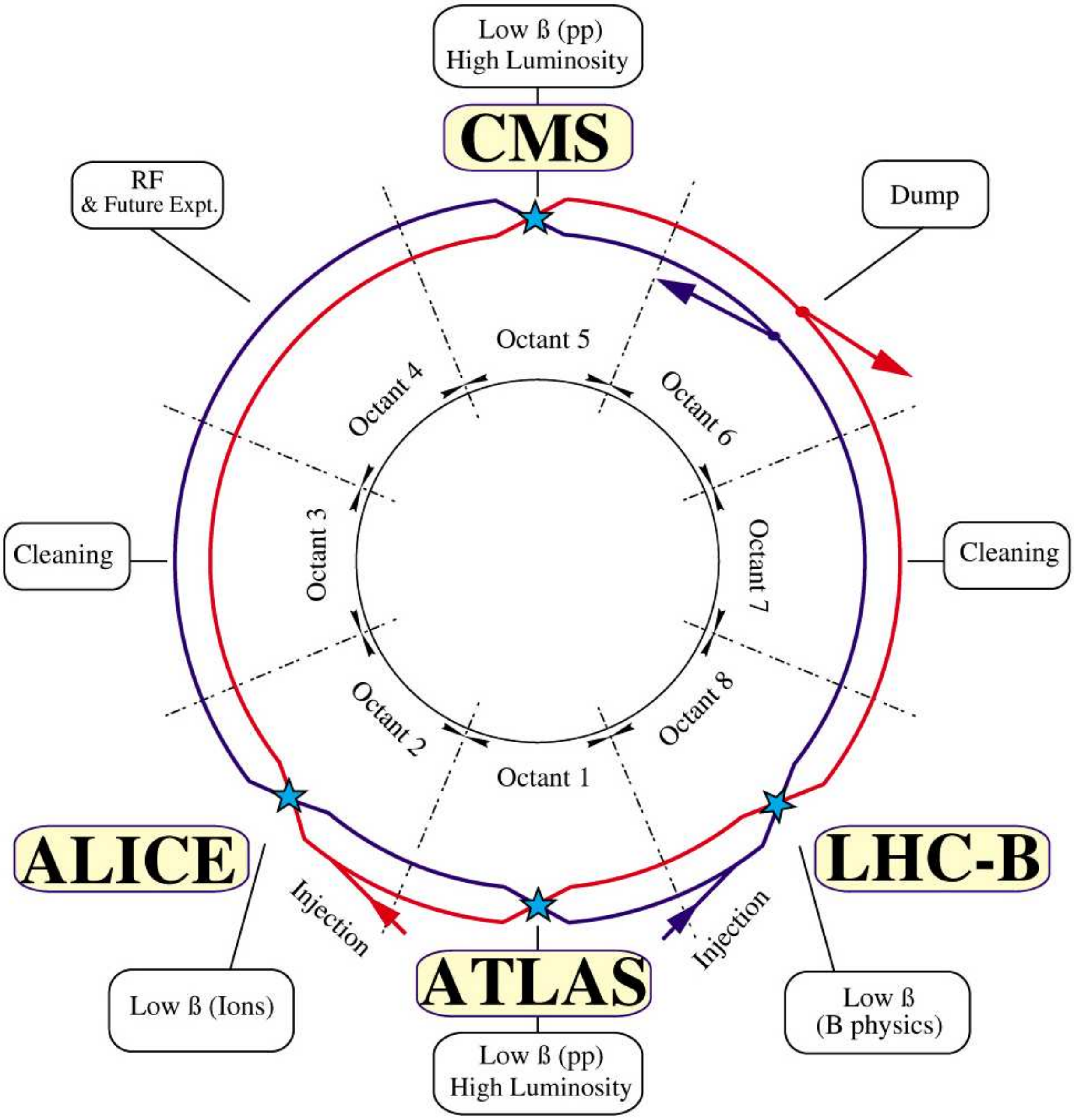

Figure 2.2: Layout of Large Hadron Collider & its experiments

ters to be installed in the magnet, improving the detection and energy measurement of electrons and photons. Precise tracking exploits both the constant field within the magnet and the field inside the return yoke. Moreover, tracks exiting the yoke point are returned back to the interaction point, a property that can be used for track reconstruction. Multiple scattering within the yoke, however, degrades the resolution of muon system.

2.3 The Compact Muon Solenoid Detector

The Compact Muon Solenoid detector is one of two large general-purpose particle physics detectors being built on the Large Hadron Collider at CERN in Switzerland. About two thousand scientists and engineers from scientific institutes all over the world formed the collaboration to build this detector. It will be located in an underground chamber at Cessy in France, just across the border from Geneva. The completed detector will be cylindrical, 21 meters long and 16 meters diameter and weigh approximately 12500 tonnes.

The main design goals of CMS are:

(*i*) a high performance muon system

(*ii*) the best possible electromagnetic calorimeter

(*iii*) a high quality central tracking

(*iv*) a hadron calorimetry with sufficient energy resolution and good hermiticity

2.3.1 Overall Design

The CMS design is driven by the choice of its magnet, a 13 m long superconducting solenoid with a diameter of 5.9 m cooled with liquid helium, it will generate a magnetic field of 4 T, which is kept uniform by a massive iron return yoke (YB,YE). The yoke will also host the muon system (MB,ME), composed by drift tube detectors in the barrel region and cathode strip chambers in the endcaps up to $|\eta| < 2.4$, complemented by a system of resistive plate chambers with a coverage of $|\eta| < 2.1$.

The calorimeters and the inner tracker are installed inside the coil. The innermost tracking detector is essential for precise vertex reconstruction and b-tagging and has to deal with a very high track density. A silicon pixel detector was chosen to have a very fine segmentation. In the baseline design it consists of 3 barrel layers and 2 forward disks. Outside the pixel detector a silicon strip detector is installed, extending up to a radius of about 1.2 m. The full silicon tracker allows charged tracks reconstruction with at least 12 measurement points and a coverage of $|\eta|$<2.5.

Photons and electrons are measured by a homogeneous electromagnetic calorimeter (ECAL), composed by PbWO_4 scintillating crystals covering the region $|\eta| < 3.0$ (EB,EE). In the endcaps, it will be supplemented by a lead/silicon preshower detector, to improve the resolution in the determination of electron and photon direction and help pion rejection.

Jets and energy imbalance are measured by a sampling hadronic calorimeter (HCAL) installed just before the coil. It is composed of a copper alloy and stainless steel instrumented with plastic scintillators. The barrel and endcap parts (HB,HE) have the same $|\eta|$ coverage as the ECAL, and are complemented by a very forward calorimeter (HF), which extends the coverage up to $|\eta| < 5.3$, enhancing the hermeticity of the detector and its ability to measure missing transverse energy. The overall view of the CMS detector is shown in figure 2.3.

2.3.2 CMS Central Tracker

The design goal of the central tracking system is to reconstruct isolated high p_T tracks with an efficiency of better than 95%, and high p_T tracks within jets with an efficiency of better than 90% over the rapidity range $|\eta| < 2.6$. Particular emphasis has been given to reconstruct isolated high-p_T muons and electrons, with a momentum resolution better than $\Delta P_T/P_T \approx 0.1\ P_T$ (TeV/c), with high efficiency over a wide range of rapidities. This value was defined using benchmark processes for the detection of an intermediate mass

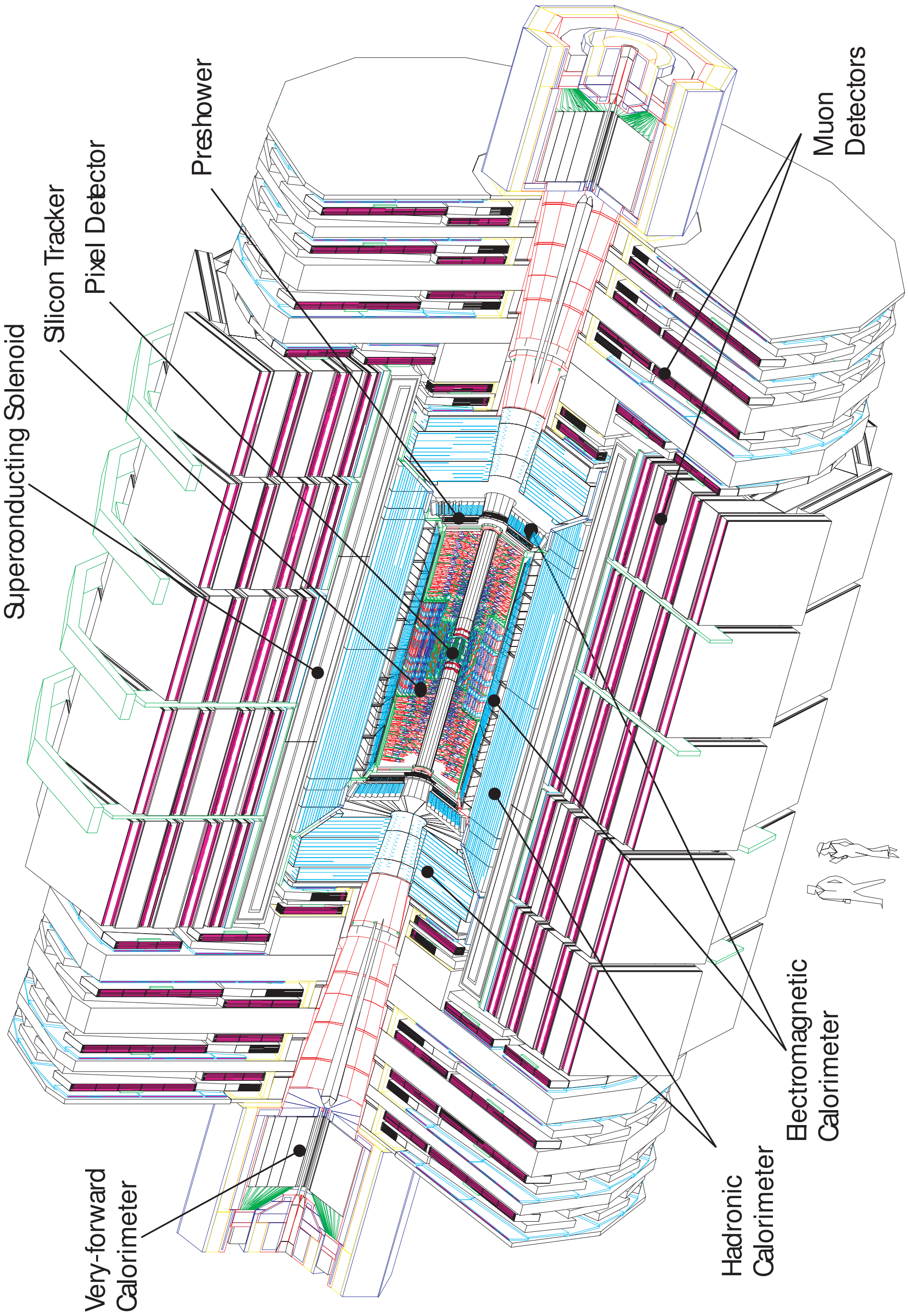

Figure 2.3: The overall view of the CMS detector

Higgs boson, $H \rightarrow ZZ^* \rightarrow 4l^{\pm}$. The high momentum resolution minimizes all possible background contributions under the mass peak and high momentum precision is a direct consequence of a high magnetic field [3].

Important discoveries may depend on the ability of the tracking system to perform efficient b-tagging even at the highest luminosity. This has led to add a few layers of silicon pixel detector close to the interaction vertex. Another important task performed by a tracking subsystem is the identification and measurement of secondary vertices e.g for Higgs coupling to mass, the detection of heavy quark and lepton decays is an important ingredient in Higgs searches. These heavy objects are unstable and decay weakly into lighter quarks and leptons respectively.

The design goal is to achieve an impact parameter resolution at high p_T of order $20\mu m$ in the transverse plane and $100\mu m$ in the z-direction. For pattern recognition at high luminosities, detectors with small size are required. Solid state pixels and microstrip as well as gas microstrip detectors can provide the necessary granularity and precision. Strip lengths of the order of 10 cm are needed to maintain cell occupancy below 1%. This leads to a large number of channels (of the order of 10^7). The tracking volume is given by a cylinder of length 7 m and diameter 2.6 m which consists of three components namely:

(1) silicon pixel detectors

(2) silicon strip detectors

(3) microstrip gas chambers (MSGC)

In the barrel region, a track with reasonable high momentum (P_T >5 GeV/c) will first cross two layers of Si-pixels which has r-ϕ pitch of 10-15 μm, then three layers of Si-strips with a pitch of 60/83/125 μm and finally seven layers of MSGCs with a pitch of 200 μm . The expected resolution per point is typically $15\mu m$ for silicon detector and better than $50\mu m$ for the MSGCs. In the forward and backward region, tracking detectors are configured in the form of discs. A 3D view of the whole Pixel System is shown in the figure 2.4 [4].

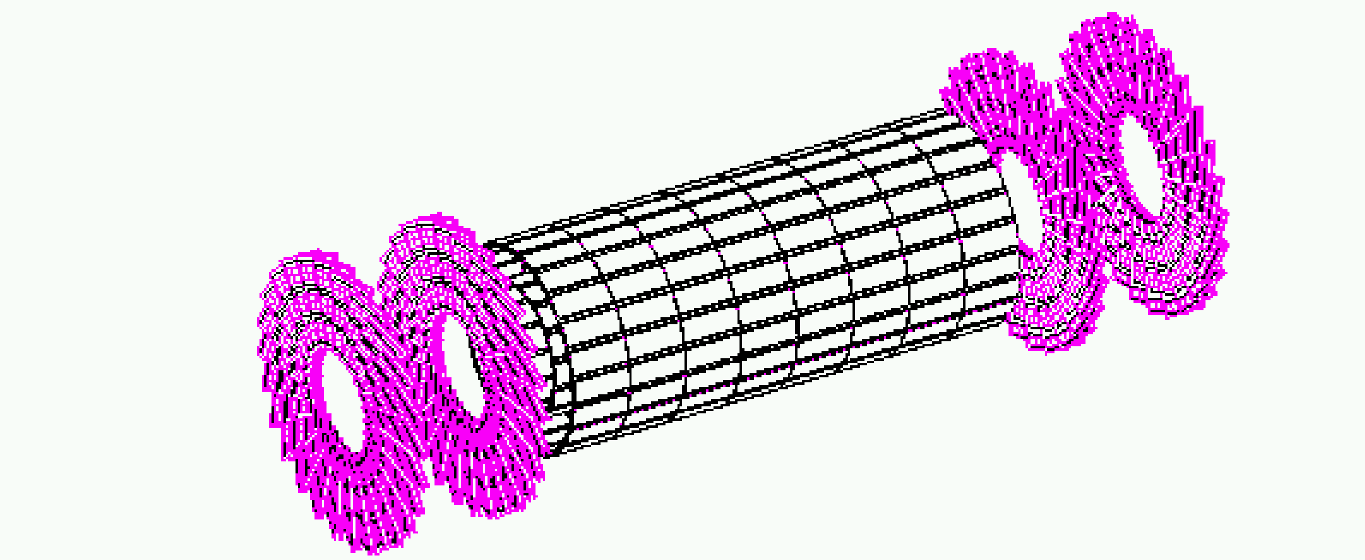

Figure 2.4: Stereo view of the CMS pixel system

Several inner layers of silicon pixel detectors have been incorporated to increase the power of the central tracking system for vertex detection and flavour tagging. These detectors provide three dimensional space points suitable for the high track density close to the interaction vertex and guarantee high precision for secondary vertex detection. Precisely measured points close to the primary vertex significantly reduce combinatorial ambiguities and guarantee the detection and high precision measurement of secondary vertices.

Microstrip detectors are the natural choice for the layers following the pixels. High spatial precision and time resolution combined with adequate radiation hardness make silicon strip detectors ideal for intermediate tracking region. The outer tracking layers employ microstrip gas chambers (MSGC). The fast charge collection from the thin gas volume ensures good time resolution. Good spatial resolution in the less congested outer region is provided by detectors with a pitch that is coarser (200 μm) than that of the silicon strip detectors (50 μm).

2.3.3 CMS Electromagnetic Calorimeter

The next detection subsystem which a particle encounters in exiting from the production point is the electromagnetic calorimeter (ECAL). It consists of Lead Tungstate crystals, a homogeneous medium which is the absorber and a scintillating medium at the same time. Its conception is based on the need to optimise the discovery potential of the light Higgs particle, with a mass $m_H < 150$ GeV, decaying into two photons. The detector resolution is the crucial factor in its performance. Beyond the benefit of a homogenous calorimeter, Lead Tungstate has been chosen for several reasons. It has a fast scintillation emission with a light decay time, which matches the LHC bunch crossing time of 25 ns.

The two basic characteristic radiative processes, which create an electromagnetic shower, are bremsstrahlung radiation by the electrons and electron-positron pair production by the photons. There is a characteristic length scale for radiative processes in the material of the calorimeter called a radiation length, X_o which is 0.56 cm in lead. Since an electromagnetic shower is initiated and runs its course in about 20 radiation lengths equivalent to 11.2 cm in lead, an electromagnetic calorimeter can be quite compact.

There is a characteristic energy, which defines the termination of electromagnetic shower multiplication processes called critical energy E_c. This is the energy below which radiative processes largely cease and particles in the shower lose energy only by ionization or other non-radiative processes. At this depth in the shower, called shower maximum, the number of particles in the shower is a maximum and all particles have approximately the same energy, the critical energy. Given the absence of further particle production, the particles in the shower then lose energy and eventually come to rest. For typical materials used in electromagnetic calorimeters, the critical energy is approximately 2.5 MeV.

There is a characteristic transverse size of a shower, also roughly X_o. This means that photons & electrons can be well-localized transverse to the incident point of impact on the calorimeter measurement. Thus, the calorimetric techniques measure both energy & position, although the position measurement is crude compared to tracking data. Approximately all the energy is deposited in a single segment, or pixel, of the electromagnetic calorimeter. This fact, and the existence of an associated track determine the particle identity. The existence of a neutrino in the final state is inferred by the failure to balance transverse energy. Electromagnetic calorimeters may be calibrated in energy by exposing them to well-prepared particle beams and recording the energy deposit.

In order to facilitate γ/π^O separation in the forward and backward region, a pre-shower silicon strip detector is included in the baseline CMS design. These detectors would be placed just in front of the two crystal endcap modules. This gives accurate information about the starting position of an EM shower, while the location of shower center is determined from energy distribution of the calorimeter cells. The layout of the CMS ECAL is shown in figure 2.5.

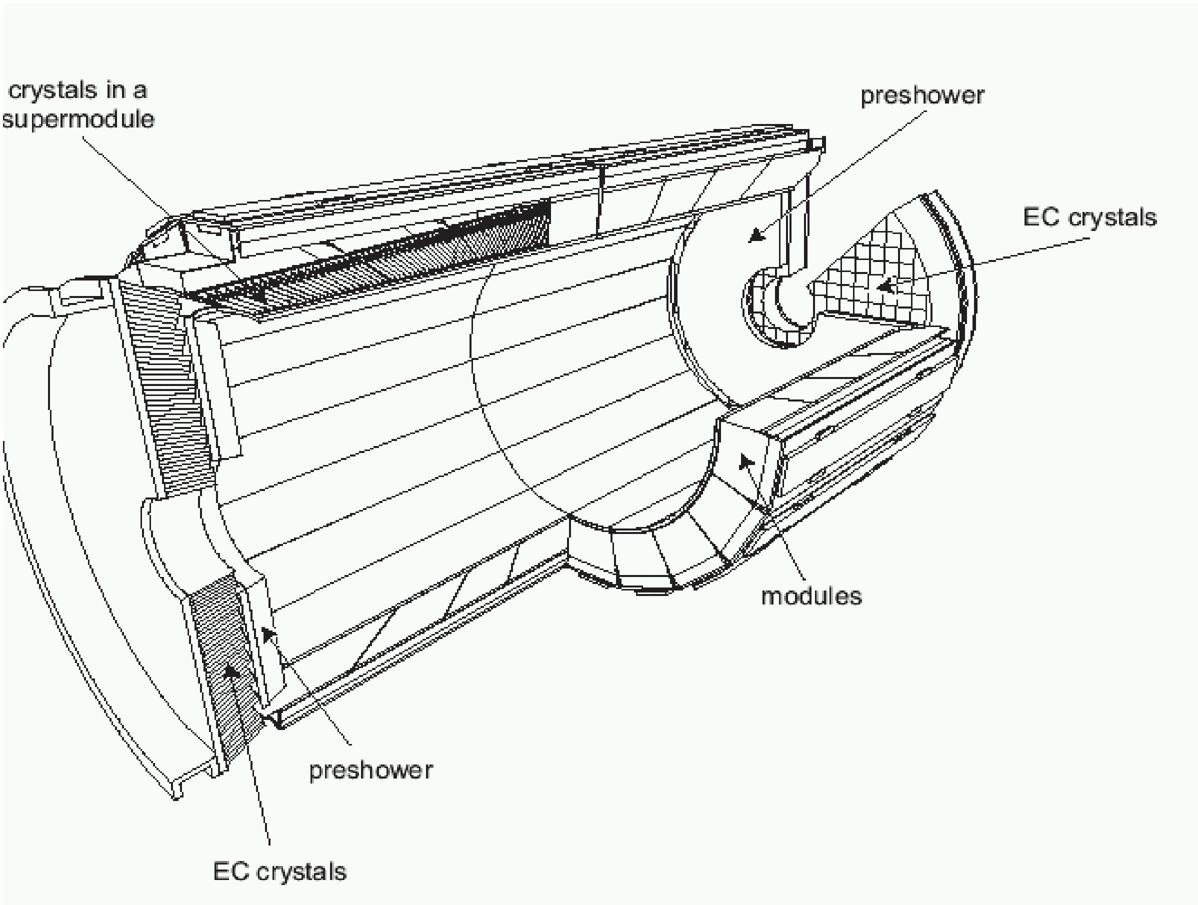

Figure 2.5: The CMS electromagnetic calorimeter

The ECAL barrel electromagnetic calorimeter is designed to have an inner radius of 1.24 m and a granularity $\Delta\eta \times \Delta\phi = 0.0175 \times 0.0175$. Avalanche Photodiodes are used as photodetectors. The barrel ECAL covers the pseudorapidity region $|\eta| < 1.48$. The ECAL end-cap calorimeter is designed along a similar scheme, however using 22 cm long crystals owing to the presence of a 3 X_o thick preshower in front and with $24.7 \times 24.7\ mm^2$ front face dimensions. The endcap ECAL covers the pseudorapidity region $1.48 < |\eta| < 3.0$. Using all these parameters, the ECAL consists of approximately 80000 crystals.

The hadron flux in the calorimeter is almost entirely due to neutrons, and it is expected to reach $2 \times 10^{13} n/cm^2$ in the ECAL barrel for an integrated luminosity of $5 \times 10^5 pb^{-1}$ (equivalent of 10 years of running at LHC). However, no damage by neutron irradiation has been seen [5], while a sample-dependent effect is observed with photon irradiation. It has been shown that the scintillation mechanism is not damaged, nor is the scintillation emission spectrum changed [6, 7]. The degradation of light output is namely due to radiation-induced absorption, i.e the formation of color centers, which reduce the crystal transparency. In the CMS detector it will be thus possible to monitor transmission losses due to irradiation using a light injection system in the calorimeter, and to apply corrections for them.

2.3.4 CMS Hadron Calorimeter

The hadron calorimeter (HCAL) surrounds the electromagnetic calorimeter and acts in conjunction with it to measure the energies and directions of particle jets, and to provide hermetic coverage for measuring missing transverse energy. The relevant benchmark processes which define the HCAL performance requirements are decays of massive Higgs bosons $H \rightarrow WW \rightarrow l\nu l\nu$, $H \rightarrow ZZ \rightarrow lljj$. Since these processes suffer from heavy background, in addition to leptons one or two forward going jets will be used to tag the Higgs boson. So the factors that determine the required performance of HCAL are jet energy and missing E_T resolution.

The central rapidity range $|\eta| < 3.0$, is covered by the hadron calorimeter barrel (HB) and endcap (HE) calorimeters which sit inside the 4T field of the CMS solenoid. These are the sampling calorimeters consisting of plastic scintillators as active material inserted between copper absorber plates. The absorber plates are 5cm thick and plastic scintillator tiles are 4 mm thick. The scintillator tiles are read out individually by green wavelength shifting fibers coupled to clear plastic fibers which transport light to the transducers outside the calorimeter. Since calorimeter would be in a high magnetic field, Hybrid Photo Diodes (HPD) would be used for readout. The HCAL tiles are arranged in projected tower geometry of granularity $\Delta\phi \times \Delta\eta$= 0.087 × 0.087 [8]

Because of narrow space in the magnetic coil, HCAL resides between 1.9 m and 2.9 m radially equivalent to 89 cm in sampling depth ($\approx 5.8\lambda$), which is somewhat thin. This is not sufficient for complete hadronic shower containment. Hence it is necessary to extend the barrel part of HCAL beyond magnet and make additional sampling of the shower. This is essential to improve the missing E_T resolution.

With this aim, Outer Hadron calorimeter (HO) has been included in CMS baseline design with additional layer of scintillators. One layer of the HO would be stationed just after magnet coil at 3.82 m radially (Layer 0) and another (Layer 1) at 4.07 m before the muon station (MB0). Indian Institutes comprises of Panjab University, Chandigarh and TIFR, Mumbai took whole responsibility of designing, fabricating, testing and installing the HO in CMS. Fabrication and testing of HO has been done and it is ready to install in CMS. The details of HO will be given in chapter 3.

A large rapidity coverage up to $|\eta|$=5 is required to measure the E_T^{miss} which is needed to detect forward jets. So CMS employs a separate forward calorimeter located 6m downstream of the HE endcaps. The HF calorimeter covers the region 3.0< $|\eta|$ <5.0. It uses the quartz fibers as the active medium embedded in a copper absorber matrix. There are two Forward calorimeter units, one at each end of CMS. Each unit has an active radius of 1.4 m and consists of iron absorbers, fibers embedded into the absorbers, and phototubes. The embedded fibers have two different lengths to differentiate between shower processes. Longer fibers will provide light from electromagnetic and hadronic showers in the absorber. Shorter fibers will only see the hadronic showers [9]. The long and the short fibers are read out by separate PMTs. The iron absorber length (1.65 m) is 10 nuclear interaction lengths.

The HF calorimeters are located ∼11 m away from the interaction point. The HF calorimeter improves the measurement of the missing transverse energy and enables very forward jets to be identified and reconstructed. These jets are distinguishing characteristics of several important physics processes, in the case of heavy Higgs production, they materialize through WW and ZZ fusion. In the case of slepton, chargino and neutralino searches, they are background signatures.

The LHC will be operating at a luminosity of $10^{34} cm^{-2} s^{-1}$, and the average particle multiplicity at the interaction point per crossing is about 5700 with an RMS value of 1200. This corresponds to a rate of $2.3 \times 10^{11} s^{-1}$, equivalent to 280 particles/crossing/rapidity unit. The region $4.5 < |\eta| < 5.0$ will experience a flux of about $6.0{\times}10^{6} cm^{-2} s^{-1}$ and absorbed doses will reach about 100 Mrad/year. Therefore, the detector must be designed to survive in an exceptionally high radiation field. The CMS experiment has chosen the quartz fibers as the active material for the HF region because the high-purity quartz is known to be very radiation-hard [10].

A calorimeter with optical quartz fibers embedded into an absorber matrix was proposed by HCAL group for producing extremely fast signal as well as radiation hardness. The fast charged particles in the hadronic shower produce Cherenkov light in the quartz fibers. These particles are mostly relativistic electrons and positrons with speeds above the Cherenkov threshold for quartz. The HF calorimeter is insensitive to the low energy charged particles and neutrons that are abundant in hadronic showers. Being sensitive to the hard particle core of the shower has other benefits. The distribution of the relativistic particles in the shower shows a narrow profile, even narrower than its corresponding Moliere radius. It is also shorter than the full shower profile. Hence using Cherenkov-radiation-in-quartz-fiber method enables to have a more compact design for the HF Forward Calorimeter [9]. This type of shower detection is fast since the tail in the time distribution is caused by slower particles that do not produce Cherenkov radiation.

2.3.5 CMS Muon Systems

The muons exiting from the vertex are charged particles, and thus have their vector position and momentum measured accurately first in the tracking subsystem. However, muons are rarely produced, and the job is to pick out which track is a muon in order to trigger on it. Particle identification is achieved by exploiting the fact that muons of energy $<$300 GeV do not radiate appreciably, nor do they undergo a strong interactions. Therefore, they pass through the calorimetry depositing only ionization energy. As they pass through the return yoke of the magnet, all the other particles having been absorbed by the calorimetry. Therefore particles which are observed in the muon system are assumed to be muons, and the issue is to trigger cleanly on these seldom produced particles. The most accurate momentum measurement of the muon comes from the tracking subsystem, while a redundant momentum measurement crosscheck and particle identification comes from the muon tracking chambers. The two distinct measurements are illustrated schematically in figure 2.6.

Here the muons are first bent in the central magnetic field and detected/measured in the tracking subsystem. After traversing the calorimeters and magnet coil the muon is subsequently bent in the steel return yoke and re-measured in the muon chambers embedded in the steel. The main function of the muon system is to perform particle identification on the muons and to provide a muon trigger. The trigger is drastically simplified because almost the only particles that survive to enter the muon detectors are

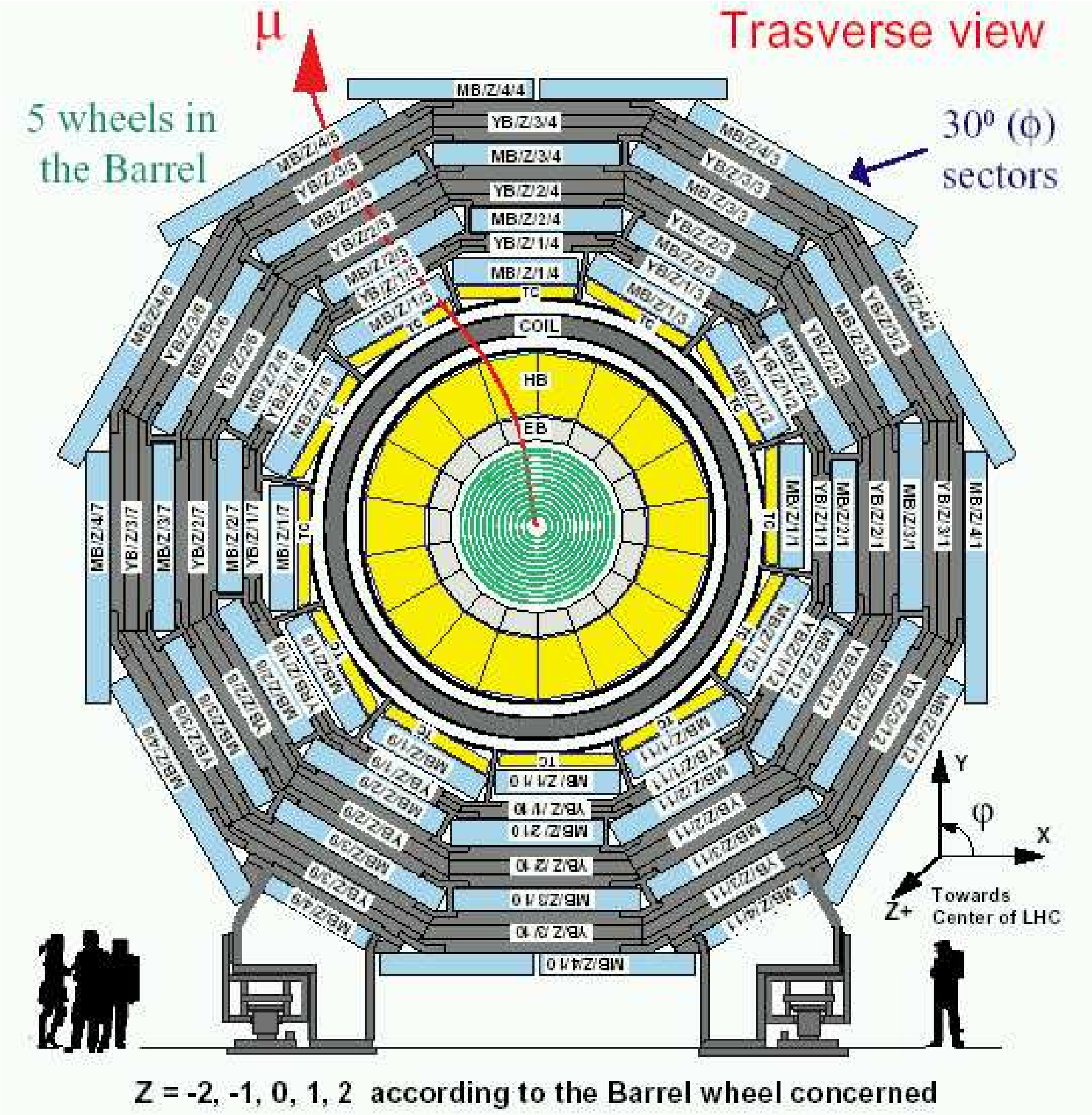

Figure 2.6: Schematic azimuthal-radial layout of muon detection in the CMS experiment

muons. Therefore, the first task is to "pattern recognize" a clean trajectory in the muon detectors in an environment which is quite sparsely populated with particles.

Since its inception, CMS has put highest emphasis on its muon system which should provide high quality muon reconstruction. To effectively detect muons from the Higgs boson, W, Z and $t\bar{t}$ decays, the acceptance of the system has to extend over a wide range of rapidity. To guarantee sharp trigger thresholds and a robust momentum measurement, the system has to have a high momentum resolution in its standalone mode. For the best detection and momentum measurement, four separate muon stations are inserted in a solenoid return yoke (MB1-MB4) in barrel.

Muon detectors in the barrel do not operate in particularly demanding conditions, since the occupancy in this region is low and the magnetic field is well contained in the iron plates of the return yoke. For this reason, drift tubes (DT) were chosen. Each muon station consists of three groups of four drift tubes. Two groups measure the r-ϕ coordinate and one group measures Z. Each station measures a muon vector in space of 100 μm precision in position and better than 1 mrad in Z-direction.

Cathode strip chambers are multi-wire proportional chambers with good spatial and time resolution, that can operate at high occupancy levels and in the presence of a large inhomogeneous magnetic field. Because of the high rates and the high magnetic field in the endcap region, cathode strip chambers (CSC) were chosen for the endcap muon system (ME). The DT and CSC systems cover the region $|\eta| < 2.4$.

Redundancy is obtained with a system of resistive plate chambers (RPC), that are installed in both the barrel and the endcaps. RPCs have limited spatial resolution, but fast response and excellent time resolution, providing unambiguous bunch crossing identification. They are also used to complement DTs and CSCs in the measurement of the transverse momentum. The RPC system covers the region $|\eta| <2.1$.

The Longitudinal view of one quarter of the muon system is as shown in figure 2.7. The muon chambers are arranged in such a way that all muon tracks traverse four

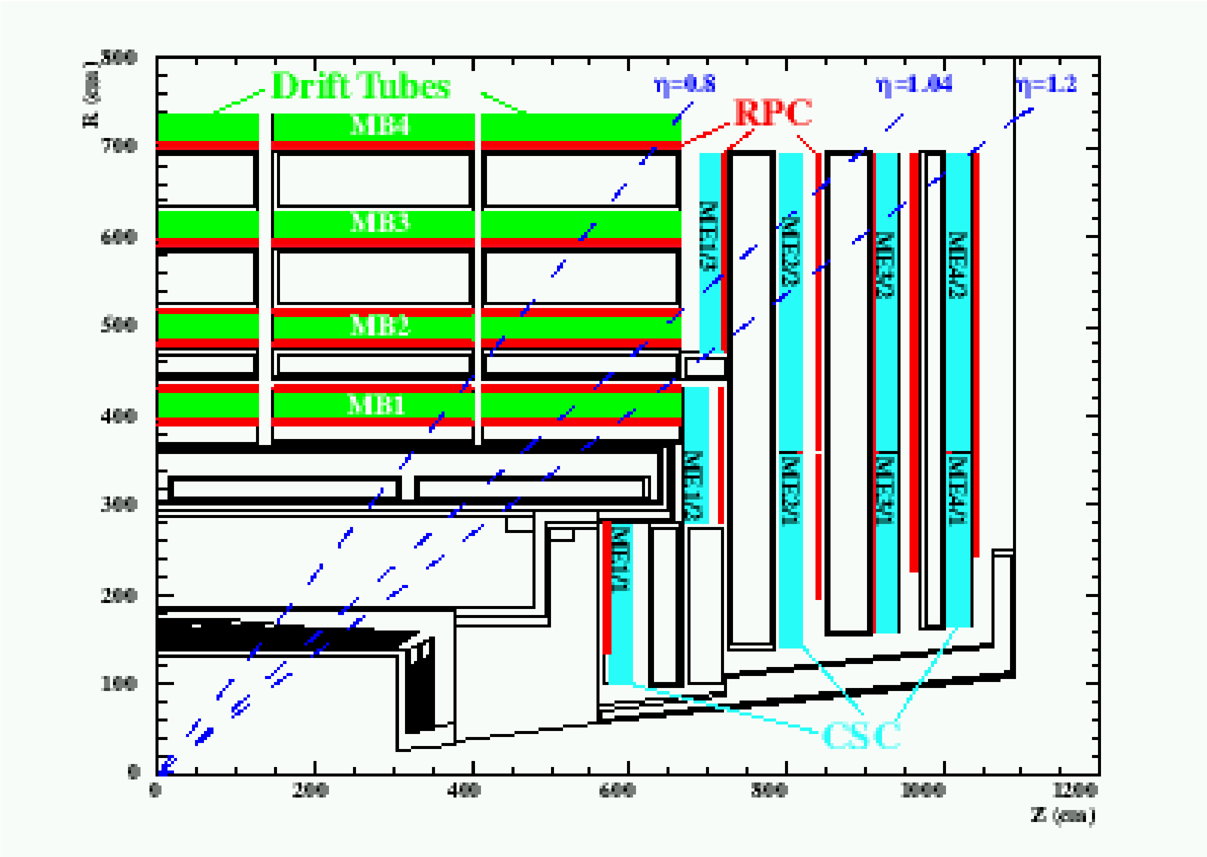

Figure 2.7: Longitudinal view of one quarter of the muon system

stations at all rapidities. The space resolution of muon system is 200 μm per plane for barrel and 100 μm for endcap. The measurement of muon momentum are made three times, inside the central tracker, after the coil and in the iron return yoke. Thus the muon momentum measurement remains accurate in the full rapidity range with resolution better than 5% for $p_T = 1$ TeV and $\approx$ 10 % for $p_T = 2$ TeV in the central rapidity region.

2.4 Physics with LHC and the CMS Detector

Due to the high center-of-mass energy and high luminosity, the LHC has a significant physics potential not only for the discovery of the Higgs, but also in many other fields like electroweak precision measurements, supersymmetry and b-physics.

2.4.1 Higgs Physics

The Higgs particle, the only remaining undiscovered particle in the Standard Model (SM), is a particle which we need to discover and understand well. It is the particle that is responsible for the mass of elementary particles. One of the essential physics programs of LHC will be to confirm or disprove the existence of Higgs bosons. This will require the study of several final states, depending on the mass of the Higgs boson. Assuming that at least one type of Higgs boson is discovered, the next step will be, the detailed study of its properties such as mass, decay width, production rates, branching ratios, spin-parity, couplings etc. Some details of the search of the Higgs particles will be discussed in detail in Chapter 5.

2.4.2 Electroweak Physics

Due to the high collision energy and the large cross-section for many Standard Model processes, the Large Hadron Collider experiments will be able to perform precision electroweak measurements in new kinematic regions. The mass of top quark, W and Higgs bosons are related through radiative corrections. Since top quark will be produced copiously at the LHC, it will allow precision measurements of m_t and m_W and set limits on m_H and subsequently test the Standard Model (SM) and Supersymmetry (MSSM). The final uncertainty on m_t is expected to be better than about 2 GeV. Several other measurements will be possible in the top quark sector e.g rare top decays, the determination of $t\bar{t}$ production cross-section and observation of single top production.

The measurement of the interaction among vector bosons is crucial in understanding electroweak symmetry breaking [11]. Indeed, data from LEP-II have already determined triple vector boson couplings and a first measurement of quartic couplings has been made [12]. It is important to explore what additional information can be supplied by future LHC experiments. At high energy, the process of vector boson scattering becomes dominant. This process is particularly sensitive to the electroweak symmetry breaking mechanism and violates unitarity at a scale of ∼1 TeV. In the SM, this is corrected with the introduction of the Higgs boson. In the absence of the Higgs new physics must couple to this channel. Whatever the scenario will be, vector boson scattering will therefore probe the mechanism of electroweak symmetry breaking. It is thus important to measure the WW scattering cross-section as a function of the invariant mass of the WW system upto a scale of ∼ 1 TeV.

The measurement of the Drell−Yan lepton pair production and the production of W and Z bosons will allow one to constrain the quark and anti-quark densities of the proton at a scale given by the invariant mass of the lepton pair over a widerange in Bjorken-x. The Drell-Yan (DY) process $q\bar{q} \rightarrow l^+l^-$ $(l = e, \mu)$ constitutes in some sense the equivalent of $e^+e^- \rightarrow hadrons$ which was extensively studied at LEP and SLC, and, like it, at the Z mass peak may provide a measurement of $sin\theta_W$ from the observation of a forward-backward asymmetry A_{FB}.

Preliminary studies show that, provided a reliable identification of leptons in the forward region is available, a statistical error of $\Delta sin^2\theta_W \sim 1.4 \times 10^{-4}$ is expected for 100 fb^{-1}, comparable with the one from electron-positron collider. Further studies are needed to estimate if systematic errors from limited knowledge of the parton distribution functions, the lepton acceptance and radiative corrections can be controlled to the required level such that this measurement becomes significant.

2.4.3 Supersymmetry

Supersymmetry (often abbreviated SUSY) is a symmetry that interchanges bosons and fermions. In supersymmetric theories, every fundamental fermion has a bosonic superpartner and vice versa. If SUSY exists at the electroweak scale, then its discovery at the LHC should be straightforward. The SUSY cross-section is dominated by gluinos and squarks production, which are strongly produced with large cross-sections. Gluinos and squarks then decay via a series of steps into the Lightest SUSY Particles (LSP).

These decay chains lead to a variety of signatures involving multiple jets, leptons, photons, heavy flavors, W and Z bosons, and missing energy. The combination of a large production cross-section and distinctive signatures makes it easy to separate SUSY from the Standard Model background.

Therefore, the main challenge is not only to discover SUSY, but to separate the many SUSY processes that occur and to measure the masses and other properties of the SUSY particles. In most cases, the backgrounds from other SUSY events dominate over the reducible SM backgrounds.

2.4.4 CP-violation in the B-Meson System

The LHC would also be working as a B-factory, producing $10^{12} - 10^{13}$ $b\bar{b}$ per year, which would open the way for precise measurements of parameters characterizing the CP-violation effects in the B-system. The detector having very good tracking, calorimetry and muon system, would be able to detect most promising decay channels which have small branching ratios like, $B_d^o \rightarrow J/\psi K_s^o$ and $B_d^o \rightarrow \pi^+\pi^-$; with $J/\psi \rightarrow \mu^+\mu^-$ and $K_s^o \rightarrow \pi^+\pi^-$. These channels would measure two β and α angles of the unitarity triangle. The first reaction has a relatively high branching ratio and clear signature. It is easier to trigger on multi-muon with low p_T or a single muon. With an integrated luminosity of $10^4 pb^{-1}$ in CMS, an accuracy in the measurements of $sin 2\alpha$ and $sin 2\beta$ can be achieved. Both LHC machine and CMS detector are very favorable to study this aspect of discovery physics. Furthermore by observing the time development of $B_S^o - \bar{B}_S^o$ oscillations the mixing parameter χ_s can be measured for values up to 20 [13].

Bibliography

[1] http://www.symmetrymagazine.org/cms/?pid=1000092

[2] www.cern.ch/Public/ACCELERATORS/LHCacc.html

[3] http://hep.ucsb.edu/people/incandel/CMS_Tracker_Incandela.pdf

[4] CMS The Tracker System Project Technical Design Report,CERN/LHCC 98-6,CMS TDR 5, 15 April 1998.

[5] R.Chipaux, O.Toson, Resistance of lead tungstate and cerium fluoride to low rate gamma irradiation or fast neutron exposure, CMS Technical Note CMS TN/95-126, CERN, Geneva, Switzerland (1995)

[6] A.N.Annenkov, Systematic study of the short-term instability of $PbWO_4$ scintillator parameters under irradiation, CMS NOTE 1997/055, CERN, Geneva, Switzerland (1997) abd Radiation Measurements 129 (1998) 27.

[7] R.Y.Zhu, A study of the properties of lead tungstate crystals, Nucl. Instr. Meth. A 376 (1996) 577

[8] The HCAL Technical Design Report, CERN/LHCC 97-31, CMS TDR 2, 20 June 1997

[9] A.S.Ayan, Results from the Beam Test of the CMS Forward Quartz Fiber, Calorimeter Pre-Production Prototype (PPP-I), CMS Note IN 2002/021, (2002)

[10] U.Akgun and Y.Onel, Radiation-Hard Quartz Cerenkov Calorimeters, CMS Collaboration

[11] D. Green, ArXiv:hep-ex/0309031, Sept 3, 2003

[12] G. Delmeire, ArXiv:hep-ex/0305023, May 13, 2003

[13] J.B.Singh, Pramana, Vol. 54, No.4 April 2000 pp. 519-532

Chapter 3

CMS Outer Hadron Calorimeter

The hadronic calorimeter plays an important role in CMS experiment for the measurement of jets, missing energy and lepton identification. CMS HCAL is subdivided into following components, Barrel (HB) [1] covering the central rapidity region $|\eta| \leq 1.4$, Endcap (HE) covering rapidity regions $1.4 < |\eta| < 3.0$ and Forward (HF) covering $3.0 < |\eta| < 5.0$. Outer Hadron Calorimeter (HO) covers the central rapidity region $|\eta| < 1.26$ occupied by the five muon rings. Figure 3.1 shows the longitudinal view of the CMS detector. The dotted lines are at some fixed η values.

3.1 Need for Outer Hadron Calorimeter

Both HB and HE are inside the 4-Tesla solenoid coil. HB inside the 4T solenoid is relatively thin. To ensure complete shower containment, the hadron calorimeter is extended outside the solenoid and is called Outer Hadron Calorimeter (HO). HO will utilize the solenoid coil as an additional absorber equal to $1.4/sin\theta$ interaction lengths and will be used to identify the late starting showers and to measure the shower energy beyond the geometrical reach of HB. Outside the vacuum tank of the solenoid, the magnetic field is returned through an iron return yoke designed in the form of five 2.536 m wide rings along z-axis. HO is placed as the first sensitive layer in each of these five rings.

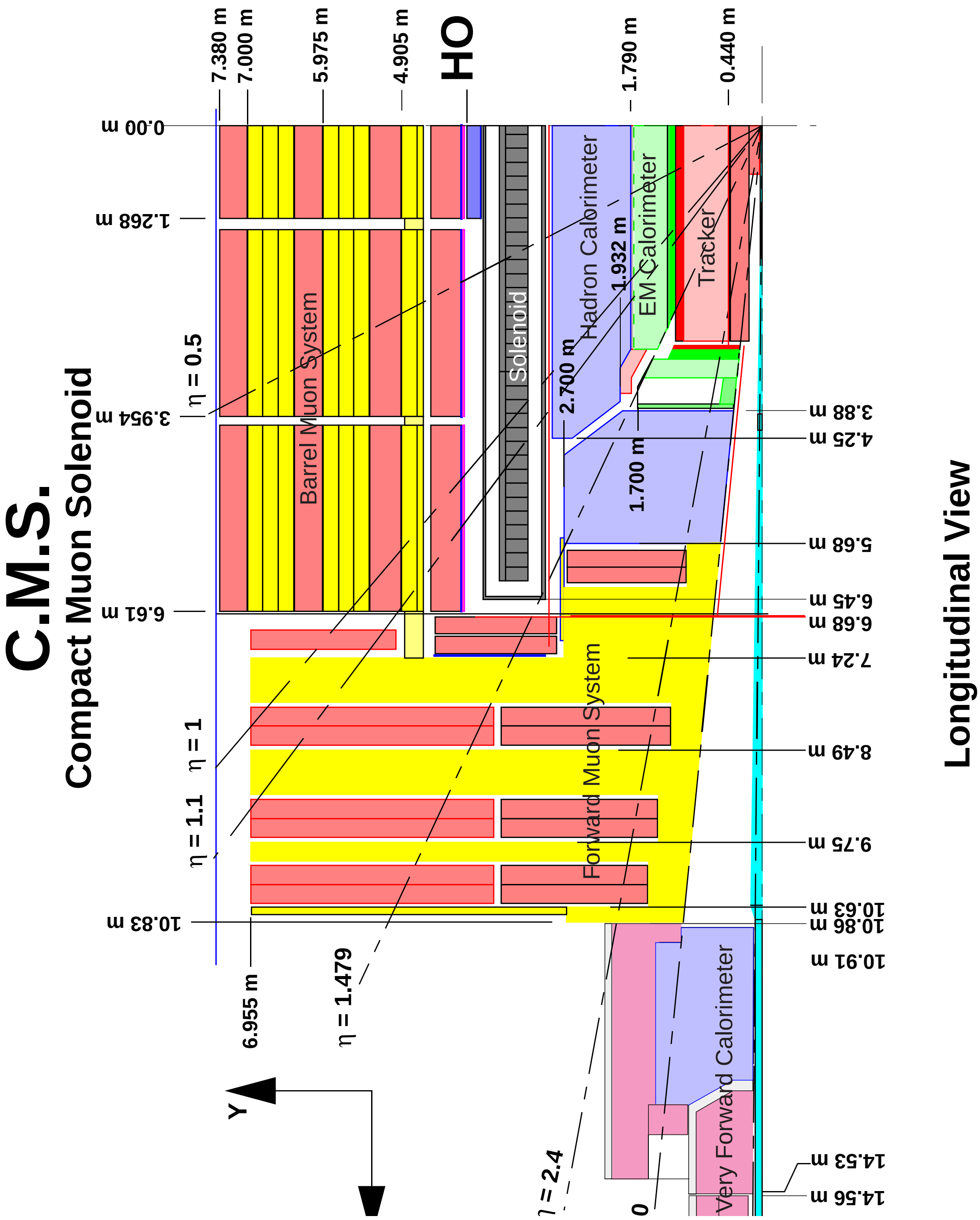

Figure 3.1: Longitudinal view of the CMS detector along with some fixed η lines

Close to the interaction point at $\eta = 0$, HB provides minimum interaction length to the hadrons produced in $p-p$ collisions. Therefore, the central ring which is a Ring 0 has two layers of HO scintillators on either side of a 19.5 mm thick piece of the tail catcher iron at radial distances of 3820 mm and 4070 mm respectively. All other rings have a single HO layer at a radial distance of 4070 mm. The total depth of the calorimeter system is thus extended to a minimum of 11.8λ as shown in figure 3.2 [2], except the barrel-endcap boundary region

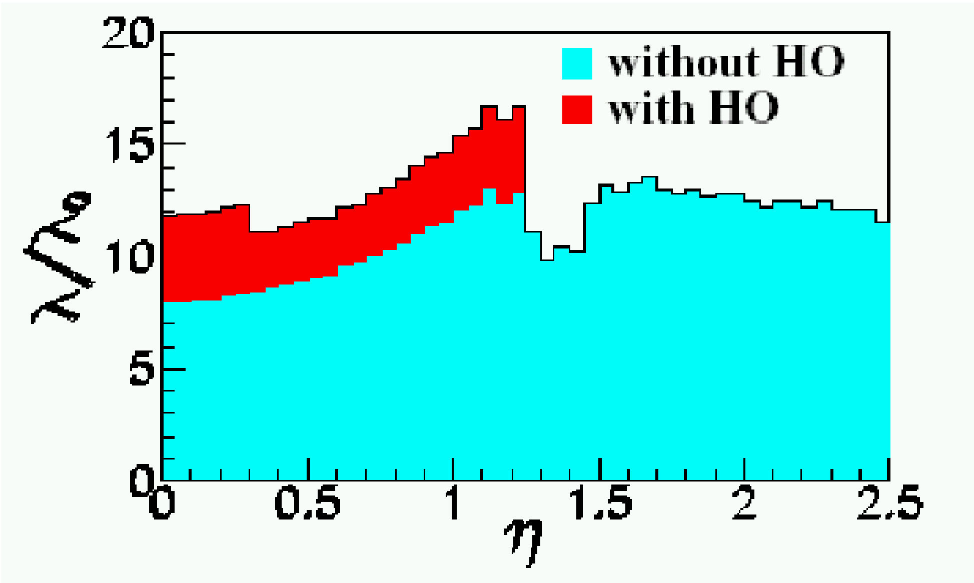

Figure 3.2: Number of interaction lengths till the last sampling layer of the hadron calorimeter as a function of η. The two shaded region correspond to the setups with or without the Outer Hadron calorimeter (HO)

The physics of Outer Hadron calorimeter has been studied [3] using the simulation tool of the CMS detector. Single pion of fixed energies are shot at specific towers and the total energy is calculated by adding the energy deposited in electromagnetic calorimeter and hadronic calorimeter. Figure 3.3 shows distributions of measured energy scaled to incident energy for 200 GeV pions at η= 0. The solid and dashed lines in the figure indicate measurements without and with HO. By looking into the figure, we see that there are many events which have $\frac{E}{E_{inc}} < 1$ means measured energy is less than the incident energy indicating leakage in energy absorption in HCAL. By adding HO, the energy graph becomes more gaussian with respect to 1, indicating the compensation done by HO. The response of pions at various energies on same η tower has been studied [3], it has been observed that the leakage starts when energy of incident pion reaches 70 GeV and the leakage increases with energy. There is some evidence of leakage in HCAL without HO in ring 1 but with reduced intensity. The amount of leakage in ring 2 is found to be negligible.

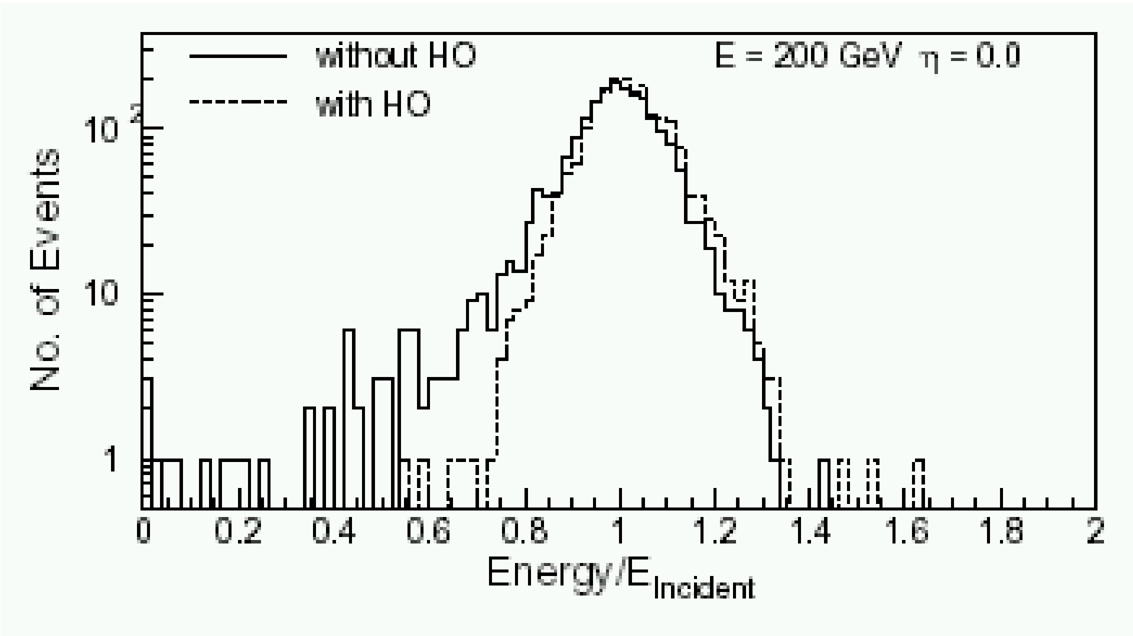

Figure 3.3: A simulation of the distribution of measured energy scaled to incident energy for pions with incident energies of 200 GeV at $\eta = 0$

The effect of shower leakage has a direct consequence on the measurement of missing transverse energy E_T in an event. Study of QCD events shows that the cross-section for those events where at least one particle has E_T above 500 GeV runs into several pico-barn [3]. Clearly these events will be affected due to leakage of energy in the hadron calorimeter and the HO would be useful to decrease the leakage and improve the energy measurement. The missing E_T is essentially a major effect due to lack of hermeticity and leakage in the detector. Figure 3.4 shows missing E_T measurements in high p_T QCD jets, with and without HO. One can see that the inclusion of HO reduces the amount of missing E_T significantly and is important for searches for supersymmetric particles. Thus HO adds significantly to the search potential of the CMS detector.

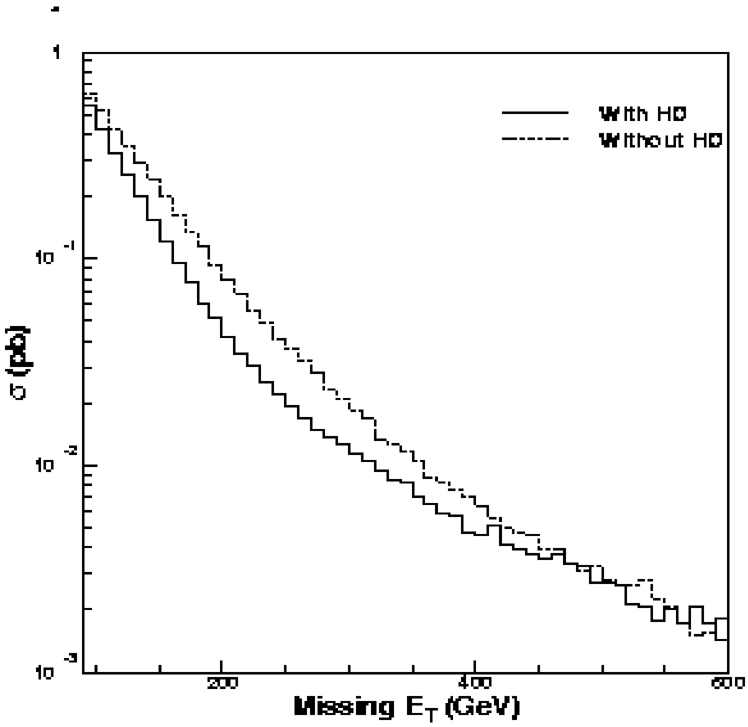

Figure 3.4: Missing E_T spectrum in high p_T QCD jets with or without HO

3.2 Design of CMS Outer Hadron Calorimeter

The HO layer is physically located inside the barrel muon system. It consists of scintillator embedded in the five rings of the barrel return yoke. The design of HO is constrained by the geometry and construction of the muon system. The position of HO layers in the rings of the muon stations is shown in figure 3.5 [4].

Each ring has the 12 identical ϕ-sectors, which are separated by 75 mm thick stainless steel beams. These steel beams hold successive layers of iron of the return yoke as well as the muon system. The space between successive muon rings in the η direction

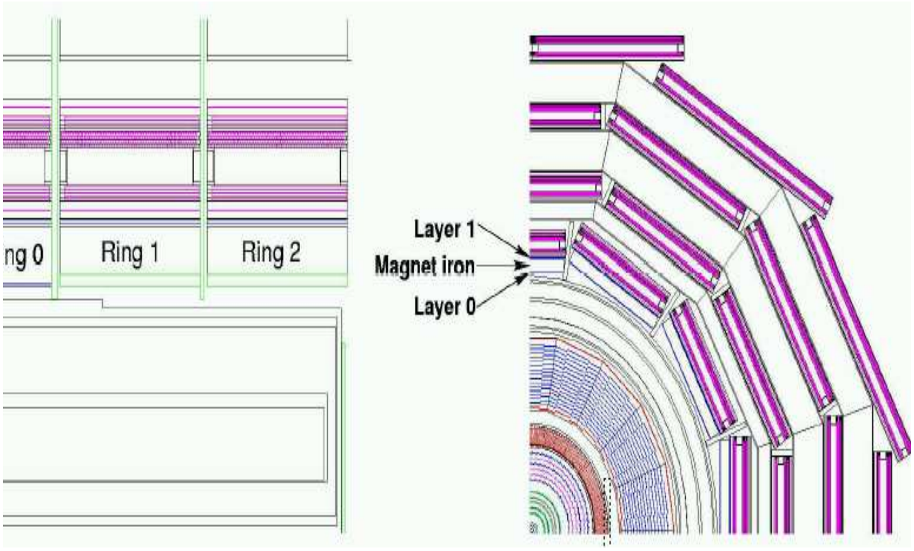

Figure 3.5: Figure showing the position of HO layers inside muon stations

and the space occupied by the stainless steel beams in the ϕ direction are not available for HO. In addition, the space occupied by the 'chimneys' in few sectors of a ring are also not available for HO. The chimneys are used for the transfer lines and power cables of the magnet system. Finally, the mechanical structures needed to position the scintillator trays further constrains HO along ϕ.

In the radial direction, each HO layer has been allocated a total of 40 mm space of which only 16 mm is available for the detector layer, the rest being used for the aluminium honey comb support structures for the scintillator trays on both sides of it. In addition, the HO modules are independently supported from the steel beams located on either side of each ϕ sector. The thickness and position of the iron in the yoke structure further constrains the shape and segmentation of the HO. The sizes and positions of the tiles in HO are supposed to roughly map the layers of HB to make towers of granularity 0.087 $\times$ 0.087 in η and ϕ. In case of Rings ± 1 and ± 2, HO consists of one layer of scintillator tiles and in case of Ring 0, two layers of scintillator tiles located in front of the first layer of the barrel muon detector. Scintillation light from the tiles is collected using multi-clad

Y11 Kuraray wave length shifting (WLS) fibers of diameter 0.94 mm and transported to the photo detectors located on the structure of the return yoke by splicing a multi-clad Kuraray clear fiber of same diameter with the WLS fiber.

The CMS detector is segmented in η, ϕ coordinates. The HO is physically divided into five rings in η direction. The rings are numbered -2, -1, 0, 1, 2 with increasing η. Each ring of the HO is divided into 12 identical ϕ sectors and each sector has 6 slices or trays in ϕ direction. The ϕ slices of a layer are identical in all the sectors. The widths of the slices along ϕ are given in Table 3.1 [5]. Each ϕ slices of the scintillator is further divided into η. The smallest scintillator unit in HO thus obtained is called a **tile**. Both

Ring	Layer	Width along ϕ in mm					
		Tray 1	Tray 2	Tray 3	Tray 4	Tray 5	Tray 6
0	0	274	343	332	327	327	268
0	1	300	364	352	347	347	292
$\pm1, \pm2$	1	317	366	354	349	349	406

Table 3.1: Dimension of tiles along ϕ for different trays. Each tray corresponds to one ϕ - slice in a ϕ sector

layers of Ring 0 has 8 η-divisions i.e 8 tiles namely -4, -3, -2, -1, 1, 2, 3, 4; Ring 1 contains 6 η-divisions namely 5, 6, 7, 8, 9, 10 and Ring 2 has 5 η-divisions namely 11, 12, 13, 14, 15. Ring -1 and Ring -2 has the same number of divisions with negative indices. The η-dimensions of any tile with a negative tower number is same as the one with positive tower number.

The scintillator tiles should map to the towers of Hadron Barrel calorimeter with granularity of 0.087 $\times$ 0.087 in the η and ϕ direction. All the scintillator tiles in a ϕ-slice of a layer in a ring are packed in a mechanical unit called **tray**. Thus the width of each tray is equivalent to segmentation of 5^o in ϕ direction.

Because of the constraints imposed by the gap between successive muon chambers, part of the tower number "4" belonging to Ring 0 is merged with tower number "5" of Ring 1. Same has been done for tower number "-4" and tower number "-5" of Ring 0 and ring 1 respectively. Thus, HO has a left-right symmetry about the Z = 0 plane and 12-fold symmetry in ϕ. Length of a full tray is 2510 mm whereas the size of shorter tray which is constructed without the last tile of a tray, depends upon the length of the last tile.

3.2.1 Geometrical Design of a Scintillator Tile

The CMS HO scintillator tile is made from organic plastic scintillator sheets of Bicron Company. It has 4 identical σ-shaped grooves which are 1.65 mm deep from the surface of the tile as shown in figure 3.6. The grooves closely follow the quadrant boundary. The

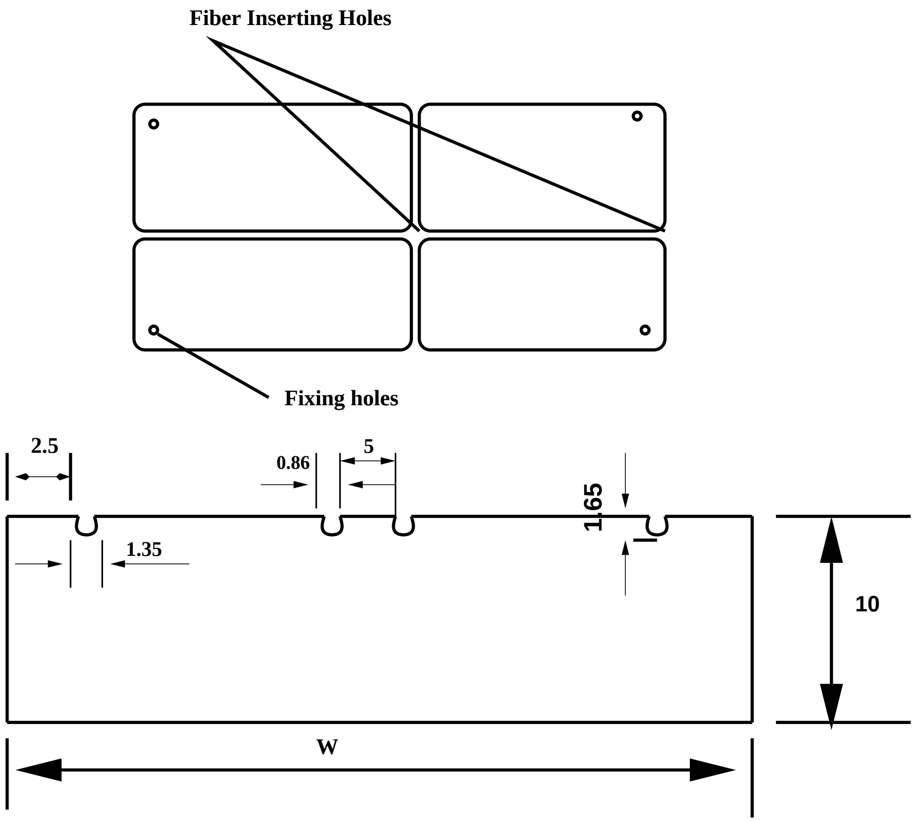

Figure 3.6: The top view and cross section of a typical HO scintillator tile (unit = mm)

corners of the grooves are rounded to prevent damage to the fiber at the bend and also to ease fiber insertion. Entry point of the fiber in a groove is specially designed for easy insertion. The groove design is slightly different for the tile at the optical connector end.

The WLS optical fibers which are used for transportation of light from tile to readout unit are held inside the tile in grooves with key hole cross-section. Each groove has a circular part of diameter 1.35 mm inside the scintillator and a neck of 0.86 mm width. Apart from the grooves, the tiles have four holes for fixing the tiles between plastic tray covers. The HO has 95 different tile dimensions, 75 for Layer 1 and 20 for Layer 0 and total number of tiles is 2736 (2160 for Layer 1 and 576 for Layer 0).

3.3 Readout Box for Outer Hadron Calorimeter

Optical signals from each tile is to be readout by hybrid photodiodes (HPD) and converted into electrical signal passed on to Data Acquisition System (DAQ). These HPD's are placed in a special type of box called Readout Box or RBX. Each RBX has four Read out Modules (RM) and one Calibration Module (CM). Each read out module consists of one HPD and one Charge Integrator Encoder (QIE). A Calibration Module is there to calibrate the RM's. In the Calibration Module, the injected light is monitored using a pin diode. Each RBX is mechanically divided into two parts with a Z shaped alloy plate that separates the HPD and the QIE cards from each other. The QIE is a four-staged pipeline device operating at 40 MHz. Each RBX is provided with connector on the back for high voltage cables connections and low voltage cable connections. High Voltage and Low Voltage distribution box are plugged into these connectors to establish the connections of High Voltage and Low Voltage to the required modules of RBX.

3.3.1 Need of Hybrid Photo Diode

The magnetic field constraint forced us to a silicon-based solution. This was quickly narrowed down to two possibilities, either a development project using multi-channel HPD's or individual avalanche photodiodes (APD's) of the same type proposed for the electromagnetic calorimeter, producing an integrated readout solution for the combined calorimeter. The decision was made by observing pions, electrons and muons from a tile-fiber calorimeter with both readout systems in a 1995 CERN test beam run [6, 7]. The HPD response to Minimum Ionising Particles as well as to the DC signal from the radioactive source calibration demonstrated a better signal-to-noise than the APD, despite the better quantum efficiency of the APD. Unlike the CMS ECAL which requires compact individual transducers on each crystal, the HCAL fibers could be arranged in multi-pixel format leading to a less expensive solution. Since the HPD signal response was uniform over the tube and the current is very low, many channels could be driven by one High Voltage supply and bias. Overall, the HPD system has been tested to be easier to use, less expensive and more stable with respect to temperature and bias voltage.

3.4 Fabrication and Assembly of CMS Outer Hadron Calorimeter Modules

3.4.1 Cutting of Scintillator Sheets

The Scintillator Bicron sheets BC 404 of size 2590 mm × 797 mm were imported from MS Bicron USA and were used to make tiles. Thickness of the sheet used was 10^{+0}_{-1} mm. Hand-Wood-Cutting-saw is used to cut these sheets into the tiles of desired dimensions. To minimize wastage, 36 different dimension tiles were made from three sheets i.e 12 tiles could be made out of each sheets. The tiles cut to size are packed in polythene bag and sent for machining and grooving.

3.4.2 Machining of Scintillator Tiles

Machining of scintillator tiles are done in following steps

1) Bicron Scintillator sheets are cut according to the size of the respective tile keeping 3 mm extra for each side i.e 6 mm extra in length and 6 mm extra in width.

2) The edges are trimmed to the exact dimension of the tile using a conventional milling machine.

3) Grooves and holes are done on a Computer Numerical Control (CNC) milling machine which fed with the ACAD drawing for each tile. The CNC machine is programmed for making of required depth or shape of the groove. However, the size or area of the groove vary from tile to tile which is to be fed on to the machine for each tile.

4) σ-grooves are done in two steps. First a straight cutter makes the 0.86 mm wide 'neck'part of the groove. Next a 'ball cutter' is used for making the inner circular part of the groove. The picture of scintillator tile after machining is shown in figure 3.7 [8].

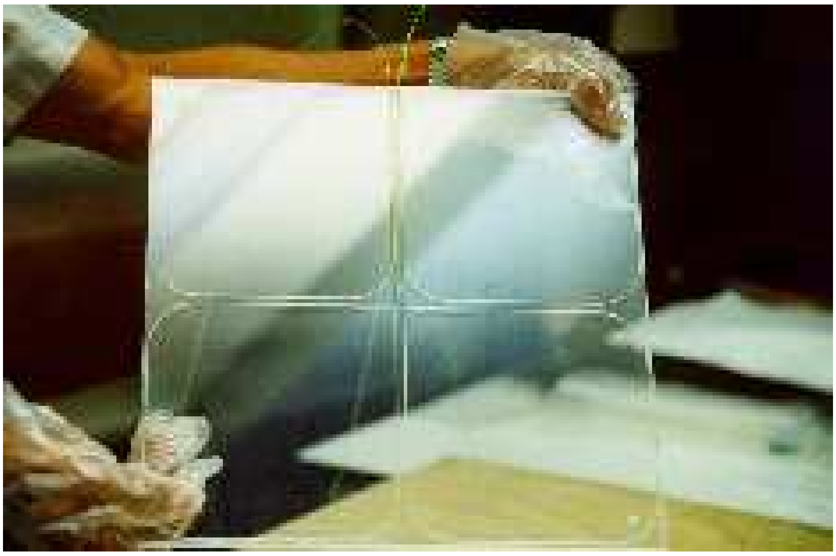

Figure 3.7: Picture of scintillator tray after machining

3.4.3 Making of Pigtails

A bunch of WLS fibers spliced with clear fibers attached with connectors are called pigtails. Pigtails are made in following steps

1) Wave Length Shifter fibers are cut according to the size of the groove where it is inserted.

2) One end of the fiber is polished, aluminized and is coated with a thin polymer layer. The other end is also polished.

3) Clear fiber are cut and one end is polished. The clear fiber is cut a few cm extra

than the length from groove end to the optical connector to avoid any mistake in the measurement.

4) Non-sputtered end of WLS fiber and polished end of clear fiber are put in a piece of heat-shrinking tube and spliced using the splicing machine.

5) Spliced fibers are laid in a jig made for pigtail assembly. The jig has a slot at one

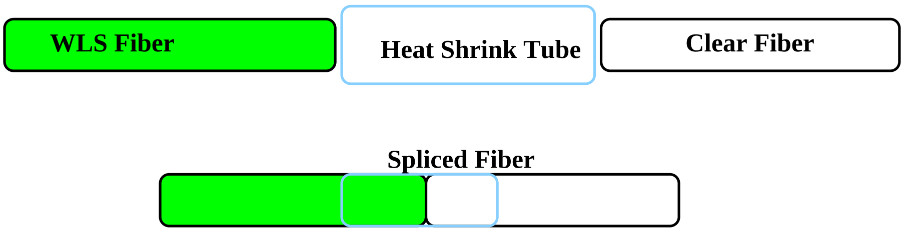

Figure 3.8: Splicing of WLS fiber with clear fiber

end for holding the optical connector. The connector is placed in a slot and clear end of a fiber is inserted in a hole of the connector. Care has to be taken so that the fibers are laid in proper order in the jig and are correctly inserted in the connector. The extra length of the clear fiber should be projecting out the connector.

6) Optical cement is prepared and poured through the socket in the connector.

7) The whole assembly is kept undisturbed for atleast 12 hours.

8) The pigtail is removed from the assembly jig and the connector is fixed in a polishing jig. First it is given a rough polish, then polished with a high speed diamond cutter.

It is to be noted that each tray has 2 pigtails and in total, 864 pigtails were made for CMS HO, 720 for Layer 1 and 144 for Layer 0. Each WLS fiber in a pigtail has to be of proper length to match the groove length and each clear fiber has to be of proper length to match the distance from the groove end to the optical connector at the tray end. Optical cables made of clear fiber are used to carry the light from the trays to the photo-detectors, located outside the muon stations. The cables will be connected to the fibers in tray through optical connectors. The cables will have 10, 12 or 16 fibers depending on the HO ring. The number of fibers from trays in different rings are shown in Table 3.2.

Ring	Tiles per tray	Fibers per tray	Fibers per connector
0	8	32	16
±1	6	24	12
±2	5	20	10

Table 3.2: Number of fibers from trays in different rings of HO

3.4.4 Making of Plastic Covers

The top and bottom plastic covers for the scintillator trays are made using Computer Numerical Control milling machine. First plastic sheets are cut into pieces slightly bigger than their actual size and then machined. The top side of the plastic cover is grooved according to the grooves of the tray. The trays are fully packed in the plastic covers. The fibers are inserted very carefully after putting the tray in the plastic covers.

3.4.5 Assembly of Scintillator Trays

In order to simplify the installation procedure, scintillator tiles are grouped together to form the bigger unit called tray. Figure 3.9 shows the arrangement of tiles in a tray .

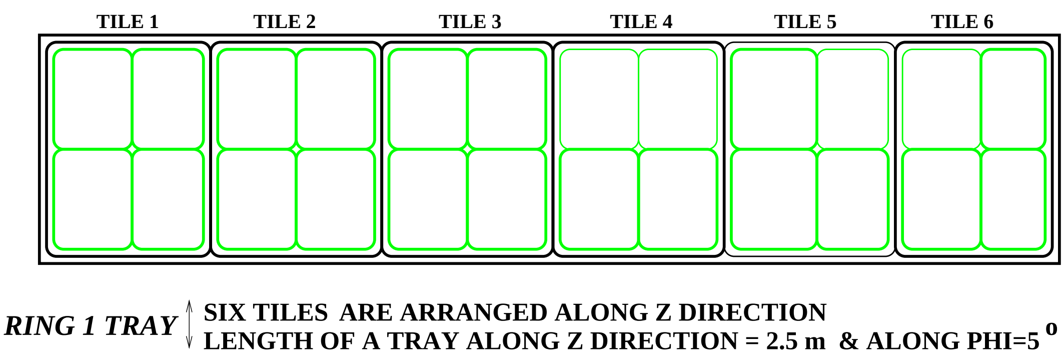

Figure 3.9: The arrangement of scintillator tiles in a tray of Ring 1

Assembly of scintillator trays is done in the following steps:

1) The tiles are cleaned and their sides are painted with Bicron reflecting paint for better light collection. Plastic covers and tray covers are also cleaned.

2) Tyvek and tedler are cut according to tray size and holes matching with those on the

lso for the

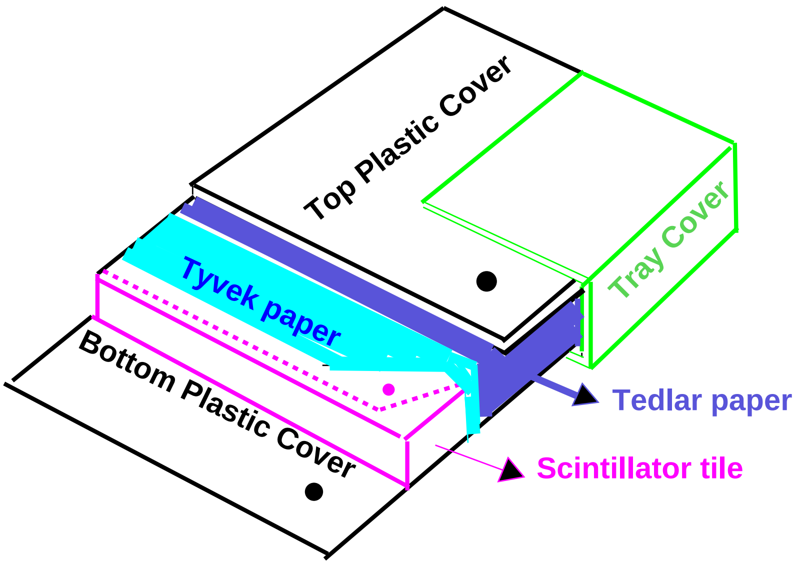

Figure 3.10: Assembly of the scintillator tray

3) The bottom plastic, tedler and tyvek are placed properly and the required number of tiles are placed on them. Two adjoint tiles are separated by strips of tedler to isolate them optically. The top plastic cover is also placed and special 6 BA countersunk screws are used to fix the whole assembly of plastic covers and tiles.

4) The plastic sheets are used to anchor the tiles in their respective positions using 6 BA countersunk screws passing through the tiles. The nut has a cylindrical shift with 6BA threads and it has a thin circular collar at the end.

5) The stainless steel tube is fitted in the groove on the top of the plastic sheet which is used for the passage of radioactive source in wire-source test. The source coupler is also

attached for connecting radioactive wire-source test to the tray.

6) Each fiber of a pigtail is carefully cleaned with alcohol before insertion.

7) The WLS part of a fiber of the pigtail were inserted carefully into the groove of a tile through the slots in top plastic cover, tedler and tyvek. The clear part of the fibers were routed along the route grooved on the top cover and fixed at several places with adhesive aluminium tapes. Care has to be taken to pick the right pigtail for a tray because the left and right pigtails are mirror images of one another. Also right fiber has to go into the right tile.

8) The optical connectors sit in their appropriate slots on the top plastic cover and are anchored by 6BA bolt and nut through holes in the plastic sheets and scintillators.

9) Finally, this whole assembly of scintillator, tyvek, tedler and plastic and fibers is placed in the tray cover of length 2.536 m and height 13.8 mm made of 0.3 mm thick stainless steel plates.

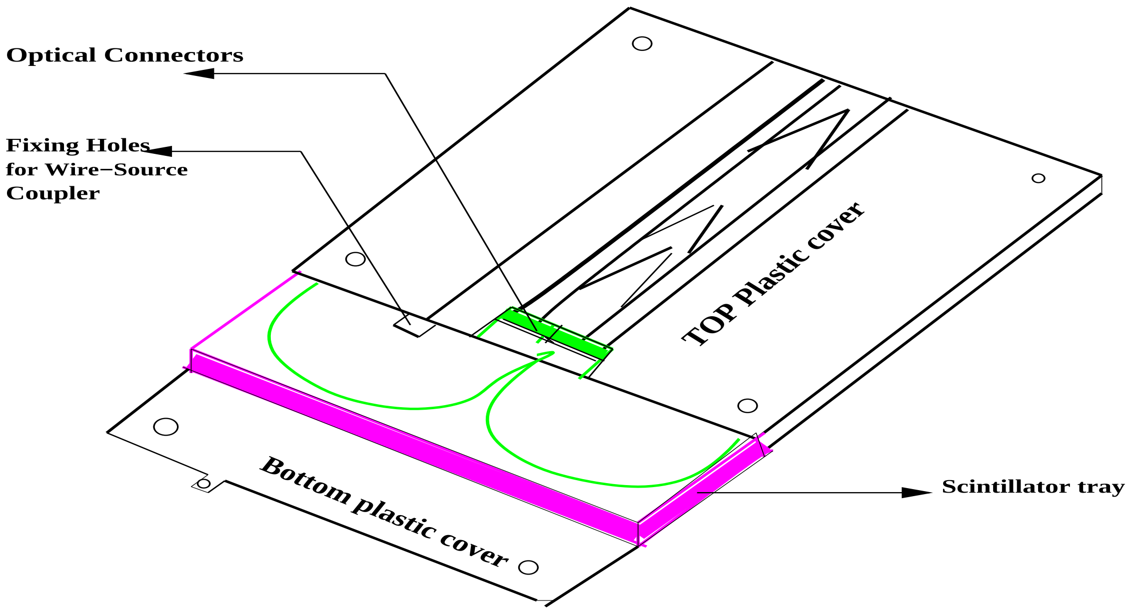

Figure 3.11: Fully Assembled scintillator tray. The components are slightly displaced from their true positions to show their matching design

3.4.6 Making of Support Structure

The scintillator trays are to be inserted in rings of Outer Hadron calorimeter which is given a space of 40 mm for placing HO trays with the support structures. The trays are more or like hanged inside muon stations i.e why it is also called hanging structures. Each tray with all its packing is expected to have a thickness of 15.44 mm. This constraints the space for width of support structure. The total weight of a full one sector consisting of 6 trays is expected to be 30.0 kg. Keeping in mind the width constraints of support structure and at the same time its capability to support this weight, a possible design was to have a pair of aluminium honeycomb panels clamped between three C-channels on the two sides and one end keeping the other end open for inserting the trays [8].

The support structure is made of aluminium honeycomb panels of thickness 10 mm for the bottom and 6 mm for the top. The top and bottom panels are put together with 20 mm $\times$ 40 mm aluminium C-channels glued on the inner side at a fixed separation for inserting the trays. Panels for the rings $\pm$ 1 and $\pm$ 2 also carry cooling tubes on one side. These serve as thermal screens to prevent passage of heat to the RPC or muon chamber assembly. The cooling tubes are made of copper and have inner and outer diameter of 6 mm and 8 mm. These are glued to the 6 mm thick honeycomb surface using araldite and fixed with copper collars. For rings $\pm$ 1, a special design is built to accommodate the short trays due to the chimneys. These hanging support structures have been tested for withstanding a much higher pressure than they are expected to hold.

3.5 Performance of Outer Hadron Calorimeter

The performance of HO scintillator modules depend on the quality of grooving of the tiles, painting on the sides, tray assembly, splicing and polishing of the fibers in the pigtail. All these are carefully monitored at the time of production and each completed tray undergoes a series of tests for quality assurance. All the tests are performed independently.

3.5.1 Testing of Individual Optical Fibers

The WLS optical fibers are inserted inside the grooves of the scintillator for light collection. Before insertion, it is very important to check the light transmission efficiency of the fibers, its attenuation length. For this a fully computer controlled fiber scanning machine is designed and fabricated at Department of Physics, Panjab University. It can also be used to calculate the light transmission across the spliced region of WLS and clear fiber. The block diagram of fiber scanner is shown in figure 3.12.

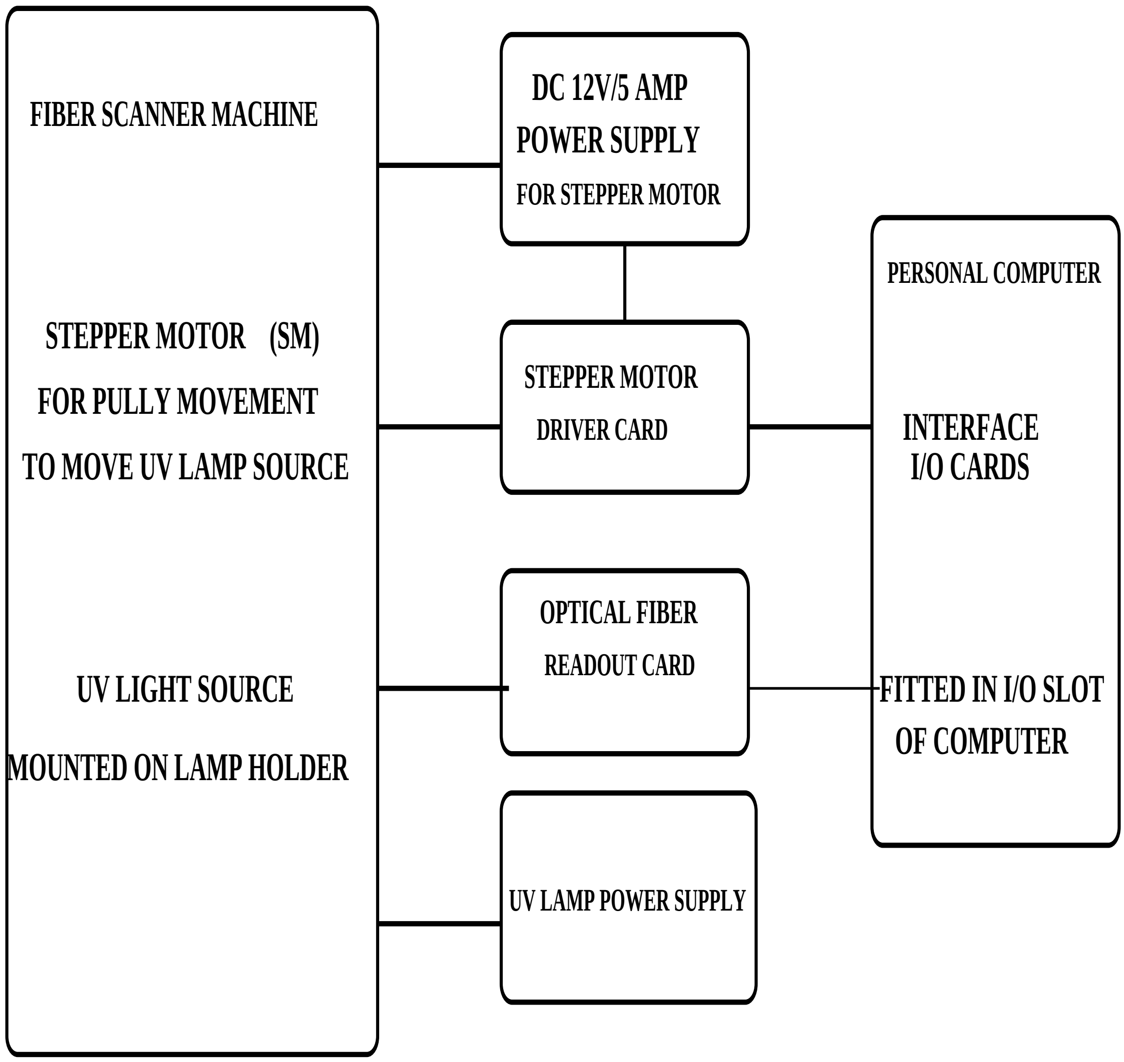

Figure 3.12: The block diagram of fiber scanning machine at Panjab University, Chandigarh

The setup consists of a computer controlled mechanical stage which houses an Ultra violet (UV) lamp. The fibers are placed in specially made strips which holds the fibers firmly making sure that the light from the source falls directly over the fibers. The lamp is moved over the fibers in a controlled steps with the help of Stepper Motor Mechanical System. The stepper motor drives the pulley which further pulls the belt on which the holder containing UV lamp is placed. At specific points according to the step size of the motor, the shutter of UV lamp is opened. The optical fibers absorb UV photons and transmit the light to a set of their respective photo diodes with which they are connected. The photodiodes are further connected to the fiber readout electronics circuits. Motor driver card and fiber readout card are further linked to I/O interface card which is installed in computer via 25 pin connector. The whole assembly is installed in light tight black box to avoid the interference of outside light. The voltage output is recorded in computer. The output of one such WLS fiber is shown in figure 3.13.

The data points are fitted by sum of two exponentials of the form

$$\mathrm{I(x)} = \mathrm{P1} \times e^{x/P2} + \mathrm{P3} \times e^{x/P4}$$

Where the coefficients P1 and P3 are

P1 = 1.365

P3 = 1.699

and slopes of the fitting P2 and P4 are

P2 = - 0.5035×10^3

P4 = - 0.1278×10^1

It is to be noted that distance between UV lamp and the fiber holding strip should remain constant. Also UV lamp should be switch-on using DC power supply. When the intensity of the lamp gets constant, switch over to AC power supply.

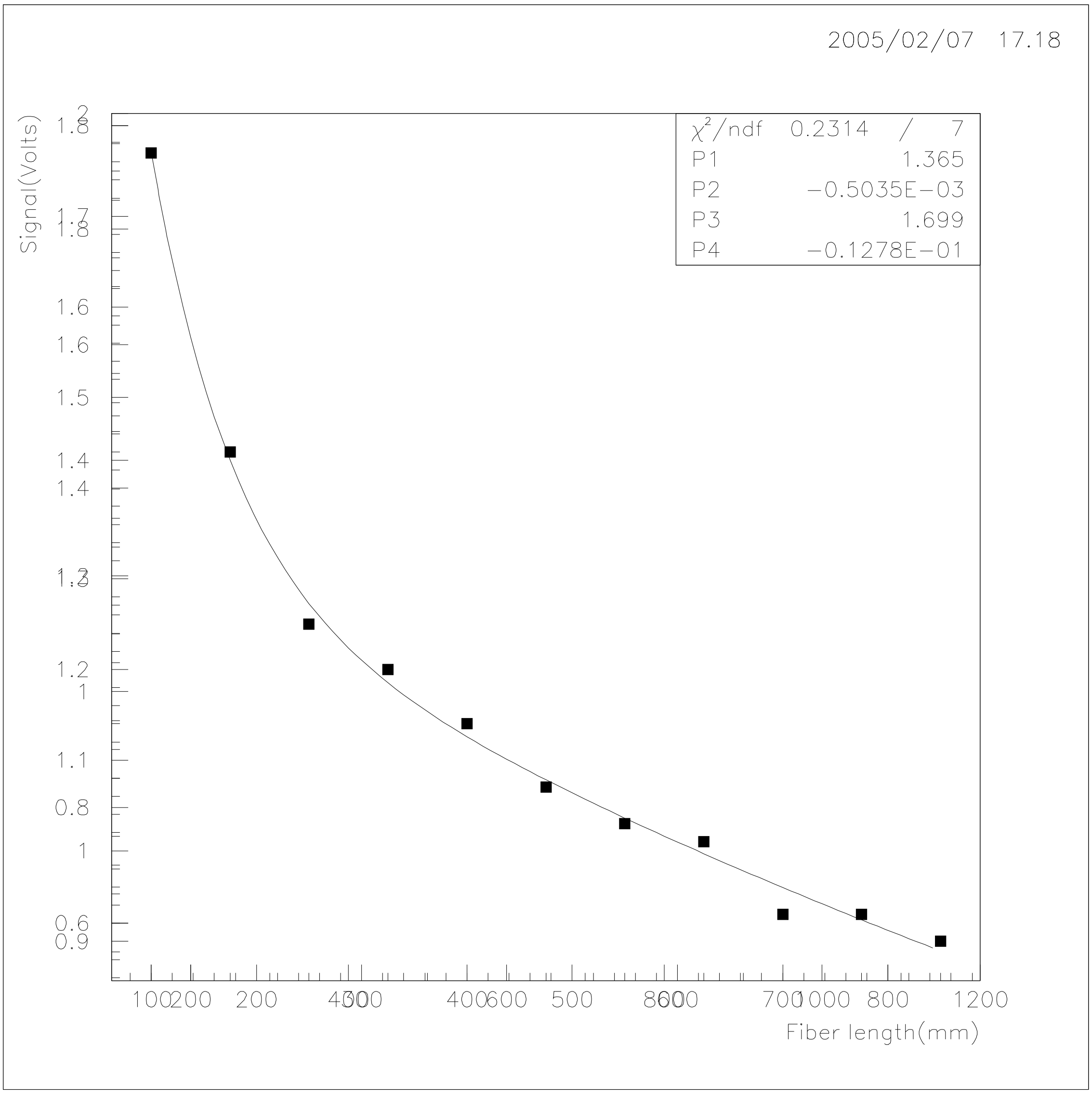

Figure 3.13: Voltage Output of WLS fiber

3.5.2 Testing of Pigtails

Pigtail is very crucial and sensitive part of tray assembly. It is very important to test the pigtails, assess the quality of splicing between clear and WLS fibers, the aluminium sputtering and the polishing quality of the pigtail connector before inserting into the scintillator trays. Though it is not possible to make absolute measurements of these individual quantities, we can monitor the overall optical performance of pigtails using the pigtail scanner.

The setup of pigtail scanner is similar to the fiber scanner explained earlier, with some modifications to connect pigtail to photo-diodes. The pigtail is connected through an optical connector to a set of 16 WLS fibers permanently mounted on the setup. The clear fibers of the pigtail are closer to this optical connector. Light from the UV lamp gets absorbed only when the lamp is above a WLS fiber. Measurements are made for all the pigtails belonging to a given layer and ring and if a pigtail is within 10% of the average in term of transmission properties, the pigtail is accepted [9].

Splicing quality of the fibers over the period of production is monitored by measuring the transmission efficiency between several composites of the two WLS fibers, before starting actual session on each day. Even though, there are no changes in the UV lamp light intensity or overall scanner response, sometimes significant change is noticed in the normalized intensity of all the fibers in a given pigtail run as compared to the same in other pigtail runs of the same test group. This is possible due to mis-alignments in mounting of pigtails on the test strip or coupling between the connectors of normalizing fiber assembly and pigtail. Therefore we need to certify the pigtail runs before we start certifying the fibers in pigtails themselves.

Normalized intensity of a fiber which is defined as the ratio of its intensity after splice in the pigtail run to its intensity at Home position in the corresponding normalizing run is used for this purpose. A pigtail run is accepted if the average normalized intensity of all the fibers in that pigtail is within 10% of the global average of this value across all the pigtails in a test group [9].

The Lengths of WLS and clear fibers at different positions on the pigtail need not be same and hence they have varying light losses. Therefore we do not expect the normalized intensity to be the same for all fibers in a given pigtail. In order to obtain this intensity distribution therefore, the normalized intensity needs to be re-scaled so that this data across all fibers and pigtails can be combined and compared. Following procedure is followed for re-scaling.

1) Fiber composites at a particular position in all twelve identical pigtails of a group have the same lengths for clear and WLS fibers. Hence we expect the normalized intensities to be the same for these composites. We determine the average of normalized intensities for each fiber position. The scale factors for a fiber position is obtained by scaling the average of normalized intensities to the unity.

2) The scaled normalized intensity for each fiber position is then obtained by multiplying the normalized intensity by the scale factor.

Now, the scaled normalized intensities from all the fibers in all the pigtails of various groups can be combined to make the comparison. The distribution of scaled normalized intensities is shown in figure 3.14 [10]. As can be seen from this figure, the

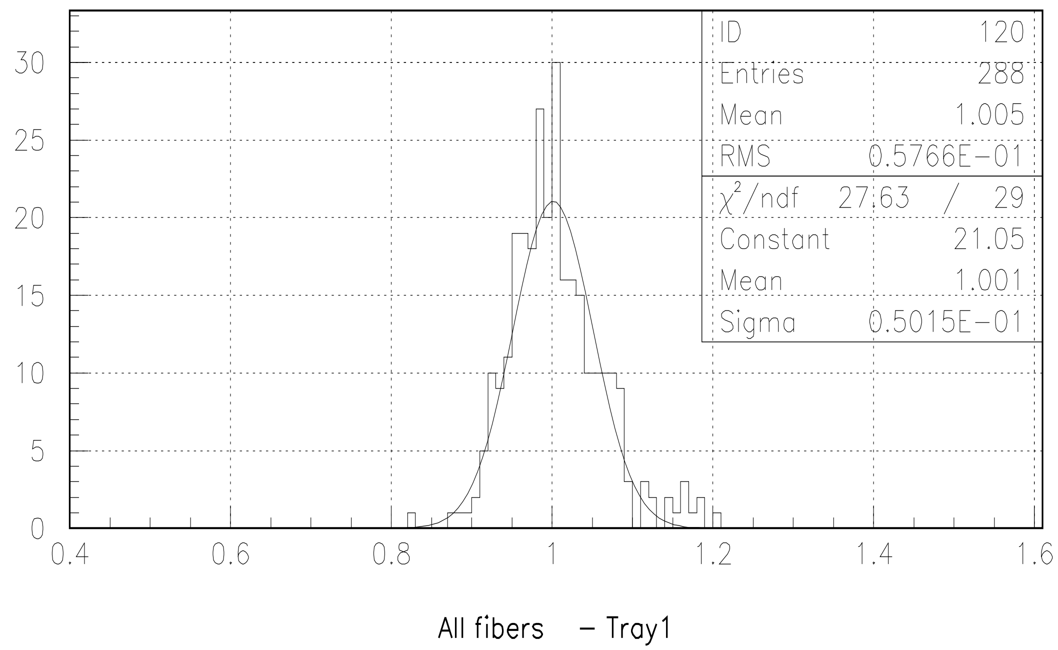

Figure 3.14: Distribution of scaled normalized intensities

mean normalized response of the pigtail fibers is close to unity with a fluctuation of about 5%.

3.5.3 Performance of Outer Hadron Calorimeter Scintillator Modules

It involves two main considerations

- *Sensitivity*:- Capability to produce a usable signal for a given radiation
- *Detector Response*:- Relation between the amount of scintillation light and the charge contained in the output signal i.e integral of the pulse w.r.t time achieved by using a Photo Multiplier Tube and a charge sensitive ADC (Lecroy 2249A)

For this three independent tests are performed :-
1) Cosmic Ray Test
2) Radioactive Wire-Source Test
3) Radioactive Test Using X-Y Scanner

3.5.4 Cosmic Ray Test

Primary Cosmic ray consists of about 85% protons, 12% are alpha particles and 3% electrons and nuclei of heavier atoms [11]. When these primary incident particles interact with the upper atmosphere, secondary particles are created such as protons, neutrons, positive, negative and neutral pions. Muons and neutrinos are the decay products of charged pions whereas electrons, positrons and gamma rays are the decay products of neutral pions. Muons are the largest component of charged cosmic ray particles because they are so massive $\sim 207 \times$ mass of the electron and have a relatively long lifetime of $\sim 2.2\ \mu$s. Most muons originate in the upper atmosphere and lose $\sim$ 2GeV by the time they reach sea level. The mean energy for muons at sea level is $\sim$ 4GeV.

Cosmic Ray muons are easy and convenient source of natural radiation and in practical case, most relativistic particles i.e Cosmic ray muons have energy loss rates close to a minimum and are said to be minimum ionizing particles or MIPS. Studying the detector response to such a MIP signal forms a good way to do the Quality Control and calculate the detector performance. The advantage of using minimum ionizing particles is that they can be used to study number of photoelectrons produced in a scintillator. This is done by examining the spectrum produced by cosmic muons.

When the muons hit the scintillator, the ultraviolet photon is produced. The material of the scintillators should be transparent to the frequency of photon produced [12]. The very best detectors have only a 10% photon collection efficiency. The muon

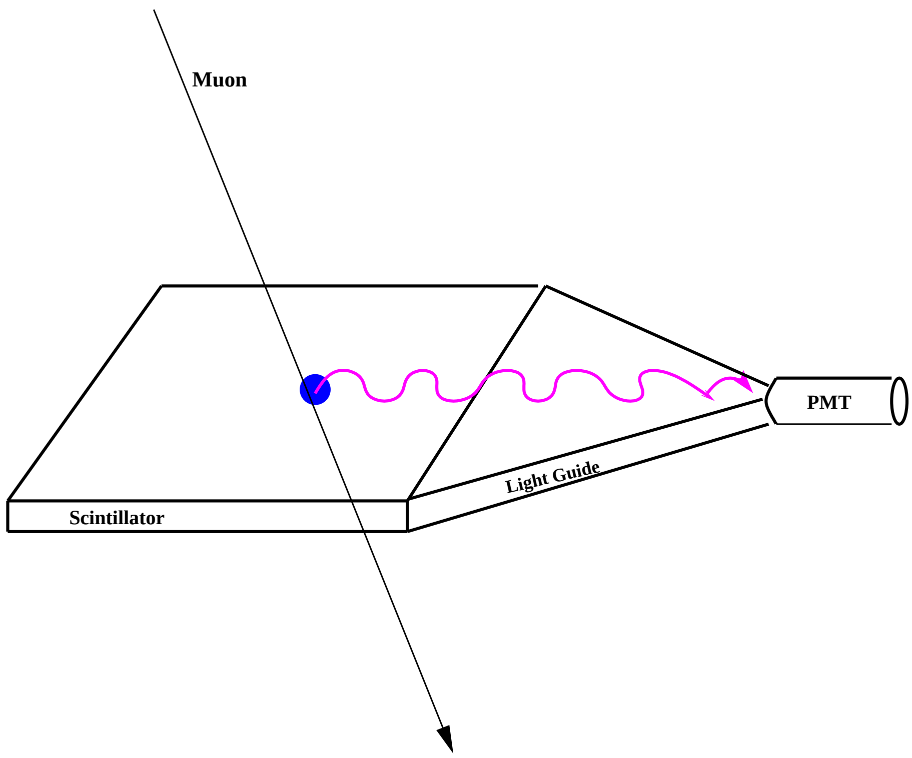

Figure 3.15: Muon exciting an atom in the scintillator. The atom de-excites, producing UV radiation

loses about 2 MeV/cm in the scintillator detector. Approximately 10% of that energy goes into the photons that make it to the Photo Multiplier Tube (PMT) at the end of the light guide. The light guide is non-scintillating plastic with an index of refraction close to that of the scintillator.

The photocathode in the PMT must be thick enough to absorb photons but thin enough to prevent absorption of the photoelectrons produced by the photon striking the photocathode. Photocathodes tend to be Cs-Sb or K-Cs-Sb alloys. PMTs have to be powered since the dynodes need increasing voltages to accelerate the electrons. About 4-5 electrons are kicked out on each dynode per incident electron. In the end, 10^5 - 10^7 electrons per incident photon reaches the anode.

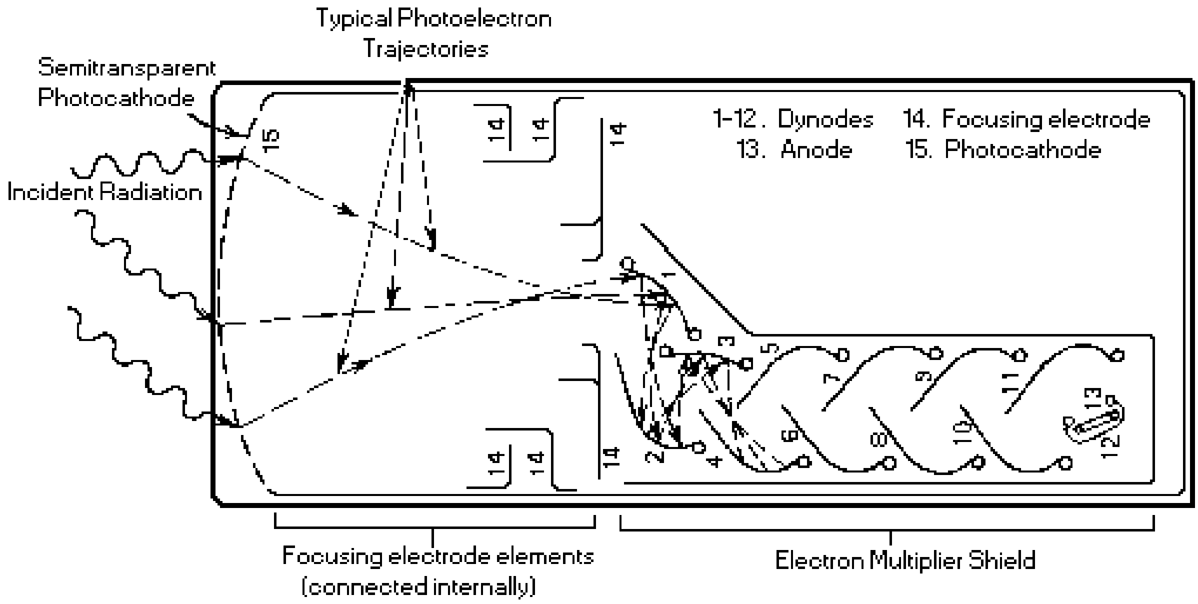

Figure 3.16: An example of a phototube, showing the dynodes.

The pulse height of the scintillator detector depends upon the voltage applied to the PMT. To operate safely, the voltage applied to PMT's should always remain within the range supplied by the manufacturer. The range of voltages for the PMT's used were from 1100 to 1800 V. In this voltage range, we observed well formed voltage pulse in the Cathode Ray Oscilloscope (CRO). To find the optimum voltage of the PMT, we used pulse counting technique. In this technique, we register the number of counts in 5 minutes using scalar when PMT is at the lower end of the voltage. We slowly increased the voltage and register the number of counts until we get the higher end of the voltage. We observed that the counts first increases sharply and then remains constant for a while and then again increases sharply. The voltage range where the counts remain constant is called flat plateau. By fixing the voltage in the middle of the flat plateau, we get the optimum voltage for the PMT. At optimum voltage, there is minimum variations due to drift in the PMT or voltage supply.

Particles are always streaming down from the sky and not all of them are interesting. We are looking for air showers, those secondary cosmic rays which are produced by a high energy primary particle. There will be more particles per square meter for this type of air shower than the regular old background. There are 2 classes of counter used in this experiment, data counters and trigger counters. The data counters or test counters are used for data collection. The trigger counters are used to determine when an air shower occurs. The configuration for cosmic ray test is to put two trigger counter on the top and two trigger counters on the bottom as shown in figure 3.17. The basic principle of the coincidence technique is that we convert the analog signals from the detectors into logic signals and send them to a coincidence unit called logic unit. The logic unit we used is AND gate which gives output only when both the signal arrives at the same time. This

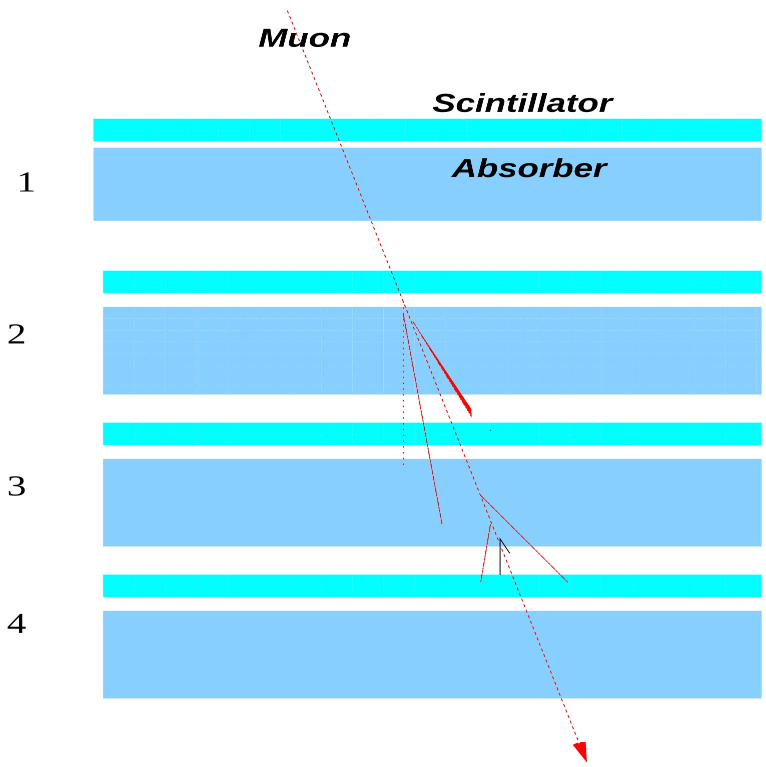

Figure 3.17: Four fold coincidence trigger

configuration is ideal for calibrating the counters as they have the same particles going through them. Triggering in this configuration follows this logic, if all 4 triggers see a particle, take data i.e 4 fold Coincidence [12]. The data counters is placed in between the trigger counters.

The trigger signal is passed through discriminator. What a discriminator does is filter out signals that are below a certain threshold. Input voltages can be anything but the output is either in Emitter Coupled Logic (ECL) or a SUM output. The greater the threshold voltage, the more energetic particles have to be for them to be considered valid. The output that we really want from the discriminator is Nuclear Instrument and Module (NIM) for the gate input on the ADC, to tell the ADC whether or not the signal from data counter's should be integrated. However, the discriminator only outputs in ECL, so we have to take that ECL and put it through a level translator to convert it into a NIM signal. The ADC gate should be longer than the signal produced by the second discriminator. We send the level translator's NIM output through a gate generator. This resulting NIM signal with certain duration is then used for the ADC's gate.

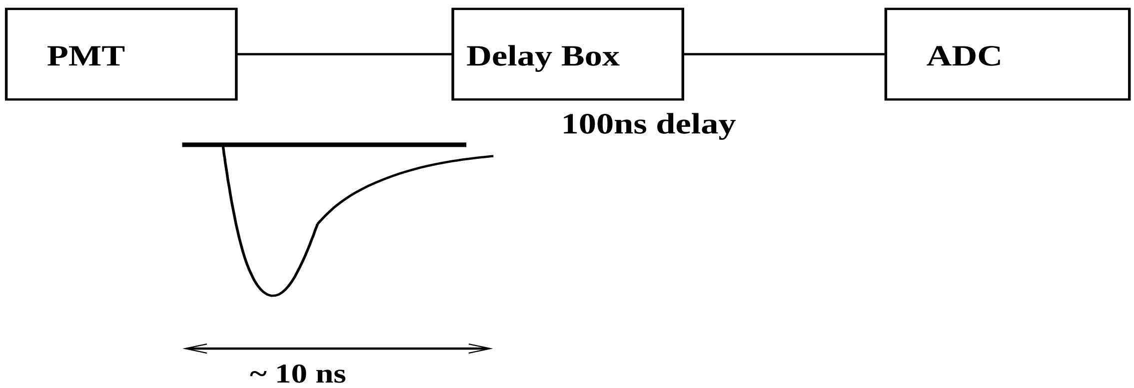

Figure 3.18: Signal path for the trigger counters to produce a gate for the ADC.

Because the trigger signals have to go through so much hardware and the data counters get particle hits at the same time as the trigger counters, the data signals have to be delayed in some way so they can arrive at the ADC within the gate window to be integrated. This is done by delaying the data signals with longer cable. We used delay boxes which are just modules with big length of cable. When the data signals arrive in the ADC input channels, the gate has already been set and the ADC proceeds to integrate the charges. If a channel has no signal, only background noise gets integrated. This is

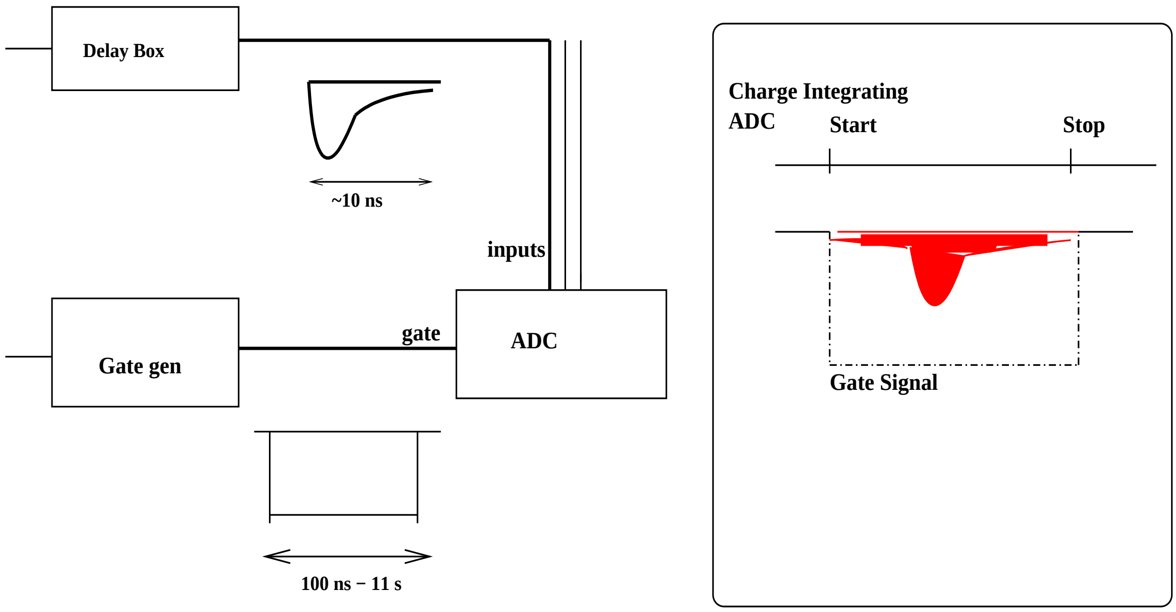

Figure 3.19: Data signals get integrated during the ADC's gate window.

known as the pedestal for that ADC channel. A normal pedestal is about 22 ADC counts, or in terms of charge i.e 5.5 pC.

The hardware modules discussed are not stand-alone. The ADC, TDC are placed in slots of a Computer Automated Measurement and Control crate (CAMAC). The total number of slots are 12, all are not usable here. In the two right-most slots of any CAMAC crate is the Crate Controller. This is the module that is the interpreter between the other modules and the computer. Modules talk to the Crate Controller and the Crate Controller talks to the computer. The discriminator, gate generator, logic unit, scalar used are Nuclear Instrument and Module modules (NIM). The delay boxes are made with a NIM module shell. The HV power supplies are NIM modules but they don't need the NIM bin for power [13].

Procedure for Cosmic Ray Test of Machined Scintillator Tiles

To test the efficiency of the grooved tiles, these tiles were checked both manually and electronically. Electronically, Cosmic Ray Test setup is made and installed at Panjab University, Chandigarh. All the tiles were checked before going for the next step i.e fabricating the detector tray. In this, the tiles under test are cleaned thoroughly, polished with white paints on the edges and wrapping it with special white and black paper called tyvek and tedlar to make it light tight. One end of WLS fibers are inserted into the grooves and other end is connected to Photo Multiplier Tube (PMT) through cookie.

The scintillator tile under test coupled with PMT is called test counter. The test counter is placed in between the well calibrated scintillator paddles. The paddles are the detectors in which the scintillator tile is directly attached to light guide. For coupling the light to PMT, a cookie of the same size as of photocathode is attached to the light guide with the help of optical glue. Optical Grease is used for making optical contact between PMT and the cookie. The whole assembly is wrapped with the tyvek and tedlar paper for efficient collection of emitted photons and transporting to PMT.

The optical signals from the test counter and the paddles are converted to electrical signal by PMT. The signal from the PMT's is fed into the Data Acquisition system (DAQ) as shown in figure 3.20.

The functions of the individual components of the DAQ is already described in earlier sections. The basic criteria is to test the detection efficiency of the machined tiles. The test counter is placed between the two paddles with such solid angle that there will be maximum muons passing through all three simultaneously. The test counter is given the required high voltage and the pulse signal is observed on the oscilloscope for its height, amplitude alongwith noise. The threshold for the discriminator is setup to reject the noise. The paddles and the test counter are connected with Logic Unit in such a way that in the final output, we get 2 Fold and 3 Fold in addition to the counts in the individual paddles and test counter. Here 2 Fold (2F) is made with AND coincidence unit for output

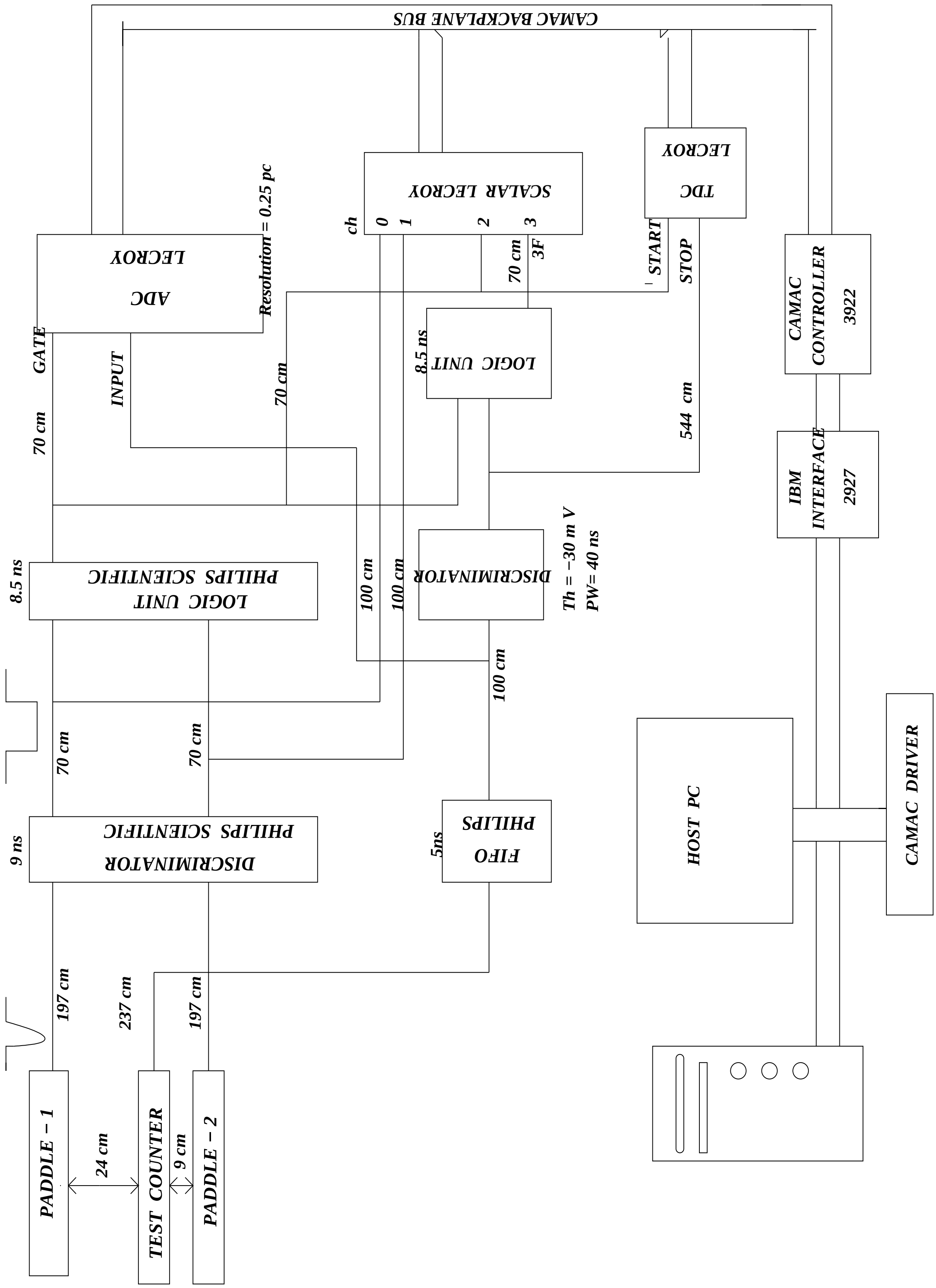

Figure 3.20: Diagrammatical view of DAQ for Cosmic Ray Test setup at Panjab University

of upper and the lower paddles and 3 Fold (3F) is made with AND coincidence unit for 2 Fold and the output of test counter. The output counts are recorded in PC using scaler module. The efficiency of the scintillator tile is calculated as

$$\frac{3F}{2F} \times 100\%.$$

It means the Muons which pass through the upper and the lower paddles must have been passed through the scintillator tile under test placed in between the above two and our tile under test should be capable of detecting all the Muons passing through it. The typical efficiency of the tiles were around 99.9%. The ADC output of one such tile is as shown in figure 3.21.

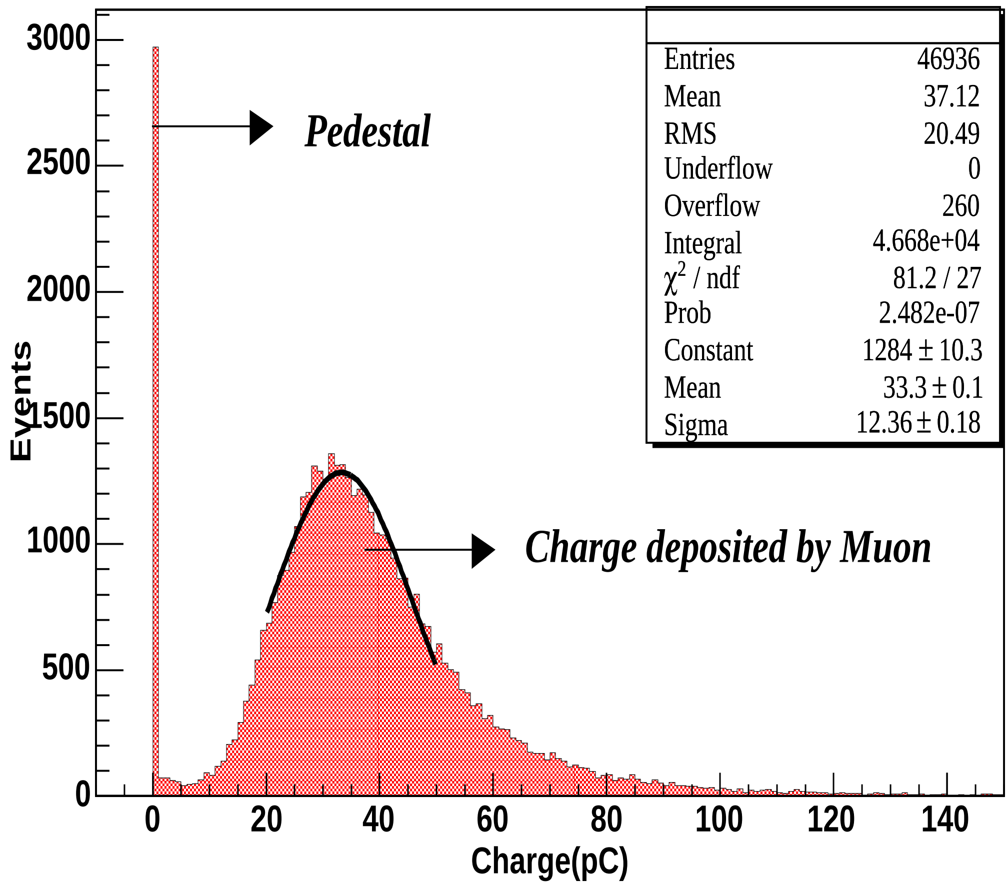

Figure 3.21: ADC output of one scintillator tile under test at Panjab University

By looking into the ADC plot, we conclude that the scintillator tile under test is very efficient in detecting the MIPs. The Pedestal value is well separated from the Signal ADC value.

Cosmic Ray Test for Fully Fabricated Scintillator Trays for Outer Hadron Calorimeter

The fully fabricated scintillator trays comprises of several tiles have been tested for their responses to MIPs using cosmic rays in a special stand designed for this purpose. This test gives the actual photoelectron yield of the individual tile.

The fully assembled trays are placed in a black box which contains 8 paddles on the top and 8 on the bottom known as trigger paddles. Each paddles has 2 scintillators grouped together with PMT read out. Vertical muons are selected using 4-fold coincidence trigger logic. The tray to be tested is placed in between the standard telescopes in such a way that every tile of the tray is right in between the standard paddles so that we can assume that the muon which pass through the upper and lower paddle must have been passed through the scintillator tiles of the tray. The distance between the upper or lower paddles and the scintillator tray should be such that it makes good enough the solid angle(figure 3.22) to collect the muons. If any of the paddles registers a coincidence, data from the tray are read out together with the information of the telescope causing the trigger using a latch circuit.

High voltage of negative polarity is used for the PMTs of both trigger paddles and test trays. The output signal from the PMT is sent to ADC for converting it into digital one. The PMTs are well calibrated using LED light to get number of ADC counts per photoelectron. Online data is acquired and can be monitored in a PC via GPIB-CAMAC interface. The pulse height spectrum is analyzed offline to determine number of primary photoelectrons produced. The HO trays are expected to supply at least 10 photo-electrons for a minimum ionizing particles if a PMT were used in the readout

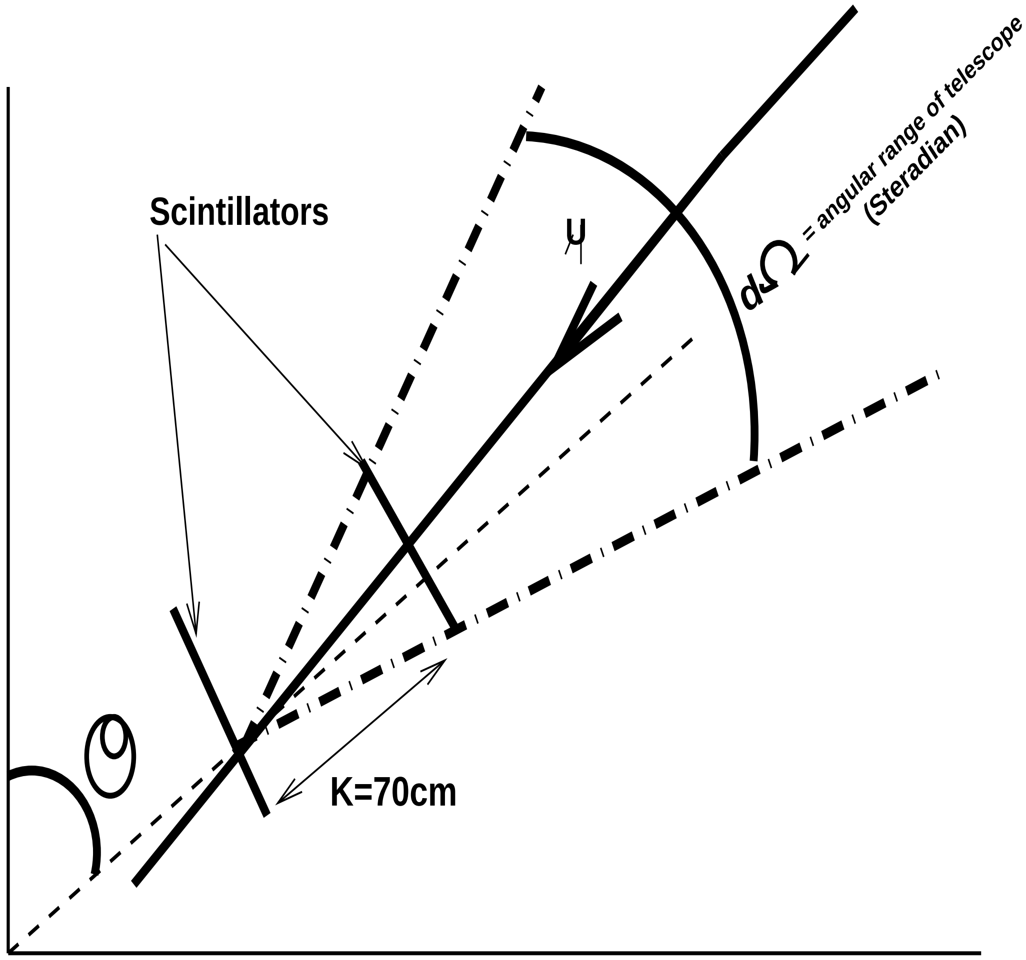

Figure 3.22: The solid angle made by scintillator counters

It is to be noted that the trigger rate of each telescope is 10-12/min. Typically for an approximately 90,000 events, about 14 hrs of data collection is required.

Analysis

Pedestal subtracted ADC charge of all the 6 tiles of a tray of Ring 1 are shown in figure 3.23. The mean of the pedestal subtracted charge of the first tile is 90.320 and the PMT calibrated value is 5.2 (ADC/p.e), the number of photoelectron produced is 90.320/5.2 = 16.422. The number of pedestal events out of the total number of events is the inefficiency of the scintillator tile of the tray, so the efficiency = 1 - inefficiency = 1 - 16.422/14251 =

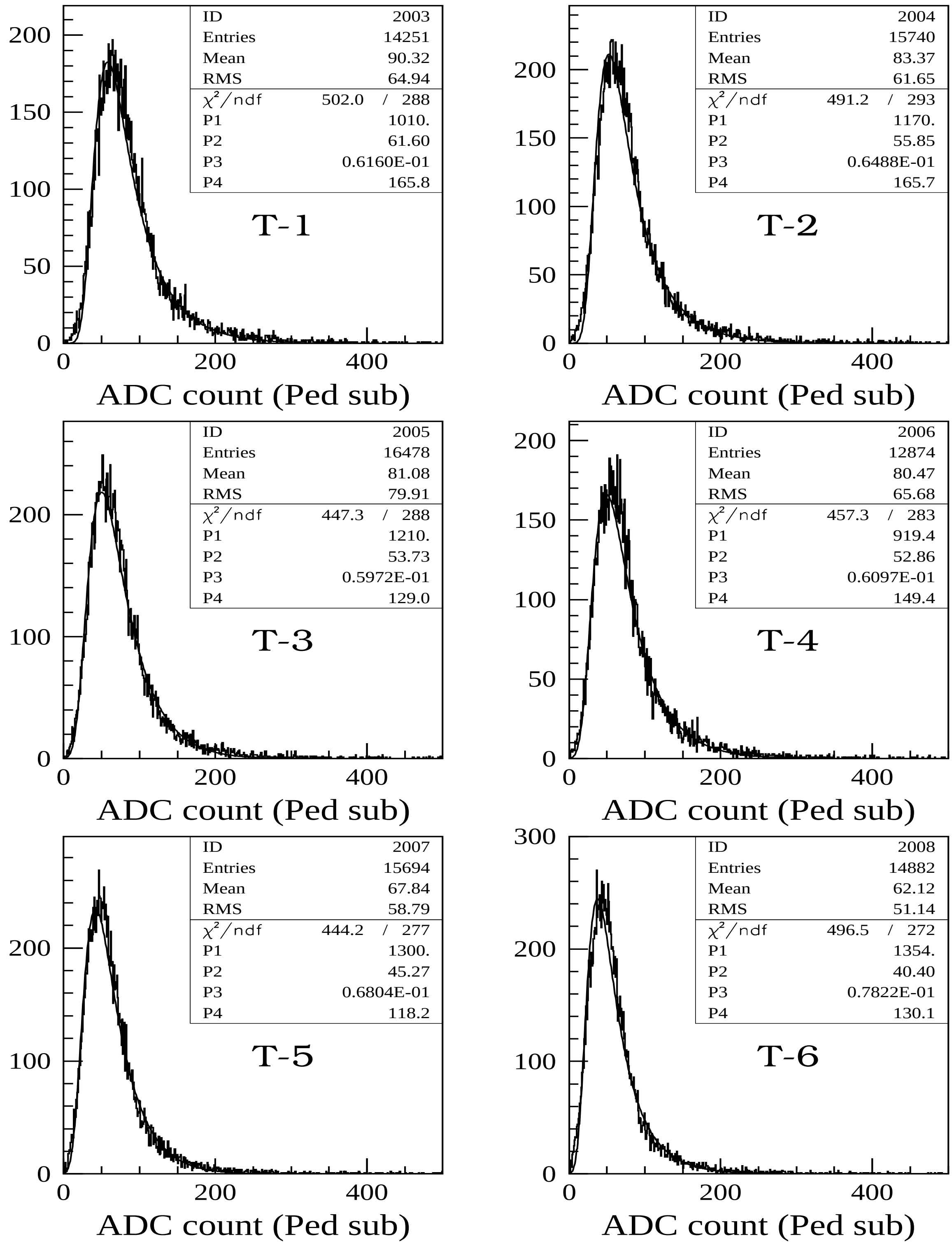

Figure 3.23: ADC (Pedestal sub charge) for each 6 tiles of tray of Ring 1

0.999 or 99.9%.

The Photo-electron yield of individual tiles of the scintillator trays is calculated for all the trays and of one such tray of Ring 1 is shown in Table 3.3. The photoelectron

Tile no.	efficiency(%)	Ped.sub. mean	Photo-electron yield
+1	99.9	90.320	16.422
+2	99.9	83.370	15.158
+3	99.9	81.078	14.742
+4	99.9	80.465	14.630
+5	99.9	67.844	12.335
+6	99.9	62.117	11.294

Table 3.3: Photoelectron yield of tiles in tray of Ring 1

yield of all tiles of tray "1" of all sectors of a Ring +1 is shown in figure 3.24. Each tray of Ring 1 consists of 6 tiles and there are 12 sectors in a Ring. The photoelectron yield of all the tiles are above the acceptance criteria (>8 pe). From the figure 3.24, it is clear that the photoelectron yield decreases once we go to higher tile number. The higher tile number means that we are counting the tiles away from the connector. The bigger the tile number means more distance from the connector, more length of fiber needed to transport the light to the connector, more is the attenuation of light. Therefore the tiles farthest from the connector has less number of photoelectron yield due to comparatively less amount of light reached to the pigtail connector.

The trays of all 12 sectors of particular tray number are of same geometry. So their output should be nearly same. The comparison of the photoelectron yield of tray

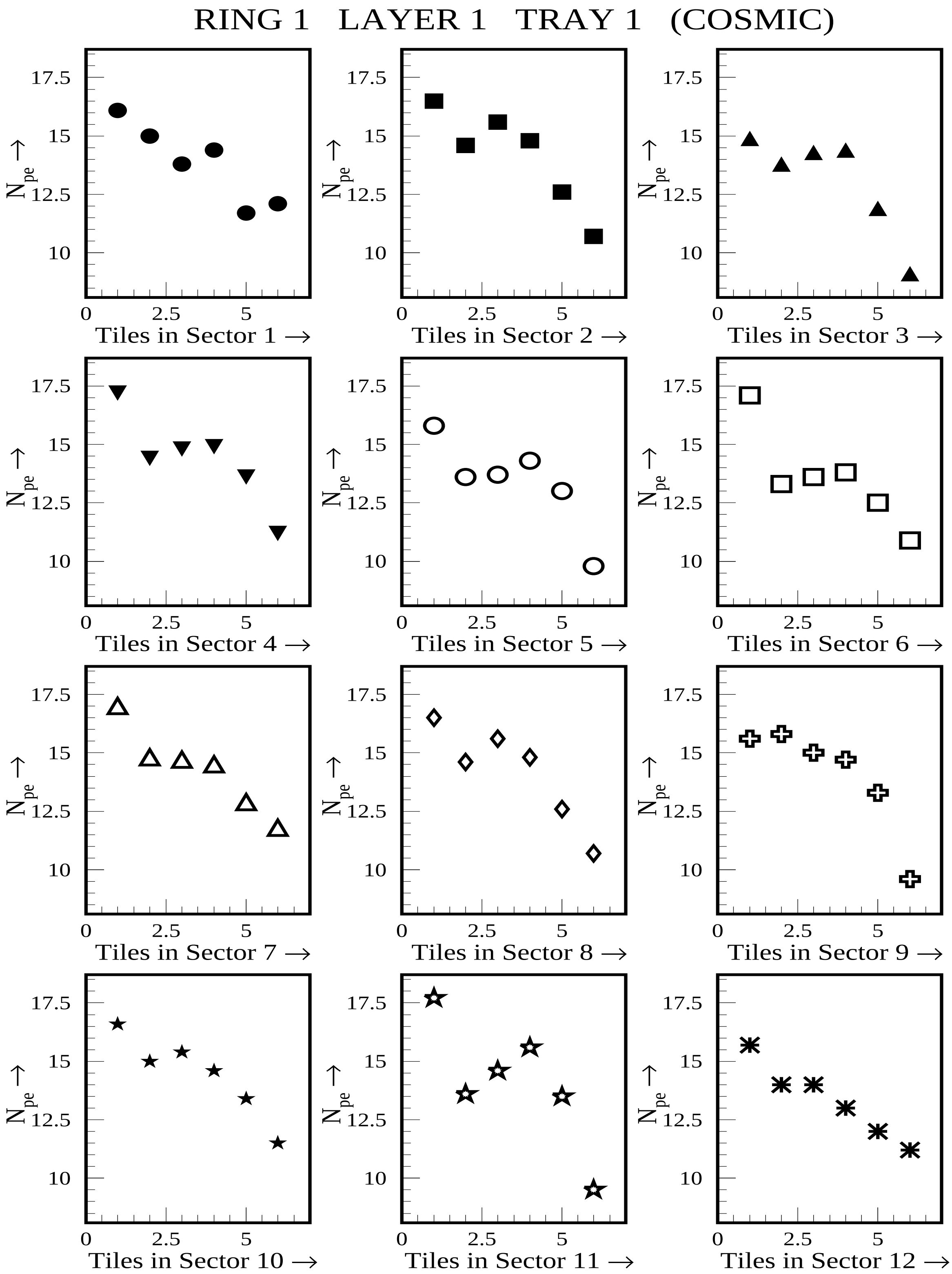

Figure 3.24: Number of photoelectrons of tiles of tray No. 1 (all sectors) of Ring +1

position with all the sectors of that ring is made. Figure 3.25 shows a plot of average number of photoelectrons obtained using muons in cosmic ray test as a function of the tile number in a set of 12 trays belonging to ring 1 layer 1 position 1. As shown in figure, all the tiles have mean number of photoelectrons greater than 8 which is the main acceptance criteria and the r.m.s spread is also within the acceptance range.

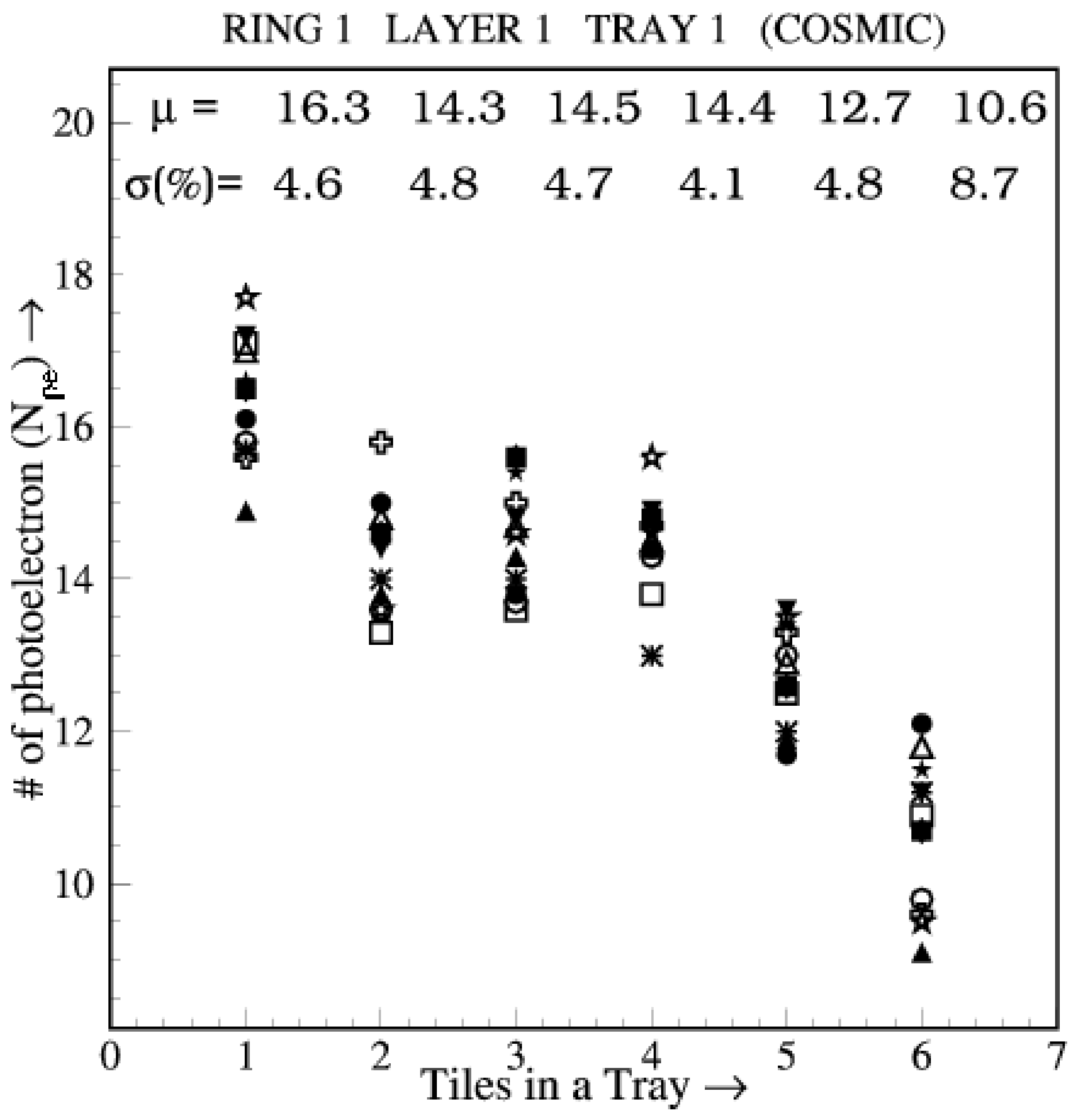

Figure 3.25: Number of photo-electrons for the tiles in a set of 12 fully assembled trays (of 12 sectors) belonging to ring 1 layer 1 tray position 1

3.5.5 Radioactive Wire-Source Test

The wire-source test is one of the quick quality control test of the completely assembled Outer Hadron calorimeter trays done with the help of a radioactive wire-source scanner.

All the trays of Outer Hadron calorimeter are equipped with thin stainless tubes and source coupler that will graze radioactive sources along the length of the tray. A wire with a pointlike radioactive source Co^{60} of strength less than 3 millicurie was pushed through these tubes by a specially built scanner which works on remotely controlled system of drivers. The DC current induced by the source traversing one tile of a tower will provide an accurate measurement of the response of the entire measuring chain. The output voltage is stored in computer for offline analysis.

Change of response due to PMT or electronics will show up as a change of the response of all tiles of a given tower and can be compensated by an adjustment of the overall calibration factor of PMT. For the radioactive wire-source test, calibrations has to be done periodically. During run time, it will be important that the front-end electronics allow simultaneous digitization of the DC current from the photodetector and of fast pulses, both beam-related and from laser light injection. PMT's with high leakage currents would compromise the ability to do the source calibrations.

The steps involved for doing the wire source test are:

1) The tray under test is positioned inside the test shelf after making sure that the wire-source tube and the coupler are properly mounted on the tray.

2) The flexible black tube from the wire-source driver end is inserted in the brass source coupler fixed to the tube on the tray.

3) The high voltage and the signal cables should be connected at the decoder box end and the high voltage supplies have to be made to set them.

4) Allow about 15 minutes interval before taking the data.

The output is monitored as a function of position of the Co^{60} source on the tray. It is monitored twice during a run, once while stretching the wire and again while retreating to the garage position. Figure 3.26 shows the result of trays position “1” of all 12 sectors belonging to ring 1 layer 1.

The height of the signal is largest near the connector end because of shortest fiber path and therefore less attenuation as compared to the point farthest from the connector. There are several spikes in the voltage output which corresponds to center of the tiles where the source is right above the WLS fiber(s) . The wire-source response depends on the length and area of the tile, the location of the source tube, and on the thickness of the scintillator.

It should be noted that this test is not an absolute test like cosmic ray test but its a relative test i.e we compare the response of all the trays of same sector of a ring whose dimensions are equal with one another and the tray whose response deviates more than 20% are rejected or remade. Also, the source can move only on one side of the tray into the stainless steel tube and so we cannot get the response of tray material on the other side. This test is very easy and quick which can be done after the installation of the detector to calibrate our detector when there will be shutdown period in between the runs.

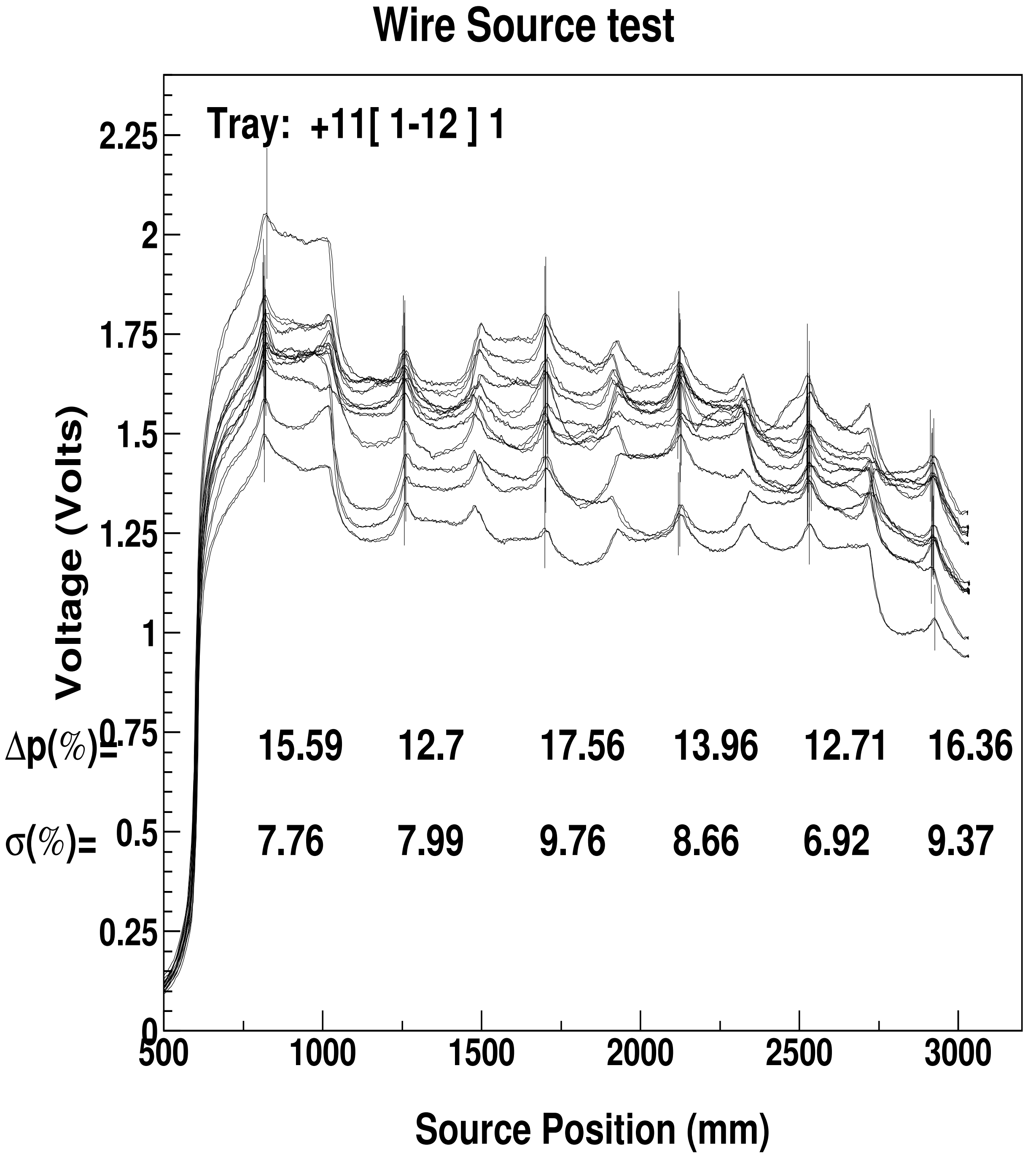

Figure 3.26: Wire-source test output of a tray No.1 of all sectors of Ring +1

3.5.6 Radioactive X-Y Scanner Test

We have tested the tray along the length of the tray with the help of wire-source scanner. In order to test the fully fabricated scintillator trays for CMS HO along the whole surface i.e along the X direction as well as Y direction, radioactive X-Y scanner is used for the purpose as shown in figure 3.27. With the help of this, we can see the response of scintillator tray at every desired point.

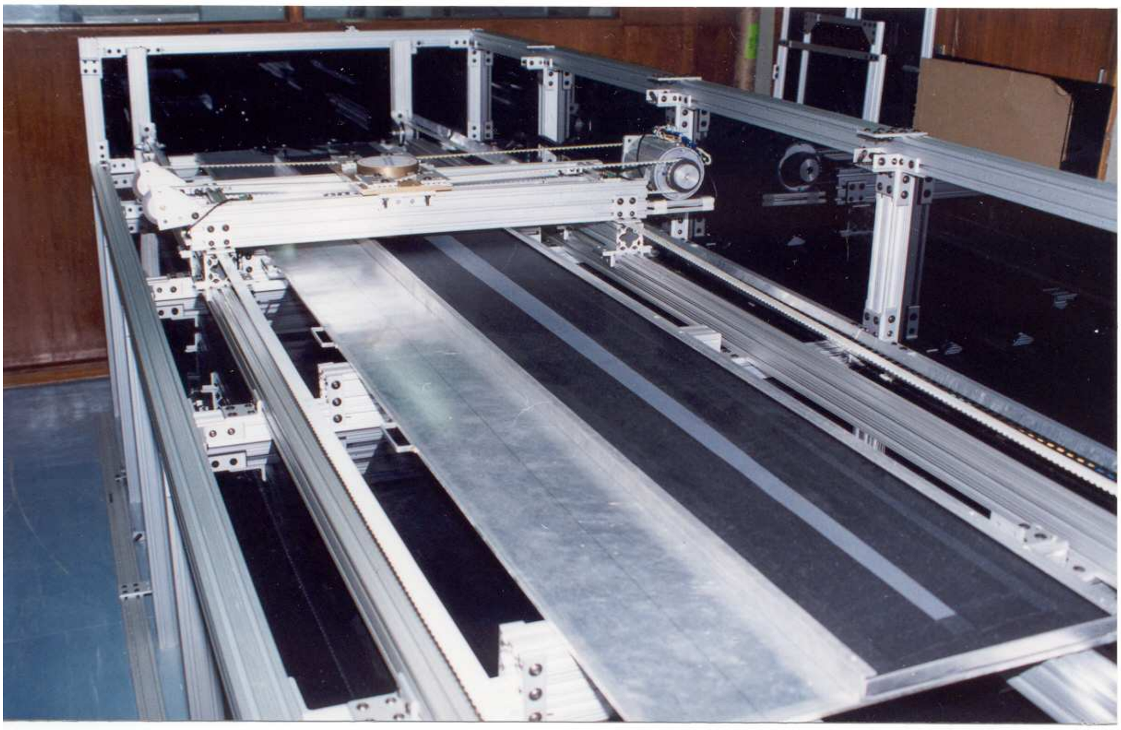

Figure 3.27: The X-Y scanner apparatus

This scanner moves the well collimated radioactive source Cs-137 of strength 10 millicurie over the whole surface of a fully fabricated scintillator tray to check the response of tray. The source is shielded using a lead and brass container which can move over X-Y direction all over the surface of the tray.

Structure of X-Y scanner

The basic framework as well as the X-Y positioning mechanical sub-system of the scanner has been designed using extruded special aluminium channels. The stepper motor driven belt and pulley scheme has been used on X-Y drives. The X-Y motion control, its monitoring as well as light readout are implemented in terms of PC based control and driver hardware modules. The small scintillator tile called calibration tile is permanently fixed on one end of the scanning table to cancel out day to day gain variation in the readout system.

Procedure for doing the test

The detector tray is mounted on the aluminium bed such that the connector end of the tray along with its tray carrier are fully aligned with place made specially for the purpose. The connectors of the tray under test are connected to the PMT's of the readout using optical cable connectors. There are two pairs of optical cables to carry light from the tray to the PMT assembly - one using 12 pin and the other using 18 pin connectors. In each pair, left and right connectors are labeled accordingly. Appropriate pair of cables should be connected to the pigtail connectors on the tray, while the other pair of cables are stored inside a black cloth. Entire tray along with the optical cables and the PMT assembly should be covered with black cloth. Turn ON the PMT supply and wait for approximately 15 minutes. Before taking the run the Current-to-Voltage converter's power supply as well as the stepper motor's power supply should be turned ON.

Figure 3.28 shows the ADC output at several x and y points over the surface of twelve trays of tray type 2 belonging to Ring 1. One clearly sees that signal size for the tiles close to the connector is largest and it slowly decreases for tiles with larger fiber length. There are several spikes which corresponds to the center of the tile where WLS fibers of all four sigma grooves collects the light simultaneously and also little peak on the extreme right which corresponds to the signal from calibration tile used to normalize the signals from the trays of the same group.

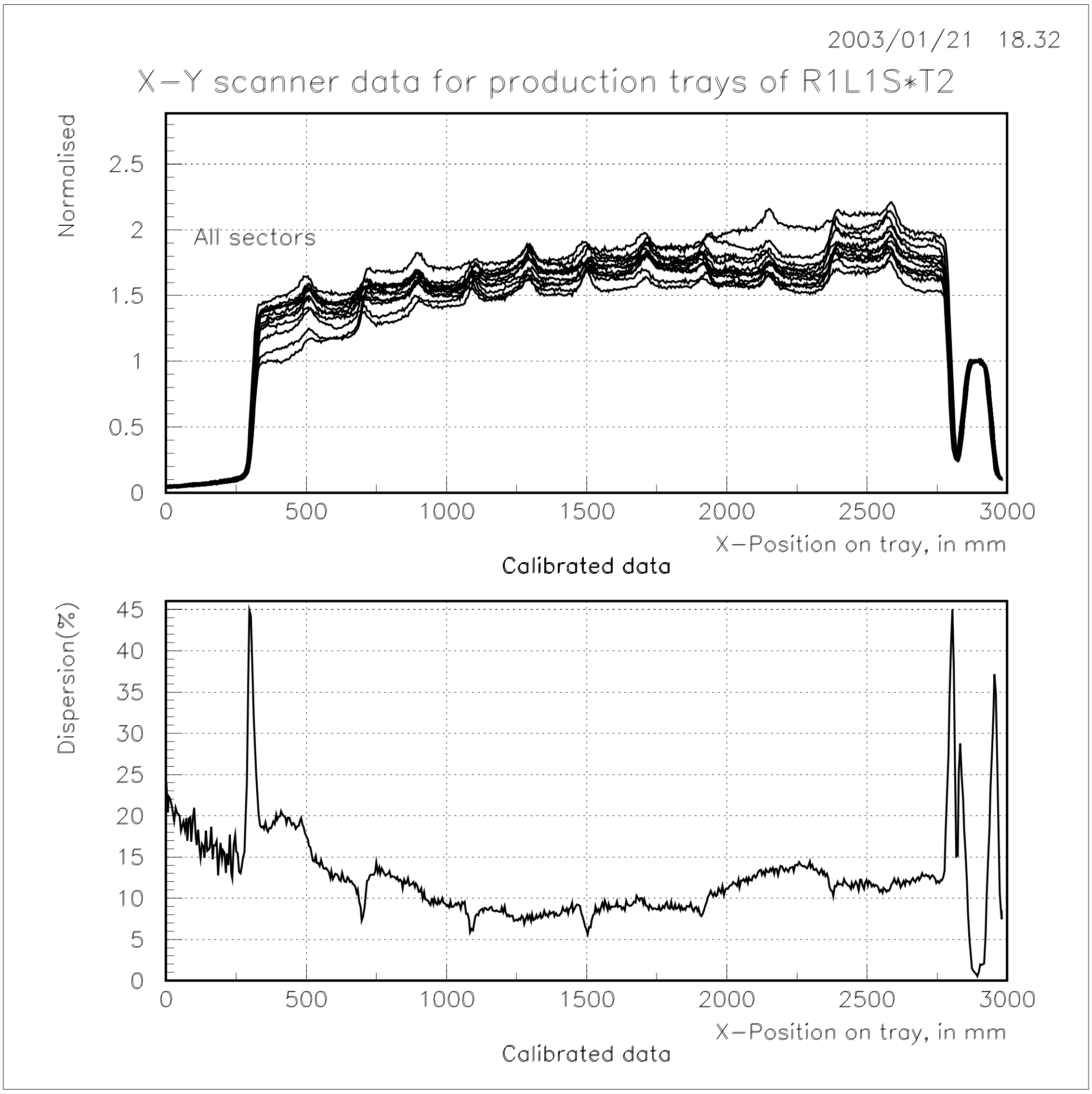

Figure 3.28: X-Y scanner test output of scintillator tray No.2 (all sectors) of Ring 1

It is to be noted that this test is also relative test i.e we compare the response of all the trays of same sector of a ring whose dimensions are equal with one another and the tray whose response deviates more than 20% are rejected or remade. Also using this test, we can get the response of each and corner of the tray but this test cannot be done after installation of the detector.

3.6 Correlation of the Tests

As described earlier, the fully assembled trays are tested with mainly three types of tests, cosmic ray test, radioactive wire-source test, radioactive X-Y scanner test. Correlation between number of photoelectron in cosmic test and voltage signal peaks in the wire-source and x-y source test was done and shown in figure 3.29. These are found to be fully correlated. Statistical errors are found to be less than 1%. Here the readout system for cosmic ray test and wire-source test is the same whereas for X-Y scanner, it is the different set of PMT's and optical connectors.

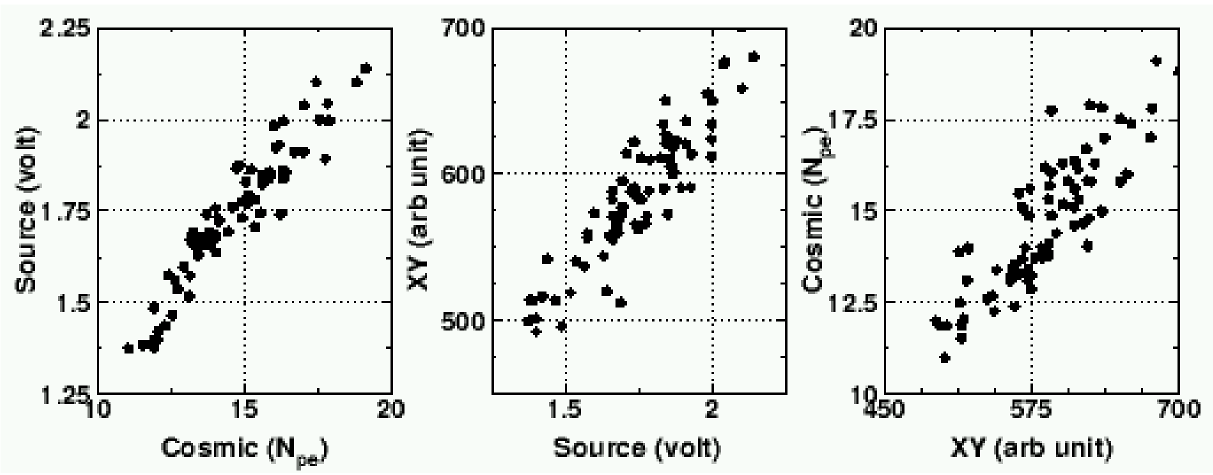

Figure 3.29: Correlation between number of photoelectron in cosmic test and signal peaks in the wire-source and x-y source test

All the HO trays were fabricated, tested and were transported to CERN lab, Geneva for installation at CMS detector. Prior to installation, all the trays were again tested with both radioactive wiresource and x-y scanner so as to check the response of the trays after transportation and geographical change. All the trays were found to be good at CERN. The two sets of measurement of one such tray (No.4) of Ring -2 are seen to be fully correlated as shown in figure 3.30.

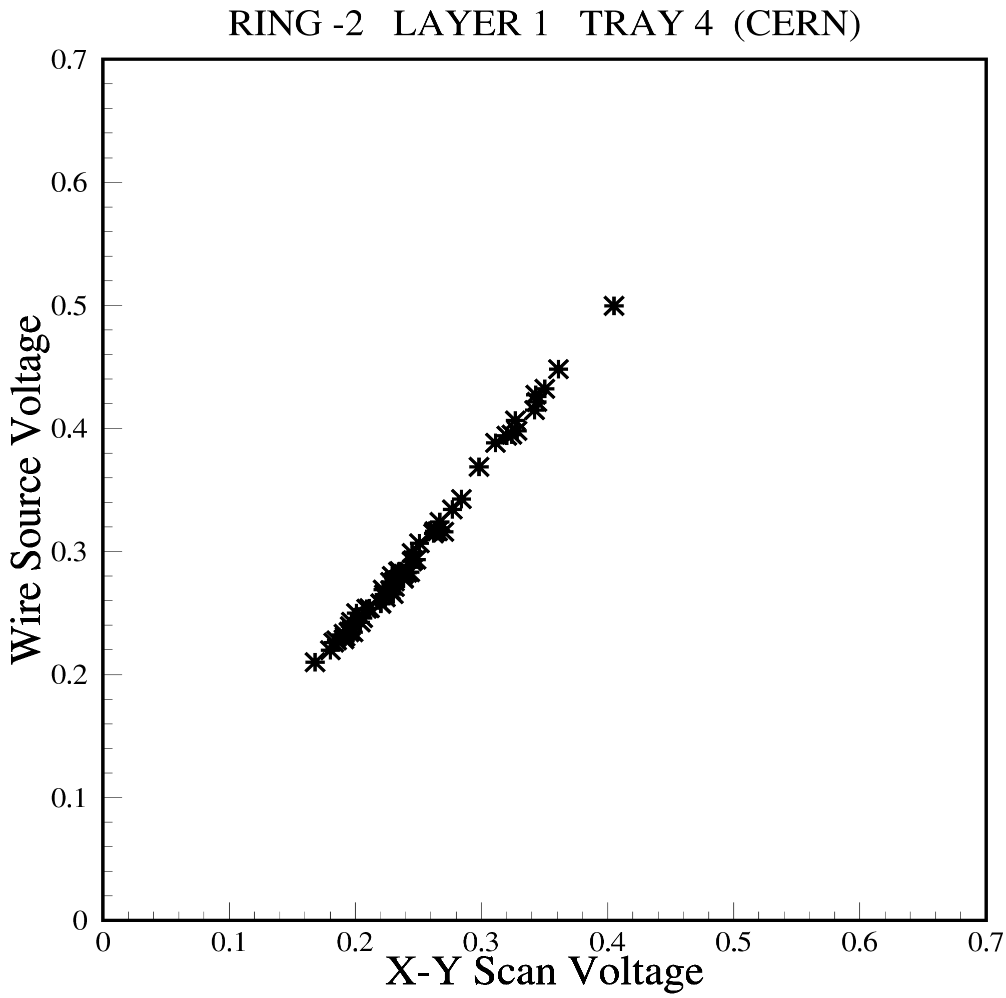

Figure 3.30: Correlation of the signal peak positions in the wiresource and XY scan on the same tile at CERN

3.7 Quality Control Test of Outer Hadron Calorimeter Readout Boxes

RBX operation without any malfunction is a crucial part of the entire HCAL performance. It is important to know in detail every parameter of the read out electronics performance. For this reason, Quality Control (QC) test of HO RBXs was performed before they finally installed on the CMS detector.

3.7.1 Burn-In Test

Hybrid Photo Diode (HPD) is operated under 8 kV high voltage. It is important to know how a hybrid photo diode behaves for long periods of time. For this purpose a special test was set up at the CMS detector construction site. Each RBX with inserted RM's were placed under high voltage, and some amount of light was sent to RM's and to the CM pin diode. Data from each RM was read out and stored for further analysis. During the burn-in test, two kind of runs (In our case "run" means a file containing readout data from the QIE) were taken, pedestal run and LED run. During the pedestal run, light was not injected to the HPDs but QIE responses were read out and stored. During LED runs, light from a Light Emitting Diode was injected using optical cables to the HPD's. Each RBX with four RM's and one CM were held under high voltage for one week. Data were taken before, during and after each one week test period to compare outputs of RM's before and after burn-in. Special scripts were developed for this purpose, providing an immediate possibility to check the RBX performance. All the HO RBXes were tested for burn-in before installing into the Rings. The mean charge in all 4 RM's of one such RBX is shown in figure 3.31.

For Ring 0, 16 out of 18 pixels are active and two are dummy (dead) pixels. The timing of the HPD (response) should not vary too much of all HPD's relative to each other. One such Root Mean Square (RMS) plot of timing of HPD's is shown in figure 3.32. The time response of all HPD's are identical.

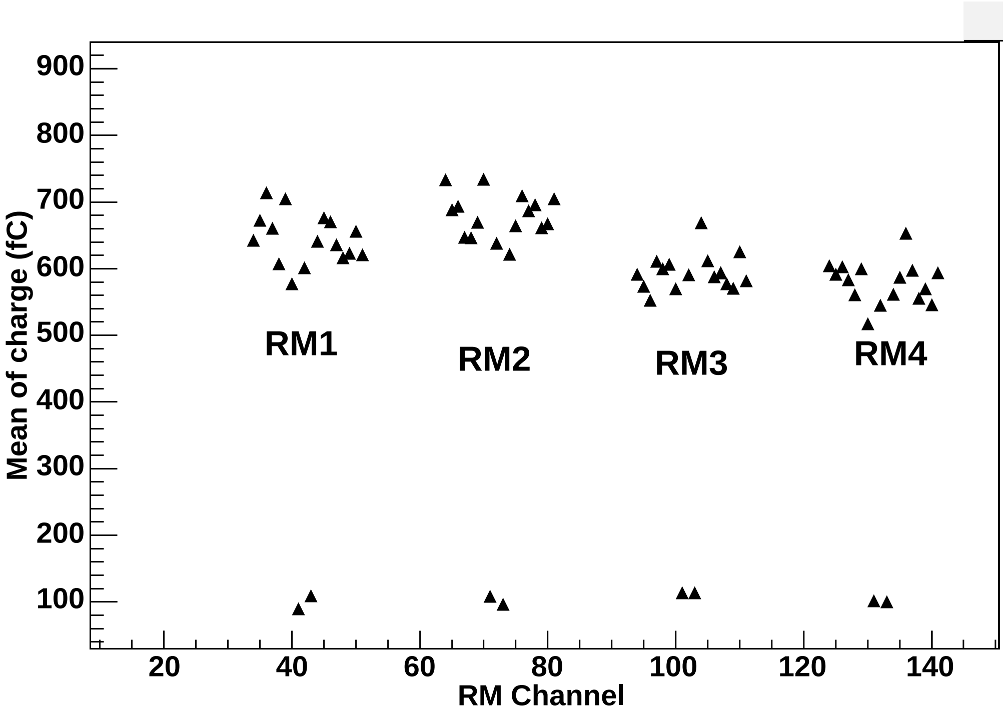

Figure 3.31: Mean of the charge (fC) of all 4 HPD's of one Readout Box

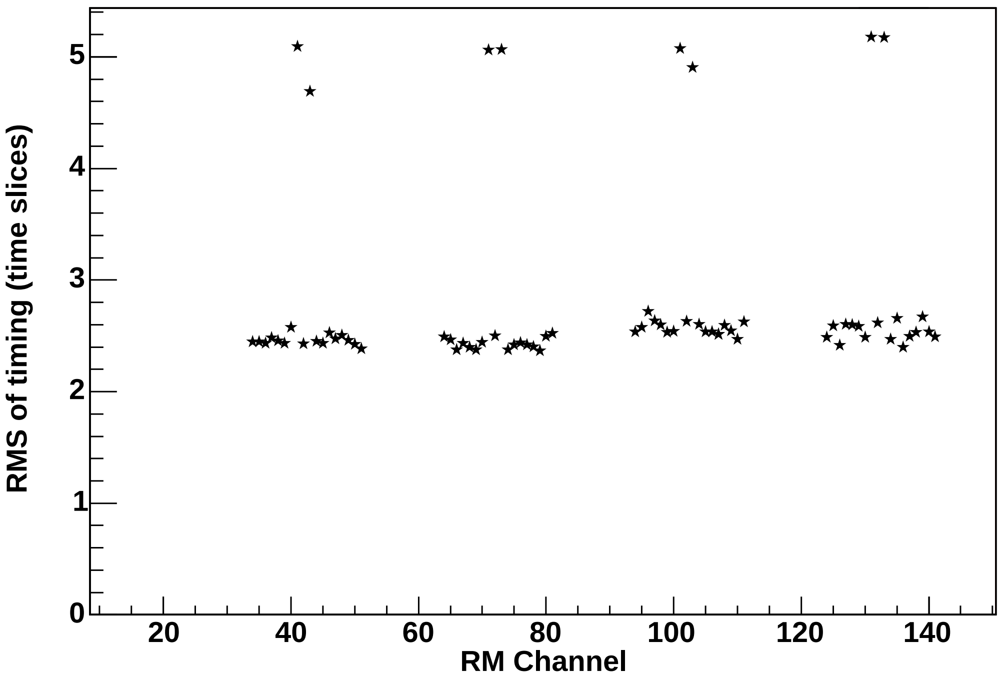

Figure 3.32: RMS of the timing (in timeslices) of all 4 HPD's of one Readout Box

3.8 Summary of the contribution of Panjab University in HO Detector Development

The Indian Institutes, Panjab University Chandigarh and TIFR, Mumbai took the full responsibility of designing, fabricating, testing and installing the Outer Hadron Calorimeter in CMS detector at CERN, Geneva. Out of the five Rings of HO namely +2, +1, 0, -1, -2, Panjab University took the responsibility of machining and grooving the HO scintillator tiles for two Rings +1 and -1. The scintillator sheets were imported from Bicron company, United States . These sheets were cut into desired shape and grooved in Computer Numerical Control Machine.

Each tray of Ring $\pm$ 1 corresponds to 6 tiles and there are 6 trays in every sector of a Ring. So in total there are 36 tiles in each sector. There are 12 sectors in each ring. In total, the contribution of Panjab University in fabrication of Rings $\pm$ 1 are 864 tiles. In order to make sure that the machined and grooved tiles meet the necessary requirements, a number of quality checks and procedures have been adopted, during and after production phase. Quality control of scintillator tiles includes manual inspection of the tiles, recording the thickness variations of the surface of the tiles.

The cosmic ray test stand were setup at Panjab University and this test were performed for all these tiles before assembly into bigger unit called tray. This test was done to check the efficiency of individual scintillator tiles. Those which did not met the requirement are rejected and replaced with new ones. The fiber scanning machine was fabricated and installed at Panjab University to check the transmission of optical fibers. The optical fibers are tested and verified before doing cosmic ray test for scintillator tiles.

In addition to the fabrication of Ring $\pm$ 1 scintillator tiles, we participated in assembly and testing of all trays for all the rings alongwith TIFR, Mumbai. Both Panjab University and TIFR are also participating in ongoing installation of Outer Hadron calorimeter at CMS detector in CERN, Geneva.

Bibliography

[1] CMS Hadron Calorimeter Technical Design Report, CERN/LHCC 97-31, CMS TDR 2, June 20, 1997

[2] J.B.Singh, India in CMS , DST Linear Collider Meeting Nov 10-11, 2003

[3] Sudeshna Banerjee and Sunanda Banerjee, CMS NOTE 1999/063

[4] B.S.Acharya et al, The CMS Outer Hadron Calorimeter, CMS NOTE 2006/127

[5] Outer Hadron Calorimeter Engineering Design Review, TIFR/CMS-99-01

[6] V. V. Abramov, B. S. Acharya, N. Akchurin, A. Ball, S. Banerjee, P. de Barbaro, et al., Studies of the response of the prototype CMS Hadron Calorimeter, including magnetic field effects, to pion, electron, and muon beams, Nucl. Instr. Meth. vol. A457, pp. 75-100, 2001

[7] G. Anzivino, H. Arnaudon, P. Baillon, P. Benetti, L. Boskma, P. Burger, et al, Review of the Hybrid photo diode tube (HPD) an advanced light detector for physics, Nucl. Instr. Meth. vol. A 365, pp. 76-82, 1995

[8] H.S.Bawa, M.kaur, J.M.Kohli et al, The CMS Outer Hadron Calorimeter, CMS NOTE 2006/127

[9] Software utility for HO pigtail certification, *http://www.hecr.tifr.res.in/~bsn/CMS/pigtailQC/ptnote.html*

[10] S.R.Dugad, V.S.Narasimham and B.Satyanaraynana, Pigtail certification scheme for Outer Hadron Calorimeter,
http://www.hecr.tifr.res.in/%7Ebsn/CMS/pigtailQC/ptnote.html

[11] *http://en.wikipedia.org/wiki/Cosmic_ray*

[12] *http://adweb.desy.de/mdi/documentation/BLMat/desy/pm_szintil.html*

[13] *http://www.umsl.edu/ thompsoj/quarknet/2004/gen/leigh_camac.doc*

Chapter 4

CMS HCAL Beam Test

The CMS Hadron Calorimeter is the crucial component of the detector. It is required for the discovery potential of Higgs between masses of 100 to 800 GeV. Jet physics is not possible without the hadron calorimeter. It is the most important goal of the CMS experiment to have a working and calibrated hadron calorimeter on the first day of data taking. One of the goals of the Hadron Calorimeter testbeam is to study the performance of the detector in measuring single electrons, pions and muons. In addition, the goal is to test its ability to measure hadrons, their energy response and resolution, and their dependence on energy. It contains a description of the CMS calorimeter system including its configuration, calibration and run conditions.

In CMS HCAL testbeam, various sections of the calorimeter have been tested using various particle of different energies. The calorimeter towers were exposed to pions, electrons and muons over a large energy range. More than 100 million events were read-out. The channels of two Hadron Barrel Calorimeter wedges , Outer Hadron calorimeter, Hadron Endcap and Hadron Forward Calorimeter were tested in a detector configuration which included an aluminium slab representing the solenoid material and a mock-up of the electromagnetic calorimeter.

4.1 Beam Test Setup

The CMS HCAL has a permanent test beam facility in the CERN H2 beam. The figure 4.1 shows the diagrammatical view of testbeam setup [1]. The beam was fixed to the laboratory frame and a moving table is used to change the relative direction of the beam with respect to the detector. This allows the beam to test different HCAL towers as a function of η and ϕ. The range of motion of the rotating platform was limited to $1 < \phi < 6$ i.e 6 ϕ's. The position of the platform was measured electronically and recorded in the data stream. The detector response provides an accurate calibration of detector position with respect to beam.

A special table was constructed for two Hadron Forward calorimeter (HF) wedges that can be moved up and down, sideways and tilted to fully simulate the detector in the testbeam, all under computer control. There were two separate Data Acquisition systems (DAQ), one for HF and one for HB, HE and HO. High voltage, Low voltage, Slow Controls, moving radioactive wire source, LASER and LED pulsing system completes the major items of the testbeam facility. The beam were used in bunches that are 25 ns apart to simulate the LHC [2].

Two configurations of the beam line were used [3]. For particles with momenta between 10 GeV/c and 300 GeV/c, the normal magnetic configuration of H2 were used. The primary proton beam from the Super Proton Synchrotron (SPS) accelerator with momentum = 400 GeV/c strikes the primary target. From the primary target, a secondary hadron or electron beam is made in the momentum range from 10 GeV/c to 400 GeV/c. To generate beam of particles with momenta less than 10 GeV/c, an additional target and a beam stop were inserted into the beam line. Additional beam focussing and bending elements were introduced along the very low energy (VLE) path in order to make a well-defined beam with momenta between 2 GeV/c to 9 GeV/c. Particle identification was performed with Cherenkov counters CK1 and CK2. The gas pressure in Cherenkov counter was adjusted to identify electrons so that pions with momenta less than 20 GeV/c

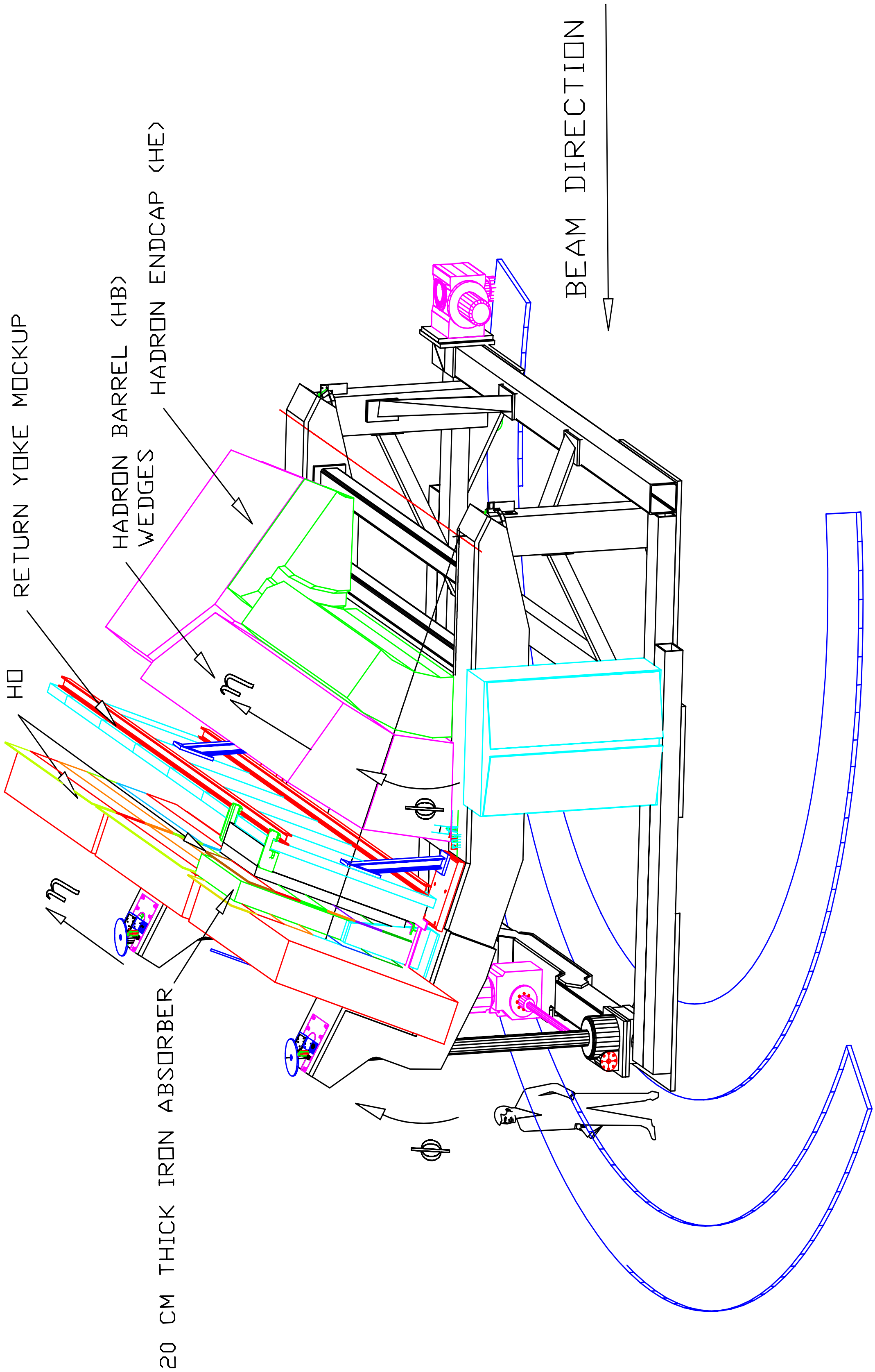

Figure 4.1: Diagrammatical view of CMS HCAL testbeam Setup

emit no cherenkov radiation in CK1. Cherenkov counter CK2 was used to veto protons and kaons in the positively charged beams with momenta between 5 GeV/c to 9 GeV/c. The gas pressure in CK2 was set to give signals from pions with momenta greater than 3.5 GeV/c, muons with momenta greater than 2.65 GeV/c and protons with momenta greater than 23.5 GeV/c.

The beam line is equipped with two scintillator tiles to trigger the events and set of three wire chambers to monitor the beam transverse (x−y) position and incident direction, event by event. All three wire chambers have two perpendicular planes of wires to measure the horizontal and vertical coordinate of any charged particle traversing the chamber. All three wire-chambers had multi-hit electronics allowing the detection of showers from the upstream interaction of particles along the beam line. In the VLE configuration of the beam line, an additional scintillator was included to assure that the beam particle followed the VLE path during the very low energy data taking. This was necessary to eliminate any muons created in the beam just after secondary target.

4.1.1 The Detector Configuration

The detector includes the mock-up of the ECAL, consisting of an aluminium box which contains a 7×7 $PbWO_4$ crystal matrix. This box may be translated and rotated for the beam to run along any of the 49 crystals . The crystals are tapered so that they have a slightly smaller upstream cross-section. At the end of the ECAL crystal, a plastic light guide transmits the crystal light to photomultiplier tube. The ECAL box is followed by two HB wedges positioned together as in the real CMS setup. The active medium of the HB calorimeter is plastic scintillator with read out as wavelength shifting optical fibers. This technique uses scintillator tiles to sample the shower. Wave-shifting fiber embedded in the tile traps the scintillator light and clear fiber spliced to the WLS fiber carries the light to photo-transducers. An aluminium slab accounts for the solenoid material and precedes the outer hadronic calorimeter (HO). The HO contains fully fabricated plastic scintillator trays with readout using WLS fiber spliced with clear fiber. The HO consists of two layers of scintillators in case of Ring 0 and one layer in case of Ring 1 and 2 surrounding an iron block followed by an iron plate acting as a tail catcher. For the HB and HO, the light from the scintillators is transported to the Hybrid Photo Diodes through clear fibers. The signal is then processed by the Charge Integration Electronics (QIE) which gives short output pulses. A picture of the experimental apparatus during CMS HCAL testbeam 2003 is shown in figure 4.2 [3].

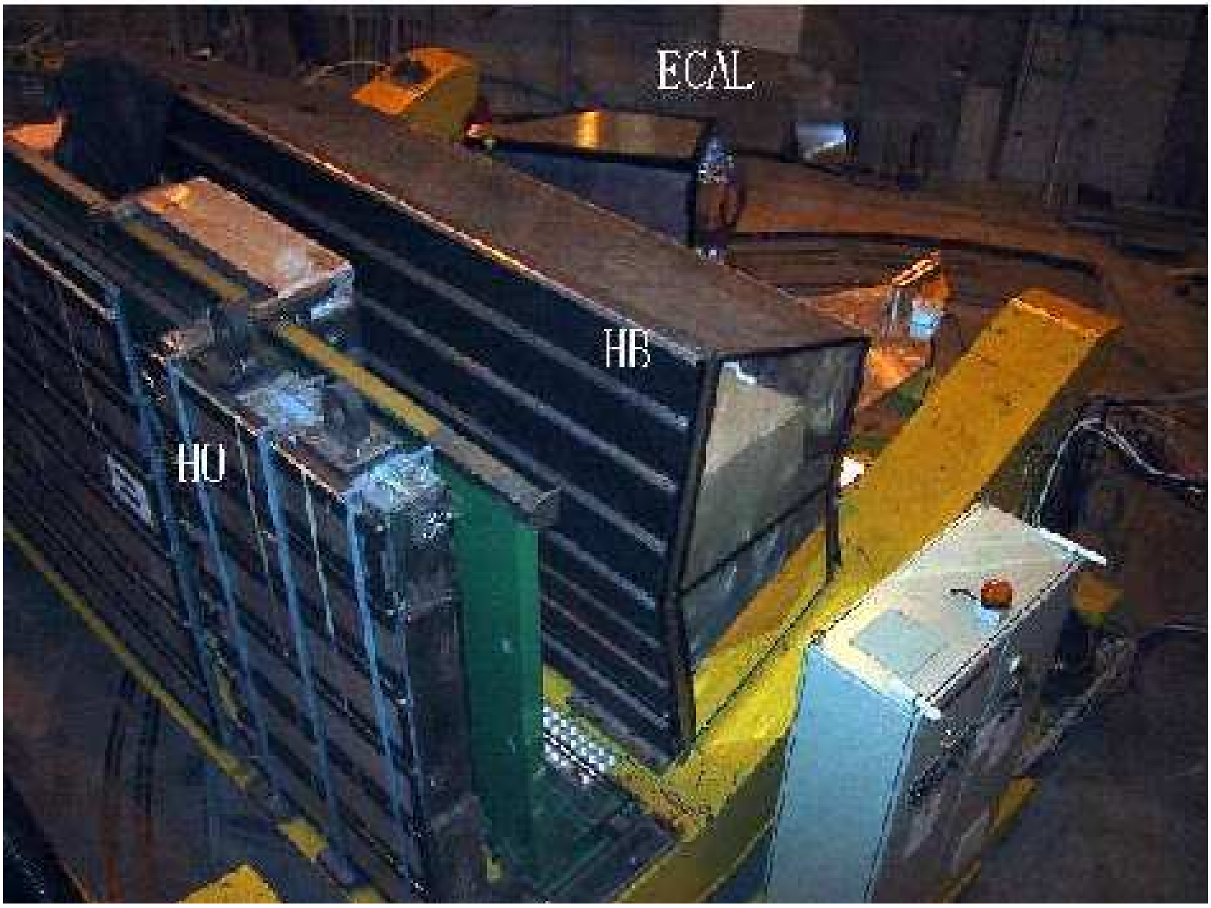

Figure 4.2: HCAL testbeam Facility at CERN

4.2 Data Acquisition of CMS HCAL Testbeam Setup

The chosen technology for the HCAL is sampling calorimetry with a non magnetic brass absorber and plastic scintillator plates that act as a detection medium. The plastic scintillator absorber plates are segmented into tiles whose geometry has been chosen such that tiles from the successive layers of the scintillator form towers pointing towards the interaction point. Light created in scintillator tiles is captured in wavelength shifting fibers embedded in grooves of the tiles. The wavelength shifted fibers is further guided towards photo-detectors through clear optical fibers spliced onto WLS fibers. All the light from the consecutive tiles in a given projective tower is guided into the same pixel of a Hybrid Photo Diode and read out by one channel of the read-out electronics chain. The requirement to minimize light loss in the optical waveguides has led to the installation of photodetectors and the readout and digitizing electronics on the edge of the detector as close to the scintillators as possible.

All the components of the front-end electronics are required to operate in a 4T magnetic field. The chosen photodetectors were HPDs which have good linearity over wide dynamic range, relatively small size and can operate in strong magnetic field when the field is aligned with the axis of the applied electric field. Their relatively low gain of about 2000 has imposed special requirements on readout and calibration systems.

This technology of hadron calorimetry is implemented in the pseudorapidity range up to $|\eta| = 3$. For high eta region, $3 < |\eta| < 5$, the expected radiation doses exclude use of plastic scintillators and the chosen technology for the Hadron Forward calorimeter is the detection of cherenkov light produced by hadron showers in radiation hard quartz fibers that act as both detection medium and light guides. As HF is situated outside the central magnetic field, the readout of the produced light is performed with PMT's. The front-end and readout electronics for HF are the same as for the rest of HCAL.

4.2.1 Front End

Operation in LHC conditions demands that the HCAL front-end electronics should have low noise, high frequency of approximately 40 MHz, high sensitivity of approximately 1/3 fC least count and wide dynamic range of approximately 16 bit. In addition, there are requirements on reliability, radiation tolerance, magnetic field immunity, cross talk and capabilities for DC current measurement [4]. The CMS Hadron Calorimeter Front-End Module is shown in figure 4.3 & is used to digitize the analog signals of over 10,000 detector channels.

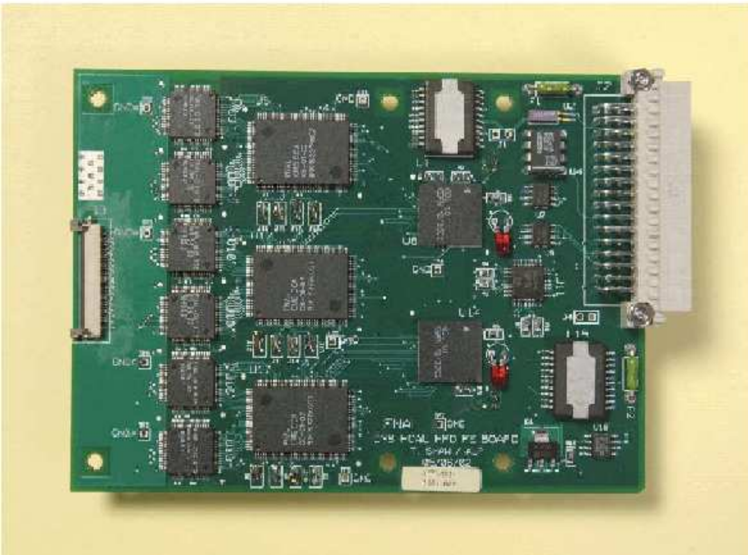

Figure 4.3: Picture of Front End Module for HCAL/HO

4.2.2 Trigger and Readout Chain

Figure 4.4 shows the readout chain from detector to Data Acquisition Personal Computer (DAQPC). The scintillation light from the HCAL panels is collected by wavelength-shifting fibers and transported to a hybrid photodiode which converts the light into electrical charge. The charge signal is measured and encoded into a non-linear digital scale by the Charge Integrator IC (QIE).

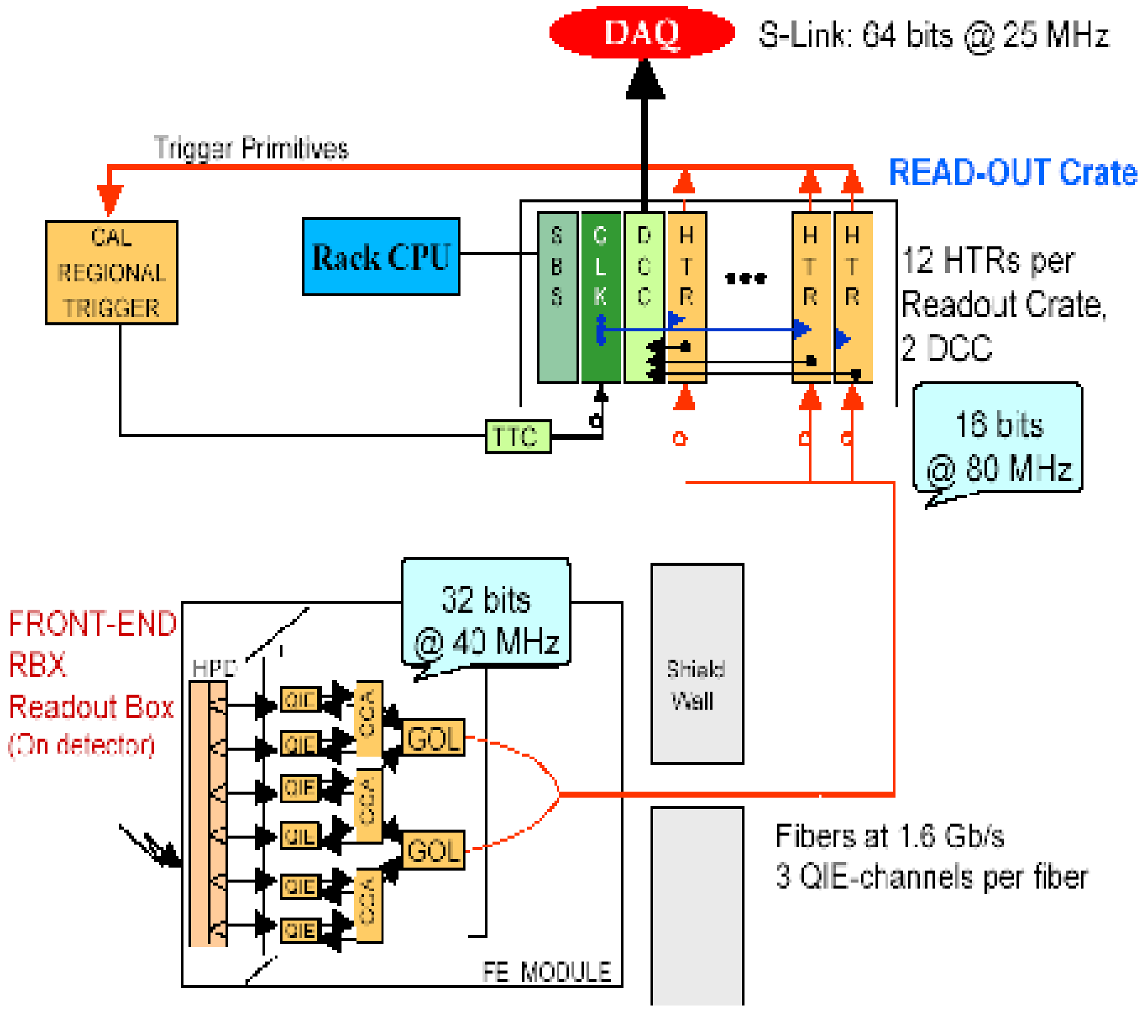

Figure 4.4: Schematic depiction of the HCAL testbeam readout chain from HCAL to DAQ PC

The QIE uses the LHC clock to divide time into regular bins and measures the accumulated charge in each time bin. Internally, the QIE uses capacitors to accumulate the charge and measure the voltage. There are four such capacitors in each QIE referred to as Cap-id 0, 1, 2 and 3. These four capacitors of four integrators with weighted equivalent capacitance are attached to a current splitter. The QIE uses each capacitors, in-turn discharging it for two clocks before using it again. In other words, one set integrates the input current for one LHC bunch crossing interval, the other three sets of integrators are simultaneously settling, being readout and being reset. Thus each subsequent time sample comes from a different Capacitor-id or Cap-id. In the final system, each time bin will be 25ns long [5].

Channel Control Asic (CCA) is a custom built module whose basic functions are to supply clocks for QIEs with individually programmable delays, align the data received from QIEs and send them to the GIGA-bit optical Link (GOL) chips [6]. Other CCA functions are to provide a serial interface for programming the CCA, adjust QIE pedestal values, set QIEs to fixed or auto ranging modes for calibration or physics, as well as to issue resets, test patterns and test pulse triggers.

Control of the front-end cards as well as delivery of clock and Trigger Timing Control (TTC) signals is performed through a Clock and Control Module (CCM) that communicates with the Detector Control System through an optically isolated RS422 interface [7].

Data from the QIE arrive into HCAL Trigger and Readout (HTR) modules through optical fibers. HTRs are designed to receive data on optical links, determine the energy for each tower, identify the bunch crossing and send trigger primitives to the regional calorimeter trigger module at 40 MHz. If a trigger is maintained, the raw data is transferred from pipeline storage to a data concentrator card (DCC) over copper twisted-pair cables.

The DCC receives data over up to 18 serial links from the HTR cards, performs error checking, monitoring and transmits the data to DAQ system through 64-bit S-Link interface, a CERN specification for an easy-to-use FIFO-like data link. It has event-building logic, error-checking and monitoring logic as well as data buffering and formatting logic. There is a possibility to read the data through VME interface for monitoring purposes [8].

4.2.3 Data Acquisition System

A data acquisition system for the test beam was based on the XDAQ toolkit and contained a custom built single components event builder. Run configuration and management tools were built using MySQL database and Java editing tools. A light-weight Java-based Run Control was developed and communication with readout and trigger electronics was done using SBS (ex-Bit3) PCI-VME interfaces [9].

The DAQ hardware system consisted of a 9U VME crate housing a fanout card for TTC signals, as well as HTR cards and the DCC. A second 6U VME crate contained TDCs and ADCs as well as TTCvi, TTCex and a custom built Trigger that performed delivery of trigger signals to the TTC system, triggering of calibration pulses such as LED & LASER and generation of gates for TDCs and ADCs.

The system clock has been provided from the main transmitter and after processing in the TTC machine interface crate (TTCmi), it was distributed through TTC opto coupler module (TTCoc) to front-end and readout cards. Trigger were obtained through a coincidence of two scintillating counters situated upstream from the detector.

4.3 Data Sets Collected in CMS HCAL Testbeam

Several data sets were recorded during HCAL test beam in H2 beamline at CERN in May-August 2003. The main task performed in CMS HCAL testbeam were

1) Calibration of Electromagnetic calorimeter towers using electron beam.

2) Calibration of Hadron Calorimeter towers using Minimum Ionizing Particle (MIP) or muon

3) Energy scans using pion beams from 30 to 300 GeV, provided measurements of the performance of combined ECAL+HCAL system.

4) Studied the detector response to pions at the boundary between Barrel or Endcap and the crack between two HB wedges.

5) Calibration data using Radioactive Wire-Source, LED and Laser systems.

4.4 Analysis of Data

Raw data have been processed and stored on disk in the form of ntuples with following information

a) Run Number, Event Number, Event Type i.e whether pedestal or beam event

b) Raw ADC Information for all towers of ECAL and HCAL for beam events and pedestal events.

4.5 Calculation of Pedestal

The Pedestal refers to the background noise produced by the experimental setup. By recording the magnitude of the pedestal, we can subtract it from the measurements to find the results we wish to obtain without any effects from the background noise. For each HPD channel which is equivalent to output of one scintillator tile, pedestal value is calculated by taking the mean value of the ADC values of that channel for all pedestal events throughout the run. The average pedestal for each tile is subtracted from the raw ADC value for each event for each tile to extract the signal coming from the passage of particles.

Since the pedestal could be noise produced by electronics or by the QIE which uses capacitors to accumulate the charge and measure the voltage, it is always advisable to monitor the pedestal values of all the four Capacitor's named Cap-id's individually to test their working. The pedestal of all the four capacitor's individually when muon beam of momenta 150 GeV/c is shooted into the tower of HO Ring 0 is shown in figure 4.5. The pedestal of each individual Cap-id is almost same indicating well functioning of all 4 Cap-ids.

There are 18 channels or 18 towers of the calorimeter connected to DAQ with one spigot. The mean pedestal of all the four Cap-id's for one particular spigot or 18 channels connected to Ring of Outer Hadron Calorimeter is shown in figure 4.6. The r.m.s spread of all four capacitor individually for one particular spigot is well within range .

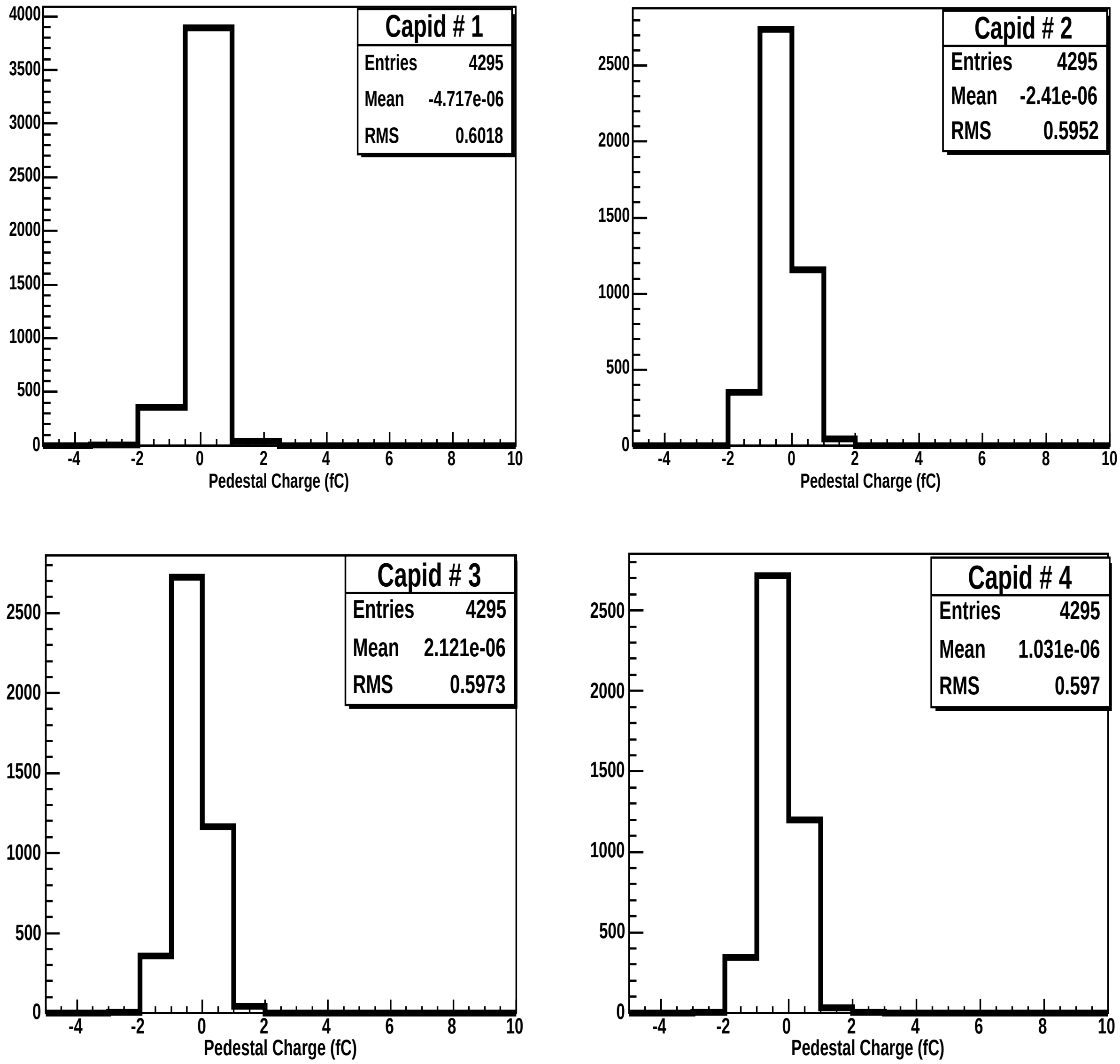

Figure 4.5: Pedestal values for all the four Cap-id's during Muon run for Outer Hadron calorimeter

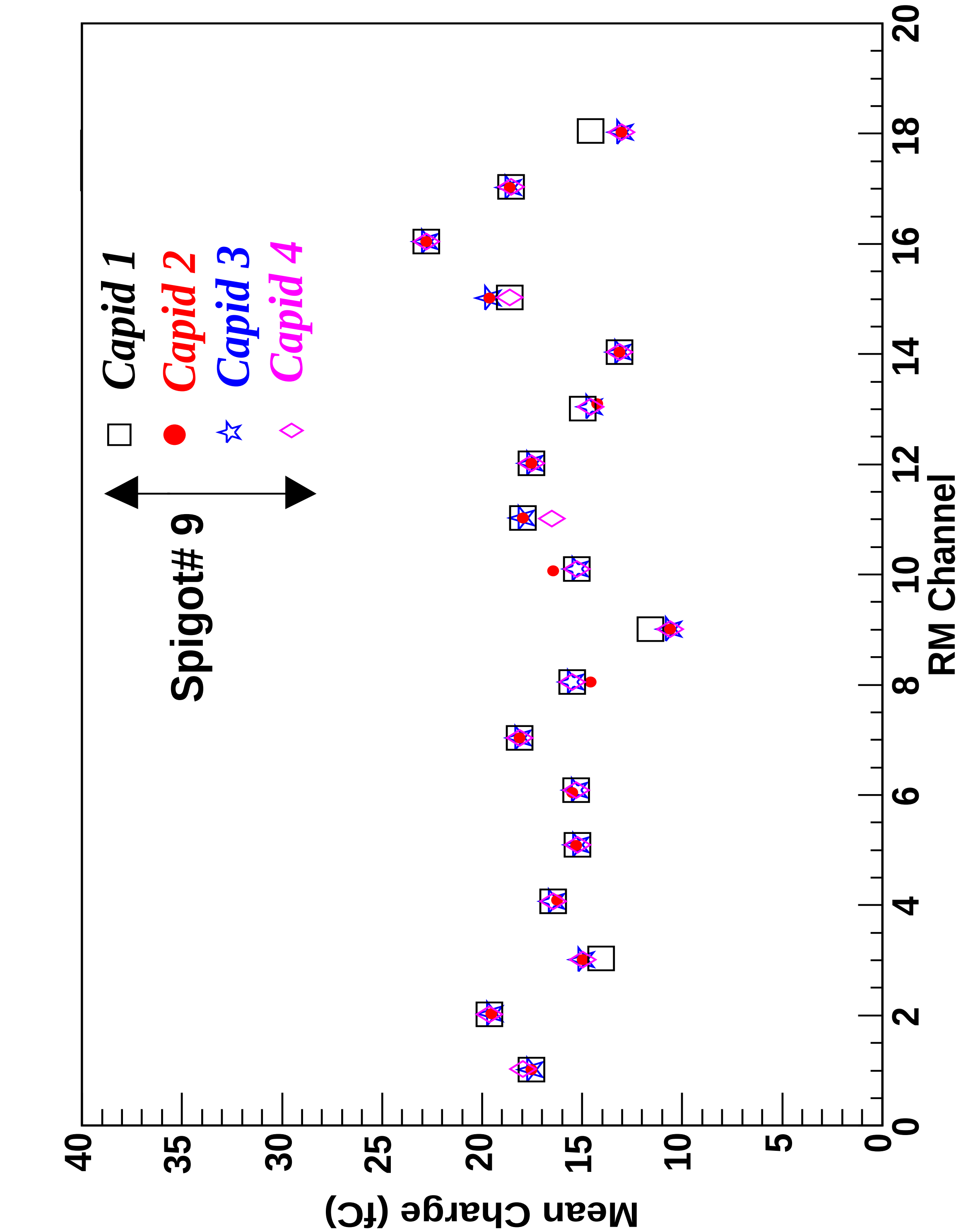

Figure 4.6: Mean pedestal of all 4 Cap-id for all the 18 channels of one spigot of Outer Hadron calorimeter

4.5.1 Subtraction of Pedestal from Signal

For every event, we record twenty time slices. Figure 4.7 shows average QIE pulse as a function of time for muon run of 150 GeV energy. Almost 90% of the signal comes in 4 timeslices (14-17), therefore the ADC Charge during that four timeslices is total Signal charge . The average charge during any four slices other than the signal time slices corresponds to the pedestal charge. The pedestal subtracted from total ADC charge of the Signal gives the pedestal subtracted charge.

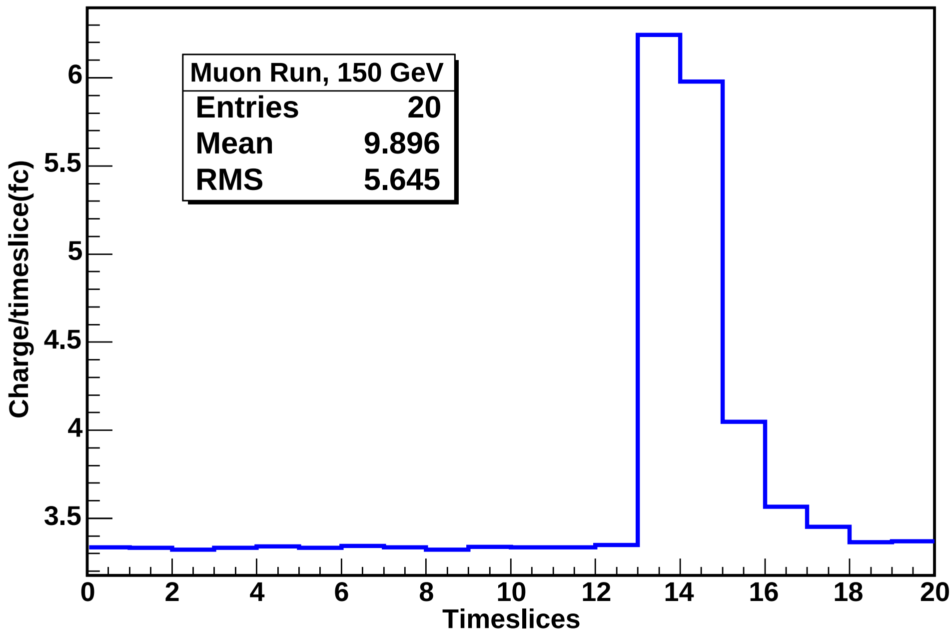

Figure 4.7: Average QIE pulse as a function of time slice (25ns). For each event, we record twenty time slices

4.6 Calibration of Detectors

Calibration refers to the process of determining the relation between the output or response of a measuring instrument to the value of the input quantity or attribute, a measurement standard. In non-specialized use, calibration is often regarded as including the process of adjusting the output or indication on a measurement instrument to agree with value of the applied standard, within a specified accuracy.

4.6.1 Calibration of ECAL

In order to achieve accurate calibration of the CMS hadron calorimeters, it is essential that the influence of the lead tungstate crystal ECAL is fully understood and accounted for. A prototype ECAL module was placed on a support table which allowed positioning the crystals in the beamline, in front of any chosen HCAL tower, thus approximating the ECAL calorimeter that will be placed in front of HCAL in the CMS experiment.

The ECAL module was extensively calibrated with electron beams. There were two ECAL calibration periods, one before HCAL testbeam period and one during the HCAL testbeam period. During the initial period, a preliminary calibration of the electromagnetic calorimeter was made. The early runs were used to determine the apparatus functionality, in particular the performance of the charge to digital converter (QADC), and provided a preliminary calibration. The high voltage of the photomultiplier tubes was adjusted to reduce gain variations of the individual channels. This allowed a relatively quick calibration of the ECAL during the second test beam period when the calibration of HCAL was the main interest. The final gains of the ECAL were determined so they could be used for combined ECAL + HCAL analysis.

Crystal Calibration

In order to calibrate a given crystal, the attempt has been made to center the beam on this particular crystal as much as possible. After the run was recorded, the data was analyzed to see if the beam was properly centered by looking at the left-right and up-down asymmetry of the energy deposited in the off-center crystals. Once the beam was properly centered on a crystal, 70%-80% of the electromagnetic shower was contained in a single targeted crystal.

The gain g_i of the crystal is the ratio of the energy deposited E_i in the crystal from QDC counts Q_i to GeV.

$$E_i = \frac{Q_i}{g_i}$$

More than 97 % of the electromagnetic showers developing inside crystals are well contained in a 3×3 matrix of crystals centered around targeted crystal. Thus the energy E deposited by electrons in ECAL is defined as:

$$\mathrm{E} = \sum_{i=1}^{g} E_i = \sum_{i=1}^{g} \frac{Q_i}{g_i}$$

Individual runs were dedicated to collecting the calibration data for each crystal with 100 GeV/c electron beam centered on this particular crystal. The analysis was performed by iterating simultaneously all 49 crystal gains. The average event energy was then used to define new gains for each crystal.

$$g_J^{new} = \frac{<E_j>}{100} g_i^{old}$$

where J is the crystal index which runs from 1 to 49 and the average energy $< E_j >$ is determined from the data. Since raw QADC counts for 100 GeV/c electron run had typical values of 1000 counts, the initial gain for all the crystals was set to 10.

4.6.2 Calibration of HCAL (HB & HO)

The schematic diagram of Outer Hadron Calorimeter Setup in CMS HCAL beam test is as shown in figure 4.8. The fully fabricated scintillator trays are placed in front of the beam in such a way that the calibration of individual tiles of a tray could be done.

Performance of different scintillator tile is different due to size, splicing quality of WLS to clear fiber and quality of connection at the optical connector. Therefore, a calibration of the tiles needs to be done. The following are the methods to calibrate the tiles.

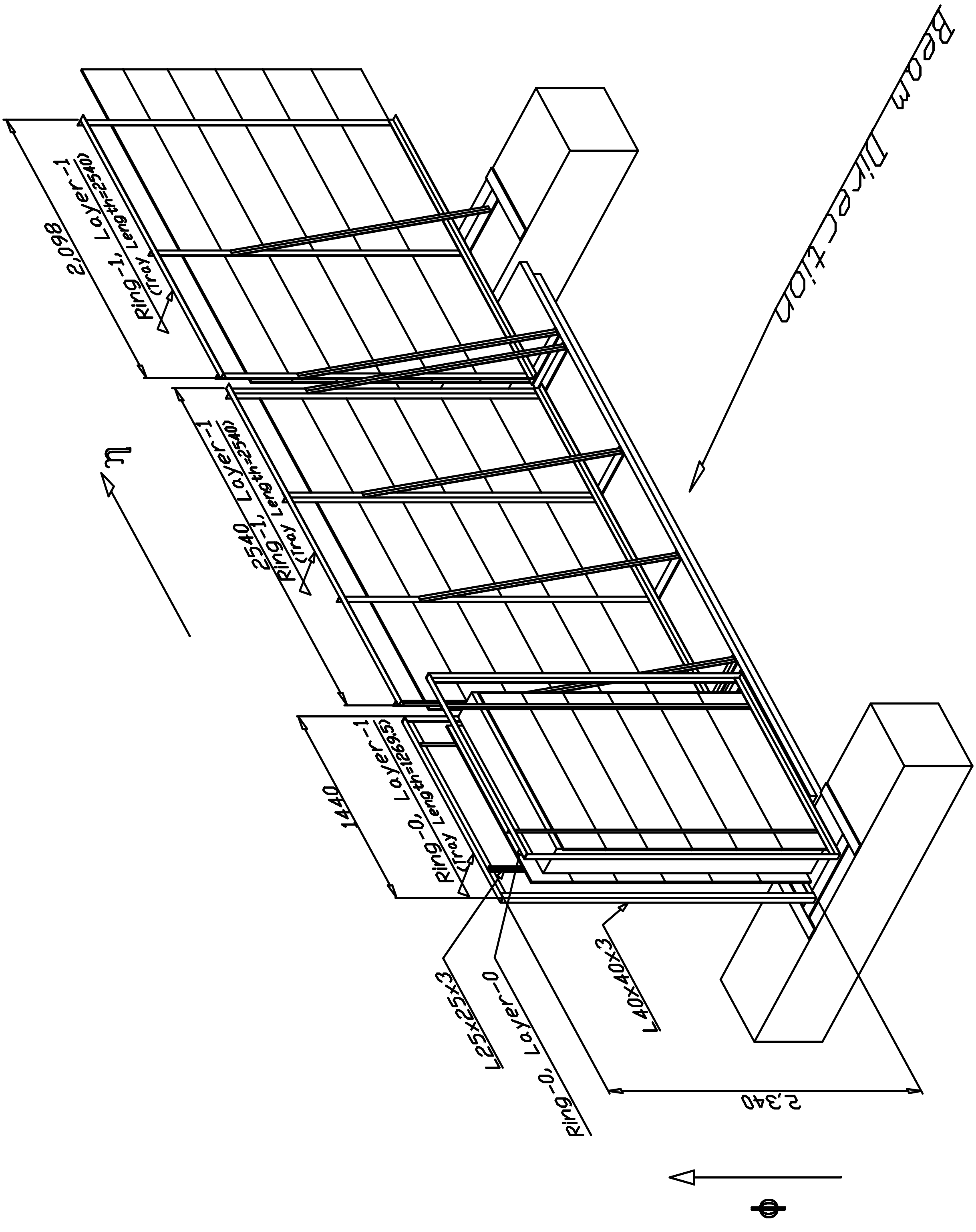

Figure 4.8: Outer Hadron calorimeter Setup for CMS HCAL testbeam

Using Muon Beam

The Calibration of the HCAL (HB & HO) tiles were performed using the Minimum Ionising Particle beam or muon beam. It is important to understand the response of HCAL to muons for not only overall calibration purposes but also because a muon bit will be set in the trigger primitives for use in higher level event selection. The Calibration of HO towers was done for each tower. The HB & HO is divided into towers in η,ϕ coordinates as shown in figure 4.8.

To Calibrate each tower of HCAL i.e HB and HO, the pedestal subtracted ADC distribution is plotted for a muon run for each longitudinal segment of a tower. The resulting ADC distribution is fitted to gaussian and the peak of the gaussian is taken as the MIP response of the scintillator tile or tower and can be used as Normalization constant in case of pion runs. If due to low gain of the HPD, the peak of the signal is not clearly visible, then the mean of the muon ADC distribution is taken as the MIP value. These values of all the channels are stored in separate file and is used to calibrate the towers for the pion runs.

CMS HCAL Testbeam 2003

In CMS HCAL testbeam 2003, the scintillator trays of all the three rings of HO were exposed to the muon beam of energy 150 GeV. The figure 4.9 shows the pedestal subtracted ADC distribution for HB Ring 0 and figure 4.10 shows the same for HO Ring 0 when they are exposed to muon beam of energy 150 GeV. The ADC charge of HB is obviously more than that of HO because the output of HB is summed output of 18 scintillator layers as compared to that of HO which has only two layers in case of Ring 0. We compared the muon signal in the towers of all the three Rings 0, 1, 2 for HB & HO as shown in figure 4.11 and figure 4.12 respectively due to their difference in size. As expected, HB Ring 2 tower gives maximum charge because it has the largest l/A ratio and HO Ring 0 tower gives maximum charge because it is the collection of two layers $l0$ and $l1$. Ring 2 tower

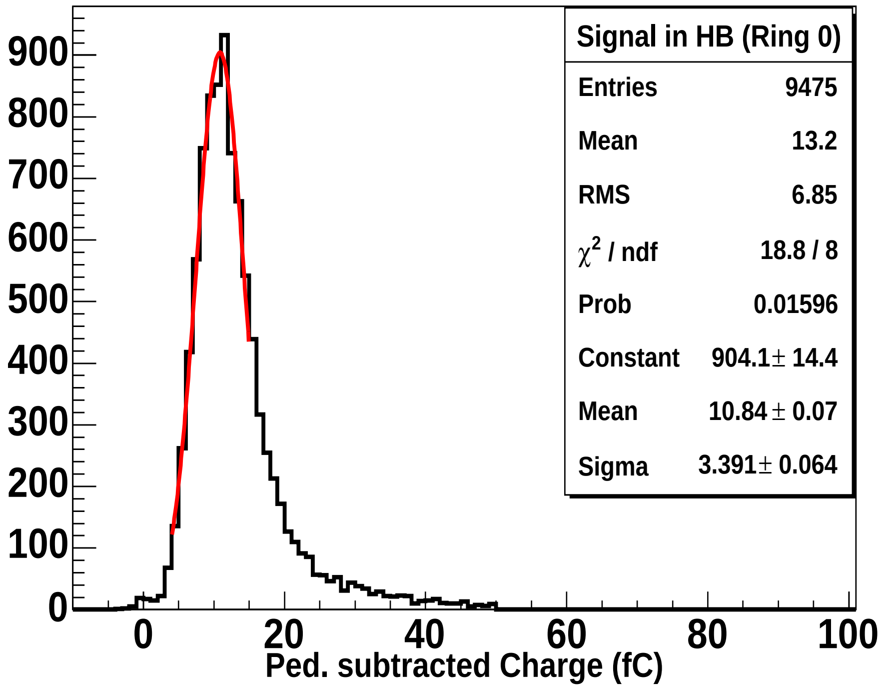

Figure 4.9: The pedestal subtracted ADC charge for Muon shooted in the tower ($\eta = 4, \phi = 4$) of HB Ring 0

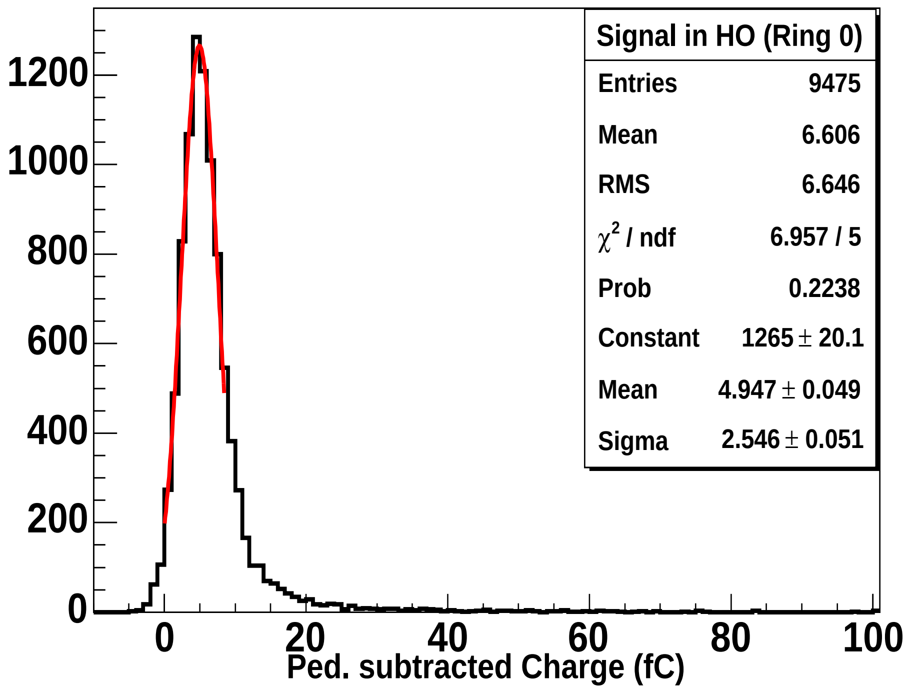

Figure 4.10: The pedestal subtracted ADC charge for Muon shooted in the tower ($\eta = 4, \phi = 4$) of HO Ring 0

in HO gives higher charge than Ring 1 due to its more l/A ratio.

CMS HCAL Testbeam 2004

In CMS HCAL testbeam 2004, Production trays were exposed to the muon beam for calibration. These production trays are installed into the Outer Hadron calorimeter of CMS Detector after testbeam. The plots for the Muon scan of production trays are shown for all the three different Rings of HO showing superposition of signal & pedestal values. It is clearly seen from the figures 4.13 that the signal from Ring 0 is well separated from the pedestal due to the addition of signals from two layers L0 & L1 while the signal from Ring 1 & Ring 2 are slightly overlapped but separated from pedestal.

Calibration Using Radioactive Source

All the trays of HO that have been used in the testbeam runs are equipped with 1 mm diameter stainless steel tubes that run along the length of these trays. These tubes sit in grooves on the top plastic cover of the trays. A Cs-137 radioactive source mounted at the tip of a thin wire is pushed through each tube by a remotely controlled system of drivers. A DC current induced in the scintillator by the source traversing the tube provides an accurate measurement of the gain of the entire measuring chain. This system was used to calibrate the towers which were not exposed to the beams.

4.7 Energy of Particles

4.7.1 Energy of Electron in ECAL

The energy of electron in ECAL can be calculated as follows

$$\text{ECAL} = \frac{1}{Normalization\ Constant} \sum_{i=1}^{49} ADC_i \times \text{ Tower } Weight_i$$

In the above equation ADC_i is the pedestal subtracted ADC value of the particular tower. The Normalization constant is found using data from a 100 GeV electron run. The sum

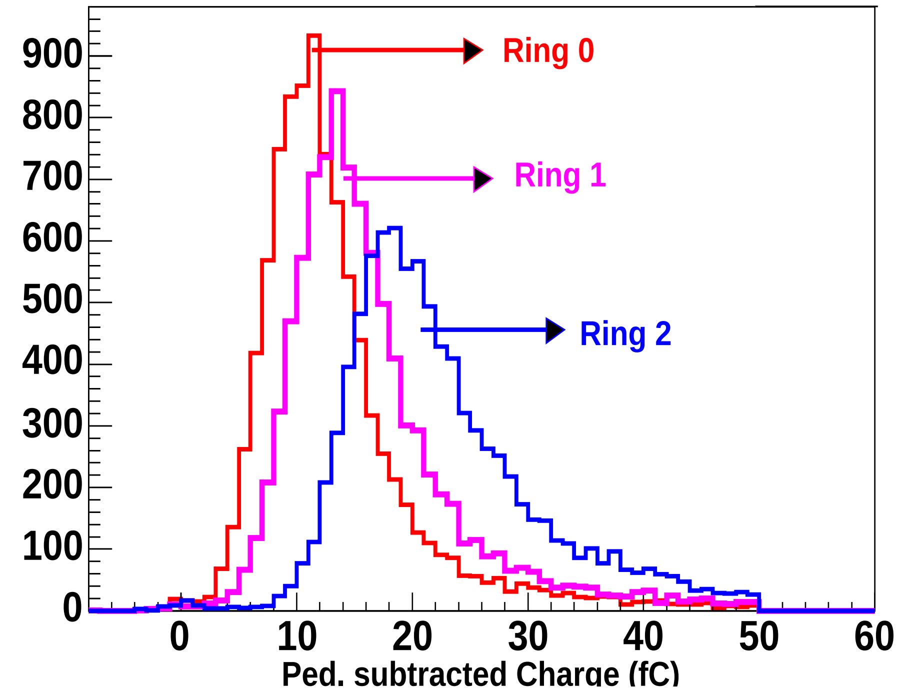

Figure 4.11: The pedestal subtracted ADC charge for Muon shooted in the towers of HB Ring 0, Ring 1, Ring 2

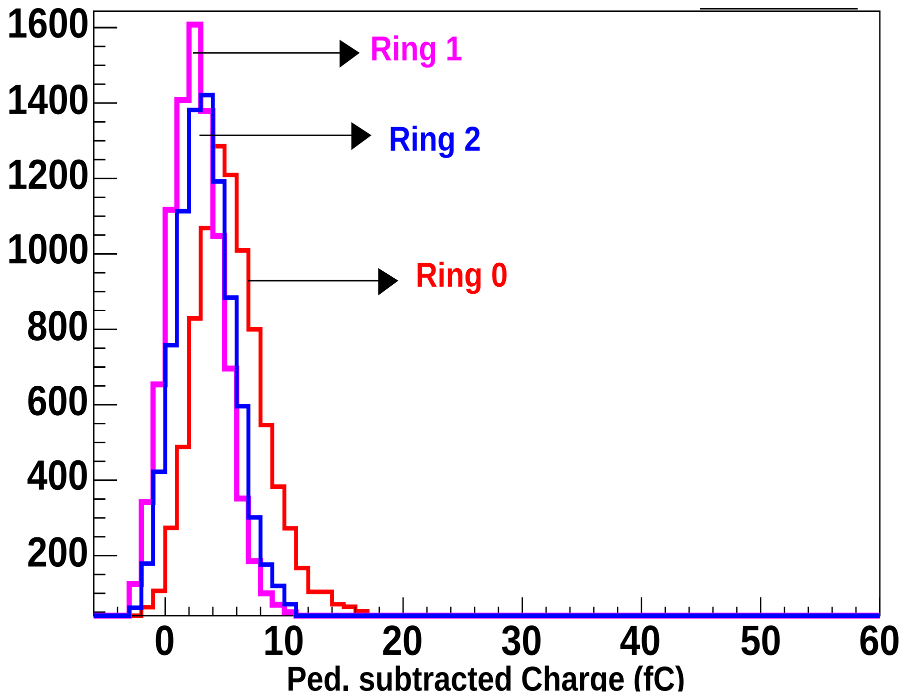

Figure 4.12: The pedestal subtracted ADC charge for Muon shooted in the towers of HO Ring 0, Ring 1, Ring 2

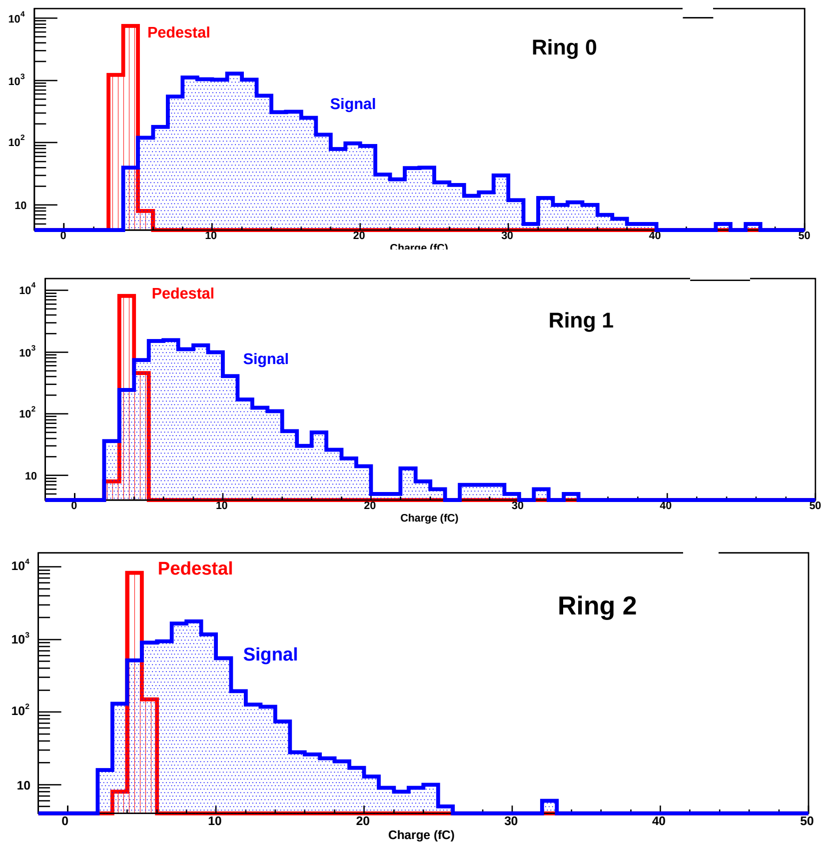

Figure 4.13: ADC pedestal subtracted signal & pedestal for Ring 0, Ring 1, Ring 2 of HO. The scale used is logarithmic scale

can represent 9 central towers (3×3) or 25 central towers (5×5) or all 49 towers (7×7). Normally for electrons a (5×5) energy sum is sufficient to calculate the energy properly. The 7×7 sum adds only to the width of the distribution. The Output of 120 GeV electron in ECAL is shown in figure 4.14 [10].

4.7.2 Energy of Pions in ECAL + HCAL System

Pions deposited most of their energy in passive material like the brass or steel. Less than 1% of the pion energy is readout from the HB scintillators since HB is a sampling calorimeter. In ECAL + HCAL system, the total pion energy can be estimated by adding the energies deposited in ECAL and HCAL. Total energy deposited in HCAL is found by

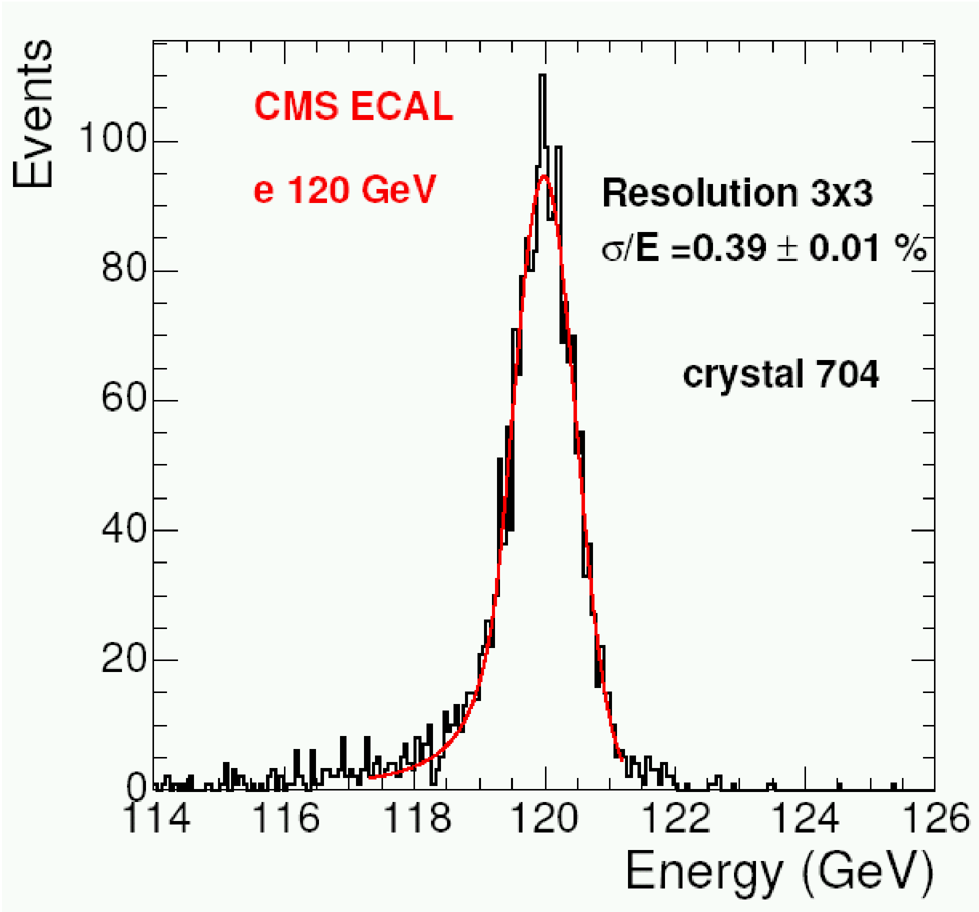

Figure 4.14: Reconstructed Energy of 120 GeV electron in ECAL

adding towers as maximum as possible centered around the beam.

The energy of the pion can be calculated using ADC charge information as follows

$$E_{pion} = \frac{1}{Normalisation\ constant} \times \sum_i ADC_i$$

In the above equation ADC_i is the pedestal subtracted ADC value of the particular tower. The Normalization constant is found using data from a muon run (explained earlier). For the pion beams, to get the total energy correctly, all the towers need to be added up as hadronic showers are expected to spread more than electromagnetic showers.

Even after calibrating the Electromagnetic Calorimeter and Hadronic Calorimeter systems separately, there are some differences between them. This can be taken care of multiplying their energy values by a weight. To make the total energy least biased for different kinds of particles, the energy deposited in HCAL is weighted.

Total energy can be estimated as follows.

$$\text{Total Energy} = W_1 \times ECAL + W_2 \times \Sigma HB + W_3 \times \Sigma HO$$

The Sum is over 25 (5×5) towers in each HCAL section. W1, W2, W3 are the weight factors which are needed to adjust for the differences between ECAL and HCAL.

4.8 Results and Discussion

Two types of configuration used

1) ECAL + HCAL (HB and HO)

2) HCAL (HB and HO)

4.8.1 ECAL + HCAL (HB + HO) Subsystem

This configuration is used to test the capability of full detector system, ECAL +HB +HO, in detecting the shower particles. As pion deposits energy in ECAL through electromagnetic interaction & HCAL through strong interactions, it is very useful to study the response of combined detector to pions at different energies.

The figure 4.15 gives the scatter plot of energy deposited by 300 GeV pion in ECAL with energy deposited in Barrel Hadron Calorimeter (HB). As shown in figure, there are many events where the energy deposited in ECAL is substantial as compared to that deposited in HB. This is due to the electromagnetic component of shower in ECAL. The majority of events deposits more energy in HB as compared to ECAL because the hadronic shower begins to develop late and is well accommodated in the towers of HB. There are many events with energy close to zero. That is muons contamination in pion beam.

The figure 4.16 gives the scatter plot of energy deposited by 300 GeV pion in ECAL + HB system with that in HO. It is clear that the combined system ECAL + HB is capable of containing almost all the shower but there are some events which deposits energy in HO clearly indicating the leakage in ECAL + HB system and importance of HO in reducing energy leakage.

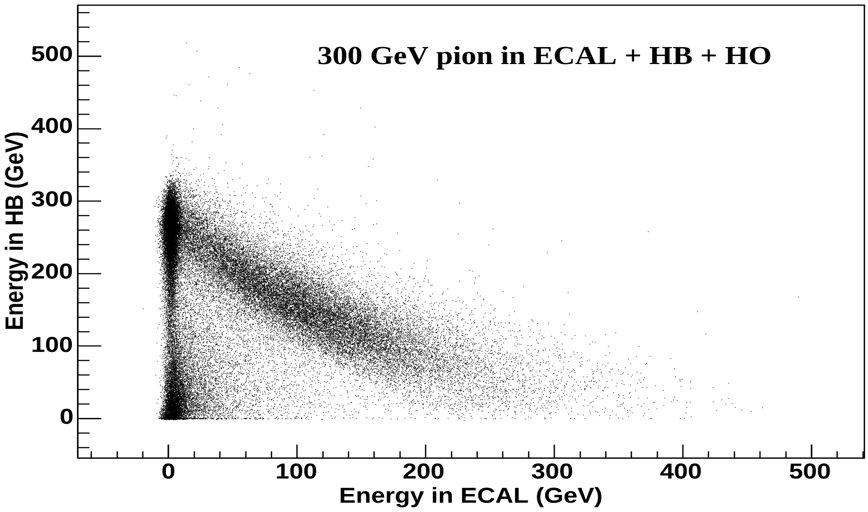

Figure 4.15: Reconstructed Energy observed in ECAL vs HB for 300 GeV pion

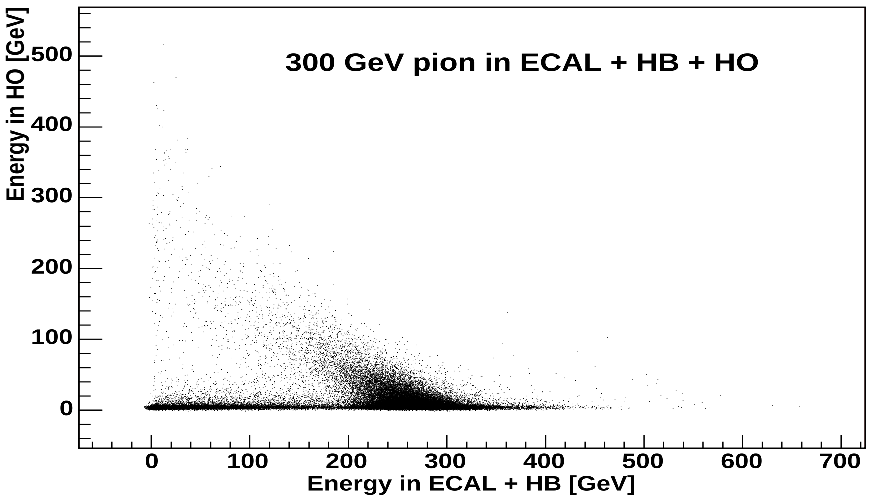

Figure 4.16: Reconstructed Energy observed in ECAL + HB vs HO for 300 GeV pion

4.8.2 HCAL Only, No ECAL

This configuration doesn't include ECAL in front of HCAL (HB + HO). This type of setup is useful in studying the response of hadron calorimeter to shower particles particularly pions. The pions of different energies ranging from 50 GeV to 300 GeV are shooted to that particular tower which is surrounded by atleast 3×3 towers, preferably 5×5 towers because hadron showers are more widely spread and surrounding towers gets substantial amount of energy during the run. One such run of pion of 300 GeV shooted to the tower of HCAL only with and without applying normalization is shown in the figure 4.17. By looking into the figure, one can clearly see that after applying normalization there is the shift of the peak close to 300 GeV.

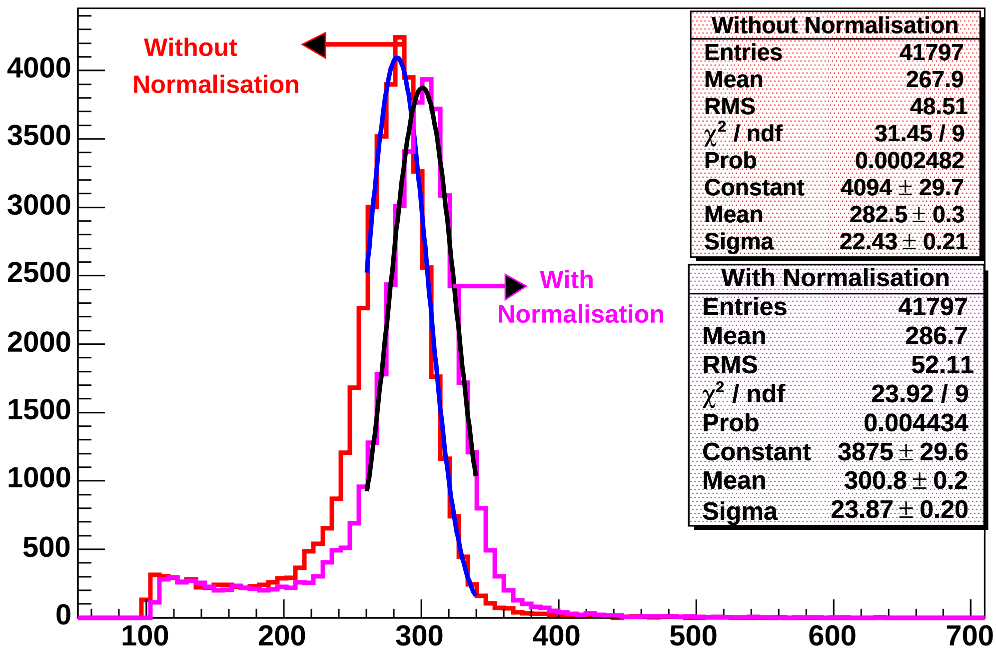

Figure 4.17: Reconstructed Energy of 300 GeV pion in HCAL (HB + HO) before and after normalization

To estimate the importance of HO , we calculated the energy of 300 GeV pion with and without HO. The superposition graph of these two conditions is shown in figure 4.18.

It is clearly shown that adding HO to HCAL Barrel (HB) improves energy resolution of the calorimeter and reduces the amount of energy leaking out of the calorimeter.

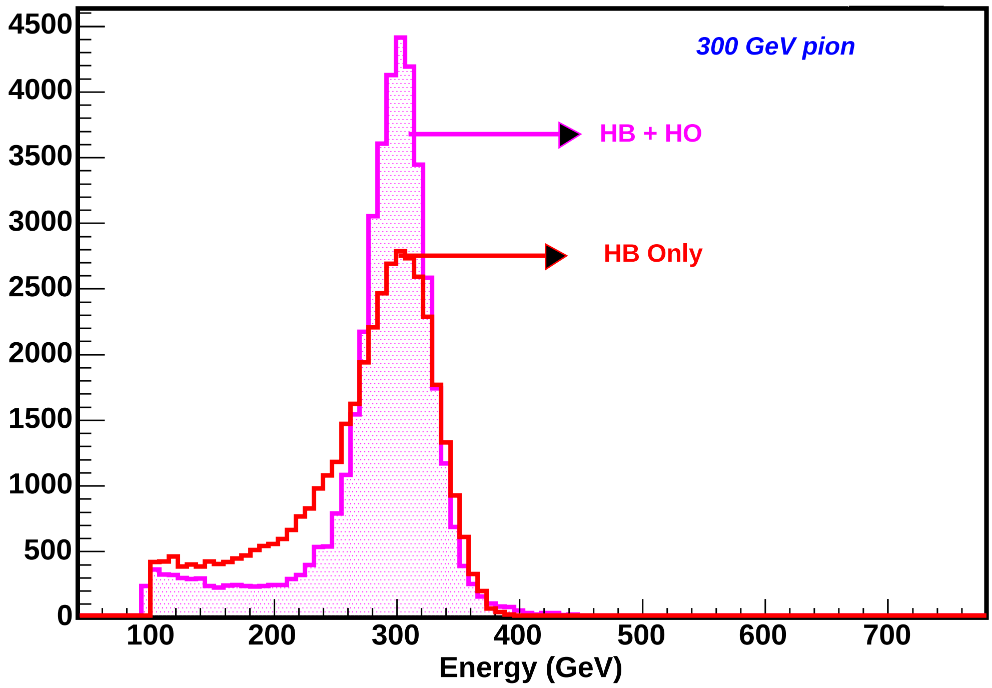

Figure 4.18: Reconstructed Energy of 300 GeV pion calculated with and without HO for Ring 0 towers

Energy Resolution in Calorimeter

The ultimate limit for the energy resolution of a calorimeter is determined by fluctuations inherent in the development of showers and by instrumental and calibration limits. The basic phenomena in showers are statistical processes, hence the intrinsic limiting accuracy, expressed as a fraction of total energy, improves with increasing energy as:

$$(\sigma/E)_{fluct} \propto 1/\sqrt{E}$$

Over much of the useful range of calorimeters, this term dominates energy resolution.

There are other contributions than statistics, though a second component is due to instrumental effects being rather energy-independent, its relative contribution decreases with E:

$$(\sigma/E)_{instr} \propto 1/E$$

This component may limit the low-energy performance of calorimeters.

A third component is due to calibration errors, non-uniformities and non-linearities in photomultipliers, proportional counters, ADC's etc. This contribution is energy-independent:

$$(\sigma/E)_{syst} = const$$

This component sets the limit for the performance at very high energies.

Energy Resolution of HCAL

Intrinsic limits on the energy resolution of hadronic calorimeters are:

1) A fluctuating π^o component among the secondaries which interacts electromagnetically without any further nuclear interaction ($\pi^o \rightarrow \gamma\gamma$). The average fraction of π^o's is given by 0.10 log(E) [E in GeV]. Showers may develop with a dominant electromagnetic component.

2) A sizeable amount of the available energy is converted into excitation and breakup of nuclei. Only a small fraction of this energy will eventually appear as a detectable signal and with large event-to-event fluctuation.

3) A considerable fraction of the energy of the incident particle is spent on reactions which do not result in an observable signal. Such processes may be energy leakage of various forms like:

a) Backscattering

b) Leakage due to μ, ν or slow neutrons

c) Nuclear excitation, nuclear breakup, nuclear evaporation.

CMS HCAL Testbeam 2003

In CMS HCAL testbeam 2003, the response of HCAL (HB +HO) with pions of energy 300 GeV, 200 GeV, 100 GeV & 50 GeV is calculated.

The energy graphs of pions at different energies in HCAL with & without HO were then fitted to the function

$$(\frac{\sigma}{Energy})^2 = (\frac{\alpha}{\sqrt{Energy}})^2 + (\beta)^2$$

A chi-square minimization method was used to find the best values of α & β. The values of α & β for the configuration with and without HO is as shown in Table 4.1.

Configuration	α	β
Without HO	73.15 %	9.564 %
With HO	84.06%	7.06%

Table 4.1: Parameters α & β with and without HO

The resolution (σ/energy) versus incident pion beam energy starting from 50 GeV to 300 GeV is shown in figure 4.19. This shows that the presence of HO in addition to the barrel improves the energy resolution of the calorimeter.

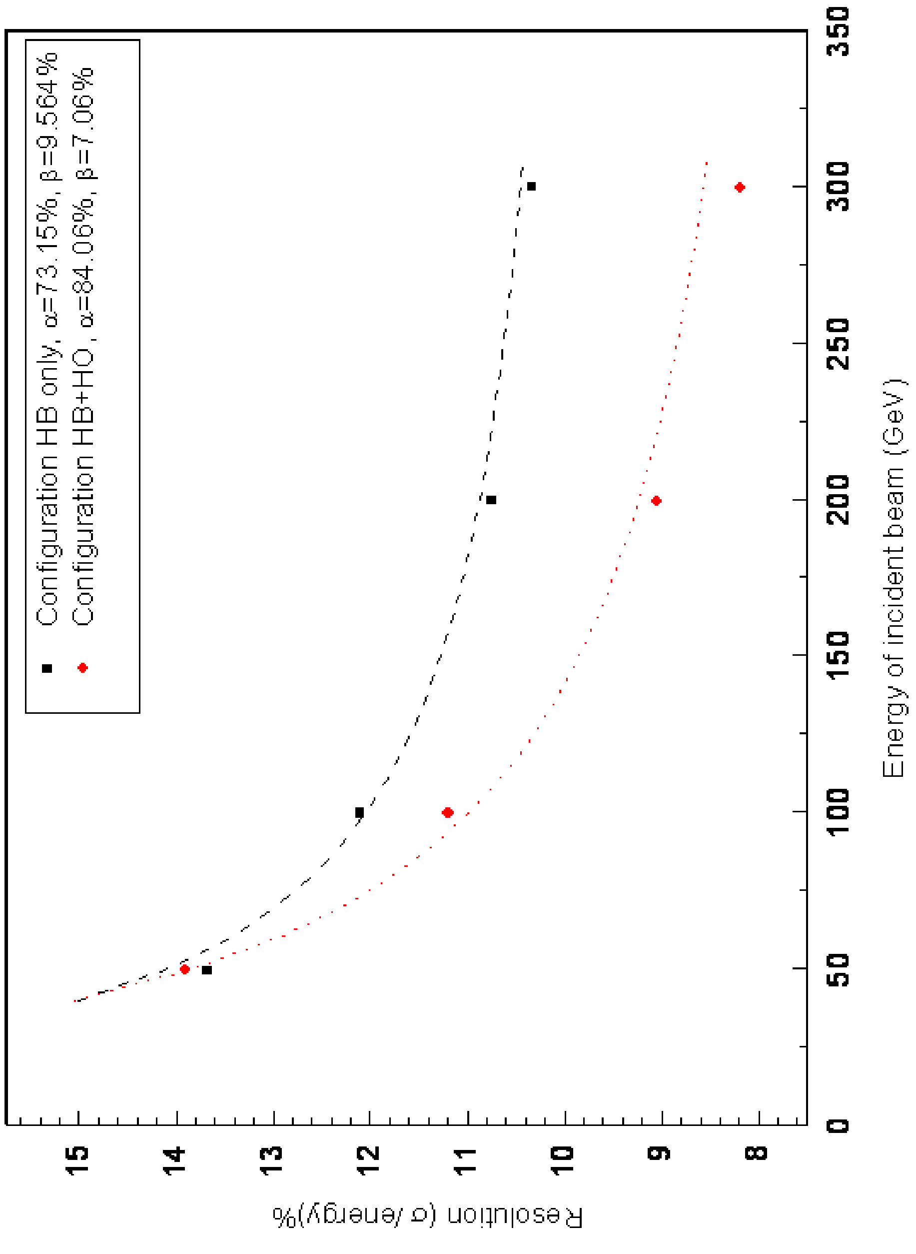

Figure 4.19: Energy Resolution vs. incident beam energy for pion beams

4.9 Longitudinal Shower Development Study in HB

In CMS HCAL testbeam 2004, Hadron Barrel Calorimeter was connected in two different ways as shown in the figure 4.20 [11].

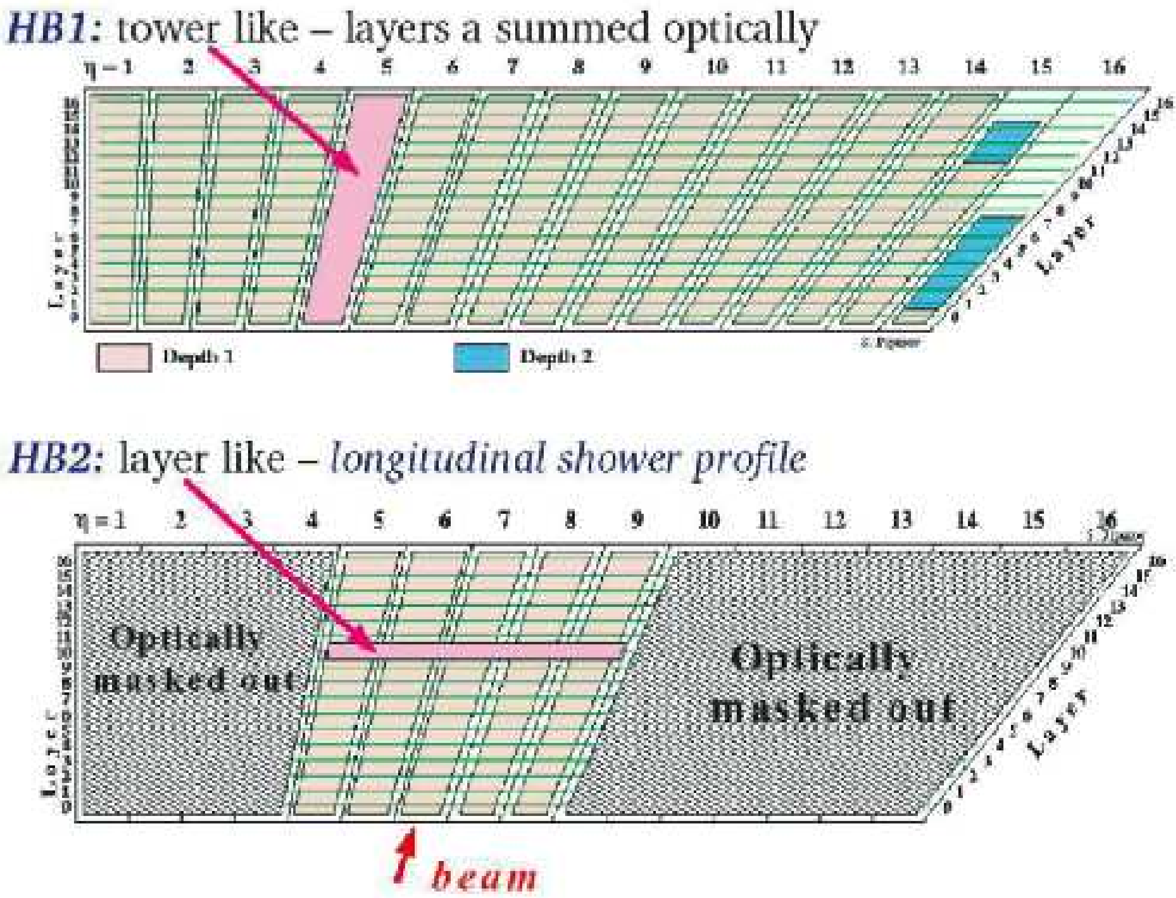

Figure 4.20: Readout segmentation for the two HB wedges. HB1 has the normal CMS readout configuration while HB2 has a special longitudinal readout of each scintillator

One of the two HB wedges (HB1) was configured according to the normal CMS design such that light from all the scintillator tiles in each tower were summed optically and routed to one pixel of an HPD photodetector. Thus, this configuration has only transverse segmentation and no longitudinal segmentation. The second HB wedge (HB2) was configured to measure the longitudinal shower development in the calorimeter. This was implemented by replacing the normal optical decoding unit (ODU) in the readout box with a special ODU. Due to the limited number of HPD channels available in a readout box, this special ODU summed the light from the scintillator tiles along η at the same depth in the center HCAL towers (5-9). The remaining towers were optically masked out to reduce the possible contribution from the halo muons. The resulting energy measurements from each of 17 HCAL layers provided a complete longitudinal sampling of the hadron shower.

CMS HCAL Testbeam 2004 results

The longitudinal shower profile for pions at 300 GeV is shown in figure 4.21 and the same for pions of different energies is shown in figure 4.22. The shower profiles shown indi-

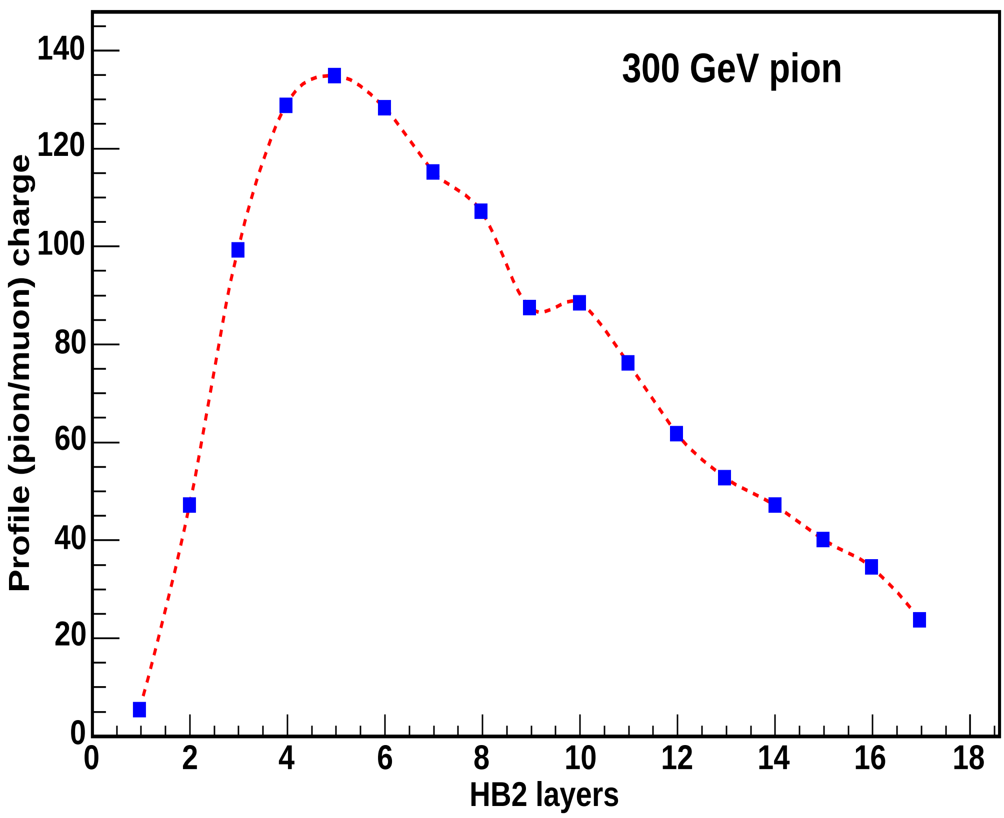

Figure 4.21: Energy observed in HB2 layers when pion of 300 GeV shooted to tower (η=7,ϕ=6)

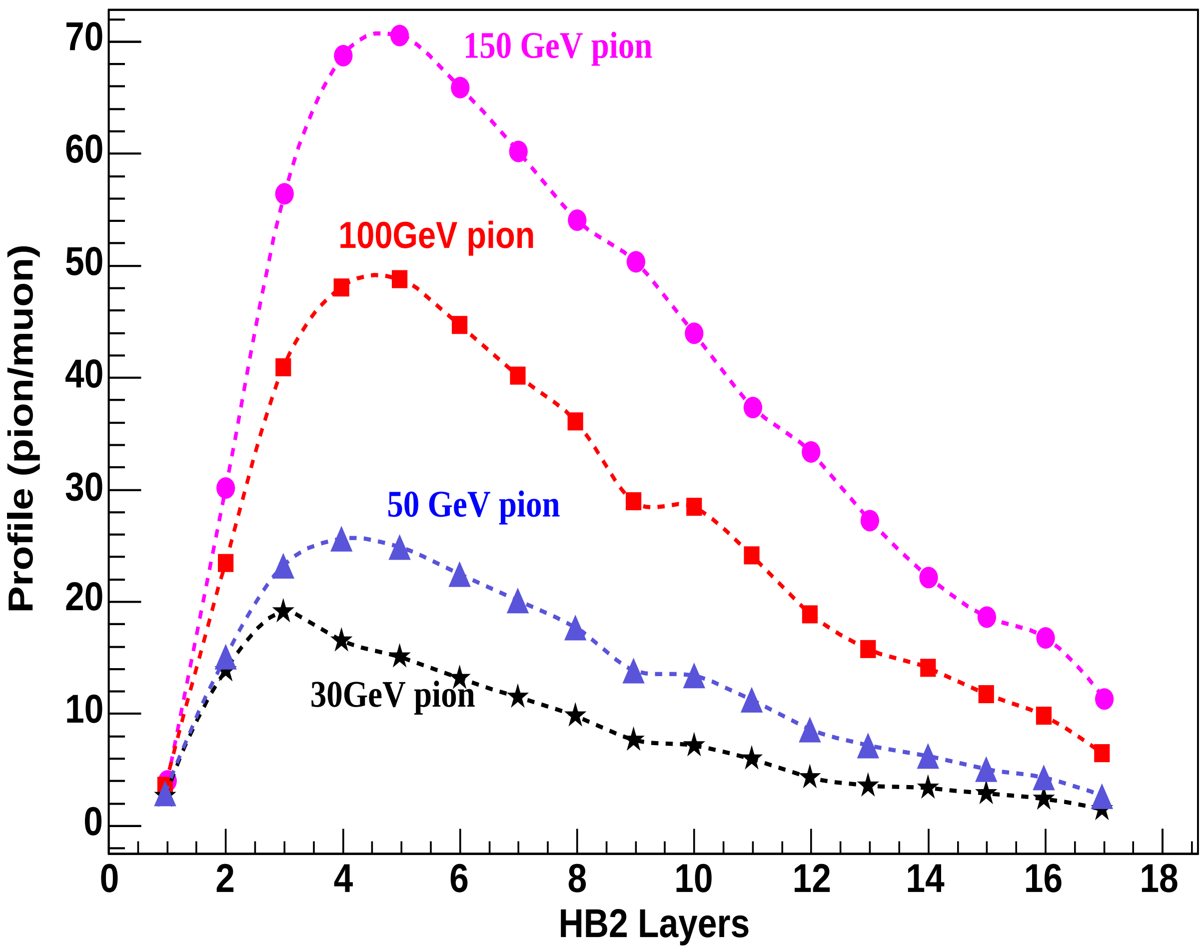

Figure 4.22: Energy observed in HB2 layer when pion of different energies shooted to tower (η=7,ϕ=6) of HB2 configuration

cates that the location of the shower maximum observed where hadronic shower started beginning in HB2 layers starts from layer 3 at 30 GeV to layer 5 at 300 GeV . After that the energy of the secondaries started decreasing due to their interactions with more and more passive layers. In the last layer there is still some energy left for pion which could leak from HB2 layers thus showing the need for extra layers to prevent the leakage except for 50 GeV & 30 GeV pion which hardly left with enough energy to pass HB layers.

The sum of energies in a matrix of 3×5 towers at each depth was used to measure the deposited energy from pions. This ensures full shower containment in the transverse plane. The distribution of summed pion energy in HB2 (all layers) when pion of 300 GeV shooted at (η=7,ϕ=6) in HB2 configuration is shown in figure 4.23. Figure 4.24 shows the energy deposited by the same in HO.

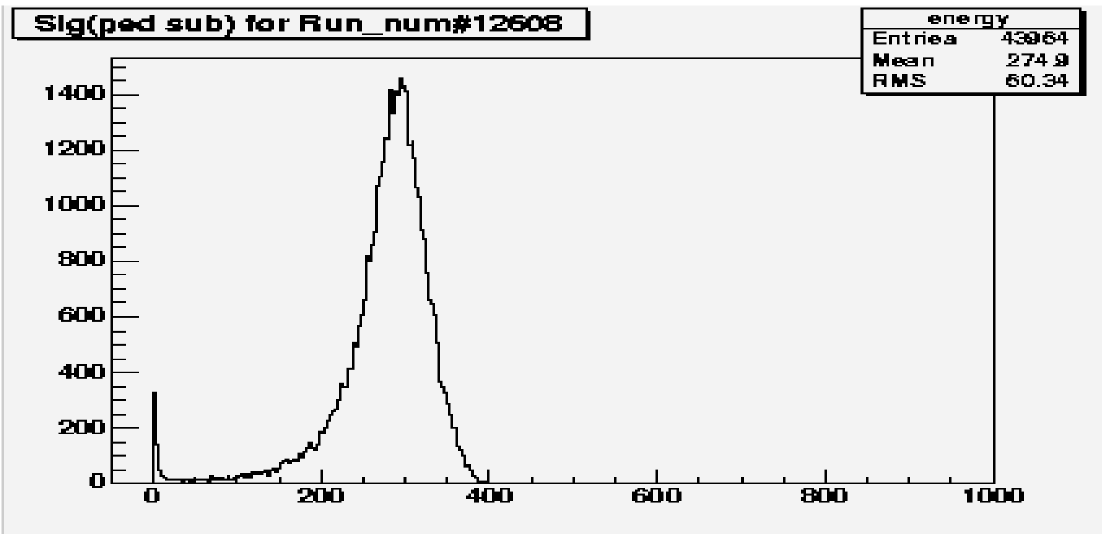

Figure 4.23: Energy observed in HB2 when pion of 300 GeV shooted to tower (η=7,ϕ=6)

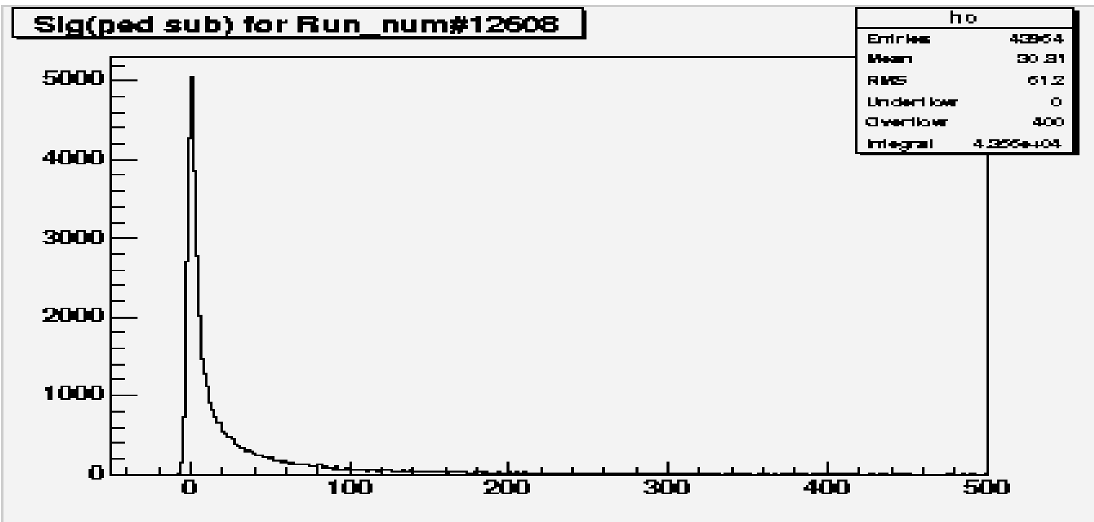

Figure 4.24: Energy observed in HO when pion of 300 GeV shooted to tower (η=7,ϕ=6)

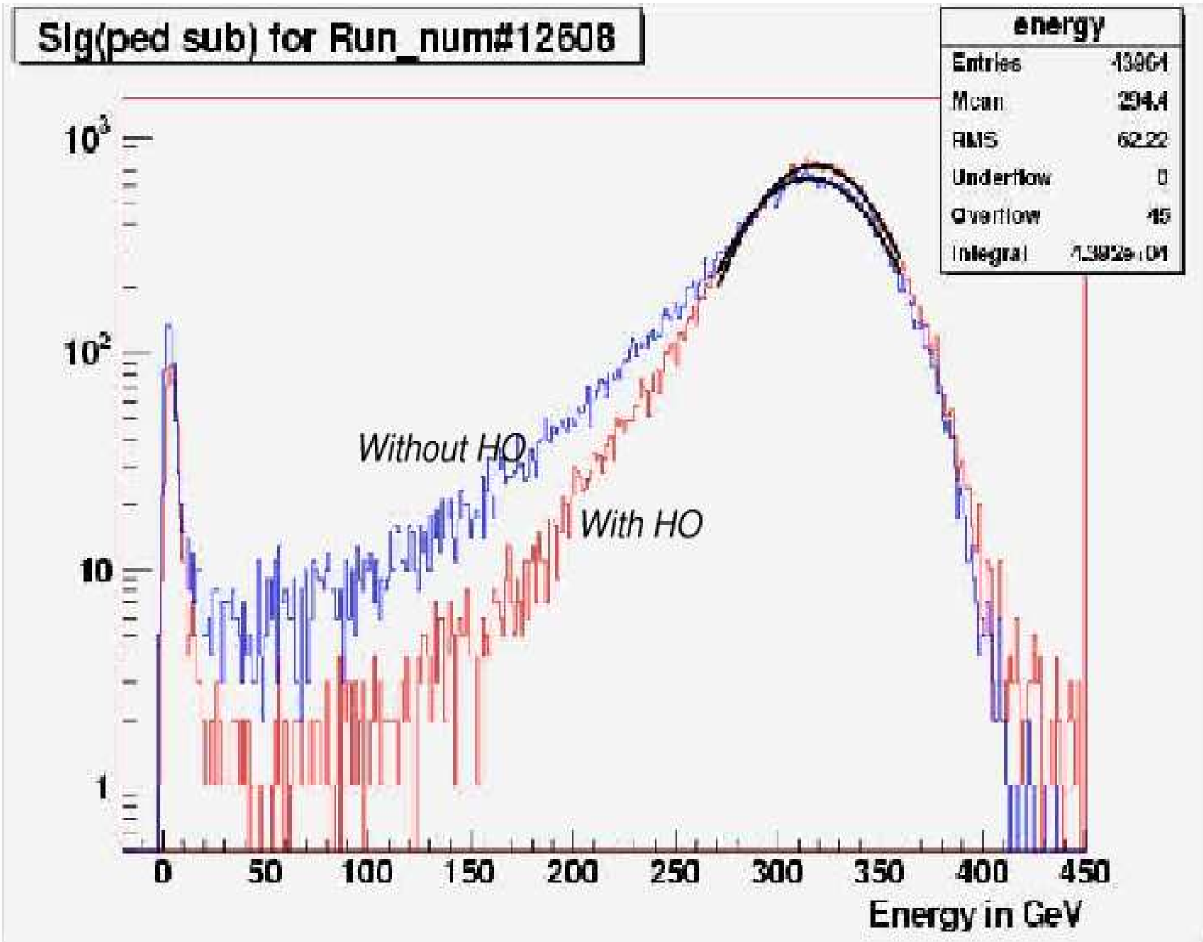

Figure 4.25: Energy distribution with and without HO using 300 GeV pion beam

4.9.1 Improvement in Energy Resolution

The total energy deposited by 300 GeV pion in HB2 configuration is calculated by adding the energy deposited in all layers of HB2. The total energy was calculated with & without Outer Hadron calorimeter (HO) and is shown in figure 4.25. By looking into the figure, it is clear that adding HO layer to HB2 configuration helps in increasing the resolution of the energy of the calorimeter and reduces the leakage of energy from the calorimeter thus describing the importance of HO.

4.9.2 Conclusion

We briefly described the goals and the setup for the CMS HCAL testbeam at CERN. We also described briefly the Data Acquisition system used in CMS calorimeters. We participated in CMS HCAL testbeam where fully fabricated HO scintillator modules are tested with beam of particles at different energies. We have shown how the calibration constants are calculated and the resolution parameters of the Outer Hadron calorimeter. It is also shown the importance of HO in reducing the energy leakage in HCAL and helps in increasing the resolution of HCAL. Also, the calibration constants and resolution parameters calculated can be used to determine the energy of any particle passing through the calorimeter.

Bibliography

[1] Sudeshna Banerjee, Performance of Outer Hadron Calorimeter (HO) in 2002 test-beam, December 2002

[2] Pawel de Barbaro, Vasken Hagopian, The CMS Hadron Calorimeter : Progress report and test beam results, Proceedings Cosmo-2003-11

[3] S.Abdullin, H.S.Bawa et al, Design, Performance and Calibration of CMS Hadron-Barrel Calorimeter Wedges, Submitted in Nucl. Instr. Module

[4] D.Lazic, Beam tests of CMS HCAL Readout Electronics, http://lhc−electronics−workshop.web.cern.ch/LHC−electronics−workshop/2003/sessionsPDF/Eleccal /LAZIC.PDF

[5] Data Acquisition and High-Level Trigger, The TRIDAS Project, Technical Design Report, Volume 2.

[6] R.J.Yarema, A. Baumbaugh, J.E.Elias, T.Shaw, Channel Control ASIC for the CMS Hadron Calorimeter Front End Module, Proceedings of the Eight Workshop on Electronics for LHC Experiments, Colmar, France 2002

[7] S.Holm, T.Shaw, J.Elias, S.Sergeev, Design and testing of a Radiation Tolerant Clock, Control and Monitor (CCM) Module for the CMS HCAL Electronics, 2002 IEEE Nuclear Science Symposium and Medical Imaging Conferencem Norfolk, VA USA 2002

[8] E.Hazen, J. Rohlf, S.Wu, A.Baden, T.Grassi, The CMS HCAL data concentrator: a modular, standards-based implementation, Proceedings of the Seventh Workshop on Electronics for LHC Experiments, Vol. 347, Stockholm, CERN 2001-05 and CERN/LHCC/2001-034, 2001

[9] J.Mans, I.Suzuki, D.Charak, DAQ Software used in the 2003 HCAL Testbeam, Submitted as CMS Note

[10] M.Imboden, P.de.Barbaro, D.Ruggiero, R.Kellogg, C.Jarvis, D.Lazic, Calibration and performance of lead tungstate electromagnetic calorimeter for HCAL testbeam 2002, CMS IN 2002/057

[11] S.Abdullin et al, Longitudinal Shower Profiles Measured in CMS HCAL and Comparison with Geant 4, Prepint submitted to Elsevier Science, 9 June 2006

Chapter 5

Physics Simulation Studies

5.1 Introduction

Since at Large Hadron Collider, the real data will emerge only after the year 2007, at present simulated data is the need for the physics analysis. Simulations are performed by using the different Monte-Carlo methods and event generators. In an event generator, the objective strived for is to use computers to generate events as detailed as could be observed by a perfect detector. This is done by factorizing the problem into a number of components, each of which can be handled reasonably accurately. The output of an event generator should be in the form of events with the same average behavior and same fluctuations like in the real data. In real life, an accelerator provides events.

The real events are registered in a detector as electronic signals. A data acquisition stores a digitized version of the information. In an event reconstruction program, the digitized electronic signals are turned back into a list of particle momenta and charges. The reconstructed events can then be used for physics analysis. In simulations, event generator takes the role of the accelerator in providing the events. The response of the detector is then modeled in a detector simulation program. This program provides an output in a format identical to that of an experimental data acquisition and original physics event input is also kept for later reference. Therefore the same reconstruction program can be used, and the same physics analysis strategies.

The Complexity and the number of simulation programs for hadron collider has grown considerably with the prospects of LHC physics [1]. To generate a single process, it is becoming feasible to use one program to produce a hard process, another to evolve the event through a parton shower algorithm and perhaps a third to hadronize the colored products of the shower. With this sort of modularity, the complexity of Monte Carlo simulation tools is reaching that of a complicated detector system.

5.1.1 Monte Carlo Methods

Monte Carlo methods can be described as the methods that utilize sequence of random numbers to perform the simulation. The Monte Carlo methods may be contrasted to numerical discretization methods applied to ordinary or partial differential equation describing physical system. The physical system can be described by a probability density function. Once the probability density functions are known, the Monte Carlo simulation can proceed by random sampling from them. Many trials are then performed and the desired result is taken as an average over the number of observations. One can predict the statistical error or variance in this average result and get an estimate of the number of Monte Carlo trials that are needed to minimise error. The Monte Carlo simulation can proceed by sampling from these probability density functions which requires a fast and effective way to generate random numbers uniformly distributed on some intervals.

5.1.2 Event Generators

Theoretical predictions form an integral part of any particle physics experiment. They help to design the detectors and to define the experimental strategies. To serve such a purpose, these predictions must reproduce as closely as possible the collision processes taking place in real detectors. A largely successful way of achieving this goal is through the so called event generator codes, which are used to produce hypothetical events with the distribution predicted by theory. For an unambiguous interpretation of the experimental results like extracting with high precision the non-computable parameters of the theory or deciding whether some new physics phenomenon has been observed, other types of tools which we shall call cross-section integrators are better suited than event generators. These tools can also output events. However, such events can be used only to predict a limited number of observable for example the transverse momentum of single-inclusive jets, without a faithful description of actual events taking place in a real detector. There are many such generators like ALPGEN, MADGRAPH, PYTHIA, HERWIG, ISAJET etc. Out of these, many are general purpose event generator while some are for specific processes.

5.2 Higgs at Hadron Colliders

5.2.1 Higgs Mass Limits and Bounds

On the experimental side, the negative search results for the Higgs boson at LEP lead to a lower bound of $M_H \geq 114.4$ GeV at 95% Confidence Limit (CL) [2]. From the theoretical side, the bounds on the Higgs boson mass depend strongly on the underlying model. In the Standard Model, the Higgs mass is a free parameter. However, certain limitations arise from the requirement of the non-trivial Higgs potential with a meta-stable vacuum. New physics effects, appearing at a scale λ, may change the Standard Model shape of the Higgs potential. The detailed investigation outcome [3] is that if the Standard Model should obey both of these requirements upto the GUT scale, the Higgs boson mass must be between 100 and 200 GeV. Other values of M_H require new physics effects at a lower scale.

5.2.2 Higgs Production Modes

With the shutdown of LEP, Higgs searches are focused almost exclusively on hadron colliders. The current Run II of the Tevatron with c.m.s energy of 2 TeV in $p\bar{p}$ collision has an expected reach of discovering a Higgs in the mass range of about 130 to 180 GeV at the 5 σ level if an integrated luminosity of $30 fb^{-1}$ can be achieved [4]. Scheduled for 2007, the Large Hadron Collider, a proton-proton collider with 14 TeV center of mass energy, should be able to discover a Higgs boson in the full mass range between the current experimental lower bound and M_H= 1 TeV. The Higgs production cross-section is as shown in figure 5.1

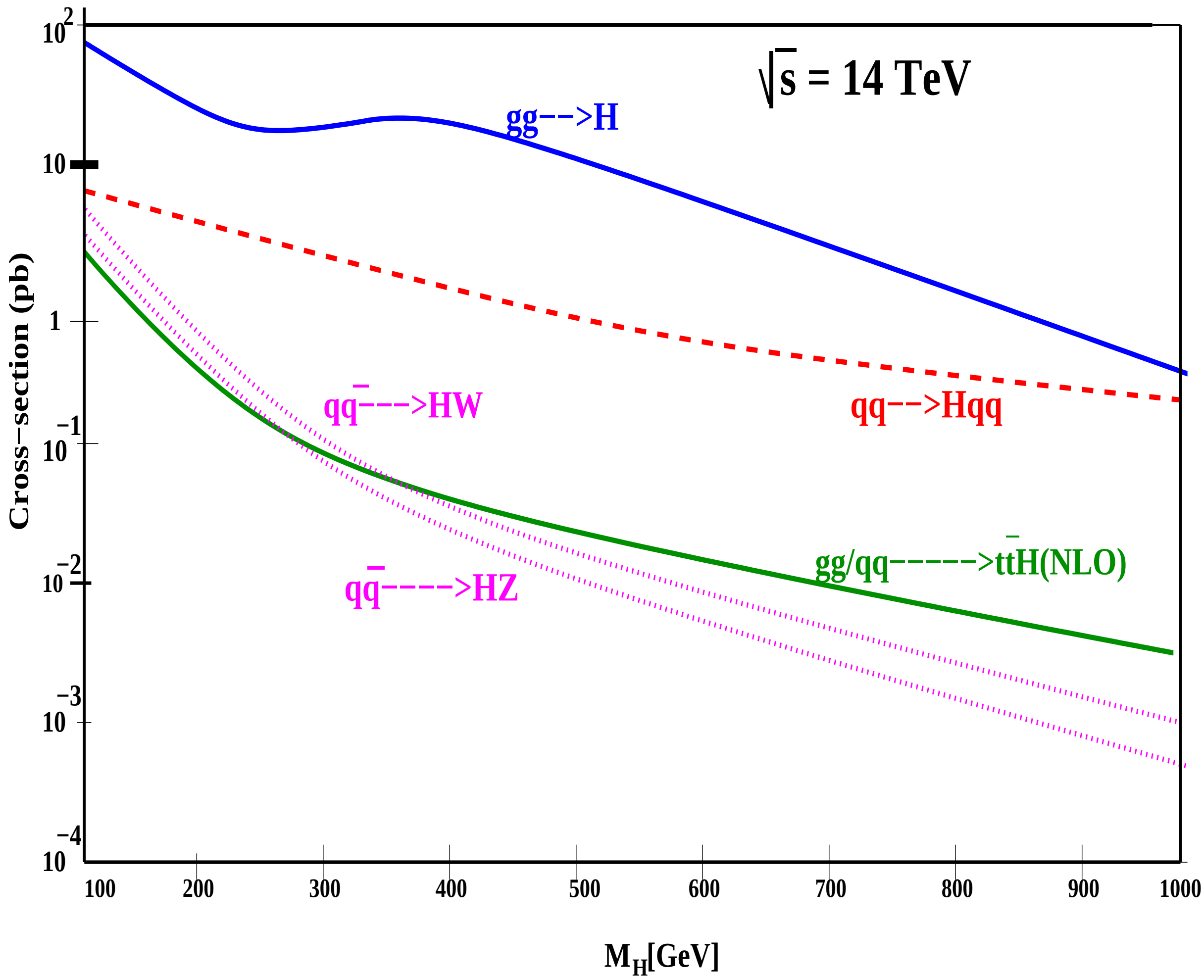

Figure 5.1: Production cross-section of Higgs at hadron collider

The Higgs boson coupling is proportional to the mass of the particle that couples to it. But the constituents of (anti-) protons at Tevatron and LHC are essentially massless. This means that the Higgs production has to be mediated by third-party particles that couple the Higgs to the light quarks and gluons. The four most important production vertices are as follows :-

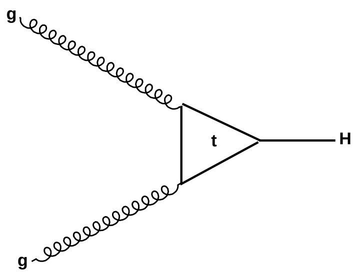

Figure 5.2: Gluon fusion :- gg→ H via a heavy quark(top) loop

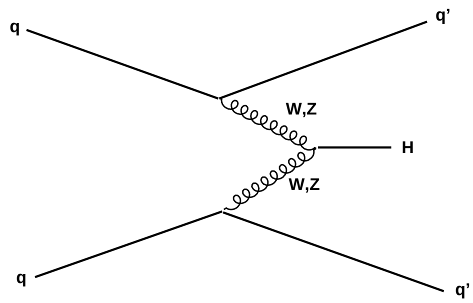

Figure 5.3: Weak-boson fusion :- $qq \rightarrow qqH$("WW,ZZ fusion")

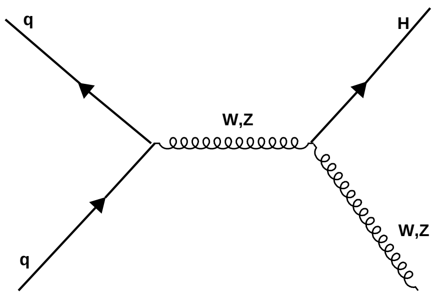

Figure 5.4: Higgs-strahlung :- $qq \rightarrow W(Z)H$

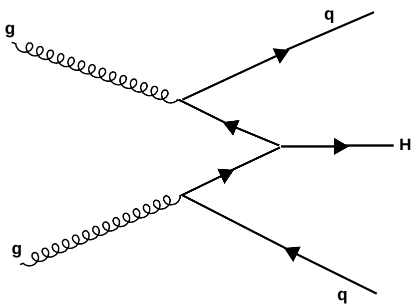

Figure 5.5: $t\bar{t}(b\bar{b})H$ associated production

1) **Gluon Fusion :-**

Gluon Fusion shown in figure 5.2 is the dominant production mode at both the Tevatron and the LHC. The coupling between the gluons and the Higgs boson is mediated by a top quark loop. The high gluon luminosity at the Tevatron and the LHC as well as the large top-Yukawa coupling as predicted by the Standard Model compensate for the loop suppression and let this mode dominate over all the other channels for the Higgs production. The fact that the leading order contribution to the gluon fusion mechanism is given by massive one-loop triangle diagrams makes the evaluation of QCD corrections very challenging. Fortunately, this problem can be simplified by restricting it to a limiting case, which turns out to be extendable to the general case almost without any loss in accuracy. This approximation is given by the heavy-top limit, meaning that the top quark is taken to be much heavier than the Higgs boson.

2) **Weak Boson Fusion**

The process of Higgs production through vector boson fusion shown in figure 5.3 will be important mostly for high Higgs masses where the coupling to longitudinal polarized vector bosons is strong. At the high energies where a heavy Higgs particle is created, the vector bosons act essentially as massless particles and can be treated as particles present inside the colliding protons. With this simplification, the full process can be separated into a calculation of the vector boson structure function in the proton and a calculation of Higgs production in colliding vector boson beams. The method is called the effective W approximation. For all possible values of the Higgs mass, the cross-section is below the gluon fusion process but with the additional signature of the two outgoing quarks participating in the process, the identification will be easier in this production channel for a large Higgs mass.

3) **Higgs Strahlung**

The Leading Order diagram for the Higgs strahlung process at hadron colliders is shown in figure 5.4. The Higgs boson is produced in association with a weak gauge boson. This is the most important mode at the Tevatron in the low mass region. The QCD corrections can be derived from the Drell-yan process and give a 30% increase with respect to the Leading Order prediction [5]. The cross section is almost one order of magnitude smaller than for gluon fusion. However, the benefit of this mode is that the b-quarks from the Higgs decay can be distinguished from the background through the tagging of the W and Z decay product.

4) **Associated Production**

Even though the cross section for the production of a Higgs with a $t\bar{t}$ pair is rather small, this mode is very attractive because of its remarkable signature of four b quarks in association with two W bosons. In addition, this process is directly sensitive to the top-Yukawa coupling. At the Tevatron, the cross-section is dominated to about 95% by the $q\bar{q}$ initial state. At the LHC, the gluon-gluon channel is dominant.

5.2.3 Higgs Decay and Branching Ratios

After discovery of a Higgs particle, it will be important to study the decay channels of the Higgs boson and to check if the coupling strength is in proportion to the mass for all fermions as the standard model predicts. If the decay width to a final state i is Γ_i, then the total decay width Γ is $\Sigma\Gamma_i$ and the branching ratio is $BR = \frac{\Gamma_i}{\Gamma}$. As shown in figure 5.6, the width becomes extremely narrow at low Higgs masses, few MeV at $m_H\sim$ 100 GeV and 1 GeV at $m_H\sim$ 200 GeV. At higher masses, it becomes broad, $\Gamma >$ 100 GeV above m_H = 600 GeV.

The branching ratio (BR) of Standard Model Higgs is shown in the figure 5.7 [6]. The rapid variation of branching ratio with Higgs mass making it necessary to have different strategies for the Higgs identification depending on its mass. The Higgs width is very small below WW threshold. The width into quark scale is proportional to square of the quark mass. The heaviest available quark pair is $b\bar{b}$. It dominates below WW threshold at a mass of about 160 GeV. The charm pair branching ratio is estimated to be $BR(c\bar{c}) \sim (m_c/m_b)^2 \times BR(b\bar{b}) \sim (1.2GeV/4.5GeV)^2 \sim 0.1$ i.e of the order of 1/10 of the branching ratio of $b\bar{b}$. After WW threshold, the WW decay is the dominant decay mode followed by ZZ decay with approximately half the rate of WW decay. The decay into $t\bar{t}$ is allowed only after the mass threshold of 350 GeV.

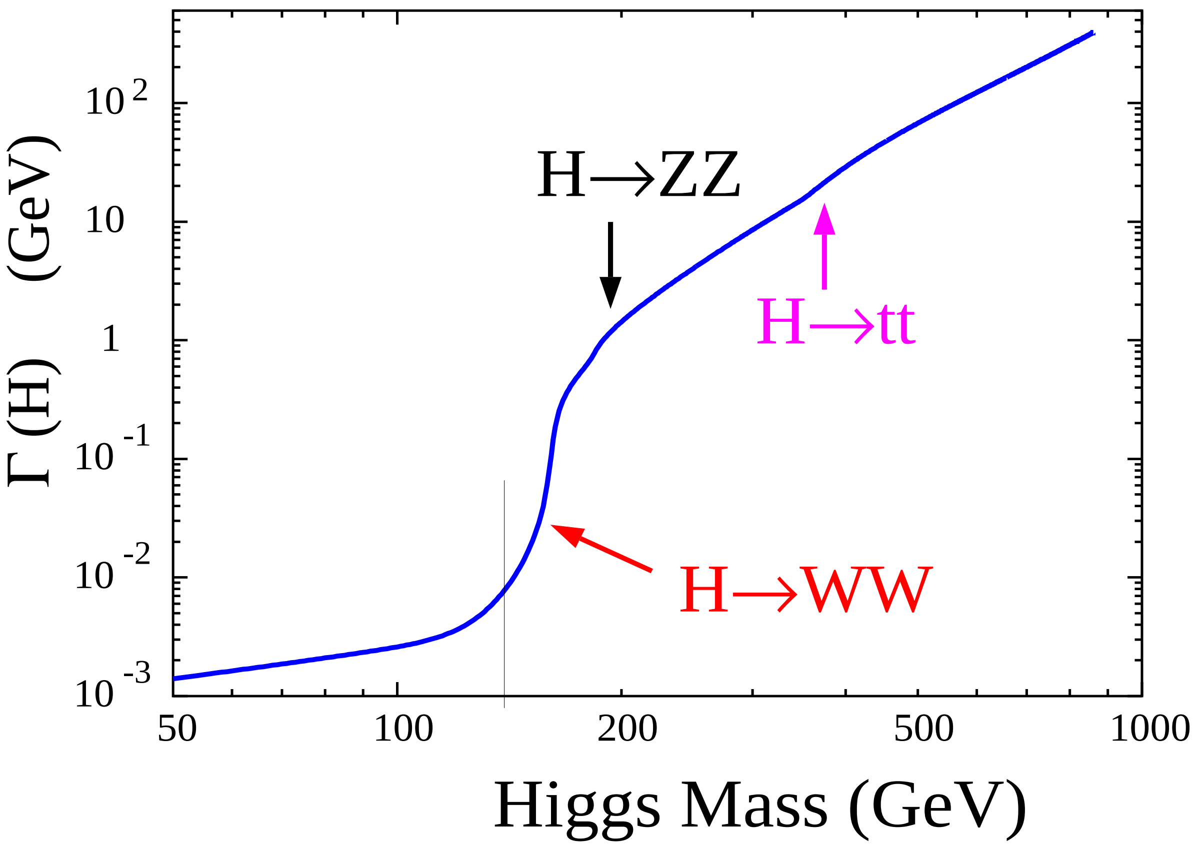

Figure 5.6: The decay width of Higgs boson as function of its mass

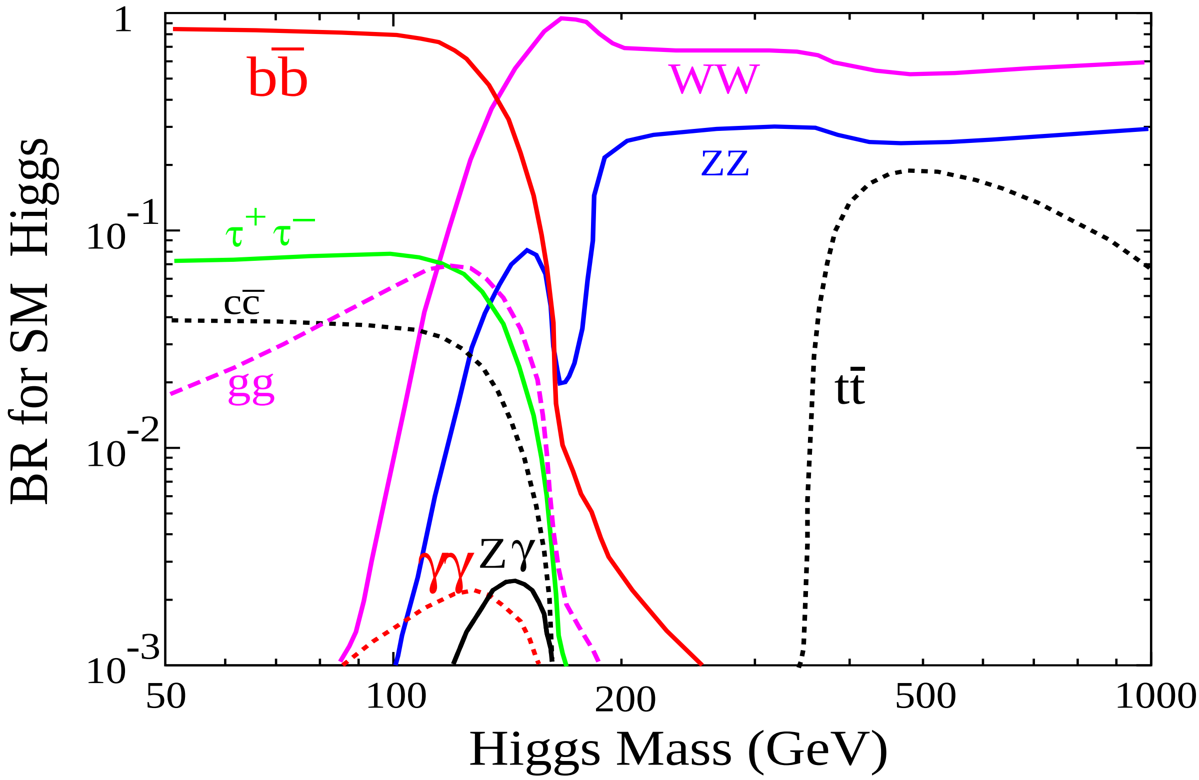

Figure 5.7: The branching ratio of Higgs boson as function of its mass

5.2.4 Searching an Intermediate Mass Standard Model Higgs

The Standard Model Higgs can be searched in intermediate mass range, $114.4 < m_H < 2m_Z$ [7]. The most dominant channel within this mass range is Higgs decay to $b\bar{b}$ due to its large branching ratio. This channel lacks any trigger as this channel neither has high jet energies nor has any isolated leptons in the final state. Also this channel will be overwhelmed by large di-jet rate as the final state b-quarks will also fragment into jets. The enormous QCD background can be reduced to some extent by searching for Vector Boson Fusion produced Higgs in which Higgs is produced with two high transverse energy (E_T) jets in opposite rapidity region. These high E_T jets in opposite rapidity can be used to tag the events in which Higgs is produced and helps in reducing the QCD backgrounds.

The other way to search in intermediate mass range is associative production of Higgs. Here Higgs can be produced with either top quark pair or Vector Boson. In this channel, the problem of getting trigger is solved by using high energy lepton from one of the top quarks or Vector Boson decay. Since due to longer lifetime of b-quark, it can be used to tag the events. Out of the above two modes, associated production of Higgs with $t\bar{t}$ pair is more favorable as compared to associated production with Vector Boson. The HW will have two b-quarks in the final state whereas $Ht\bar{t}$ will have four b-jets as top can decay to b-quark. Therefore, the use of multiple b-tagging in $Ht\bar{t}$ can provide larger rejection of jets which overcomes the low cross-section.

The other way of identifying the Higgs in intermediate mass range is to look out for $H \rightarrow \gamma\gamma$ decay. This decay channel is very rare and needs fairly high cross-section and decay branching ratio. The trigger for this channel is two electromagnetic clusters. The main source of backgrounds are from direct production of photons or photons behaving as fake jets. While $H \rightarrow \gamma\gamma$ channel suffers relatively very low branching ratio compared to $H \rightarrow b\bar{b}$, the backgrounds for this channel is much lower due to the clear signature of two isolated photons in the final state.

5.2.5 Searching a Heavy Standard Model Higgs

The Standard Model Higgs in the heavy mass range between $2m_Z$ or 180 GeV to 650 GeV decay mainly through channel $H \to ZZ \to l^+l^-l^+l^-$. This is the golden channel for Higgs decay in this mass range. Both the lepton pairs will have on-shell Z mass which will give the possibility to reduce many different backgrounds. The main source of background for this channel is direct ZZ production. To suppress the backgrounds, the conditions have to apply to transverse momentum of atleast one Z to be more than half the Higgs mass. The reduced production rate and the increased width of the Higgs defines the upper mass limit for this channel. The reduced production rate is the most serious problem and increased width increases the irreducible backgrounds.

5.2.6 Searching a Very Heavy Standard Model Higgs

In the very heavy mass range, $m_H > 650$ GeV, the channels where Higgs boson can be detected gets fewer and fewer due to the fall in production cross-section with increasing Higgs mass. The Higgs decaying into vector bosons is the dominated channels for the heavy Higgs. The production rate for the channel $H \to ZZ \to l^+l^-l^+l^-$ is very less for Higgs mass above 650 GeV. The only possible decay channel remains is Higgs decaying into pair of vector boson with atleast one vector boson decaying into neutrinos or jets i.e $H \to W^+W^- \to l\nu jj$, where j is the jet from a quark in the W decay. The large backgrounds from the direct jW and $t\bar{t}$ production can be reduced by requiring forward jets in the event. There can be another channel $H \to ZZ \to l^+l^-\nu\bar{\nu}$ which has very high branching ratio as compared to four lepton channel.

5.3 Study of Higgs Channel $H \to b\bar{b}$ produced via Weak Boson Fusion

The dominant decay of a Higgs boson for a low or intermediate Higgs mass is $H \to b\bar{b}$ due to its large branching ratio. The signal for the Higgs boson produced in isolation is impossible to extract. There is, as yet, no conceivable trigger for the process and the background production of $b\bar{b}$ is enormous. But to improve the analysis of $Hb\bar{b}$ Yukawa coupling, one can consider the decay of Higgs to $b\bar{b}$ pairs. One way to reduce the enormous background is to search for Higgs produced via Weak Boson Fusion as shown in figure 5.8.

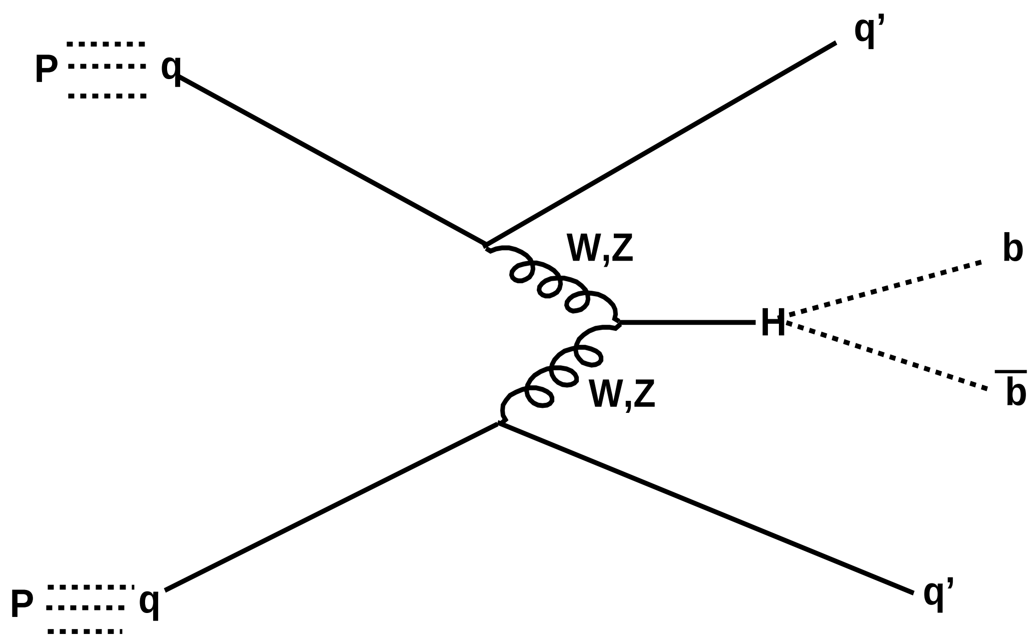

Figure 5.8: Higgs produced via Weak Boson Fusion decaying into $b\bar{b}$

5.3.1 Motivation for Weak Boson Fusion signature

For the intermediate mass range, $M_H < 200$ GeV, the production of Higgs via gluon fusion has the largest cross-section as compared to other production channels. There are substantial QCD background for this mechanism. The transverse momentum of the decay products and the resonance in their invariant mass distribution can be used to separate backgrounds from the signal. The second largest production cross-section for the standard model Higgs boson is predicted for weak-boson fusion (WBF), $qq \rightarrow qqVV \rightarrow qqH$ where V is the Vector Boson. WBF events contain additional information in the observable quark jets. Techniques like forward jet tagging can be exploited to reduce the backgrounds.

Once the Higgs is observed in both $gg \rightarrow H$ and WBF process $qq \rightarrow qqH$, the cross-section ratio of these modes measures the ratio of Higgs coupling to top quark and to W or Z. This value is fixed in Standard Model but deviations are expected in more general models like supersymmetry with its two Higgs doublets [8].

Also depending upon the mass of the Higgs, WBF channel requires low integrated luminosity for Higgs discovery as compared to other production channels e.g $gg \rightarrow H$ with same decay modes. One can calculate very precisely the Higgs coupling with low integrated luminosity of data.

Another most important feature of WBF signal is a lack of color exchange between initial state quarks. Color coherence between initial and final state gluon bremsstrahlung leads to suppressed hadron production in the central region between two tagging jet candidates of the signal. This is in contrast to color exchange in t-channel and thus lead to enhanced hadronic activity in the central region. One can exploit this feature to isolate signal from the backgrounds.

5.3.2 The WBF Signature

The WBF Higgs Signal can be described at lowest order by two single-Feynman-diagram processes, $qq \rightarrow qq$ (WW,ZZ) $\rightarrow qqH$ where WW and ZZ are emitted from the incoming quarks. The task is to identify the search region for these hard Hjj events. Features of the signal are a centrally produced Higgs which tends to yield central decay products and two jets which enter the detector with large rapidity as compared to the decay products shown in figure 5.9. The basic acceptance requirements must ensure that the Higgs decay products as well as the two tag jets must observed inside the detector. In case of the tag jets, the outgoing quarks or gluons must lie within the reach of hadron calorimeter with sufficient p_T to be identified as jets. In case of Higgs decay products, they must lie within electromagnetic calorimeter. The tag jets and the Higgs decay products must be well separated from each other.

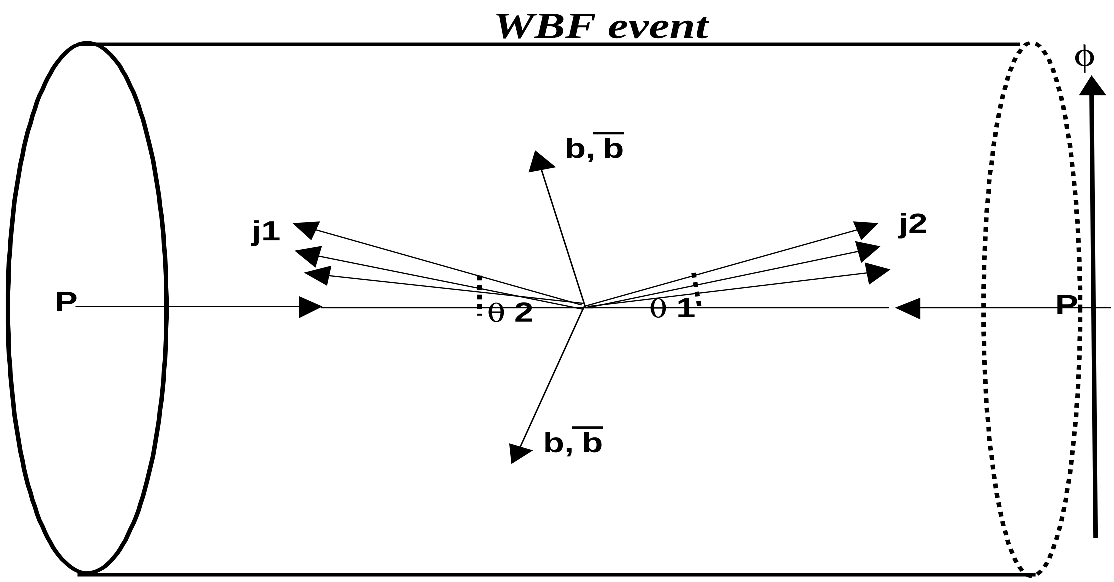

Figure 5.9: A typical Weak Boson Fusion event

5.4 Backgrounds Considered

We have considered four backgrounds for this process [9]

1) QCD production of $b\bar{b}jj$ final states, where j indicates a jet originating from a light quark (u, d, s, c) or a gluon. Here two b-quarks alongwith two final state light jets are produced with $p_T^b > 30$ GeV and $p_T^j > 60$ GeV.

2) QCD production of $jjjj$ final states. This process has the largest cross-section because it is a strong interaction process and the gluons are the dominant partons in the proton at low x values.

3) Associated production of $Z^*/\gamma^* \rightarrow b\bar{b}$ and light jets where the invariant mass of $b\bar{b}$ pair is in the Higgs signal region either because of imperfect mass resolution or because of the high-mass tail of the intermediate vector boson.

4) $t\bar{t}$ production. Here we studied the particular case where both the top quarks decay hadronically where the final state is difficult to disentangle since we have $bbjjjj$. We can loose two jets either because they are too forward or because they are too soft or collinear.

5.5 Procedure

5.5.1 Generation of Monte Carlo Events

The generation of the signal and background events is based on the numerical iterative procedure ALPHA, as implemented in the library of Monte Carlo codes ALPGEN [10]. ALPGEN is designed for the generation of Standard Model processes in hadronic collisions with emphasis on final states with large jet multiplicities. It is based on the exact leading order evaluation of partonic matrix elements with the inclusion of b and t quark masses (c masses are presented in some cases, where necessary) and t and gauge boson decays with helicity correlations. The code generates events in both a weighted and unweighted mode and provides book keeping utilities for a simple online histogramming of arbitrary kinematical distributions. Weighted generation allows for high-statistics parton level studies. Unweighted events can be processed in an independent run through shower evolution and hadronisation programs. The ALPGEN program does not include any form of hadronisation, thus the final states consist of bare quarks and gluons. The kinematics of the all hard objects in the event are explicitly represented and it simply assumes that there is one to one correspondence between hard partons and jets.

Signal events are generated [11] as 1 Higgs plus 2 back to back jets in the forward and backward rapidity region using ALPGEN generator. The generation process includes initial set of cuts on quark-jets shown in equation (1)

$$p_T^j > 60 \text{ GeV}, \qquad 2.5 < |\eta_j| < 5, \quad \Delta R_{jj} > 0.7 \qquad \text{where } \Delta R_{jj} = \sqrt{\Delta\eta_j^2 + \Delta\phi_j^2} \quad (1)$$

The background events are also generated using ALPGEN generator. These events are generated in such a way that they mimic the signal. QCD backgrounds $bbjj$ and $jjjj$ are generated with the same initial cuts as signal. $t\bar{t}$ events are generated with both the top quarks decay hadronically. zjj background is generated with z produced alongwith 2 jets in opposite rapidity and $z \to b\bar{b}$. Table 5.1 shows the cross-section of all processes determined from the event generator ALPGEN.

Events	Cross-section(pb)
WBF Signal($qq \to qqH$)	0.0992373
qcd_{bbjj}	6348.53
qcd_{jjjj}	2150450
$t\bar{t} \to W^+W^- \to b\bar{b}jjjj$	241.179113
$zjj \to b\bar{b}jj$	0.416801

Table 5.1: ALPGEN Cross sections

The unweighted events of signal and backgrounds from the ALPGEN generator are interfaced with showering and hadronisation generator named PYTHIA [12]. These programs which employ parton shower approach are general purpose tools to simulate a wide variety of initial and final states. Higher order effects are added by evolving the event using the parton shower which allows partons to split into the pairs of other partons. The resulting partons are then grouped together or hadronize into color-singlet hadrons and resonances are decayed.

The package used for interfacing ALPGEN output with PYTHIA is CMKIN [13]. CMKIN offers standard way to interface generators like PYTHIA, HERWIG, ISAJET etc with CMS detector simulation. The interface is based on a common block HEPEVT- a HEP standard to store particle kinematics information for one event. For each generator, a set of routines is used to convert from generator event structure to HEPEVT common. Some of the routines are found from Standard High Energy Physics package. The HEPEVT common block is converted to HBOOK n-tuple for input output.

5.5.2 Simulation of Material Effect

The effect of detector material to events is studied. In CMS, Object-oriented Simulation for CMS Analysis and Reconstruction (OSCAR) [14], in C++ is used. OSCAR is based on the Geant 4 simulation toolkit and the CMS object-oriented framework for simulation and reconstruction.

Geant 4 provides a rich set of physics processes describing in detail electromagnetic and hadronic interactions. It also provides the tools for the implementation of the full CMS detector geometry and the interfaces required for recovering information from the particle tracking in the detectors. This functionality is interfaced to the CMS framework, which allows the user to selectively load desired modules and to configure and tune the final application. OSCAR manages all CMS detectors, both central and forward as well as several testbeam layouts and prototypes. It implements their sensitive detector behaviour, track selection mechanisms, hit collections and numbering schemes.

The OSCAR design is based on COBRA which is Coherent Object-oriented Base for Reconstruction, Analysis and in particular the COBRA Mantis subsystem for the simulation framework specialization. Mantis is architecture-driven and has from its conception aimed to exploit fully the COBRA infrastructure and functionality. The COBRA profound subsystem provides the Physics, Reconstruction & Selection specific code used by both simulation using OSCAR and reconstruction using ORCA. The COBRA Detector Description Database (DDD) subsystem provides the infrastructure and services for the detector geometry modeling. The geometry data for the CMS detectors are produced by the CMS Geometry project. Generator input is handled entirely by COBRA Mantis , the specific generator to be deployed and the events are specified at run-time with OSCAR datacards. Magnetic field services are provided by COBRA Mantis and the COBRA Magnetic Field package. The choice of field and the propagation parameters are specified at run-time with OSCAR datacards and DDD XML files. For visualization and event display Mantis relies on IGUANACMS.

As an input, detector simulation takes the generated particles in HEPEVT format. Through the hierarchy of volumes and materials, the generated particles are traced or a subset of the particles that fit into a certain, user-specified, kinematic region and the physics processes that accompany particle passage through matter are modeled. Results of each particle's interactions with matter are recorded in the form of simulated hits. It calculates how particles produced by an event generator traverse the detector, the effect in magnetic fields, shower in calorimeters and sneak out through cracks etc. SimHits contain the information of energy stored in different detector elements as a function of time.

5.5.3 Simulation of Response of Readout Electronics

The SimHits from detector level simulation requires some algorithm for readout. This step is done by using ORCA which is Object-oriented Reconstruction for CMS Analysis [15]. In this program, the event energy deposited in detector is converted into electrical signals and to digital information using Analog to Digital Convertors (ADCs) and Time to Digital Convertors (TDCs). Ideally, the output of this stage has exactly the same format as the real data recorded by the detector. The output is called Digis.

ORCA is a framework for reconstruction and is intended to be used for final detector optimizations, trigger studies or global detector performance evaluation. It is an object oriented system for which C++ has been chosen as programming language. ORCA has two logical layers or subsystems and all are within a subsystem packages. The available subsystems are shown in a figure 5.10. The packages within a subsystem typically produce a single library dedicated to cope with a certain aspect of the corresponding sub-detector e.g for Calorimetry, G3EcalDigits, G3HcalDigits, EcalCluster etc or reconstruction utility. The subsystem Workspace is for the working environment for the users private code.

5.5.4 Reconstruction of Physics or Analysis Objects

The generated particles and calorimeter reconstruction hits are read from the object oriented database e.g Digis from ORCA digitisation and further event reconstruction e.g calorimeter towers, electromagnetic clusters and jets etc is needed to do physics analysis. The Reconstruction package used is JetMetAnalysis [16]. JetMetAnalysis is a subsystem of ORCA and works as a user analysis package in the COBRA-ORCA system. COBRA has the "main()" method or function which invokes predefined various analysis methods and then invokes JetMetAnalysis. This step includes gathering the information from the Monte Carlo and detector reconstruction and performing group analysis, adding information exploitable from the data and the relation between data objects . It also involves performing user analysis and selection. Finally we get the output of the selected quantities and events. Every package of the JetMetAnalysis subsystem consists of classes whose definitions, implementations and test programs are grouped together in different subdirectories following the ORCA standard. One of the output of JetMetAnalysis package is jet which can be defined as a set of particles flow in the defined cone.

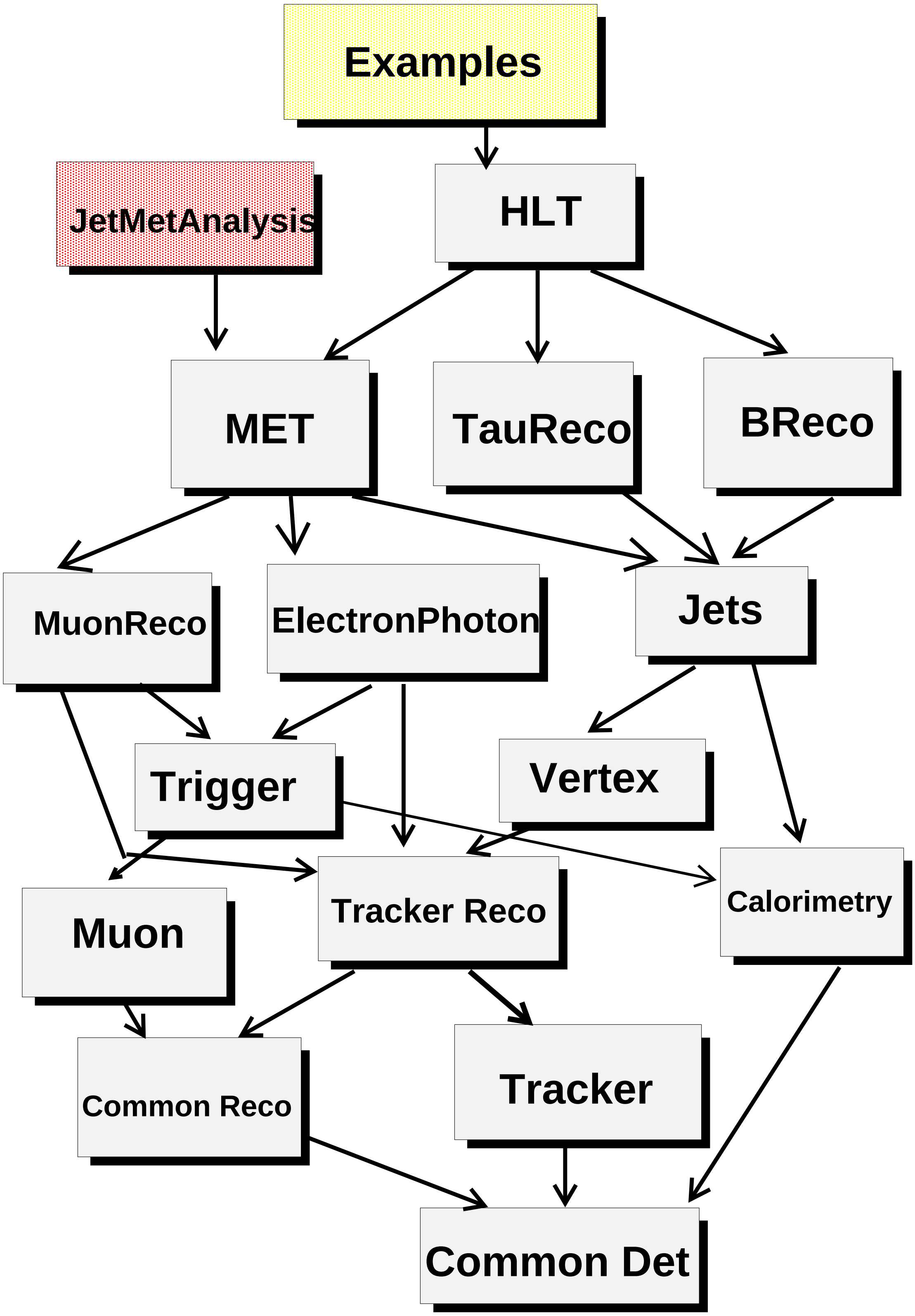

Figure 5.10: Subsystems of ORCA and their dependencies

There are several cone algorithms [17] for reconstruction of jets.

(a) Iterative Cone Algorithm

In the iterative cone algorithm, an E_T-ordered list of input objects, particles or calorimeter towers is created. A cone of size R in η, ϕ space is cast around the input object with the largest transverse energy above a specified seed threshold. The objects inside the cone are used to calculate a proto-jet direction and energy using the E_T scheme

$$E_T = \Sigma E_{T,i}$$
$$\eta = \frac{1}{E_T}\Sigma E_{T,i}\eta_i$$
$$\phi = \frac{1}{E_T}\Sigma E_{T,i}\phi_i$$

The computed direction is used to seed a new proto-jet. The procedure is repeated until the energy of the proto-jet changes by less than 1% between iterations and the direction of the proto-jet changes by 1%. When a stable proto-jet is found, all objects in the proto-jet are removed from the list of input objects and the stable proto-jet is added to the list of jets. The whole procedure is repeated until the list contains no more objects with an E_T above the seed threshold. The cone size and the seed threshold are parameters of the algorithm. When the algorithm is terminated, a different recombination scheme may be applied to jet constituents to define the final jet kinematic properties.

(b) Midpoint-Cone Algorithm

The midpoint-come algorithm was designed to facilitate the splitting and merging of jets. The midpoint-cone algorithm also uses an iterative procedure to find stable cones or proto-jets starting from the cones around objects with an E_T above a seed threshold. In contrast to the iterative cone algorithm, no object is removed from the input list. This can result in overlapping proto-jets. To ensure the collinear and infrared safety of the algorithm, a second iteration of the list of stable jets is done. For every pair of proto-jets that are closer than the cone diameter, a midpoint is calculated as the direction of the combined momentum. These midpoints are then used as additional seeds to find more proto-jets. When all proto-jets are found, the splitting and merging procedure is applied. The procedure is applied starting with the highest E_T proto-jet. If the proto-jet does not share objects with other proto-jets, it is defined as a jet and removed from the proto-jet list. Otherwise, the transverse energy shared with the highest E_T neighbour proto-jet is compared to the total transverse energy of this neighbour proto-jet. If the fraction is greater than f which is typically 50%, the proto-jets are merged, otherwise the shared objects are individually assigned to the proto-jet that is closest in η , ϕ space. The procedure is repeated, again always starting with the highest E_T proto-jet, until no proto-jets are left. This algorithm implements the E-scheme to calculate the proto-jet properties but a different recombination scheme may be used for the final jet. The parameters of the algorithm include a seed threshold, a cone radius, a threshold f on the shared energy fraction for jet merging and also a maximum number of proto-jets that are used to calculate midpoints.

(c) Inclusive k_T Algorithm

The inclusive k_T jet algorithm is a cluster-based jet algorithm. The cluster procedure starts with a list of input objects, stable particles or calorimeter cells. For each object i and each pair (i,j) the following distances are calculated

$$d_i = (E_{T,i})^2 R^2,$$
$$d_{ij} = min(E_{T,i}^2, E_{T,j}^2) R_{ij}^2 \text{ with } R_{ij}^2 = (\eta_i - \eta_j)^2 + (\phi_i - \phi_j)^2$$

where R^2 is a dimensionless parameter normally set to 1 [18]. The algorithm searches for the smallest d_i or d_{ij}. If a value of type d_{ij} is the smallest, the corresponding objects i and j are removed from the list of input objects. They are merged using one of the recombination schemes listed below and filled as one new object into the list of input objects. If a distance of type d_i is the smallest, then the corresponding object i is removed from the list of input objects and filled into the list of final jets. The procedure is repeated until all objects are included in jets. The algorithm successively merges objects which have a distance $R_{ij} < R$. It follows that for all final jets i and j, $R_{ij} > R$.

The inclusive k_T algorithm merges in each iteration step an input objects into possible final jets, so the new jet quantities, the jet direction and energy have to be calculated directly during the clustering. The cone jet algorithms like iterative and mid-point, group the input objects together in proto-jets. The final determination of the jet quantities is done in one step at the end of the jet finding.

The different recombination schemes used in the jet algorithms are listed below.

a) E-scheme

$$E = \Sigma E^i$$

$$p_{x,y,z} = \Sigma p^i_{x,y,z}$$

b) E_T-scheme for Cone Jet Algorithms

$$E_T = \Sigma E^i_T,$$

$$p_{x,y,z} = \Sigma E^i_{x,y,z},$$

$$sin\theta = \frac{\sqrt{(p_x)^2+(p_y)^2}}{\sqrt{(p_x)^2+(p_y)^2+(p_z)^2}},$$

$$E{=}E_T/sin\theta$$

c) E_T-scheme for the Inclusive k_T Algorithm

$$E_T = \Sigma E_T,$$

$$\eta = \frac{\Sigma E_T \times \eta}{\Sigma E_T},$$

$$\phi = \frac{\Sigma E_T \times \phi}{\Sigma E_T}$$

Two different groups of factors influence the jet energy resolution. One group comes from the physics of jet and second one comes from the detector effects. Fragmentation, initial and final state radiation, underlying events, minimum bias events influences particle level jet energy resolution whereas magnetic field, electronic noise, dead materials and cracks, longitudinal leakage for high p_T jets, shower size, out of cone losses, jet separations, calorimeter response to the particles influence calorimeter jet energy resolution.

The algorithm used for reconstruction of jets in the analysis is Iterative Cone Algorithm with E_T threshold 30 GeV and cone radius R = 0.5. The correction used in jets in JetMetAnalysis is MC Jets correction which is the correction for calorimeter jets.

$$Response = E_T \text{ (reconstructed jet)} / \ E_T \text{(generated jet)}$$

$$Correction = 1/Response$$

where **Generated jet** is considered as a set of particles at the vertex level in the defined cone and **Reconstructed jet** is considered as a set of calorimeter towers at the calorimeter level in the defined cone.

5.6 Analysis

The distribution of number of jets in the signal events is plotted both at the generator level and at the reconstructed level are shown in the figure 5.11. The peak at four jet final states for the signal is evident.

The particle multiplicity in generated jets is as shown in fig 5.12 and the ECAL plus

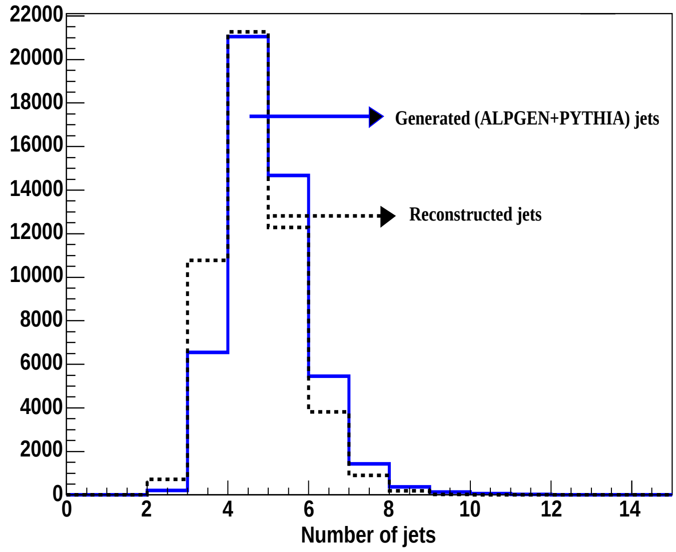

Figure 5.11: Jet multiplicity at the generator level & reconstructed level

HCAL tower multiplicity in the reconstructed jets is as shown in fig 5.13.

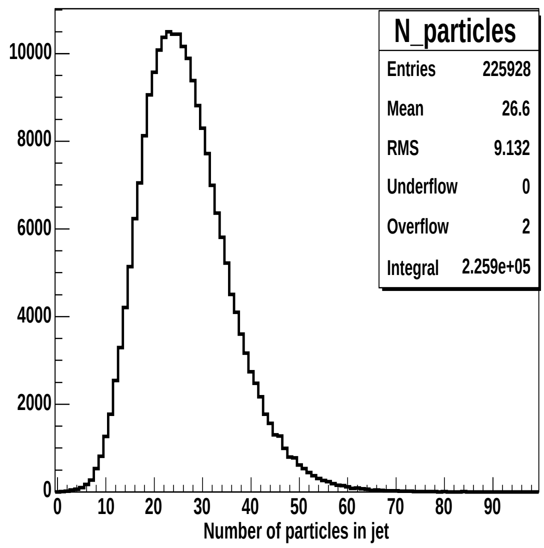

Figure 5.12: Particle multiplicity in the generator jets

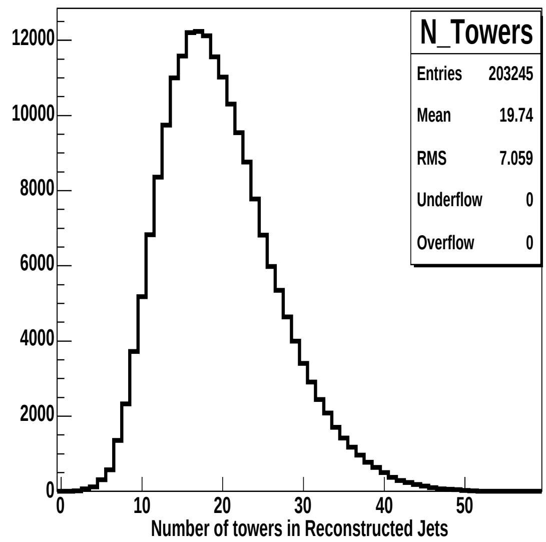

Figure 5.13: ECAL plus HCAL towers multiplicity in the reconstructed jets

At the moment no trigger will yield good results for the channel $qq \rightarrow qqH \rightarrow qqb\bar{b}$ because the default thresholds used for $2 \times 10^{33} cm^{-2} s^{-1}$ luminosity are way too high for our channel.

We figure out the way to keep events of interest in the sample while keeping the QCD events rate at an acceptable level. The basic event selection criteria is to select the events with the condition on the number of jets per event.

$$\text{Njet} \geq 4 \tag{2}$$

The four highest transverse energy (E_T) jets are selected and sorted according to their rapidity (η). The jet with least and the highest η are treated as tag jets and jets with η in between two tag jets as b-jets. The eta plot of tag jets is shown in figure 5.14. Using the jet information E_T, η, ϕ, the invariant mass of b-jets & tag jets are calculated both at generator level & at reconstruction level.

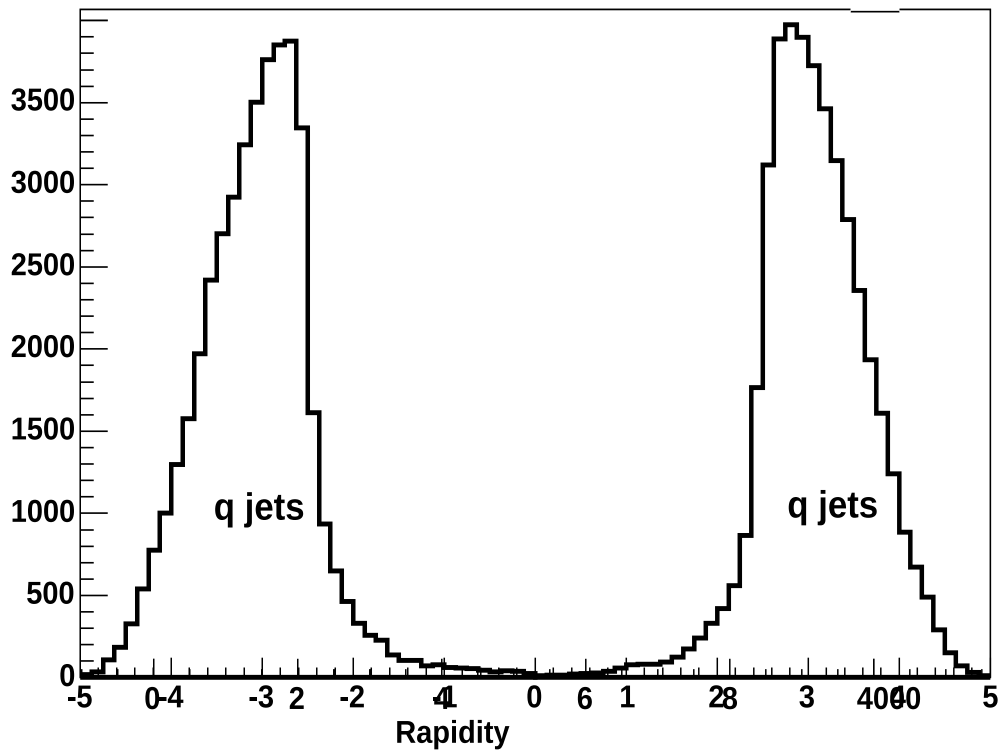

Figure 5.14: η plot of tag (quark) jets for signal events

5.6.1 Forward tag jet selection

The separation of signal & QCD backgrounds highly depends upon forward tag jet selection. The selection procedure for the tag jets is divided into two steps.

1) The large mass cut $M_{jj} > 1000$ is selected to reduce backgrounds due to QCD jets as much as possible as shown in figure 5.15.

2) A cut at $2.5 < |\eta_j| < 5$ was applied to the jet pseudo rapidity. This requirement ensures that jets are well within CMS calorimeters and are well forwarded. In addition, we require a large separation ($|\Delta\eta_{jj}| > 4.2$) in pseudorapidity between the two tag jets in opposite hemisphere as depicted from figure 5.16.

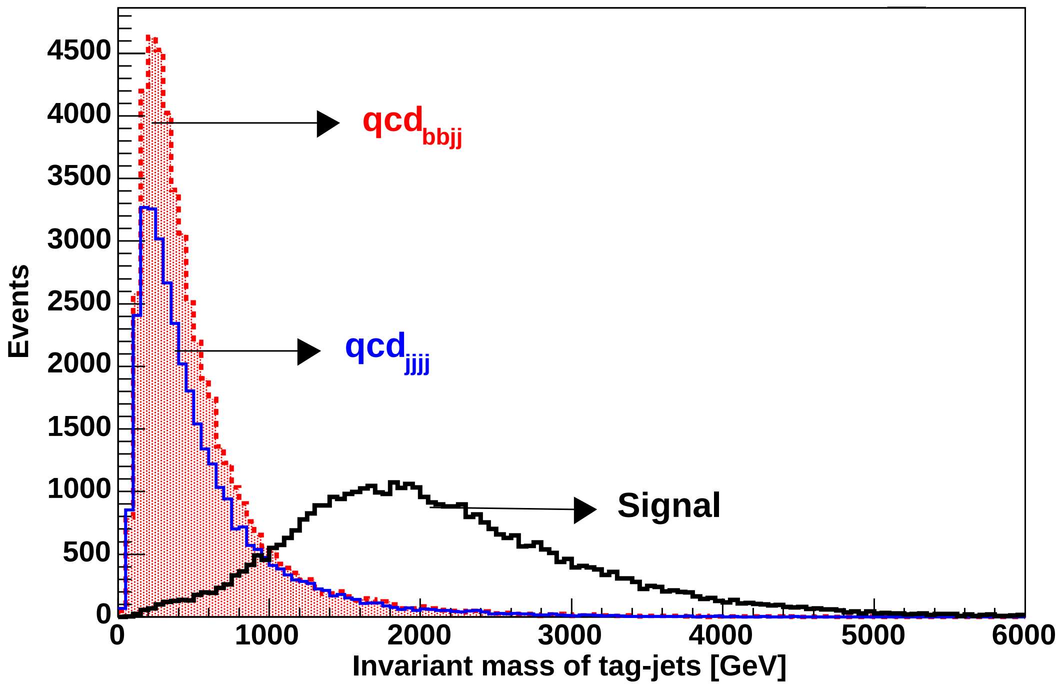

Figure 5.15: Invariant mass of two tag-jets for signal & QCD backgrounds

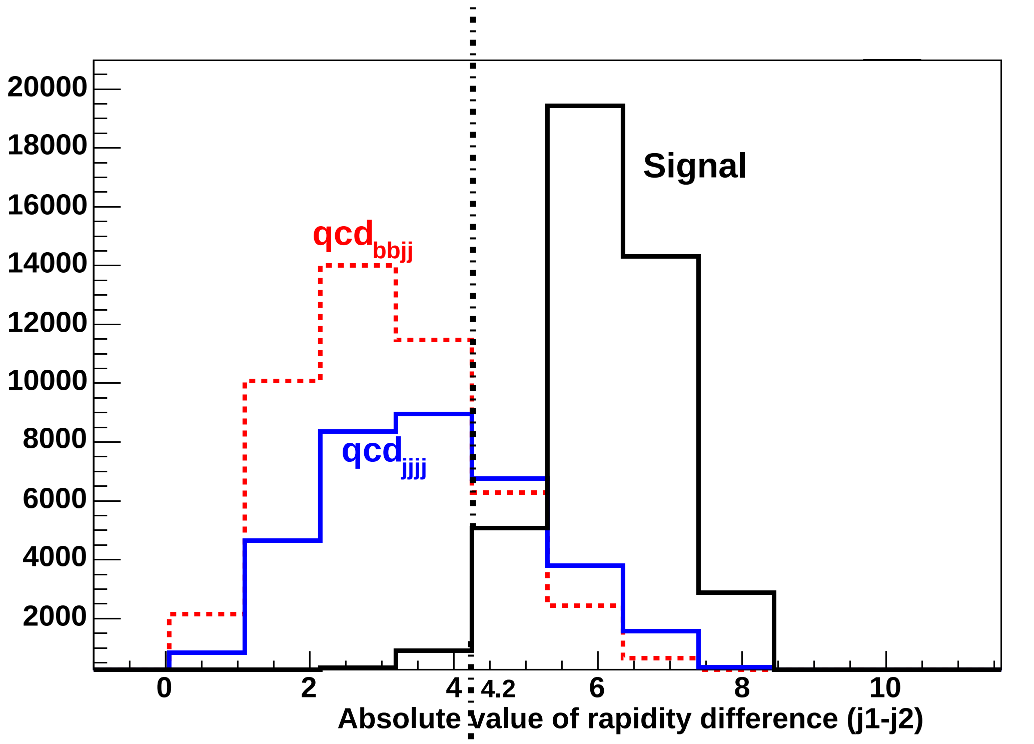

Figure 5.16: Absolute value of η-difference of two tag-jets for signal & QCD backgrounds

Hence, in addition to cuts in eq (2), we also used the following set of cuts

$$p_T^b > 30 \text{ GeV}, \qquad \Delta R_{bb} > 0.5, \qquad |\eta_b| < 2.5$$

$$p_T^j > 60 \text{ GeV}, \quad 2.5 < |\eta_j| < 5 \quad \eta j1.\eta j2 < 0, \quad \Delta R_{jj} > 0.5 \tag{3}$$

$$|\eta_{j1} - \eta_{j2}| > 4.2 \qquad M_{jj} > 1000 \text{ GeV}$$

The cut $M_{jj} > 1000$ GeV, in addition to the rapidity cut $|\eta_{j1} - \eta_{j2}| > 4.2$, is efficient in removing the backgrounds from the QCD processes as shown in figure 5.17.

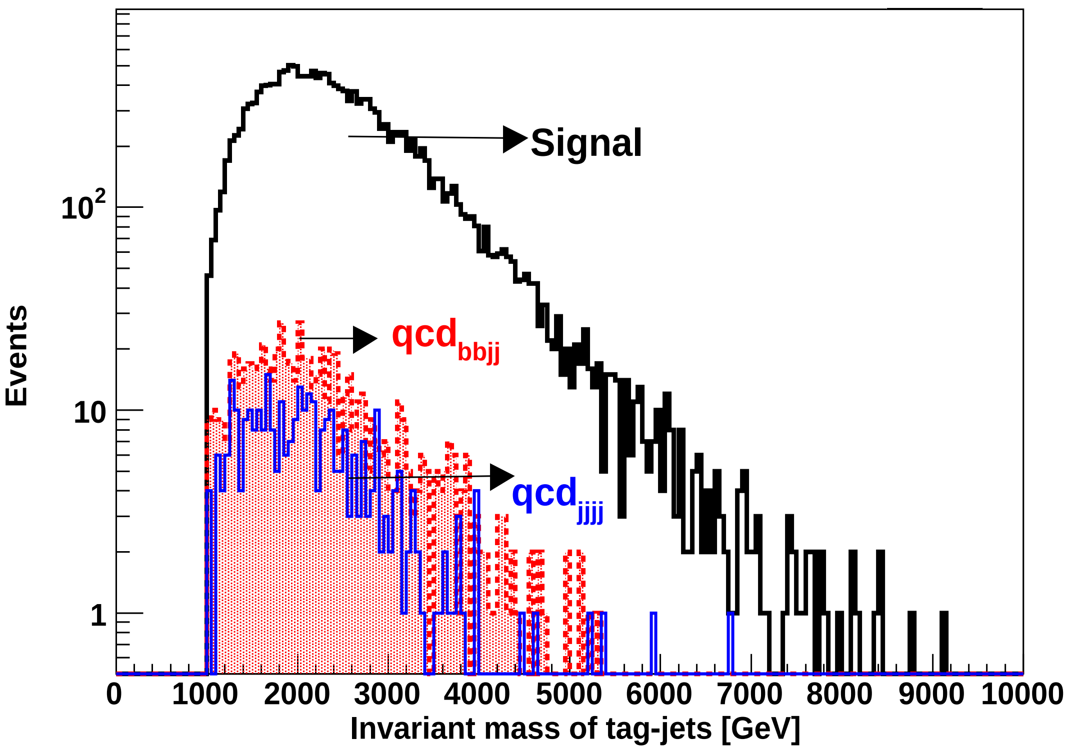

Figure 5.17: Invariant mass of two tag-jets for signal & QCD backgrounds using cuts (2) & (3)

The transverse energy E_T of the b-jets & tag jets is shown in figure 5.18. The invariant mass of b-jets at generator level both at linear and log scale is shown in figure 5.19. The invariant mass of b-jets at reconstructed level both at linear and log scale is shown in figure 5.20.

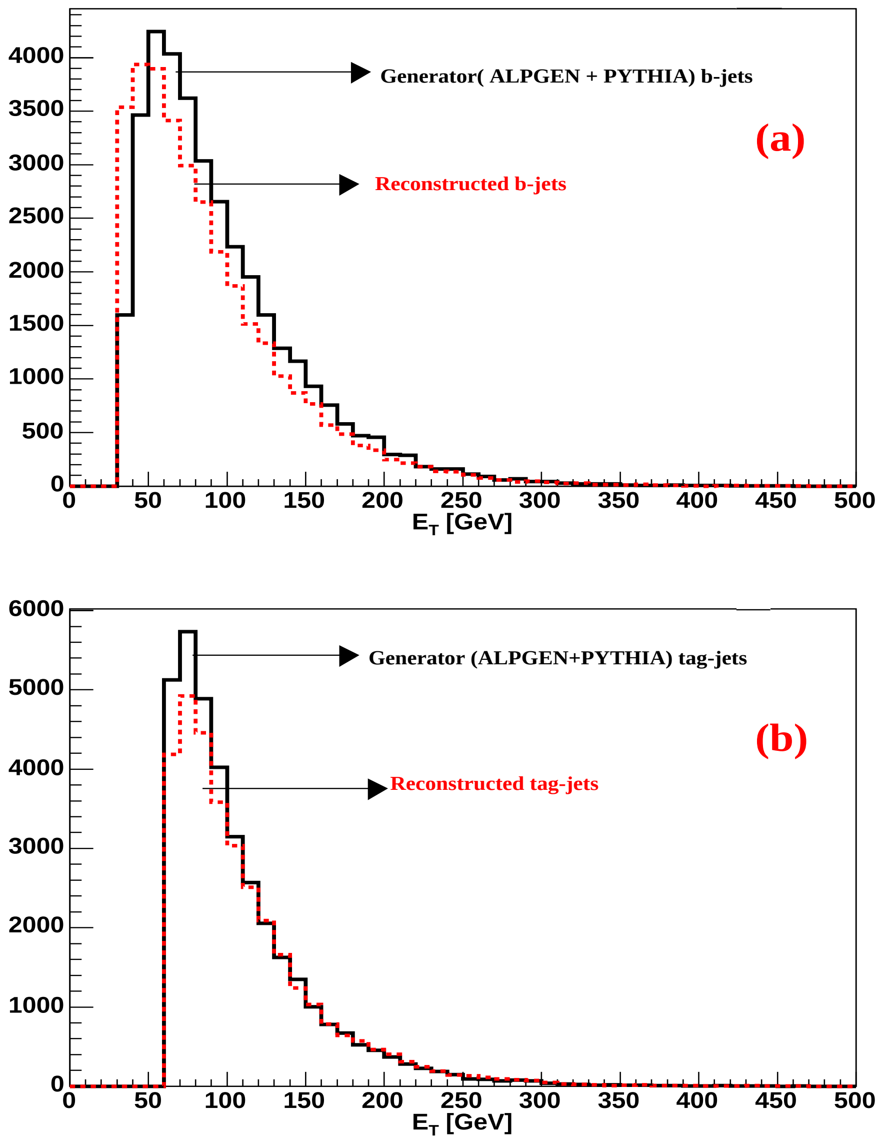

Figure 5.18: (a) E_T of b-jets & (b) E_T of tag-jets

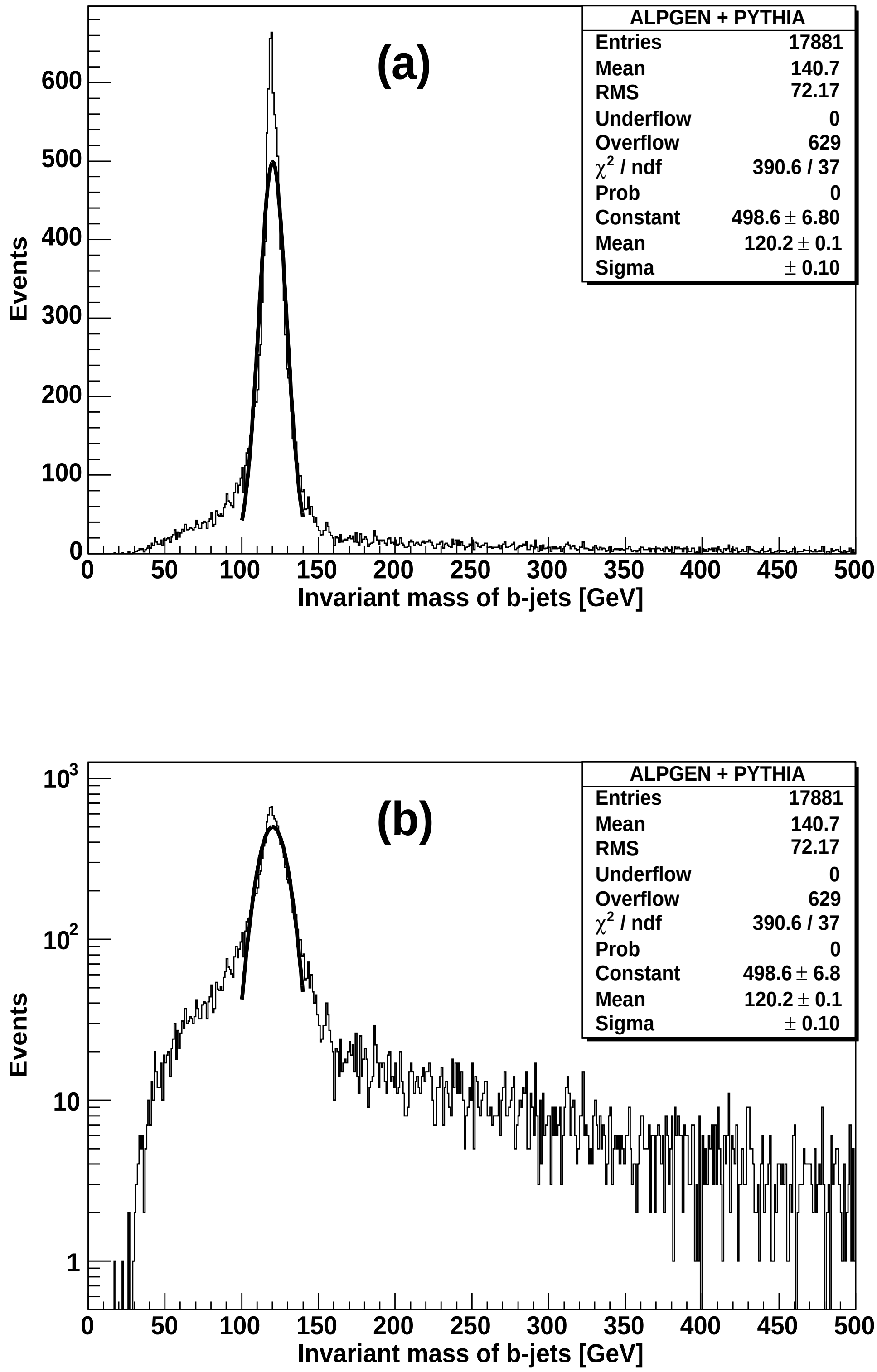

Figure 5.19: Invariant mass of b-jets at the generator (ALPGEN + PYTHIA level) (a) Linear scale (b) Log scale

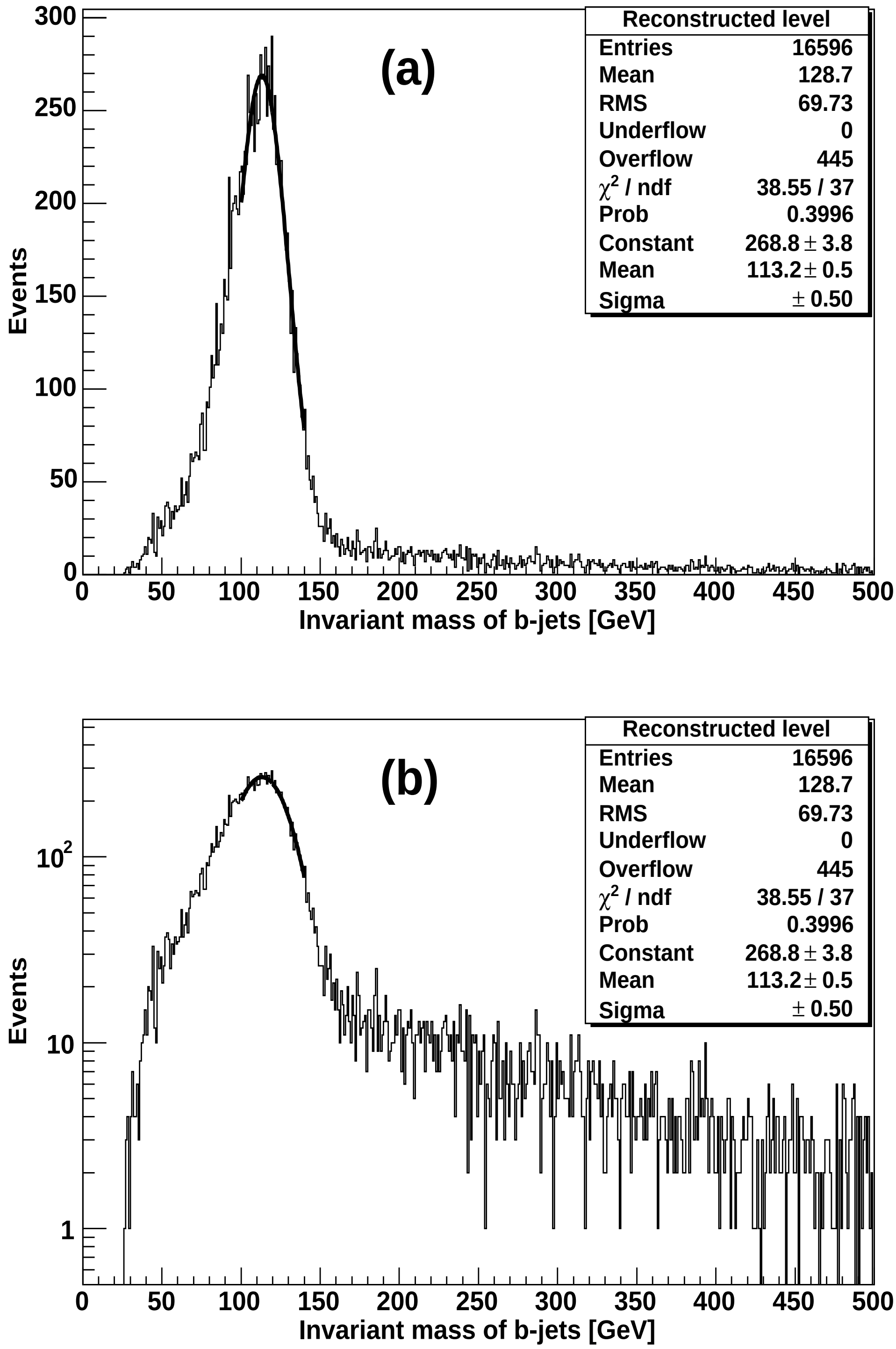

Figure 5.20: Invariant mass of b-jets at reconstructed level (a) Linear scale (b) Log scale

The number of events in different selection steps is shown in the table 5.2. The sample for the signal, QCD backgrounds ($bbjj$ and $jjjj$) is 50k events and for $t\bar{t}$ and zjj the sample is 36k and 35k respectively.

N_{evts}	Signal	Backgrounds			
		qcd_{bbjj}	qcd_{jjjj}	$t\bar{t}$	zjj
	50k	50k	50k	36k	35k
With cuts (2)	38099 (43251)	29633 (47209)	18798 (35308)	18925 (34130)	19819 (24944)
With cuts (2) & (3)	16602 (17881)	403 (685)	224 (331)	47 (53)	4283 (4884)
With cuts (2)&(3) & 100< M_H <140 GeV	8327 (11354)	91 (128)	45 (63)	3 (5)	557 (720)

Table 5.2: The number of events in invariant mass calculation at reconstructed level (*generator level*)

By looking into E_T plot of b-jets, it is noticed that there are more events at the lower E_T cutoff for reconstructed level than for generator level showing thereby that some fake jets are reconstructed. To get rid of these fake jets we revise cuts by taking into account the σ_{E_T} as given by :-

$$(\frac{\sigma_{E_T}}{E_T})^2 = (\frac{120}{\sqrt{E_T}})^2 + (5)^2\% \tag{4}$$

Calculating 2σ for the E_T of b-jets and tag-jets, we get

$$\text{for } E_T = 60 \text{ GeV, we get } 2\sigma = 20 \text{ GeV for quark jets}$$

$$\&$$

$$\text{for } E_T = 30 \text{ GeV, we get } 2\sigma = 15 \text{ GeV for } b\text{-jets.}$$

Including the 2σ cut, momentum cuts are revised to 45 GeV for b-jets and 80 GeV for tag-jets. The Revised set of cuts are shown in eq. (5)

$$\begin{gathered} p_T^b > 45 \text{ GeV}, \quad \Delta R_{bb} > 0.5, \quad |\eta_b| < 2.5 \\ p_T^j > 80 \text{ GeV}, \quad 2.5 < |\eta_j| < 5 \quad \eta j1.\eta j2 < 0, \quad \Delta R_{jj} > 0.5 \\ |\eta_{j1} - \eta_{j2}| > 4.2 \quad M_{jj} > 1000 \text{ GeV} \end{gathered} \tag{5}$$

The transverse energy E_T distribution of the b-jets and the tag-jets with revised cuts are shown in figure 5.21. Using jet information in terms of E_T, η & ϕ, the invariant mass of b-jets with revised cuts at generator level both at linear and log scale is shown in figure 5.22. The invariant mass of b-jets with revised cuts at reconstructed level both at linear and log scale is shown in figure 5.23.

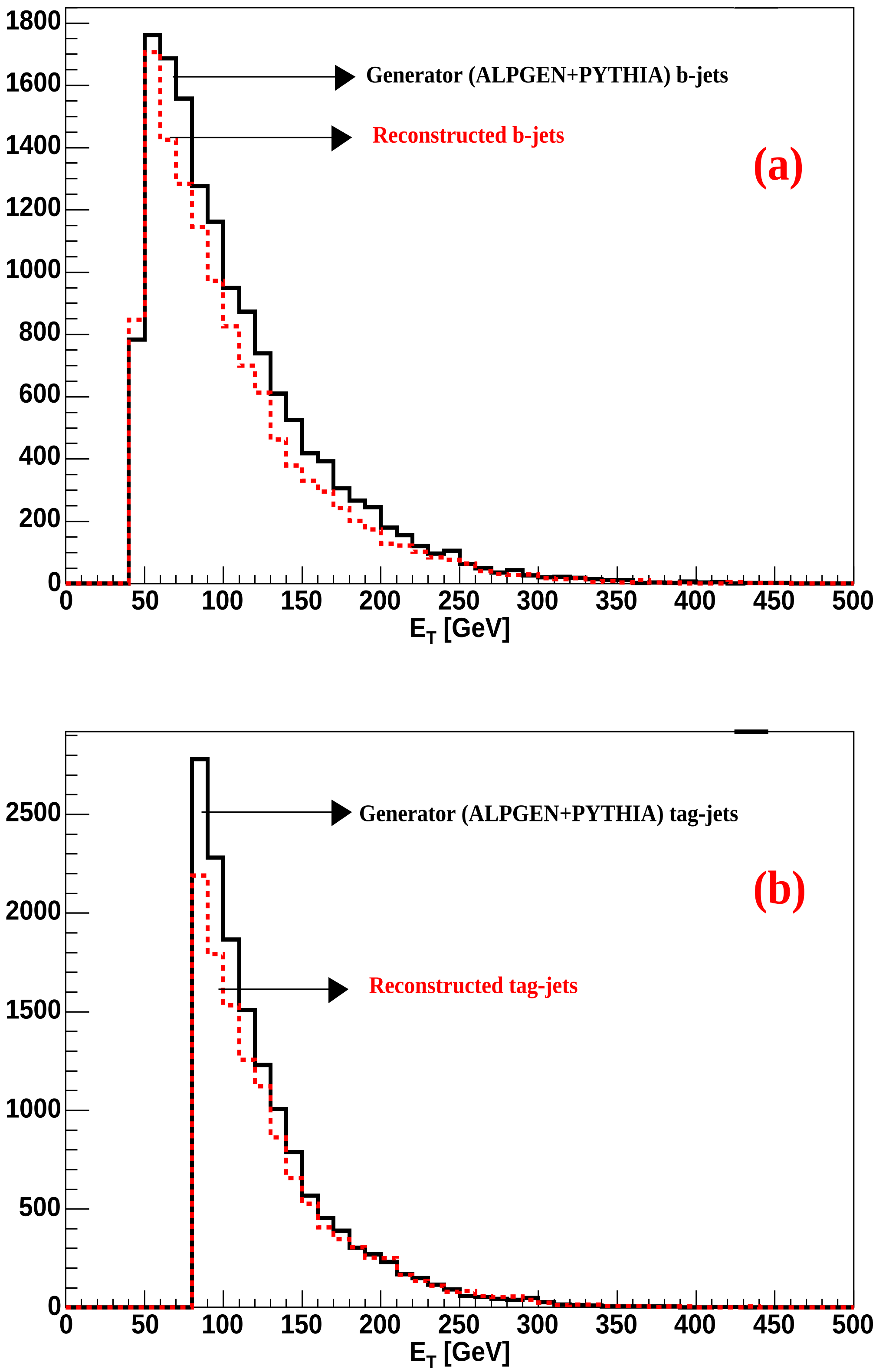

Figure 5.21: (a) E_T of b-jets & (b) E_T of tag-jets

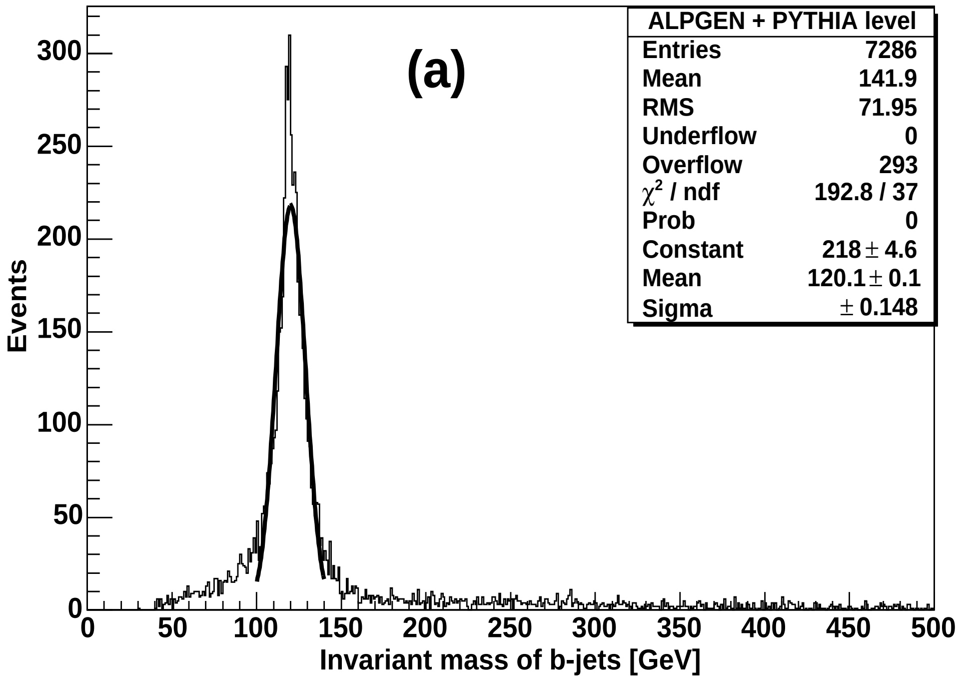

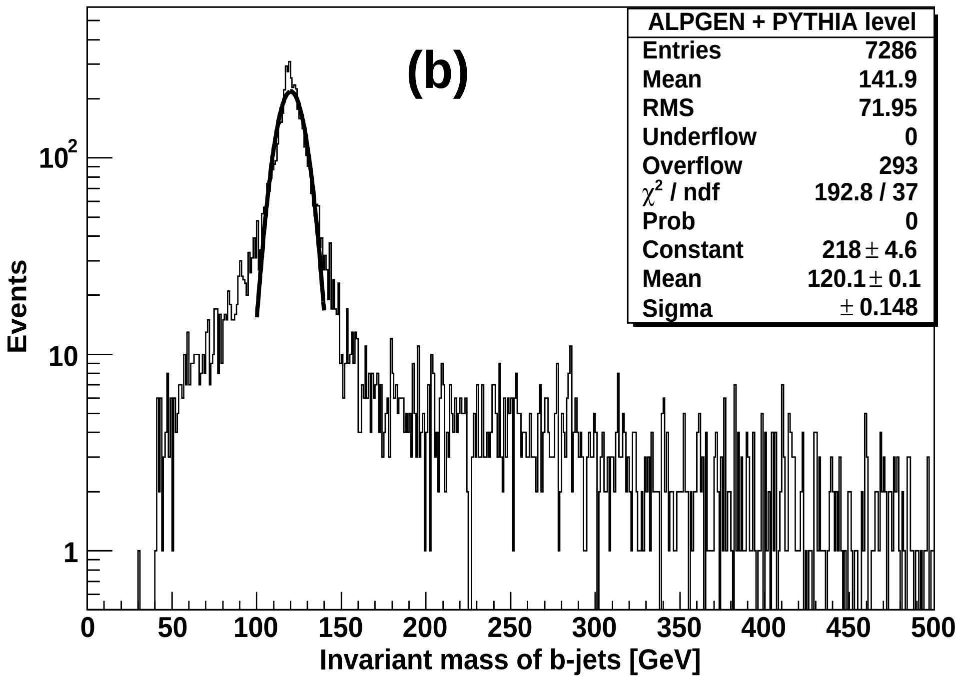

Figure 5.22: Invariant mass of b-jets at the generator (ALPGEN + PYTHIA level) using revised cuts (a) Linear scale (b) Log scale

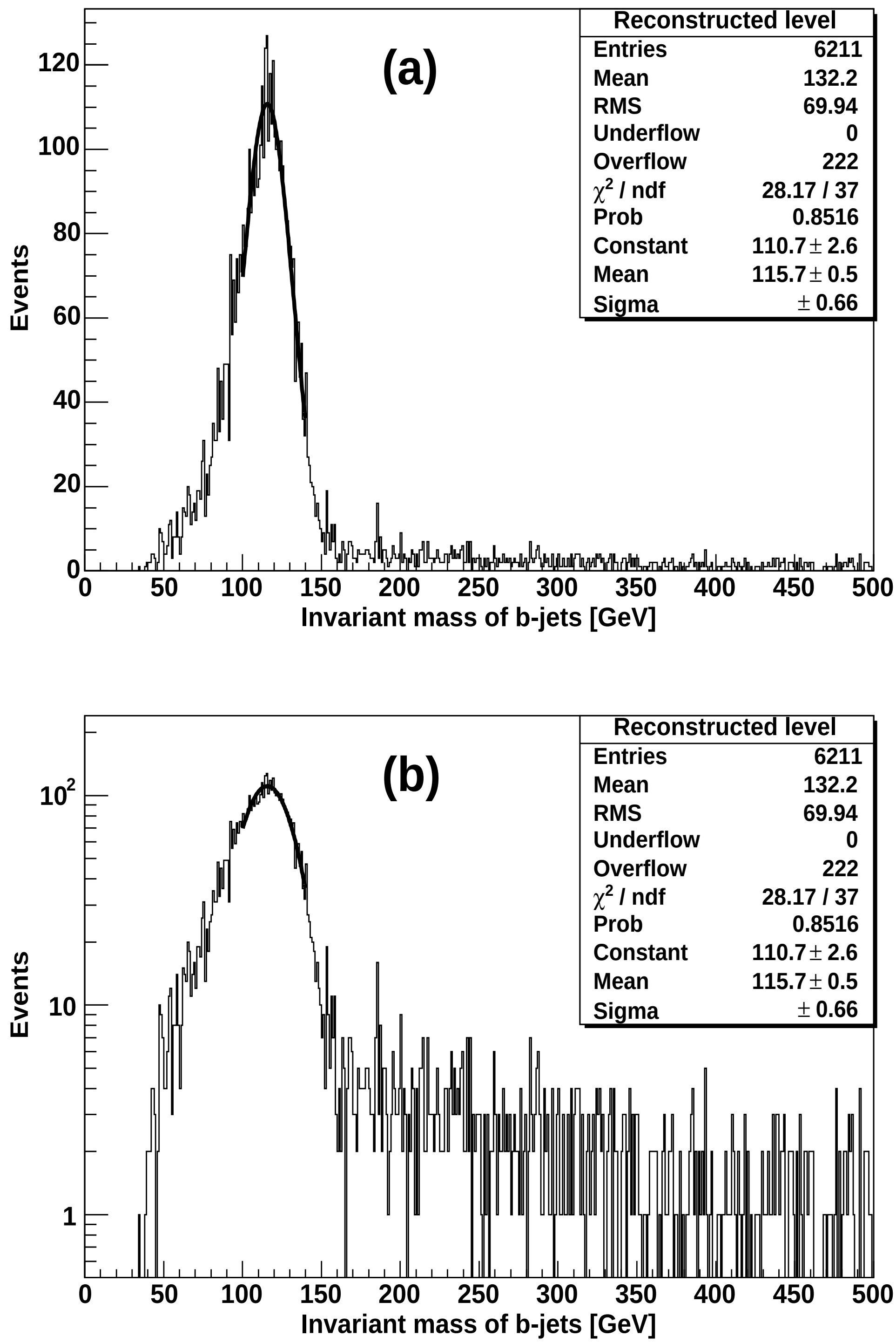

Figure 5.23: Invariant mass of b-jets at reconstructed level using revised cuts (a) Linear scale (b) Log scale

The number of events in different selection steps is shown in the table 5.3.

N_{evts}	Signal	Backgrounds			
		qcd_{bbjj}	qcd_{jjjj}	$t\bar{t}$	zjj
	50k	50k	50k	36k	35k
With cuts (2)	38099 (43251)	29633 (47209)	18798 (35308)	18925 (34130)	19819 (24944)
With cuts (2) & (5)	6211 (7286)	93 (190)	43 (57)	19 (23)	1164 (1737)
With cuts (2) & (5) & 100< M_H <140 GeV	3470 (4832)	16 (34)	9 (10)	1 (2)	161 (237)

Table 5.3: The number of events in different selection steps at reconstructed level (*generator level*) using revised cuts

5.7 Calculation

Using the number of events with 100 GeV $< m_H <$ 140 GeV, the cross-section σ for the signal & backgrounds is calculated as

$$\sigma = \frac{n}{N} \times \text{ cross-section}$$

where n = number of events surviving the cuts

N = total number of events

The cross-section using revised cuts eq. (5) is given in table 5.4. The numbers are corrected for the b-tagging efficiency to be 60% (0.6) in case of the signal events and b-mistagging efficiency of 1% (0.01) in case of QCD $jjjj$ background as

$\sigma_{signal} = \frac{n}{N} \times$ cross-section $\times$ branching ratio (H$\rightarrow b\bar{b}$) $\times$ $(b - tagging - efficiency)^2$

$\sigma_{jjjj} = \frac{n}{N} \times$ cross-section $\times$ $(b - mistagging - efficiency)^2$

Events	Cross-section(pb)	
	Generator level	Reconstructed level
signal	3.444×10^{-3}	2.473×10^{-3}
qcd_{bbjj}	4.3161	2.0311
qcd_{jjjj}	4.3006×10^{-2}	3.8705×10^{-2}
$t\bar{t}$	1.336×10^{-2}	6.68×10^{-3}
zjj	2.8222×10^{-3}	1.9171×10^{-3}

Table 5.4: The cross-section of signal and background events using revised cuts

The expected number of signal and background events for $60fb^{-1}$ integrated luminosity are shown in the table 5.5. This corresponds to one year of LHC running with low instantaneous luminosity of $2 \times 10^{33}cm^{-2}s^{-1}$.

Events	Generator level	Reconstructed level
$signal$	2.06×10^2	1.48×10^2
qcd_{bbjj}	2.589×10^5	1.218×10^5
qcd_{jjjj}	2.58×10^3	2.32×10^3
$t\bar{t}$	8.016×10^2	4.008×10^2
zjj	1.69×10^2	1.15×10^2

Table 5.5: Number of events for $60fb^{-1}$ luminosity

The Sensitivity defined as the ratio of the number of signal events divided by the square root of the number of background events is shown in table 5.6. Signal to background ratio ($S/\sqrt{B}$) significantly depends on the b-quark tagging algorithm efficiency since major background comes from the process QCD $bbjj$ & QCD $jjjj$. We are in process of generating large samples $\sim$ 100k events for signal & all backgrounds and use them for further analysis using b-tagging.

Level	($S/\sqrt{B}$)
Generator level	0.27327
Reconstructed level	0.283822

Table 5.6: Signal to background ratio

The identification of b-quark decay allows the selection of processes in which b quark are produced in particle decays. b-tagging is an example of a jet flavor tagging method which is the identification or "tagging" of jets originating from bottom quarks. Inclusive b-tagging approach is proposed for the light or intermediate mass Higgs boson which is expected to decay into b-quarks. Identifying the b-quarks helps in identifying the decay particles.

There are many methods which are based on the unique features of b-jets [19]. B hadrons containing b-quarks have the sufficiently long lifetime $\tau_B \sim 1.56ps$, which corresponds to a distance of $c\tau_B \sim 468\mu m$ before decaying as shown in figure 5.24.

The very precise silicon detector inside the particle detector can be used to identify the particles like b-quark that originate from different place. One more signature of the b-quark is that it is much massive than anything it decays into. Thus its decay products tends to have higher momentum perpendicular to the direction of b-quark making b-jets to be wider, having higher number of constituent particles and higher invariant mass. All these features can be measured and used to identify the b-jets from other type of jets.

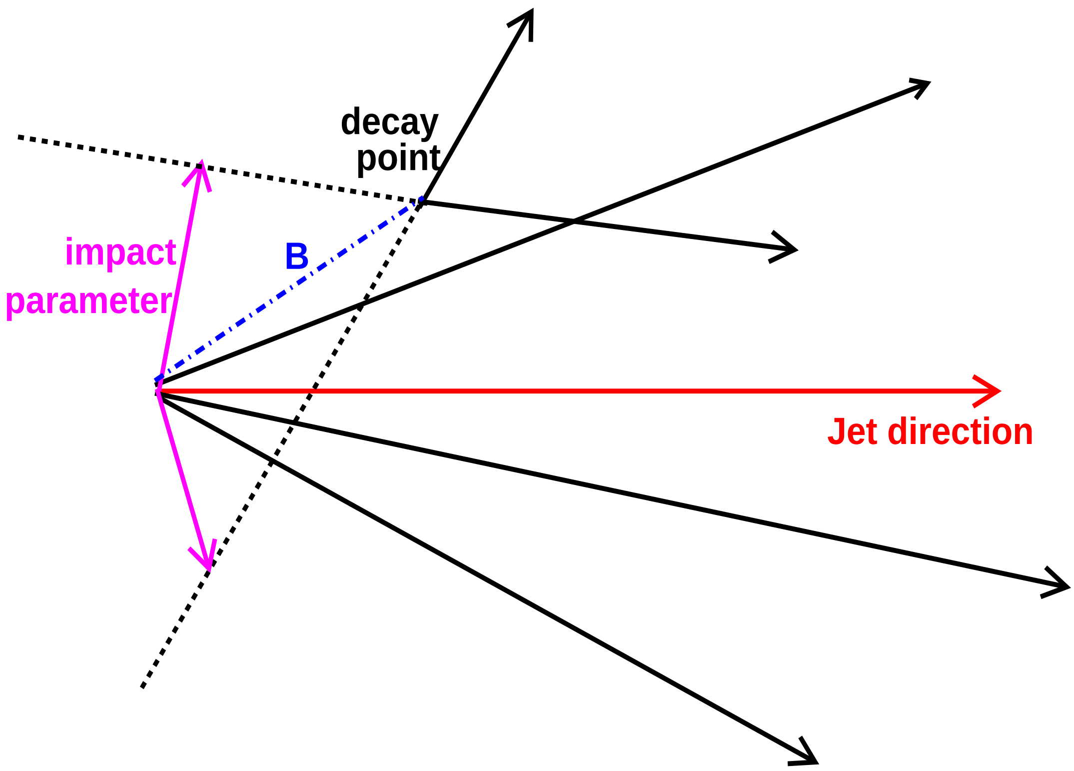

Figure 5.24: Representation of a hadron jet from b-quark

Methods based on Track Impact Parameter

The impact parameter of the track can be calculated as shown in figure 5.25. First of all, the point of closest approach of the track to the jet direction (S) is extracted corresponding approximately to the decay point of the B hadron, then tracks are linearized at that point i.e a tangent to the track is taken and the minimum distance of the linearized track from the primary vertex V i.e the three dimensional impact parameter is computed. The VO segment in figure 5.25 is called the decay length corresponds to the flight path of the B hadron.

The impact parameter can be positive or negative if the decay occurs downstream or upstream the jet i.e if the scaler product between the jet direction and the impact parameter direction is positive or negative. The arrow labeled with 'i.p' in figure 5.25 is the impact parameter. Since the jet direction approximates to the flight direction of the

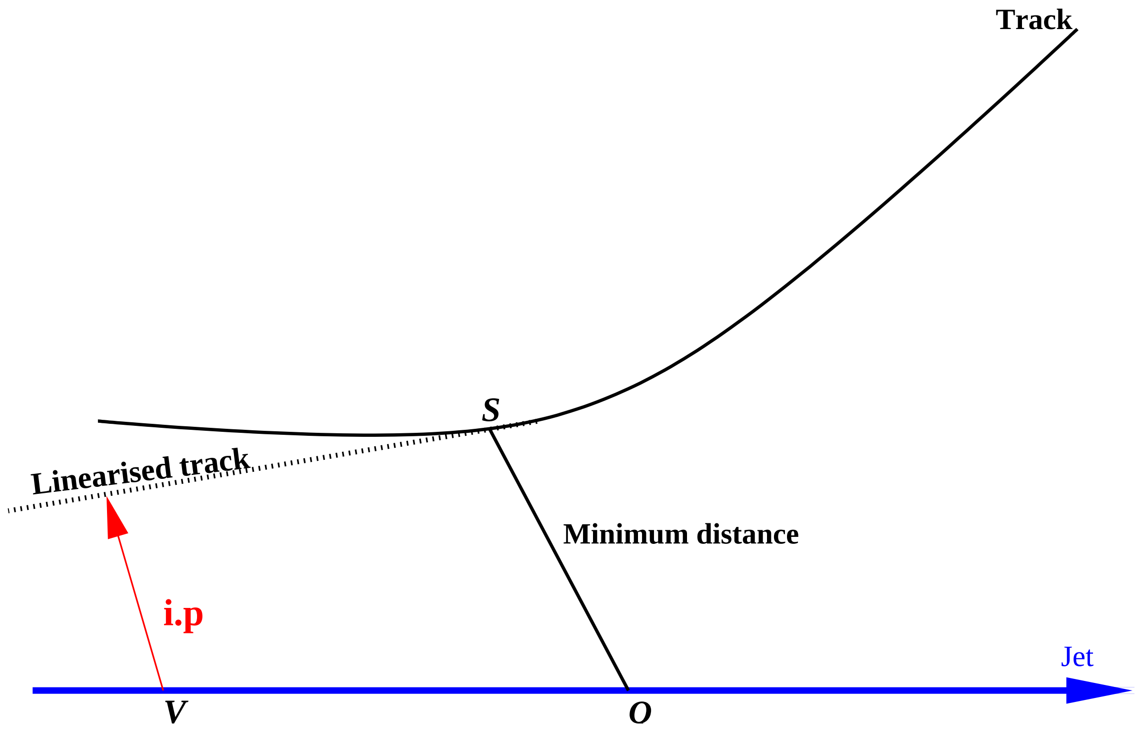

Figure 5.25: Representation of three dimensional impact parameter definition

B hadron, the tracks from a B decay have positive impact parameter. The sign of impact parameter can be flipped due to badly measured track parameters, badly reconstructed jet directions or primary vertices.

Track Counting Method

This method requires minimum number of good quality tracks with an impact parameter significance exceeding a given threshold. Different performance can be achieved by tuning the required number of tracks and choosing an appropriate threshold on the significance. The optimal choice of the parameters depends on the type of physics process under study. A very high efficiency for b-jets, with a reasonable mis-tagging rate for u-jets and c-jets can be achieved requiring atleast two tracks with an impact parameter significance larger than 3. This tagging condition is suitable for selecting processes with a large number of b-jets. On the other hand, if the signal contains a small number of jets, a reasonable

b-tagging efficiency with a very low mis-tagging rate can be achieved requiring at least 3 tracks with an impact parameter significance larger than 2.

The main advantage of Track counting method based on track impact parameters is its simplicity. It only relies on the selection of good quality tracks and lower cut on impact parameter significance. In addition, no further steps of reconstruction such as secondary vertex reconstruction are required. For $E_T \sim 50$ GeV jets, the methods based on impact parameter have a comparably good performance.

Bibliography

[1] H.Baer.et.al, Les Houches Guidebook to Monte Carlo Generators for Hadron Collider Physics, arXiv:hep-ph/0403045 v2 5 Mar 2004

[2] http://lepewwg.web.cern.ch/LEPEWWG

[3] G.Isidori, G.Ridolfi, A.Strumia, Nucl. Phys. B 609 (2001) 387; T.Hambye, K.Riesselmann, Phys. Rev. D 55 (1997) 7255

[4] Marcela Carena, John S. Conway, Howard E. Haber, John D. Hobbs, Report of the Tevatron Higgs Working Group, arXiv:hep−ph/0010338 v2 6 Dec 2000

[5] T.Han, S.Willenbrock, Phys. Lett. B 273 (1991) 167

[6] S. Darwan, L.H.Orr, L.Reina, D.Wackeroth, Proceedings of RADCOR/Loops and Legs, 2002, Sep. 8-13, 2002, Kloster Banz, Germany, ArXiv:hep-ph/0211373

[7] Urlik Egede, The search for a standard model Higgs at the LHC and electron identification using transition radiation in the ATLAS tracker, LUNFD6/(NFFL-7150) 1997.

[8] D.Rainwater, Intermediate-Mass Higgs Searches in Weak Boson Fusion, hep-ph/9908378

[9] M.L.Mangano, M. Moretti, F.Piccininni, R.Pittau and A.D. Polosa, $b\bar{b}$ final states in Higgs Production via Weak Boson Fusion at the LHC, hep-ph/0210261

[10] M.L. Mangano, M. Moretti, F. Piccinini, R. Pittau, A. Polosa, ALPGEN, a generator for hard multiparton processes in hadronic collisions, hep-ph/0206293

[11] Private communication with M.L.Mangano, M. Moretti, R.Pittau

[12] T. Sjostrand, Leif Lonnblad, PYTHIA 6.2 Physics and Manual, hep-ph/0108264August 2001

[13] V. Karimaki, A.Nikitenko, D. Bourilkov, S.Slabospitsky, User's Guide for CMS Physics Generators Interface CMKIN, CMS IN 2004/052

[14] Object-oriented Simulation for CMS Analysis and Reconstruction (OSCAR), http://cmsdoc.cern.ch/oscar/.

[15] Object-oriented Reconstruction for CMS Analysis (ORCA), http:// cmsdoc.cern.ch/orca/.

[16] P.Hidas, A.Nikitenko, S.Kunori, J.P.Wellisch, The JetMetAnalysis subsystem of ORCA ,CMS IN 2001/044

[17] A. Heister, O.Kodolova, S.Petrushanko, V. Konoplianikov, J.Rohlf, C.Tully, A. Ulyanov, Jet Reconstruction and Performance in the CMS Detector, CMS NOTE AN2005/005

[18] G.C.Blazey *et. al.*, Run II Jet Physics, hep-ex/0005012v22000

[19] CMS Tracker Technical Design Report TDR 5, CERN/LHCC 1998-6

Chapter 6

Conclusion

CMS designed as a general-purpose detector, suitable for studying many aspects of proton-proton collisions at 14 TeV, the center-of-mass energy of the Large Hadron Collider which is a particle accelerator. It contains a hierarchy of subsystems which are designed to measure the energy and momentum of photons, electrons, muons, and other products of the collisions. We fabricated and tested one of the subsystem of CMS detector called Outer Hadron calorimeter. The Outer Hadron calorimeter is an additional layer of scintillators outside the superconducting magnetic coil to sample the energy leakage from the barrel calorimeter. It increases the interaction length of the hadron calorimeter from 8 to 11.8.

The Outer Hadron calorimeter detector is made of 10 mm thick Bicron (BC-408) plastic scintillator sheets imported from United States. The large scintillator sheets are cut down to scintillator tiles of desired shape and size. Four sigma shaped grooves were made on the surface of each tile as per the design specification using Computer Numerical Control machine. All the tiles were cut and grooved with very high precision. Wave-length Shifting (WLS) optical fiber was inserted in each of the grooves and spliced with clear fiber for taking the signal from WLS fibers to the readout boxes consisting of Hybrid Photodiodes. The WLS fibers and the clear fibers were tested using fiber scanning machine before insertion. Out of the five rings of CMS outer hadron calorimeter, we fabricated 864 scintillator tiles of two rings namely +1 and -1. All the tiles subjected to various quality control test both manually and electronically. The manual inspection includes checking the thickness all along the surface. Electronically, all the tiles were tested using Cosmic ray setup to calculate their efficiency. All the machined and grooved tiles passed the acceptance criteria.

In order to simplify the installation procedure, the scintillator tiles of each ϕ slice were grouped together to form a bigger unit called a scintillator tray. The assembly of scintillator trays were done with utmost caution and precision such that the light emitted from the scintillator should not get any interference from surroundings. For this, special type of papers called tyvek and tedlar were used. The tyvek is an excellent reflector and tedlar is an excellent absorber of the light. Since each tray consists of group of tiles, the optical fibers from each tile are bunched together to form pigtails. There are two pigtails for each scintillator tray. All the pigtails were fully tested using radioactive pigtail scanner before inserting into scintillator trays. The fully fabricated scintillator trays were tested using cosmic ray test, radioactive wire-source test and radioactive X-Y scanner test. All the trays satisfied their respective acceptance criteria. In total, 432 scintillator trays and 864 pigtails were fabricated and tested for whole Outer Hadron Calorimeter. All the three tests were found to be correlated.

The fully assembled scintillator trays were shifted to CERN for installation into CMS detector. Before installation, all the scintillator trays were again tested with radioactive wire-source test and radioactive X-Y scanner test to check whether the transportation or geographical change effected the response of trays. By correlating the response of the trays before and after transportation, it is seen that there is no significant change in the output of the scintillator trays.

The scintillator trays were also exposed to beams of various particles at different energies. The Outer Hadron Calorimeter trays were calibrated using minimum ionising particle. The calibration constants are used in simulation softwares where the effect of detector modules over events are simulated. The calibration constants can also be used to monitor the behaviour of Outer Hadron Calorimeter with the passage of time. The calibration constants and resolution parameters calculated can be used to determine the energy of any particle passing through the calorimeter. Using pion beams at different energies, the importance of Outer Hadron Calorimeter in improving energy resolution of the Hadron Calorimeter is established. It was seen that the addition of HO layer(s) helps in reducing the tail in energy deposited by shower particles especially pions in Hadron Calorimeter.

The whole fabrication, testing and calibrations of the outer hadron calorimeter was done keeping in mind its importance in the energy measurement of jets in view of linearity and resolution. It will provide a net improvement in missing E_T measurements at LHC energies. The outer hadron calorimeter has a very good signal to background ratio even for a minimum ionising particle and can hence be used in coincidence with the Resistive Plate Chambers of the CMS detector for the muon trigger.

One of the main goals of CMS detector is to search for Higgs boson. There are many channels in which Higgs boson can be searched. One such channel is Higgs decaying into $b\bar{b}$ final state. We simulated the production of Higgs (H) events of 120 GeV mass and decays through H $\rightarrow$ $b\bar{b}$ at LHC energy. Since the real data will come when the CMS detector will be fully commissioned, till then, simulated data is the need for the physics analysis. The simulated data of thousands of events for both signal and backgrounds were generated using Matrix Element event generator interfaced with showering and hadronisation algorithm. The generated events were passed to detector simulation software simulating the CMS detector. The digitisation and reconstruction of all the events were performed for further analysis.

The Higgs boson at 120 GeV decays predominantly into $b\bar{b}$ final state. Inspite of the fact that the branching ratio for this channel is very high, it is the most difficult channel to search Higgs due to huge QCD backgrounds. We defined the method and strategy to reduce the enormous background to relatively low level. To reduce the enormous QCD backgrounds, the selection cuts pertaining to rapidity and invariant mass on the quark and b-jets have been optimised. We conclude that, with the combination of selection cuts on invariant mass of tag-jets which comes out to be 1 TeV and the rapidity difference of two tag-jets which comes out to be 4.2, the QCD backgrounds reduces to some extent in comparison to signal. We calculated cross-section for signal and background processes. The major source of background QCD $bbjj$ has the cross-section roughly 10^3 times that of signal. The other source of background is QCD four-jet events for which the cross-section is roughly 10 times that of signal.

The number of signal and background events with 60 fb^{-1} integrated luminosity equivalent to one year of LHC running with low instantaneous luminosity of $2 \times 10^{33} cm^{-2} s^{-1}$ has been estimated. The sensitivity of the signal is also calculated both at generator and reconstructed level. The signal significance is nearly 28 %. We conclude that the search for this channel can be refined using more specific algorithms for b-tagging in addition to the strategy and selection cuts we defined. This channel can be used for the determination of yukawa coupling of Higgs with bottom quark.

Annexure A

Some Important Concepts and Definitions

1) Units used in High Energy Physics

The fundamental constants are the velocity of light

$$c = 2.99 \times 10^{10} cm/sec$$

and $\hbar$, which is Planck's constant divided by 2π

$$\hbar = 6.6 \times 10^{-22}\text{MeV.sec}$$

From the values of $\hbar$ and c we can write:

$$\hbar c = 1.973 \times 10^{-11}\text{MeV.cm}$$

Since we have set $\hbar c$=1, length can be defined as

$$1 \text{ fm} = 10^{-13} cm = \tfrac{1}{197.3}\ MeV^{-1} \backsimeq 5\ GeV^{-1}$$

Also Cross-sections are measured in millibarns (mb), 1mb = $10^{-27} cm^2$). The following relation is very frequently used by physicists

$$1 GeV^{-2} = 0.389 \text{ mb}$$

2) Coordinates

The LHC collides the beams of protons with protons, therefore all physical observations are invariant under rotations around the beam line. Since the CMS detector is cylindrical in shape, many calculations are then simplified by using a cylindrical coordinate system with the z axis pointing along the beam direction. The polar angle θ is then measured with respect to z axis, and the azimuthal ϕ (by convention) with respect to a horizontal line perpendicular to the beam axis as shown in figure A.1

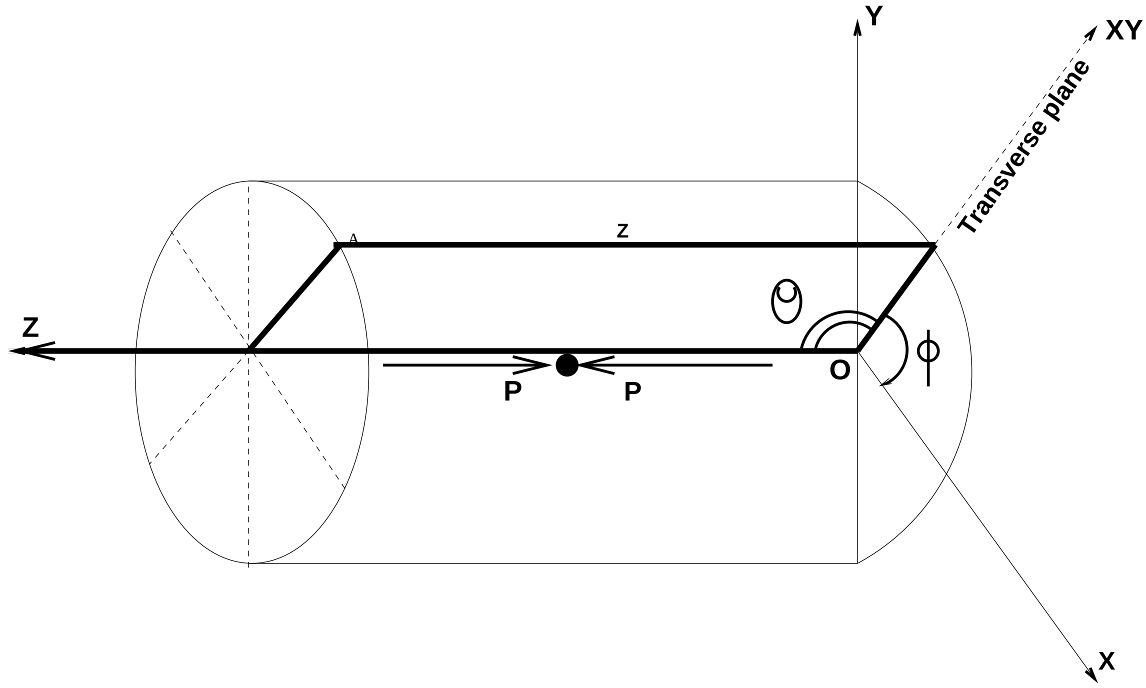

Figure A.1: Cylindrical coordinates

Since protons are composite particles, the interactions occur between individual partons and therefore the center of mass of an interaction at parton level can have a large momentum along the z axis in the lab frame of reference. To simplify calculations of cross-sections, it is customary to use a polar variable invariant under a boosts instead of a polar angle θ. We define a variable y (called "rapidity") such that

$$y = \frac{1}{2} ln(\frac{E+p_z}{E-p_z})$$

Rapidity y is usually approximated by "pseudo-rapidity" η

$$\eta{=}\frac{1}{2}ln(\frac{p+p_z}{p-p_z}) = -ln(tan\frac{\theta}{2})$$

which is independent of the mass of the particle and has a simple relationship with the polar angle. Pseudo-rapidity of a massless particle is equivalent to its rapidity; for massive particles the two are the same in the $p_T >>$ m limit.

Since in most cases one does not know the mass of a particle produced in a hadron collision (most are light- pions, kaons, baryons,..), we use pseudo-rapidity. Hence the phase space for particle production at a hadron collider is traditionally described in cylindrical coordinates with the z axis along the beam direction, transverse momentum (p_T), and Pseudo-rapidity (η).

Relation between Transverse Momentum (p_T) & Rapidity (η)

$$e^{\eta}{=}\sqrt{\frac{|p|+p_z}{|p|-p_z}} \text{ ————-(A)}$$

$$e^{-\eta}{=}\sqrt{\frac{|p|-p_z}{|p|+p_z}} \text{ ————-(B)}$$

Solving above equations $(A)\&(B)$: we get

$$|p|{=}p_T\ cosh\eta$$

where p_T is the magnitude of the transverse momentum:

$$p_T = \sqrt{p^2 - p_z^2}$$

subtracting (B) from (A) we obtain

$$p_T{=}\ p_T\ sinh\eta$$

3) Center-of-Mass frame (cms frame)

The Center-of-mass frame is the reference frame in which total 3 momentum is zero. If the total energy in the cms frame is denoted E^*, then we also have p^2= -E^{*2}.

In fixed target experiment, the cms energy for collision between A and B particles where particle B is stationary is

$$E^{*2}= -p^2=m_A^2 + m_B^2 + 2m_B E_A$$

In Collider beam experiments, the cms energy for collision between A & B moving toward each other is

$$E^{*2}=-p^2=2(E_A E_B + p_A p_B) + (m_A^2 + m_B^2) \sim 4\ E_A E_B$$

where
$m_{A,B}$ is the mass of particle A(B).
$E_{A,B}$ is the energy of particle A(B)

if m_A,m_B << E_A, E_B. This result is for head-on collision. For two beams crossing at an angle θ, the result would be E^{*2}=$2E_A E_B(1 + cos\theta)$. We note that the cms energy available for new particle creation in a collider with equal energies E in the two beams rises linearly with E, i.e. $E^* \sim$ 2E, while for the fixed-target machine the cms energy rises as the square root of the incident energy, $E^* \sim \sqrt{2m_B E_A}$. Obviously, therefore, the highest possible energies for creating new particles are to be found at colliding-beam accelerators.

4) Events and crossings

When discussing the simulation of LHC physics, a single pp interaction is referred to as an event, while a bunch-bunch interaction, which is generally the sum of several pp interactions, is referred to as a crossing.

5) Cross-section

A measure of the likelihood of a given process occurring at an accelerator. The idea is that two objects with a larger cross-sectional area are more likely to hit one another. So, larger cross-sections mean that a process is more likely to occur. Cross-sections are measured in barns, $10^{-28}m^2$. A barn is an extremely large cross-section in particle physics. Many interesting cross-sections are measured in pb (picobarns), which are equal to 10^{-12} barns.

6) Luminosity

Luminosity is the number of particles per unit area per unit time, usually expressed in either the cgs units $cm^{-2}s^{-1}$ or $b^{-1}s^{-1}$ (Inverse barn per second). The luminosity is an important value to characterize the performance of an accelerator.
For an intersecting storage ring collider:

$$L = fn\frac{N_1N_2}{A}$$

where f is the revolution frequency

n is the number of bunches in one beam in the storage ring.

$N_{1,2}$ is the number of particles in each beam

A is the cross section of the beam.

7) Integrated luminosity

It is a measure of the total data collected at an accelerator. It is the intensity of the accelerator, summed over some specified time period.

$$L_{int} = \int_{time} L.dt$$

Its unit is $barn^{-1}$. A $barn^{-1}$ (inverse barn) of data will give one event for a process that has a cross-section of one barn. A $picobarn^{-1}$ will give one event for a much rarer process that has a cross-section of one picobarn.

8) Branching Ratio

When a particle decays, it often can decay in several ways. The likelihood of it decaying to a particular mode is known as its branching ratio for that decay mode.

9) Interaction Length

The mean free path of a particle which is the measure of its probability of undergoing interactions of a given kind, before undergoing an interaction that is neither elastic nor quasi-elastic (diffractive), in a given medium, usually designated by λ.

10) Drift velocity

The drift velocity is the average velocity that a particle, such as an electron, attains due to an electric field. Since particles can accelerate arbitrarily close to the speed of light in the absence of other forces, the term drift velocity can only really apply to carriers in materials, and not to particles in a vacuum

11) Superconducting Solenoid

Solenoid refers specifically to a magnet designed to produce a uniform magnetic field in experiments in which they are being used. Typically, a solenoid is a loop of wire, often wrapped around a metallic core, which produces a magnetic field when an electrical current is passed through it. Solenoids are important because they can create controlled magnetic fields and can be used as electromagnets.

Superconducting solenoids consists of electromagnets that are partially built from superconducting materials and therefore reach much higher magnetic field intensity. Typical solenoid material used are niobium-titanium

12) Calorimeter

A calorimeter is a composite detector which uses total absorption of particles to measure the energy and position of incident particles or jets. In the process of absorption showers are generated by cascades of interactions, hence the occasionally used name shower counter for a calorimeter. In the course of showering, eventually, most of the incident particle energy will be converted into heat, which explains the name calorimeter, calor = Latin for heat, for this kind of detector, of course, no temperature is measured in practical detectors, but characteristic interactions with matter e.g. atomic excitation, ionization etc are used to generate a detectable effect, via particle charges. Calorimetry is also the only practicable way to measure neutral particles among the secondaries produced in a high-energy collision.

13) Scintillator

A scintillator is a device or substance that absorbs high energy ionizing electromagnetic or charged particle radiation then, in response, fluoresces photons at a characteristic longer wavelength, releasing the previously absorbed energy

14) WLS fibers

The optical fibers that converts the short wavelength light , $\lambda < 400$ nm, emitted by scintillator material into a longer wavelength blue light, $\lambda > 400$ nm. These fibers can absorb energy from all over their surface. Wave-Length Shifting (WLS) optical fibers are used to collect the light produced in the tiles. The plastic in these fibers have been doped with special dyes that absorb the predominantly blue light from the scintillator and re-emit green light. A fraction of this green light $\sim 6\%$ is captured in the fiber by internal reflection at the core-cladding boundary. The light is transmitted through the fiber to a photo-multiplier tube (PMT). To enhance the light yield, the other end of the fiber is polished and coated with Aluminum to make a mirror surface. Typical attenuation length of WLS fiber is $\approx$ 2m.

15) Interactions in CMS Calorimeters

Interactions are processes in which the particles respond to the force due to the presence of other particles or the particles decay into other particles. Neglecting gravity, which has no measurable effects on the scale of particle interactions, there are three basic types of interactions, Electromagnetic, Strong and the Weak Interactions.

Fundamental electromagnetic interactions occur between any two particles that have electric charge. These interactions involve the exchange or production of photons. The electromagnetic interaction is the best understood of the three interaction types most important for elementary particle physics. Fundamental weak interactions occur for all fundamental particles except gluons and photons. Weak forces are very short-ranged. Hadrons are viewed as being composed of quarks, either as quark-antiquark pairs (mesons) or as three quarks (baryons). In addition to the quark pairs there are cloud of gluons surrounds the constituent quarks, the exchange particles for the color force. Particles that interacts by strong interaction are called hadrons.The resulting hadrons have no net color charge.

16) Showers in Calorimeters

In particle physics, a shower is a cascade of secondary particles produced as the result of a high-energy particle interacting with dense matter. The incoming particle interacts, producing multiple new particles with lesser energy, each of these then interacts in the same way, a process that continues until many thousands, millions, or even billions of low-energy particles are produced. These are then stopped in the matter and absorbed.

There are two basic types of showers. Electromagnetic showers are produced by a particle that interacts primarily or exclusively via the electromagnetic force, usually a photon or electron. Hadronic showers are produced by hadrons i.e. nucleons and other particles made of quarks, and proceed mostly via the strong nuclear force.

a) Electromagnetic Shower

Electrons and positrons behave exactly the same way in a detector as far as shower is concerned. Consider an electron or positron with several GeV of energy traversing in some material. For energies above 100 MeV, the electrons lose energy almost entirely through bremsstrahlung. The emitted photon carry off a large fraction of the electron's initial energy. For photons with energy greater than 100 MeV the major interaction is pair production which gives another energetic electron or photon. Thus a single electron or photon is the starting point of avalanche of electrons, positrons and further gamma rays.

If these fast moving electrons and positrons go on to pass close to other nuclei then they will suffer accelerations due to the positive charge of protons. An accelerated charges particle will emit electromagnetic radiation. The intense accelerations can produce photons capable of producing more electron-positron pairs. Secondary particle production continues until photon falls below the pair-production threshold, and energy losses of electrons other than bremsstrahlung starts to dominate: the number of shower particles decay exponentially. Electromagnetic shower is confined to smaller regions in solids that are dense. If the material is made up of atoms with a high atomic number then the greater nuclear charges can produce greater accelerations and so the cascade process can develop more readily than it would in a material with lower atomic number

b) Hadronic Shower

The hadronic showering process is dominated by a succession of inelastic hadronic interactions. At high energy, these are characterised by multiparticle production and particle emission originating from nuclear decay of excited nuclei. The physical processes that cause the propagation of the hadronic shower are considerably different from the electromagnetic showers. Due to the relatively frequent generation of π^o's, there is also an electromagnetic component present in hadronic showers. A typical hadron is produced with a transverse momentum of ≈350 MeV/c, so that hadronic showers tend to be more laterally spreadout than electromagnetic ones. Also they take much longer to develop and are much deeper than the electromagnetic showers. To completely contain the shower, we need the detector to be deeper.

Secondaries are mostly pions and nucleons. The hadronic multiplication process is measured at the scale of nuclear interaction length, which is essentially energy-independent.

17) Partons

The constituents of protons and neutrons are quarks, gluons and anti-quarks. They are collectively known as partons. The term partons means "point like" particles

18) Parton Distribution Function

These functions parameterize the composition of various hadrons are called parton distribution function. They describe the probability of finding a given constituent with a given momentum.

19) Jets in particle physics

A jet is a narrow cone of hadrons and other particles produced by the hadronisation of a quark or gluon in a particle physics or heavy ion experiment. Because of QCD confinement, particles carrying a color charge, such as quarks, cannot exist in free form. Therefore they fragment into hadrons before they can be directly detected, becoming jets. These jets must be measured in a particle detector and studied in order to determine the properties of the original quark. Figure A.2 shows the formation of jets in p-p collisions at LHC.

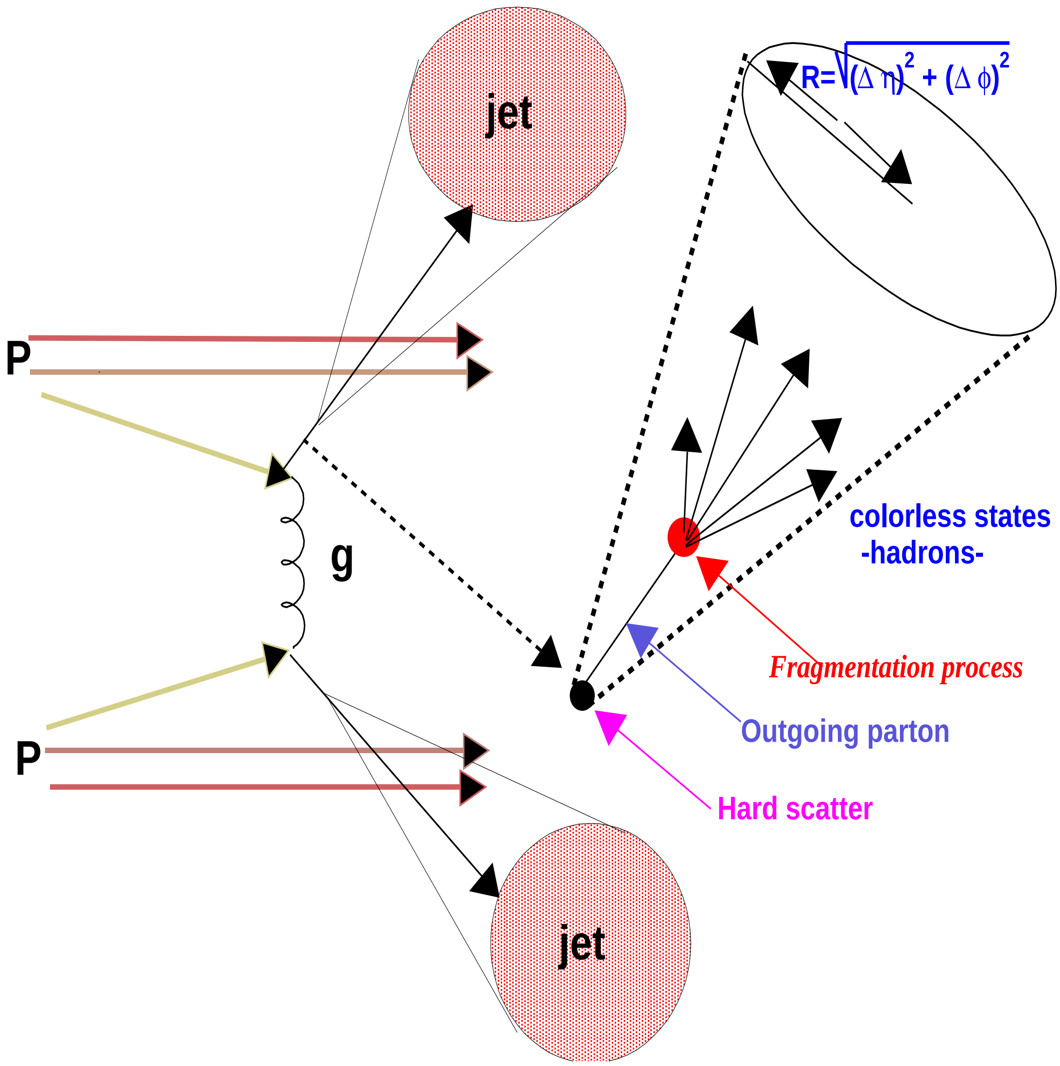

Figure A.2: Jet Formation in p-p collisions at LHC

Jets at Particle level (Generated) & Detector level (Reconstructed)

Jets at particle level (Generated) are set of particles at the vertex level in the definite cone and Jets at detector level (Reconstructed) is set of calorimeter towers at the detector level in the define cone as shown in figure A.3.

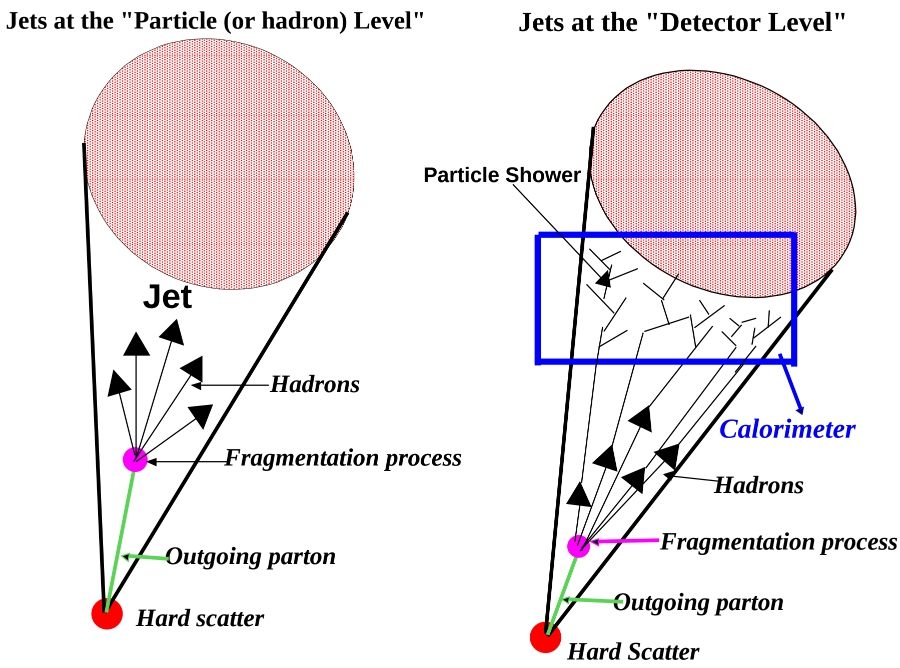

Figure A.3: Particle level & detector level jets

20) Transverse Energy of a jet (E_T)

The transverse energy (E_T) is defined as the energy in the plane perpendicular to the beam axis. The transverse energy of a jet is defined as E_T = E sin(θ), where E is the jet or calorimeter cell energy and θ is the angle between the beam direction and the direction of the jet or vector pointing from the interaction vertex to the calorimeter cell.

21) Invariant Mass

The invariant mass or intrinsic mass or proper mass or rest mass is a measurement or calculation of the mass of an object that is the same for all frames of reference. It is known as rest mass for objects, because it is the mass of an object that an observer would measure in the inertial frame of reference in which the object is at rest. For any frame of reference, the invariant mass may be determined from an object's total energy and momentum.

The definition of the invariant mass of a system of particles shows that it is equal to total system energy divided by c^2 when the system is viewed from an inertial reference frame which minimizes the total system energy. This reference frame is that in which the velocity of the the system's center of mass is zero, and the system's total momentum is zero. This frame is also known as the center of mass or center of momentum frame.

The invariant mass of a system of decay particles which originate from a single originating particle, is related to the rest mass of the original particle by the following equation

$$W^2c^4 = (\Sigma E)^2 - (\Sigma pc)^2$$

where

W is the invariant mass of the system of particles, equal to the rest mass of the decay particle.

ΣE is the sum of the energies of the particles

Σpc is the vector sum of the momenta of the particles includes both magnitude and direction of the momenta times the speed of light.

22) Weighted and Unweighted Events

The event generator generates events according to phase space distributions. The events may be weighted or unweighted. Unweighted implies generating events with unit phase space weight which could require generating many events before finding one acceptable to the population. When generating unit weight events the program must establish the maximum possible event weight . This is done in a simple minded fashion by throwing N events and recording the maximum weight from the sample. The maximum weight is needed to determine if a particular event is admissible to the population of events. It is most efficient CPU-wise to generate weighted events. When generating weighted events one must respect the event weight when counting events.